

Copyright

by

Charles Edward Webb

2007

**The Dissertation Committee for Charles Edward Webb Certifies that this is the
approved version of the following dissertation:**

**Radiation Force Modeling for
ICESat Precision Orbit Determination**

Committee:

Bob E. Schutz, Supervisor

Byron D. Tapley

Wallace T. Fowler

Hyung-Jin Rim

Daniel G. Kubitschek

**Radiation Force Modeling for
ICESat Precision Orbit Determination**

by

Charles Edward Webb, B.S.; M.S.

Dissertation

Presented to the Faculty of the Graduate School of

The University of Texas at Austin

in Partial Fulfillment

of the Requirements

for the Degree of

Doctor of Philosophy

The University of Texas at Austin

May 2007

Dedication

For my parents, Paul and Verna Webb,
whose support and encouragement fill my earliest memories.

Acknowledgements

As an Edison Engineer at the GE Astro Space facility in Princeton, New Jersey, I took what was supposed to be a six-month assignment in a group called Mission Design and Analysis. I told the manager, Mike Holman, up front, that I didn't know anything about orbital mechanics. He handed me a copy of *Fundamentals of Astrodynamics*, by Bate, Mueller and White — known to me ever since simply as BMW — and told me to start reading. I would like to thank Mike, and all of my former colleagues, especially James Swale, Tara Palamarik, and Frank Stoner, for introducing me to this remarkable field. Their knowledge and experience proved to be invaluable resources for me.

Leaving this group after more than three years, I came to graduate school at the University of Texas at Austin, hoping to fill in the gaps in my limited, and inherently practical, training. Determined to study theoretical orbital mechanics, I was told repeatedly, by professors at other schools, that there was no research money in it. I would have to do something *applied*, something in attitude dynamics and control, or in ground-based GPS receiver applications. Resisting all of these efforts to divert me, I chose to come back to Texas, and to take classes with Roger Broucke and Victor Szebehely.

Even more significantly, I found myself working as a research assistant for Bob Schutz. I would like to express my profound thanks to him, for allowing me to have exactly the graduate school experience that I wanted. After leaving me almost entirely alone for the first year, to concentrate on classes, he gradually

introduced me to what eventually became ICESat. One of my first tasks was to redesign the reference orbits for the mission, which involved a number of theoretical issues, but in a very practical context. Since then, he has either encouraged, or allowed, me to work on nearly every aspect of this mission. It has been, and continues to be, an extraordinary experience.

I would also like to thank the other members of my committee. Two of them, Byron Tapley and Wallace Fowler, taught classes, in orbit determination and mission design, respectively, that addressed a number of theoretical questions arising from my work at GE. Hyung-Jin Rim introduced me to the intricacies of his Multi-Satellite Orbit Determination Program, and patiently mentored me in the art of orbit determination simulation. Although I have yet to meet Dan Kubitschek, who volunteered to serve on this committee a lifetime ago, I am grateful that he has graciously agreed to see this process through to the end.

The actual work for this dissertation would not have been possible without the assistance of several people. In particular, I would like to thank Phil Mackey and Joe Clay, of Space Design, Inc., for their lengthy and thorough efforts to implement the radiation force algorithms presented here in the Thermal Synthesizer System (TSS). I would also like to thank Eric Kelly and Scott Mitchell, of Ball Aerospace, for their assistance with the ICESat thermal models, and Charles Baker, of the Goddard Space Flight Center, for his tutorials on the use of TSS.

Obviously, this entire experience has taken place in a much larger context, supported and facilitated by a number of people very important to me. I would like to thank Stephanie Jensen, whom I met at Cornell, when we were both very

new in the world — me, especially. I am grateful for her friendship, her unwavering confidence and trust in me, and of course, her willingness to vacation with me. I cannot imagine what this episode in my life would have been like had I not met Lori Magruder. I treasure the adventures that we shared together here, and the friendship that grew out of them. I am also indebted to Toby Emert, who went through his own version of this process just before I met him. His encouragement and quiet reassurance helped lift my spirits many times, and our shared penchant for long conversations always proved to be a welcome distraction.

It would be impossible for me to write about the time I have spent here without mentioning my nephews, Michael and William, and my niece, Katherine. I am truly grateful to have been able to witness their entire lives thus far. Their presence has changed my life in ways that I didn't know were possible. For that, and so much more, I would like to thank my sister, Laura Carvalho, who actively encourages me in my relationship with each of them. I am also grateful to her for a lifetime of sibling history, filled with shared joys and losses. Although I have alluded to my parents, Paul and Verna Webb, through the dedication of this dissertation, I would like to say, clearly, how deeply thankful I am for their constant support and encouragement. As I have gotten older, I have learned just how rare it was to be raised by people who told their children, from a very young age, that they could do anything, could be anything, they wanted.

Finally, I would like to thank Ilan Guedj, who, within a relatively short period of time, managed to make me want to think about what comes next in my life.

Radiation Force Modeling for ICESat Precision Orbit Determination

Publication No. _____

Charles Edward Webb, Ph.D.

The University of Texas at Austin, 2007

Supervisor: Bob E. Schutz

Precision orbit determination (POD) for the Ice, Cloud and land Elevation Satellite (ICESat) relies on an epoch-state batch filter, in which the dynamic models play a central role. Its implementation in the Multi-Satellite Orbit Determination Program (MSODP) originally included a box-and-wing model, representing the TOPEX/Poseidon satellite, to compute solar radiation forces. This “macro-model” has been adapted to the ICESat geometry, and additionally, extended to the calculation of forces induced by radiation reflected and emitted from the Earth.

To determine the area and reflectivity parameters of the ICESat macro-model surfaces, a high-fidelity simulation of the radiation forces in low-Earth orbit was first developed, using a detailed model of the satellite, called the “micro-model”. In this effort, new algorithms to compute such forces were adapted from a Monte Carlo Ray Tracing (MCRT) method originally designed to

determine incident heating rates. After working with the vendor of the Thermal Synthesizer System (TSS) to implement these algorithms, a modified version of this software was employed to generate solar and Earth radiation forces for all ICESat orbit and attitude geometries. Estimates of the macro-model parameters were then obtained from a least-squares fit to these micro-model forces, applying an algorithm that also incorporated linear equality and inequality constraints to ensure feasible solutions.

Three of these fitted solutions were selected for post-launch evaluation. Two represented conditions at the start and at the end of the mission, while the third comprised four separate solutions, one for each of the nominal satellite attitudes. In addition, three other sets of macro-model parameters were derived from area-weighted averaging of the micro-model reflectivities. They included solar-only and infrared-only spectral parameters, as well as a set combining these parameters. Daily POD solutions were generated with each of these macro-model sets, for eight-day intervals in four different ICESat mapping campaigns. As a group, the fitted parameters slightly outperformed the averaged parameters, based on a variety of metrics. Their impact on POD accuracy, however, was limited to the sub-millimeter level, as measured by independent satellite laser ranging (SLR) residuals. As a result, no change to the nominal macro-model parameters is recommended.

Table of Contents

Table of Contents	x
List of Tables	xv
List of Figures	xvii
Glossary of Acronyms	xx
Chapter 1: Introduction	1
1.1 The ICESat Mission.....	1
1.2 Surface Elevation Measurements	4
1.3 Precision Orbit Determination.....	9
1.3.1 Dynamic Modeling	11
1.3.2 Observation Modeling.....	13
1.3.3 The Orbit Determination Problem.....	16
1.3.4 The Epoch-State Batch Filter.....	20
1.4 Research Objectives	22
Chapter 2: Incident Radiation in Low-Earth Orbit	28
2.1 Fundamental Radiation Quantities.....	28
2.1.1 Irradiance.....	29
2.1.2 Radiosity.....	32
2.2 Direct Solar Radiation	35
2.3 Earth Albedo and Emissivity.....	40

2.4	Eclipsing	44
Chapter 3: Radiation Pressure Modeling		50
3.1	Existence of Radiation Pressure.....	50
3.2	Surface Reflection	56
3.3	Early Orbit Determination Models	61
3.3.1	Solar Radiation Pressure.....	62
3.3.2	Earth Radiation Pressure.....	66
3.3.3	TOPEX/Poseidon Macro-Model	71
3.4	ICESat Modeling	74
3.4.1	Earth Radiation Pressure.....	75
3.4.2	Satellite Attitude	76
3.4.3	Solar Array Articulation	83
3.4.4	Solar Array Inhibition.....	85
Chapter 4: Micro-Model Force History Generation		90
4.1	The Thermal Synthesizer System	90
4.1.1	Incident Heat Rate Problem	92
4.1.2	Monte Carlo Ray Tracing Formulation	94
4.1.3	Incident Heat Rates for Solar and Earth Radiation.....	101
4.1.4	Solar and Earth Radiation Forces.....	104
4.2	Simulation Methodology	108
4.2.1	Satellite Model	109
4.2.2	Orbit Generation	112

4.2.3	Satellite Attitude and Solar Array Articulation.....	116
4.2.4	Force History Generation.....	118
4.3	Simulation Results.....	125
4.3.1	Solar Array Articulation	131
4.3.2	Surface Property Degradation.....	136
Chapter 5:	Macro-Model Parameter Determination	143
5.1	Direct Determination of Parameters.....	143
5.1.1	Surface Areas	145
5.1.2	Surface Reflectivities.....	151
5.2	Estimation of Parameters	154
5.2.1	Radiation Force Model.....	155
5.2.2	Linearized Radiation Force Model	158
5.2.3	Equality and Inequality Constraints	160
5.2.4	Elimination of Equality Constraints	166
5.2.5	Transformation to Least Distance Problem	168
5.2.6	Solution in Dual Form	170
5.3	Pre-Launch Solutions and Assessment.....	171
5.3.1	Nominal BOL Solution.....	174
5.3.2	Attitude-Specific Solutions.....	186
5.3.3	Nominal EOL Solution.....	196
5.3.4	POD Simulation.....	202

Chapter 6: Post-Launch Performance	208
6.1 Evaluation Periods.....	208
6.2 DDHL Residuals	211
6.3 Orbit Overlap Differences	212
6.4 SLR Residuals.....	215
6.5 Empirical Forces	219
6.6 Orbit Differences.....	221
Chapter 7: Conclusions	223
7.1 Summary	223
7.2 Conclusions	225
7.3 Recommendations.....	228
Appendix A: GLAS Laser Reference Point	230
A.1 Laser Reference Point (GCS).....	231
A.2 Center of Mass (SCS)	231
A.3 SCS to ICRF Transformation.....	232
A.4 Combined Errors	235
Appendix B: Box-Wing Earth Radiation Pressure	
Partial Derivatives	239
B.1 Satellite Position.....	240
B.2 Macro-Model Surface Properties	242
B.3 Earth Radiation Scale Factors.....	243
B.4 Albedo Model Coefficients	244

B.5 Emissivity Model Coefficients.....	246
Appendix C: MSODP Box-Wing Earth Radiation	
Pressure Source Code	248
Appendix D: MSODP GLAS Solar Array Source Code	263
References	269
Vita	288

List of Tables

2.1	Earth Albedo and Emissivity Model Coefficients.....	44
3.1	β' Constraints for Nominal Attitude Control Frames	80
4.1	Micro-Model BOL Radiative Properties	111
4.2	TSS Orbit Simulation Parameters	112
4.3	TSS Attitude Model Euler Rotation Sequences	116
4.4	Nominal Radiation Force Simulation Cases: $\beta' \leq 0^\circ$	120
4.5	Nominal Radiation Force Simulation Cases: $\beta' \geq 0^\circ$	121
4.6	Supplemental Radiation Force Simulation Cases: $\beta' \leq 0^\circ$	122
4.7	Supplemental Radiation Force Simulation Cases: $\beta' \geq 0^\circ$	122
4.8	Representative Force History Cases	125
4.9	Micro-Model EOL Radiative Properties	138
5.1	Macro-Model Surface Areas	151
5.2	Area-Weighted Average Reflectivities	153
5.3a	Nominal BOL Solution	178
5.3b	Nominal BOL Residual Statistics	178
5.4a	Unconstrained Solution.....	179
5.4b	Unconstrained Residual Statistics.....	179
5.5a	ICESat Nominal BOL Residual Statistics.....	180
5.5b	TOPEX/Poseidon Residual Statistics.....	180
5.6	Micro-Model Cases for Attitude-Specific Solutions.....	186
5.7a	Yaw = 270° Solution	188
5.7b	Yaw = 270° Residual Statistics	188

5.8a	Yaw = 0° Solution.....	190
5.8b	Yaw = 0° Residual Statistics.....	190
5.9a	Yaw = 180° Solution	192
5.9b	Yaw = 180° Residual Statistics	192
5.10a	Yaw = 90° Solution	194
5.10b	Yaw = 90° Residual Statistics	194
5.11a	Nominal EOL Solution	197
5.11b	Nominal EOL Residual Statistics	197
5.12	Original POD Simulation Orbit Errors.....	203
5.13	Macro-Micro Model Orbit Errors.....	205
5.14	Dynamic and Measurement Model Orbit Errors: No Radiation Force Model Errors.....	206
5.15	Dynamic and Measurement Model Orbit Errors: Including Macro-Micro Model Errors.....	207
6.1	Post-Launch POD Evaluation Periods	208
6.2	Macro-Model Parameter Sets.....	210
6.3	Mean DDHL Residual RMS	212
6.4	Mean Orbit Overlap RMS	214
6.5	SLR Residuals: All Passes	217
6.6	SLR Residuals: High-Elevation Passes.....	218
6.7	Amplitudes of Estimated Empirical Forces	220
6.8	RMS Orbit Differences from Nominal BOL Solution.....	222

List of Figures

1.1	One-Way Range Geolocation Geometry	6
1.2	SCS and ICRF Position Vectors for Satellite Center of Mass and Laser Reference Point.....	10
1.3	Double-Difference High-Low Geometry	17
1.4	Typical IGS Tracking Stations in ICESat POD	17
2.1	The Electromagnetic Spectrum.....	28
2.2	Radiation Geometry for a Differential Area	30
2.3	Variations in Total Solar Irradiance at the Earth	39
2.4	Spectral Distribution of Solar Irradiance at the Earth	39
2.5	Earth Radiation Geometry	41
2.6	Cylindrical Shadow Model.....	45
2.7	Conical Shadow Model	47
2.8	Partial Eclipse of the Sun by the Earth.....	49
3.1	Bidirectional Reflection	58
3.2	Combined Diffuse and Specular Reflection	59
3.3	Earth Radiation Pressure Geometry.....	70
3.4	TOPEX/Poseidon Macro-Model.....	72
3.5	ICESat Macro-Model	75
3.6	Definition of β' Angle.....	78
3.7	Projected β' Angle During ICESat Mission.....	78
3.8	ICESat Nominal Attitude Control Frames	79
3.9	Solar Array Orientation Angle	85

3.10	Stop Angle for Solar Array Inhibition	86
4.1	General Incident Radiation Geometry	93
4.2	Incident Radiation Geometry in Low-Earth Orbit	96
4.3	MCRT Geometry for Incident Radiation.....	98
4.4	ICESat Micro-Model and Vehicle Coordinate System	110
4.5	Earth Albedo and Emissivity for $\beta' \leq 0^\circ$ and $\beta' \geq 0^\circ$	114
4.6	TSS Reference and Orbit Coordinate Systems.....	115
4.7	Micro-Model Simulation Attitude Control Frames.....	117
4.8	Case 9 Radiation Forces	127
4.9	Case 14 Radiation Forces	128
4.10	Case 21 Radiation Forces	129
4.11	Case 37 Radiation Forces	130
4.12	Solar Array Orientation Angles	133
4.13	Case 32 Radiation Forces	134
4.14	Case 33 Radiation Forces	135
4.15	Case 9 EOL–BOL Radiation Force Differences	139
4.16	Case 14 EOL–BOL Radiation Force Differences.....	140
4.17	Case 21 EOL–BOL Radiation Force Differences.....	141
4.18	Case 37 EOL–BOL Radiation Force Differences.....	142
5.1	+ x Orientation: Micro-Model and Macro-Model.....	147
5.2	– x Orientation: Micro-Model and Macro-Model.....	147
5.3	+ y Orientation: Micro-Model and Macro-Model.....	148
5.4	– y Orientation: Micro-Model and Macro-Model.....	148
5.5	+ z Orientation: Micro-Model and Macro-Model	149

5.6	$-z$ Orientation: Micro-Model and Macro-Model	150
5.7	Macro-Model Parameter Estimation Algorithm.....	172
5.8	Case 9 Nominal BOL Residual Forces	181
5.9	Case 14 Nominal BOL Residual Forces	182
5.10	Case 21 Nominal BOL Residual Forces	183
5.11	Case 37 Nominal BOL Residual Forces	184
5.12	Micro-Model Nodes Illuminated by Solar Radiation	185
5.13	Case 9 Attitude-Specific Residual Forces.....	189
5.14	Case 14 Attitude-Specific Residual Forces.....	191
5.15	Case 21 Attitude-Specific Residual Forces.....	193
5.16	Case 37 Attitude-Specific Residual Forces.....	195
5.17	Case 9 Nominal EOL Residual Forces	198
5.18	Case 14 Nominal EOL Residual Forces	199
5.19	Case 21 Nominal EOL Residual Forces	200
5.20	Case 37 Nominal EOL Residual Forces	201
6.1	Orbit Overlaps.....	213
6.2	SLR Observation Geometry.....	216
A.1	Relative SCS and GCS Orientations	233

Glossary of Acronyms

1-cpr	One Cycle Per Revolution
ADCS	Attitude Determination and Control Subsystem
AOL	Airborne Oceanographic Lidar
ASTM	American Society for Testing and Materials
AU	Astronomical Unit
BATC	Ball Aerospace and Technologies Corporation
BOL	Beginning of Life
BWERP	Box Wing Earth Radiation Pressure
BWSRP	Box Wing Solar Radiation Pressure
CF	Control Frame
CODE	Center for Orbit Determination in Europe
COM	Center of Mass
DDHL	Double Difference High Low
EDOS	EOS Data and Operations System
EOL	End of Life
EOS	Earth Observing System
ERADP	Earth Radiation Pressure
GaAs	Gallium Arsenide
GCS	GLAS Coordinate System
GFO	Geosat Follow-On
GGM01	GRACE Gravity Model 01
GGM02	GRACE Gravity Model 02

GLAS	Geoscience Laser Altimeter System
GLASSA	GLAS Solar Array
GPS	Global Positioning System
GRACE	Gravity Recovery and Climate Experiment
GSFC	Goddard Space Flight Center
ICESat	Ice, Cloud and Land Elevation Satellite
ICRF	International Celestial Reference Frame
IGS	International GNSS Service
ILRS	International Laser Ranging Service
I-SIPS	ICESat Science Investigator-led Processing System
ITRF	International Terrestrial Reference Frame
JPL	Jet Propulsion Laboratory
JSC	Johnson Space Center
LAGEOS	Laser Geodynamic Satellite
LASP	Laboratory for Atmospheric and Space Physics
LRP	Laser Reference Point
LSEI	Least Squares with Equality and Inequality Constraints
LSI	Least Squares with Inequality Constraints
LVLH	Local Vertical Local Horizontal
MCRT	Monte Carlo Ray Tracing
MGS	Mars Global Surveyor
MOLA	Mars Observer Laser Altimeter
MSODP	Multi-Satellite Orbit Determination Program
NASA	National Aeronautics and Space Administration

Nd:YAG	Neodymium: Yttrium Aluminum Garnet
NNLS	Non-Negative Least Squares
OCS	Orbit Coordinate System
OLR	Outgoing Longwave Radiation
PAD	Precision Attitude Determination
POD	Precision Orbit Determination
POE	Precision Orbit Ephemeris
RADPR	Radiation Pressure
RCS	Reference Coordinate System
RINEX	Receiver Independent Exchange
RMS	Root Mean Square
RSS	Root Sum Square
RTN	Radial Transverse Normal
SCS	Spacecraft Coordinate System
SDHL	Single Difference High Low
SI	International System (of Units)
SINDA	Systems Improved Numerical Differencing Analyzer
SLA	Shuttle Laser Altimeter
SLR	Satellite Laser Ranging
SOE	Sequence of Events
SVD	Singular Value Decomposition
TDRS	Tracking and Data Relay Satellites
TIROS	Television and Infrared Observation Satellites
TOO	Target of Opportunity

TRASYS	Thermal Radiation Analysis System
TSI	Total Solar Irradiance
TSS	Thermal Synthesizer System
UT/CSR	University of Texas at Austin/Center for Space Research
VCS	Vehicle Coordinate System
WPE	Weighted Percentage Error

Chapter 1

Introduction

1.1 The ICESat Mission

In January 2003, the National Aeronautics and Space Administration (NASA) successfully launched the Earth Observing System (EOS) Ice, Cloud, and land Elevation Satellite (ICESat) into its near-polar orbit. Designed primarily to characterize the spatial and temporal variations in the topography of the Greenland and Antarctic ice sheets, it carries onboard a single instrument, the Geoscience Laser Altimeter System (GLAS). Although the use of a satellite laser altimeter to measure ice-sheet elevation changes was originally suggested more than twenty-five years ago (Campbell et al., 1979), ICESat is the first operational satellite dedicated to this objective.

Its realization is due, in large measure, to the experience gained during the design and development of the Mars Observer Laser Altimeter (MOLA). The original version of this instrument (MOLA-1) was lost in 1993, along with the Mars Observer spacecraft. Using spare components from this effort, NASA assembled the experimental Shuttle Laser Altimeter (SLA), which was successfully operated during two Space Shuttle missions in 1996 and 1997, demonstrating the feasibility of spaceborne laser altimetry in Earth applications (Garvin et al., 1998). Also in 1996, the Mars Global Surveyor (MGS) spacecraft left Earth for Mars, carrying the improved MOLA-2 instrument, and subsequently conducted a comprehensive topographic mapping of that planet

between 1999 and 2001. Building on the heritage of these programs, in both the design of the GLAS instrument and the architecture of the ground-based data-processing systems, ICESat commenced its own altimetry mission with the first on-orbit firing of one of its lasers on February 20, 2003.

By developing a time series of precise topographic maps for the two terrestrial ice sheets, changes observed in their surface elevations can be used to infer their mass balances (Zwally, 1975). Such estimates are critical to predicting the impact of global climate change, particularly in forecasting sea-level rise (National Research Council, 1990). The mass balance is simply the difference between the mass added to the ice sheet and the mass removed from it over some interval of time. Additions in mass stem largely from precipitation, primarily in the form of snowfall, but also, occasionally, as rainfall. The removal of mass takes place through: (1) the direct evaporation of ice, or sublimation; (2) the runoff of water generated by melting at the base, and along the surface, of the ice sheet; (3) the often spectacular discharge of an iceberg into the ocean, known as calving; and (4) the transfer of uncompacted snow off the ice sheet by wind (Zwally and Brenner, 2001).

Various techniques have been used to determine the rates at which these mechanisms operate, including *in situ* measurements and numerical modeling. The advent of satellite-based radar altimetry in oceanographic missions during the 1970s also opened the door to the application of geodetic methods to ice-sheet topography. These early missions, however, with their focus on the global oceans, often limited their geographic coverage to latitudes below those needed for thorough ice-sheet surveys. Furthermore, while radar is well suited to the slowly

varying topography of the mean sea surface, interpreting the signals returned from ice proved to be considerably more complex. In particular, the required spatial and temporal averaging of multiple pulses with large (10-km diameter) beam-limited footprints, and the volume scattering associated with surface penetration, limited the accuracy of the derived elevation data (Ridley and Partington, 1988). Despite subsequent advances in the design of these radar systems and the introduction of retracking algorithms in the processing of the individual waveforms, residual uncertainties in the resulting rate estimates, along with those produced by other methods, have led to the suggestion that mass imbalances as large as $\pm 25\%$ remain undetectable, which, in terms of sea-level contributions, correspond to ± 1.4 mm/yr for Antarctica and ± 0.4 mm/yr for Greenland (Warrick et al., 1996).

During 1993 and 1994, NASA flew a laser altimeter, known as the Airborne Oceanographic Lidar (AOL), aboard an aircraft over regions of the Greenland ice sheet previously surveyed using satellite Doppler techniques (Krabill et al., 1995a). The small (1-m diameter) footprint of the laser pulse and its limited penetration into the surface helped to overcome the principal limitations of the radar-based systems. The surface elevations obtained during this period have been shown to have a root-mean-square (RMS) accuracy of 10 cm or less (Krabill et al., 1995b). While this represented a significant advance in the accuracy of ice-sheet topography, the long-term and geographically comprehensive monitoring needed to characterize mass balance accurately can best be accomplished from a satellite platform.

In its three to five year mission, ICESat is expected to produce surface elevation profiles with a RMS accuracy of 15 cm, but with a spatial density and temporal frequency that allow inter-annual and long-term elevation changes to be determined with an accuracy of 1.5 cm/yr, averaged over $100 \text{ km} \times 100 \text{ km}$ regions of the ice sheets (Zwally et al., 2002). Long-range plans call for NASA to conduct additional follow-on missions, extending the potential data set to fifteen years or more (Schutz, 1998). Simulations by Wahr et al. (2000) predicted that the uncertainty in sea-level contribution stemming from a mass imbalance in the Antarctic ice sheet could be reduced to $\pm 0.22 \text{ mm/yr}$ with a data set of this length. They also investigated using gravity measurements from the Gravity Recovery and Climate Experiment (GRACE) mission to remove contributions from post-glacial rebound — the ongoing response of the solid Earth to the melting of ice since the last ice age — and found that this uncertainty could be reduced even further, to $\pm 0.17 \text{ mm/yr}$.

1.2 Surface Elevation Measurements

The accuracy of the surface elevation profiles used to estimate the mass balances of the ice sheets depends on the individual measurements that comprise them. During the ICESat mission, the altimetry measurements are made 40 times per second, and each begins with a 6-ns, 1064-nm (infrared) pulse generated by one of the three redundant neodymium-doped yttrium-aluminum-garnet (Nd:YAG) lasers in the GLAS instrument. Once emitted, this pulse travels to the surface of the Earth, producing a 65-m diameter spot, from which a significant number of the incident photons are reflected back to the satellite and captured

by the GLAS receiver telescope. The instrument records digitized waveform representations of both the transmitted pulse and the returned signal. Subsequent ground-based analyses, made by the ICESat Science Investigator-led Processing System (I-SIPS), apply Gaussian fits to these waveforms to identify the transmit time t_T and the receive time t_R for each pulse centroid (Brenner et al., 2003).

With this information, and knowledge of the position and the orientation of the instrument, the location of each laser spot centroid on the surface of the Earth — and the elevation at that point — can be determined. For ICESat, this *geolocation* process relies on a one-way, or instantaneous, range method detailed by Schutz (2002). Summarized here, it avoids the computational intensity inherent in iterative, two-way range algorithms (see, for example, Luthcke et al., 2000), while producing comparable results (Tapley et al., 2004b).

First, the difference between the receive time and the transmit time, $t_R - t_T$, represents the round-trip, or two-way, travel time for an individual pulse. Halving this difference, and multiplying the result by the speed of light c , yields the approximate one-way scalar range to the Earth,

$$\rho = c \left(\frac{t_R - t_T}{2} \right) \quad (1.1)$$

The pulse reaches the surface at the bounce time t_B ,

$$t_B = t_T + \left(\frac{t_R - t_T}{2} \right) \quad (1.2)$$

which is defined to be the time of the instantaneous range ρ . Figure 1.1 illustrates how this range is next combined with the instrument's position \vec{r}_{inst} and its orientation \hat{u}_{laser} to establish the location of the laser spot centroid \vec{R}_{spot} .

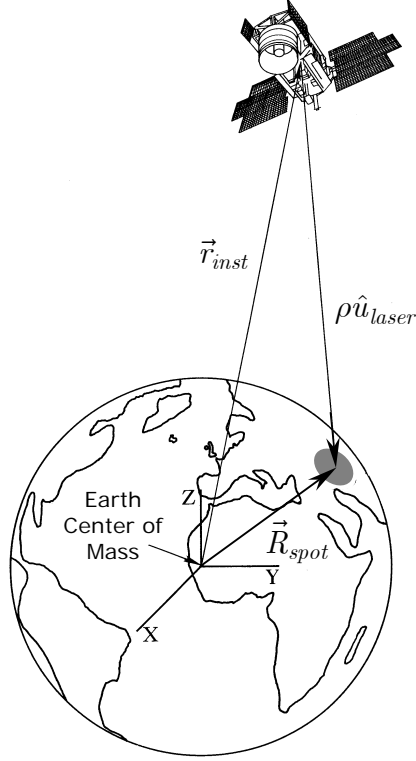


Figure 1.1. One-Way Range Geolocation Geometry

The instrument position information comes from ground-based processing of onboard Global Positioning System (GPS) data, using precision orbit determination (POD) techniques (Rim and Schutz, 2002). The resulting solution consists of Cartesian position and velocity vectors in the non-rotating, geocentric International Celestial Reference Frame (ICRF). The instrument position vector is interpolated from this ephemeris at the bounce time,

$$\vec{r}_{inst}^{icrf}(t_B) = \begin{bmatrix} X \\ Y \\ Z \end{bmatrix} \quad (1.3)$$

The orientation of the instrument, or more specifically, the laser pointing direction, is computed at t_T for each pulse through ground-based processing of the onboard star-tracker and gyro data, using precision attitude determination (PAD) techniques (Bae and Schutz, 2002). Each solution is a unit vector represented by three direction cosines,

$$\hat{u}_{laser}^{icrf}(t_T) = \begin{bmatrix} \cos \alpha \\ \cos \beta \\ \cos \gamma \end{bmatrix} \quad (1.4)$$

in which the angles α , β , and γ are measured with respect to the ICRF coordinates axes. Multiplying this laser-pointing direction by the scalar range obtained from Equation (1.1) yields the range vector,

$$\vec{\rho}^{icrf}(t_T) = \rho \begin{bmatrix} \cos \alpha \\ \cos \beta \\ \cos \gamma \end{bmatrix} \quad (1.5)$$

The vector sum of Equations (1.3) and (1.5), as suggested by Figure 1.1, uniquely determines the ICRF position vector of the laser spot centroid, which, by definition, occurs at t_B :

$$\vec{R}_{spot}^{icrf}(t_B) = \vec{r}_{inst}^{icrf}(t_B) + \vec{\rho}^{icrf}(t_T) \quad (1.6)$$

Since the location of the spot on the surface of the Earth is desired, this ICRF position vector must be rotated to the International Terrestrial Reference Frame (ITRF). The transformation between the two frames T_{icrf}^{itr} depends on several factors, including precession, nutation, Earth rotation and polar motion

(Webb, 2002). After evaluating T_{icrf}^{itr} at t_B , the ITRF position vector of the spot is given by

$$\vec{R}_{spot}^{itr}(t_B) = T_{icrf}^{itr}(t_B) \vec{R}_{spot}^{icrf}(t_B) \quad (1.7)$$

Using the TOPEX reference ellipsoid (Tapley et al., 1994), with a mean radius $a_{\oplus} = 6378136.3$ m and an inverse flattening coefficient $1/f = 298.257$, this vector can be resolved to yield the geodetic latitude φ_d , the longitude λ and the elevation h of the laser spot centroid,

$$\vec{R}_{spot}^{itr} = \begin{bmatrix} G_1 \cos \varphi_d \cos \lambda \\ G_1 \cos \varphi_d \sin \lambda \\ G_2 \sin \varphi_d \end{bmatrix} \quad (1.8)$$

where

$$G_1 = \frac{a_{\oplus}}{\sqrt{1 - (2f - f^2) \sin^2 \varphi_d}} + h \quad G_2 = \frac{a_{\oplus} (1 - f)^2}{\sqrt{1 - (2f - f^2) \sin^2 \varphi_d}} + h \quad (1.9)$$

This position and elevation are approximate, since the range of Equation (1.1) has not been corrected for path delays within the instrument or through the atmosphere. The former combine to produce an effective range bias $\delta\rho_{bias}$, which was calibrated prior to launch (Martino, 2002). The atmospheric — or more specifically, tropospheric — delay depends on the refractive index along the path traveled by the pulse. In their model for the corresponding range correction $\delta\rho_{atm}$, Herring and Quinn (1999) relate this delay to surface pressure and precipitable water vapor, computed at the bounce time and at the approximate location of the laser spot centroid. Thus, the corrected range ρ_c becomes

$$\rho_c = \rho - \delta\rho_{bias} - \delta\rho_{atm}(t_B, \varphi_d, \lambda, h) \quad (1.10)$$

With this new range value, the geolocation process is repeated, beginning with Equation (1.5) and yielding a corrected set of geodetic coordinates $(\varphi'_d, \lambda', h')$. A final correction to the elevation is made to remove the effects of solid Earth tides (McCarthy, 1996), ocean loading (Yi et al., 1999), and where applicable, ocean tides (Bettadpur and Eanes, 1994).

1.3 Precision Orbit Determination

The instrument position vector constitutes a critical component of the geolocation algorithm. To achieve the desired accuracy of the surface elevation profiles, errors in its knowledge must be limited to 5 cm in the radial component, and 20 cm, horizontally (GLAS Science Team, 1997). Specifically, this vector defines the ICRF position of a designated laser reference point (LRP) within the GLAS instrument, \vec{r}_{lrp}^{icrf} . At any time t , it can be expressed as

$$\vec{r}_{inst}^{icrf}(t) \equiv \vec{r}_{lrp}^{icrf}(t) = \vec{r}_{com}^{icrf}(t) + T_{scs}^{icrf}(t) [\vec{r}_{lrp}^{scs} - \vec{r}_{com}^{scs}(t)] \quad (1.11)$$

where \vec{r}_{lrp}^{scs} and \vec{r}_{com}^{scs} are the position vectors of the LRP and the satellite center of mass (COM) in the body-fixed Spacecraft Coordinate System (SCS), respectively. Although the LRP remains stationary in this frame, the COM moves throughout the mission, primarily as a function of propellant expenditure (Iacometti, 2002). As illustrated in Figure 1.2, the vector difference represents the offset of the LRP from the COM in the SCS. This offset can be rotated to the ICRF using the transformation T_{scs}^{icrf} , which is the transpose of the satellite attitude, and added to the ICRF position of the COM, \vec{r}_{com}^{icrf} .

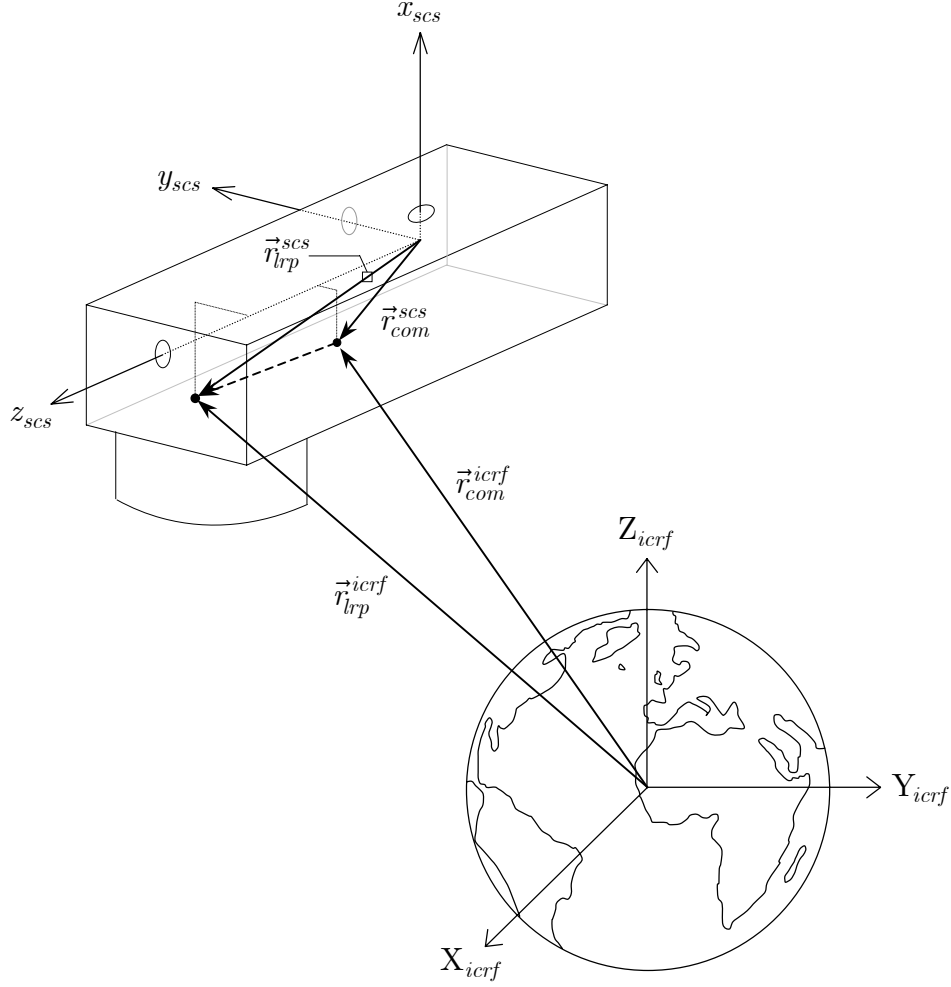


Figure 1.2. SCS and ICRF Position Vectors for Satellite Center of Mass (COM) and Laser Reference Point (LRP)

Errors introduced by the second term in Equation (1.11) tend to be comparatively small (< 1.5 cm), as discussed in Appendix A. Consequently, the errors in the ICRF position of the LRP are essentially the same as those in the ICRF position of the COM. Knowledge of the latter is acquired through POD, using tracking data collected by either of the onboard GPS receivers. During the

ICESat mission, these GPS measurements are transmitted from the satellite to ground stations in Alaska and Norway, as part of the X-band science downlink. This high-rate telemetry flows directly from these sites to the EOS Data and Operations System (EDOS) at the NASA Goddard Space Flight Center (GSFC), where the raw GPS tracking data is extracted and distributed (Laboratory for Atmospheric and Space Physics, 2003).

After receiving these binary data files, the University of Texas Center for Space Research (UT/CSR), in Austin, converts them to Receiver Independent Exchange (RINEX) format. POD solutions for ICESat are computed daily with the Multi-Satellite Orbit Determination Program (MSODP). Originally designed by UT/CSR to support GPS-based POD for the TOPEX/Poseidon mission, MSODP employs the dynamic method of orbit determination (Rim, 1992). Although other strategies have been developed in recent years, including reduced-dynamic (Wu et al., 1987) and purely kinematic (Byun, 1998) techniques, the dynamic method remains the dominant approach, particularly for altimetry missions (Davis, 1996). Its basic elements are outlined in the following sections.

1.3.1 Dynamic Modeling

The motion of a low-Earth orbiting satellite is governed by a second-order non-linear differential equation, based on Newton's Second Law and modified to account for the effects of general relativity,

$$\begin{aligned}\ddot{\vec{r}} &= -\frac{\mu}{r^3}\vec{r} + \vec{R} + T[\vec{G} + \vec{D}] + \vec{S} + \vec{E} + \vec{Y} + \vec{P} \\ \vec{r}(t_0) &= \vec{r}_0 \quad \dot{\vec{r}}(t_0) = \dot{\vec{r}}_0\end{aligned}\tag{1.12}$$

where

\vec{r} = ICRF position vector of the COM

μ = gravitational parameter of the Earth

\vec{R} = general relativistic correction

T = transformation from the ITRF to the ICRF

\vec{G} = non-spherical gravitational force

\vec{D} = atmospheric drag force

\vec{S} = solar radiation force

\vec{E} = Earth radiation force

\vec{Y} = thermal force

\vec{P} = third-body gravitational force

Each of the perturbing forces (per unit mass) in Equation (1.12) can be modeled as a function of the position \vec{r} and/or the velocity $\dot{\vec{r}}$ of the satellite. Both Davis (1996) and Rim and Schutz (2002) describe the implementation of these models in MSODP. As will be discussed in Section 1.4, the modeling of the solar and Earth radiation pressure perturbations — \vec{S} and \vec{E} , respectively — in ICESat POD was the subject of this research.

Ideally, these mathematical models would completely, and accurately, characterize the forces acting on the satellite in its dynamic environment. Given the appropriate initial conditions at time t_0 , the position and the velocity at any time $t > t_0$ could then be determined by numerically integrating Equation (1.12). In practice, however, uncertainties in the initial conditions, and in various mathematical model parameters, introduce errors into the integrated solutions, causing them to deviate from the true position and velocity of the satellite at any

given time. To compensate for these effects, orbit determination strategies incorporate observations of the satellite to correct the trajectory predicted by the differential equation of motion alone.

1.3.2 Observation Modeling

The observations reported in the RINEX files include the differences between the phases of the L1 and L2 carrier signals received from a GPS satellite and that of a reference carrier generated by the receiver (Hofmann-Wellenhof et al., 1997). In preparation for POD, these two phase measurements are combined to mitigate the frequency-dependent effects of the ionosphere. The resulting ionosphere-free phase observables are converted to ranges, or more specifically, pseudoranges, as they are biased by errors in the clocks of both the GPS satellite and the receiver. The ionosphere-free, phased-derived pseudorange $\tilde{\rho}$, between a receiver and a single GPS satellite, can be modeled as

$$\tilde{\rho} = \left| \vec{r}_r - \vec{r}_t \right| - c \delta t_t + c \delta t_r + \delta \rho_{cor} + \delta \rho_{amb} \quad (1.13)$$

where c represents the speed of light. In Equation (1.13), the subscripts r and t differentiate the positions \vec{r} , and the clock errors δt , of the receiver and the transmitting GPS satellite, respectively. The last two terms represent a range correction $\delta \rho_{cor}$, discussed later, and a phase-range ambiguity $\delta \rho_{amb}$, which stems from the frequency-dependent integer ambiguity of the phase measurements.

Differencing phase-derived pseudoranges from two different receivers to the same GPS satellite allows the clock errors δt_t associated with that satellite to be eliminated. For POD, a single-difference high-low (SDHL) measurement is

typically formed using a receiver u onboard the “low” satellite (e.g., ICESat), a ground-based receiver w , and a “high” GPS satellite p ,

$$\text{SDHL}_{uw}^p = \tilde{\rho}_u^p - \tilde{\rho}_w^p \quad (1.14)$$

Similarly, another SDHL measurement is formed for the same two receivers and a different GPS satellite q ,

$$\text{SDHL}_{uw}^q = \tilde{\rho}_u^q - \tilde{\rho}_w^q \quad (1.15)$$

The clock errors δt_r for each of the two receivers remain in both Equations (1.14) and (1.15). By differencing these single-differences, those errors are eliminated, and a double-difference high-low (DDHL) measurement is obtained,

$$\text{DDHL}_{uw}^{pq} = \text{SDHL}_{uw}^p - \text{SDHL}_{uw}^q \quad (1.16)$$

Figure 1.3 illustrates the geometry of a DDHL observation. Substituting Equations (1.14) and (1.15), and then Equation (1.13), into Equation (1.16) confirms that the clock errors for both receivers and both GPS satellites have been removed,

$$\begin{aligned} \text{DDHL}_{uw}^{pq} = & \left| \vec{r}_u - \vec{r}_p \right| - \left| \vec{r}_w - \vec{r}_p \right| - \left| \vec{r}_u - \vec{r}_q \right| + \left| \vec{r}_w - \vec{r}_q \right| \\ & + \delta\rho_{cor}^{up} - \delta\rho_{cor}^{wp} - \delta\rho_{cor}^{uq} + \delta\rho_{cor}^{wq} \\ & + \delta\rho_{amb}^{up} - \delta\rho_{amb}^{wp} - \delta\rho_{amb}^{uq} + \delta\rho_{amb}^{wq} \end{aligned} \quad (1.17)$$

The first line of Equation (1.17) contains the slant ranges between each receiver and each GPS satellite contributing to the measurement, dictated by their relative positions. Each of the $\delta\rho_{cor}$ terms in the second line includes

corrections for atmospheric signal delay, general and special relativity, phase wind-up, and phase-center offsets in the transmitting and receiving antennas. Combining the individual phase-range ambiguities from the third line into a single double-difference ambiguity C_{uw}^{pq} yields the observation equation implemented in MSODP,

$$\begin{aligned} \text{DDHL}_{uw}^{pq} = & \left| \vec{r}_u - \vec{r}_p \right| - \left| \vec{r}_w - \vec{r}_p \right| - \left| \vec{r}_u - \vec{r}_q \right| + \left| \vec{r}_w - \vec{r}_q \right| \\ & + \delta\rho_{cor}^{up} - \delta\rho_{cor}^{wp} - \delta\rho_{cor}^{uq} + \delta\rho_{cor}^{wq} \\ & + C_{uw}^{pq} \end{aligned} \quad (1.18)$$

In the orbit determination problem, a set of “computed” DDHL measurements is generated using Equation (1.18) and a reference trajectory, obtained by integrating Equation (1.12). The resulting observations are then compared to the actual, or “observed”, DDHL measurements, formed from the phase-derived pseudoranges for the onboard and active ground-based receivers. RINEX data for the latter comes from selected tracking stations in a global network operated by the International GNSS Service (IGS), such as those shown in Figure 1.4. In addition to the ICESat position, computing observations with Equation (1.18) also requires: (1) the geocentric positions of the GPS satellites and the tracking station receivers, both of which are available from the IGS and, currently, specified in the ITRF2000 (Altamimi et al., 2002); (2) mathematical models for the range-correction terms (Davis, 1996); and (3) *a priori* values for the double-difference ambiguities, typically assumed to be zero. The differences between the observed and the computed data sets can then be used to improve the accuracy of the trajectory and, if desired, to update parameters in the dynamic and/or the observation models.

1.3.3 The Orbit Determination Problem

The dynamic approach to orbit determination applies linear estimation theory to the distinctly non-linear problem posed by Equations (1.12) and (1.18) to effect the differential correction of the reference trajectory suggested in the preceding section. Provided the true satellite motion remains sufficiently close to the reference trajectory throughout a particular time interval, the equation of motion and the observation equation can be linearized through Taylor series expansions (Tapley, 1973). First, the state vector X at time t is defined to include the satellite position \vec{r} and the velocity $\dot{\vec{r}}$, along with a selected set d of dynamic and/or observation model parameters to be updated,

$$X(t) = \begin{bmatrix} \vec{r} \\ \dot{\vec{r}} \\ d \end{bmatrix} \quad (1.19)$$

Thus, Equation (1.12) can be reduced to a system of first-order non-linear differential equations,

$$\dot{X} = F(X, t) \quad X(t_0) = X_0 \quad (1.20)$$

Similarly, Equation (1.18) can be expressed as

$$Y_l = \text{DDHL}_{uw}^{pq} = G(X, t) + \varepsilon_l \quad l = 1, \dots, m \quad (1.21)$$

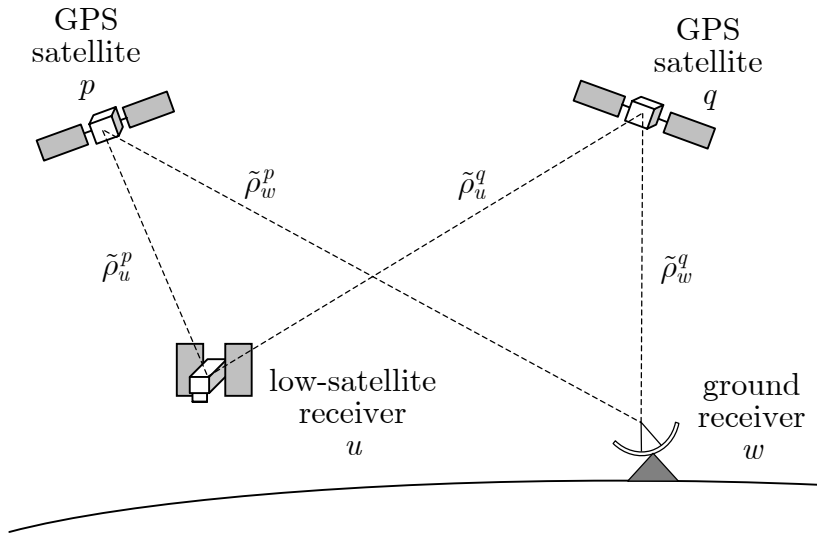


Figure 1.3. Double-Difference High-Low Geometry

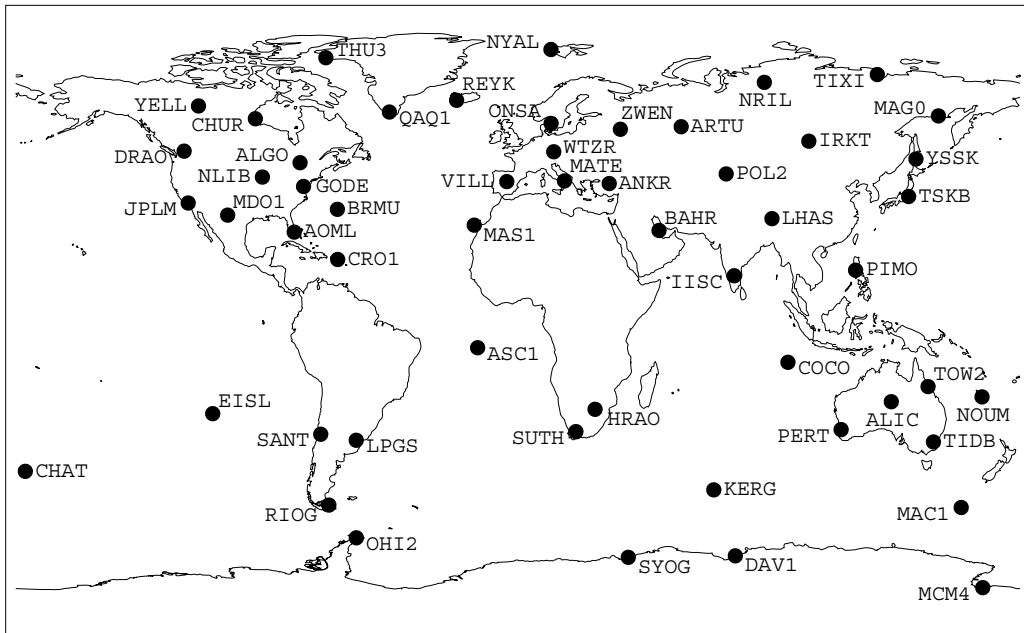


Figure 1.4. Typical IGS Tracking Stations in ICESat POD (54 Stations)

where ε_l denotes the measurement error. The number of observations m at a particular epoch t depends on the number of GPS satellites tracked by each receiver, and on their relative geometry. The double-difference ambiguity of Equation (1.18) must be estimated for each pass, defined as a series of consecutive DDHL combinations of the same receivers and GPS satellites, and each is included in the set d . Based on results obtained by Rim et al. (2000), regarding the effects of errors in the GPS satellite orbits, those orbits are routinely fixed in ICESat POD, either to the rapid or the final IGS solutions. They, along with the positions of the tracking station receivers, however, can be added to the state, if desired.

Expanding the right-hand side of Equation (1.20) in a Taylor series about the nominal state $X^*(t)$, which consists of the reference trajectory and the *a priori* values for the parameters in d , yields

$$\dot{X} = \underbrace{F(X^*, t)}_{\dot{X}^*} + \left[\frac{\partial F}{\partial X} \right]^* [X(t) - X^*(t)] + \dots \quad (1.22)$$

Truncating the series after the first-order term, and defining

$$x(t) = X(t) - X^*(t) \quad (1.23)$$

leads to a system of *linear* differential equations governing the orbit determination problem,

$$\dot{x} = A(t)x(t) \quad x(t_0) = x_0 \quad (1.24)$$

where

$$A(t) = \frac{\partial F}{\partial X}(X^*, t) \quad (1.25)$$

The general solution to Equation (1.24) takes the form

$$x(t) = \Phi(t, t_i) x(t_i) \quad (1.26)$$

where $\Phi(t, t_i)$ is a state transition matrix that maps a solution x at t_i to an arbitrary time t . It satisfies the differential equation,

$$\dot{\Phi}(t, t_i) = A(t)\Phi(t, t_i) \quad \Phi(t_i, t_i) = I \quad (1.27)$$

The right-hand side of Equation (1.21) can also be expanded in a Taylor series about the nominal state,

$$Y_l = \underbrace{G(X^*, t)}_{Y_l^*} + \left[\frac{\partial G}{\partial X} \right]^* [X(t) - X^*(t)] + \dots + \varepsilon_l \quad (1.28)$$

where Y_l and Y_l^* denote the observed and computed DDHL measurements, respectively. Truncating the series after the first-order term, substituting Equation (1.23), and defining

$$y_l = Y_l - Y_l^* \quad (1.29)$$

yields a *linear* observation equation at time t ,

$$y_l = \tilde{H}(t)x(t) + \varepsilon_l \quad l = 1, \dots, m \quad (1.30)$$

where

$$\tilde{H}(t) = \frac{\partial G}{\partial X}(X^*, t) \quad (1.31)$$

Together, Equations (1.26) and (1.30) constitute a linear estimation problem for the state $x(t)$ — the differential correction of the reference trajectory — using the observation residuals y_l .

1.3.4 The Epoch-State Batch Filter

Using the *a priori* state at t_0 in Equation (1.26), and substituting the result into Equation (1.30), yields the epoch-state batch filter,

$$y_l = \tilde{H}(t)\Phi(t, t_0)x(t_0) + \varepsilon_l \quad l = 1, \dots, m \quad (1.32)$$

This approach to the orbit determination problem maps the observation residuals y_l at time t to the initial epoch t_0 . Adopting the following notation for all of the observations M in a particular time interval,

$$y = \begin{bmatrix} y_1 \\ \vdots \\ y_M \end{bmatrix} \quad H = \begin{bmatrix} \tilde{H}_1\Phi(t_1, t_0) \\ \vdots \\ \tilde{H}_M\Phi(t_M, t_0) \end{bmatrix} \quad \varepsilon = \begin{bmatrix} \varepsilon_1 \\ \vdots \\ \varepsilon_M \end{bmatrix} \quad (1.33)$$

Equation (1.32) can be expressed as

$$y = Hx_0 + \varepsilon \quad (1.34)$$

Assuming that the measurement errors ε are random, with zero mean and a specified covariance R ,

$$E[\varepsilon] = 0 \quad E[\varepsilon\varepsilon^T] = R \quad (1.35)$$

then the best linear, unbiased, minimum variance estimate of the epoch state x_0 has been shown by Tapley (1973) to be

$$\hat{x}_0 = (H^T R^{-1} H)^{-1} (H^T R^{-1} y) \quad (1.36)$$

This solution agrees with a weighted least-squares estimate in which the weighting matrix W equals R^{-1} . The covariance matrix associated with this estimate is simply

$$P_0 = (H^T R^{-1} H)^{-1} \quad (1.37)$$

If an *a priori* estimate of the epoch state \bar{x}_0 is available, along with a state covariance matrix \bar{P}_0 , Equations (1.36) and (1.37), respectively, become

$$\hat{x}_0 = (H^T R^{-1} H + \bar{P}_0^{-1})^{-1} (H^T R^{-1} y + \bar{P}_0^{-1} \bar{x}_0) \quad (1.38)$$

and

$$P_0 = (H^T R^{-1} H + \bar{P}_0^{-1})^{-1} \quad (1.39)$$

Computing \hat{x}_0 from either Equation (1.36) or (1.38) requires the inversion of a square matrix with dimension n , equal to the number of parameters in the state vector. When this number is large — as is often the case when using GPS-derived observations — the matrix can be ill-conditioned, making an explicit

inversion numerically unstable. To avoid this problem, orbit determination algorithms typically apply orthogonal transformations to the linear system of Equation (1.34). The most common methods include singular value decomposition (SVD), Givens rotations, and Householder reflections (Lawson and Hanson, 1974). Each approach accomplishes the matrix inversion implicitly, and produces a solution equivalent to that of either Equation (1.36) or (1.38). Since \hat{x}_0 represents a differential correction to the epoch state in the original, non-linear problem, that new state is

$$X(t_0) = X^*(t_0) + \hat{x}_0 \quad (1.40)$$

Conceptually, subsequent states can be obtained in a similar manner, after mapping \hat{x}_0 forward in time with Equation (1.26),

$$X(t) = X^*(t) + \Phi(t, t_0) \hat{x}_0 \quad (1.41)$$

In practice, Equation (1.12) is usually integrated to generate the solution trajectory, using the updated initial conditions and model parameters of Equation (1.40).

1.4 Research Objectives

Given the stringent orbit accuracy requirements imposed by the scientific objectives, and the central role played by dynamic models in the epoch-state batch filter, detailed evaluations of those models were undertaken early in the ICESat mission design (Schutz et al., 1994; Davis, 1996; Rim et al., 1996). A final pre-launch study by Rim et al. (1999), at the revised mission altitude of

approximately 600 km, concluded that geopotential and atmospheric-drag model errors would dominate the overall orbit error. Furthermore, significantly smaller contributions could be expected from the solar and Earth radiation pressure models. They demonstrated, however, that the 5-cm radial and 20-cm horizontal constraints could be met by tuning the gravity field after launch and/or employing frequent estimation of empirical parameters.

Such results inherently reflect the assumptions made regarding potential error sources. In each of the pre-launch analyses, radiation pressure errors were introduced, principally, by biasing and randomly varying the parameters of a nominal satellite model. Using this perturbed model and a truth trajectory, simulated DDHL observations were generated, and then processed with the nominal model in the MSODP epoch-state batch filter. The aggregate effect of these errors was assessed by comparing the integrated POD solution to the truth trajectory, and calculating the RMS of the position differences. Based on their assumptions, Rim et al. (1999) found that solar and Earth radiation pressure model errors could each contribute slightly less than 0.2 cm to the total orbit error, with 0.1 cm manifested in the radial component.

Whether these results accurately forecast such errors for operational POD during the ICESat mission depends entirely on how well the nominal model approximates the actual forces acting on the satellite. Therefore, the three immediate and practical goals of this study were:

- (1) to develop a high-fidelity simulation of the anticipated solar and Earth radiation forces

- (2) to determine pre-launch values for the nominal satellite model parameters, and to evaluate their performance with respect to the predictions of (1)
- (3) to assess the post-launch performance of the nominal satellite model in operational POD, and to explore the feasibility of tuning its parameters

Both the overall approach and the individual objectives reflect a methodology developed to support POD for TOPEX/Poseidon, an oceanographic radar altimetry mission launched in 1992. The principal works on which this study is based originated with that effort, specifically those by Marshall et al. (1991), Antreasian (1992), and Marshall and Luthcke (1994a, 1994b).

Applying this strategy to ICESat, however, required that several important issues be addressed. First, its altitude is significantly lower than that of TOPEX/Poseidon, which orbits at about 1336 km. As a result, Earth radiation pressure is a larger perturbation for ICESat, requiring more detailed modeling. For TOPEX/Poseidon, MSODP employed a nominal satellite model, known as the *macro-model*, in its computation of solar radiation forces, but relied on a simpler “cannonball” model for the forces induced by Earth radiation. ICESat POD uses a similar satellite macro-model, but applies it to the modeling of both solar and Earth radiation pressure perturbations. Chapter 2 establishes the terminology and models used in this study to characterize the radiation environment of low-Earth orbit, while Chapter 3 describes the evolution of radiation force models in orbit determination, including the modifications made within MSODP to support the ICESat mission.

Second, beginning in the early 1990s, advances in computing speed led developers of thermal analysis tools to adopt Monte Carlo Ray Tracing (MCRT) techniques, displacing traditional grey-body methods (Panczak et al., 1991). For his high-fidelity simulation of the radiation forces affecting TOPEX/Poseidon, Antreasian (1992) adapted the Thermal Radiation Analysis System (TRASYS), which uses a latter-type algorithm to compute, among other quantities, incident and absorbed heat rates. He made a series of changes to this software, facilitating the direct calculation of radiation forces acting on the surfaces of a detailed model of the satellite, which he called the *micro-model*. The ICESat spacecraft-bus contractor, the Ball Aerospace and Technologies Corporation (BATC), created a comparable model for its own thermal analyses, using, instead, the MCRT-based Thermal Synthesizer System (TSS). Consequently, to support the first objective of this study, new algorithms were developed to compute radiation forces within this MCRT framework, resulting in modifications to the TSS software entirely different from those made to TRASYS. Chapter 4 examines this implementation, and delineates the subsequent micro-model simulation for ICESat.

Third, Marshall and Luthcke (1994a) determined pre-launch values of the macro-model parameters for TOPEX/Poseidon by applying a Bayesian least-squares fit to the solar radiation forces predicted using the micro-model. In this approach, the *a priori* covariance was adjusted to constrain the estimates for individual parameters, and in certain instances, to avoid physically unrealistic results. A preliminary study for ICESat (Webb et al., 2001) employed a similar technique, although the fit involved both the solar and Earth radiation forces

derived from the micro-model. The current study, however, discards the *a priori* covariance, in favor of incorporating equality and inequality constraints for the macro-model parameters directly into the least-squares formulation. Chapter 5 presents an algorithm for solving such a problem, and evaluates the solution obtained for ICESat.

Fourth, Marshall and Luthcke (1994b) documented many of the factors influencing the post-launch recoverability of the TOPEX/Poseidon macro-model parameters, including: (1) the distribution of the tracking data around the orbit; (2) the relative geometry of the satellite and the Sun; and (3) the aliasing of macro-model errors into empirical or other dynamic-model parameters. For ICESat, the use of globally distributed GPS tracking data provides a substantive advantage over the comparatively sparse satellite laser ranging (SLR) and Doppler data available to TOPEX/Poseidon, effectively eliminating the first concern. The lower altitude of ICESat, however, has negative consequences with regard to the other two factors. Combined with a 94° inclination, it causes the orbit plane to precess at only 0.5° per day with respect to the Sun, contrasted with 3.0° per day for the TOPEX/Poseidon orbit. As a result, the relative orientation of the satellite and the incident solar radiation changes less for ICESat during a given time interval, decreasing the observability of its macro-model parameters. Furthermore, the frequent estimation of empirical parameters, necessary to manage the larger geopotential and atmospheric-drag errors at this lower altitude, may absorb or corrupt the rather weak signals associated with errors in the macro-model, severely impacting the recovery of its parameters. In light of these challenges, Chapter 6 assesses the performance of the macro-model

parameters in post-launch POD, and considers the feasibility of tuning their values.

Finally, each surface of the satellite, according to the Stefan-Boltzmann law, emits radiant energy in proportion to the fourth-power of its absolute temperature. If the forces imparted by these emissions do not sum to zero along a particular axis of the satellite, they produce a net acceleration in that direction. Computing such thermal perturbations — \vec{Y} in Equation (1.12) — requires extensive modeling of the surface temperatures, which are influenced not only by radiation from the Sun and the Earth, but also by conduction and radiation within the satellite. Antreasian (1992) simulated these temperatures in the TOPEX/Poseidon micro-model and derived the resulting forces. Notably smaller in magnitude than even those induced by Earth radiation pressure, these forces were, nonetheless, reasonably approximated using additional macro-model parameters, determined independently of those used to model solar radiation forces (Marshall and Luthcke, 1994a). This separability in the modeling of incident and emitted radiation, combined with the comparatively small contributions of the latter to the equation of motion, led to a decision to omit thermal perturbations from this ICESat study.

Chapter 2

Incident Radiation in Low-Earth Orbit

2.1 Fundamental Radiation Quantities

Whether considered from a classical, or a quantum, electrodynamic perspective, radiant energy propagating through space transports momentum, which can be imparted to an object that intercepts it. The exact nature of the interaction depends on the characteristics of its surface and the wavelength of the incident radiation. All bodies in the solar system, either celestial or artificial, receive electromagnetic energy from the Sun, most of which falls within the ultraviolet and visible regions of the spectrum shown in Figure 2.1. Satellites in orbit about the Earth encounter additional radiation that has either been reflected or emitted from the planet. Although the former shares the intrinsic wavelengths of direct solar radiation, the latter is distinguished by its longer, infrared wavelengths.

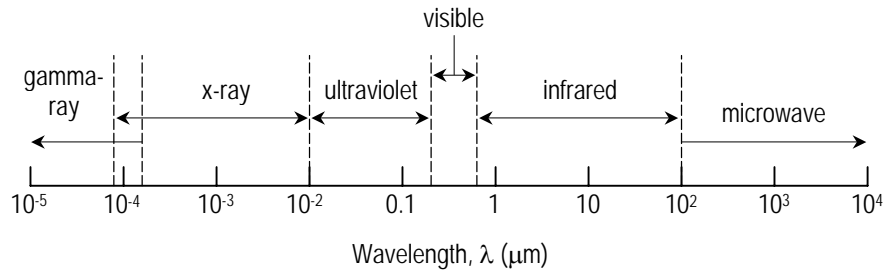


Figure 2.1. The Electromagnetic Spectrum

The momentum delivered to an object in such an environment depends directly on how much radiation of each type reaches its surface. Unfortunately, quantitative descriptions of electromagnetic energy vary from application to application, largely due to the independent development of the fields associated with light, heat and electromagnetism. As a result, the adopted terminology tends to suffer from imprecise, and even incorrect, usage. To establish a coherent framework for this study, the following sections define the relevant quantities, which are subsequently used to develop the necessary mathematical models for solar and terrestrial radiation. The chapter concludes with a discussion of the methods available for determining orbital eclipses, in which the radiant energy emitted by the sun is absent.

2.1.1 Irradiance

In modeling radiation pressure, the fundamental process to consider is that of irradiation, the illumination of a surface by an external source, as illustrated in Figure 2.2. There, the incoming radiant energy has a wavelength- and direction-dependent intensity defined to be

$$I_{\lambda,i}(\lambda, \theta, \varphi) \equiv \frac{dQ_{\lambda,i}}{dA \cos \theta \cdot d\omega \cdot d\lambda} \quad (2.1)$$

This incident *spectral* intensity $I_{\lambda,i}$ represents the electromagnetic energy of wavelength λ per unit time ($dQ_{\lambda,i}$) arriving at the differential surface dA , per interval $d\lambda$ about λ , per unit solid angle about the (θ, φ) direction, and per unit area projected normal to it. The corresponding *total* intensity I_i of this energy can be obtained by integrating over all wavelengths,

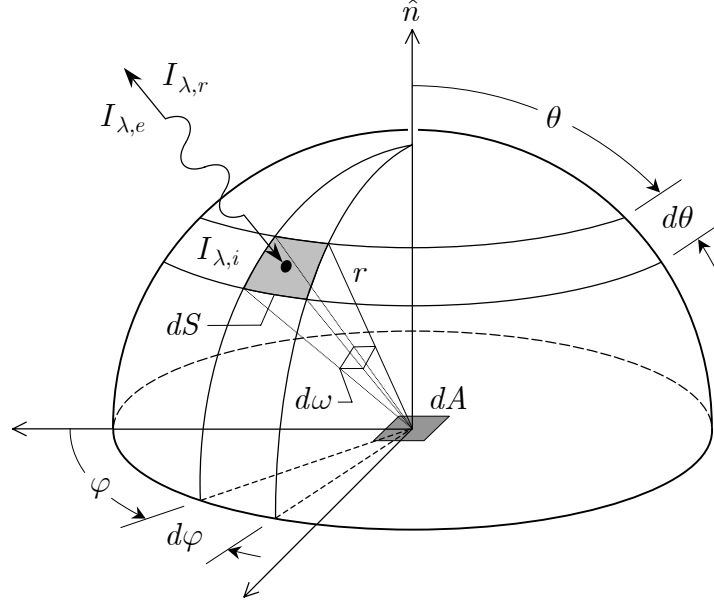


Figure 2.2. Radiation Geometry for a Differential Area

$$I_i(\theta, \varphi) = \int_0^\infty I_{\lambda,i}(\lambda, \theta, \varphi) d\lambda \quad (2.2)$$

Most applications involving radiation from the Sun, however, characterize the incoming energy by its *irradiance*, rather than its intensity. The *spectral irradiance* G_λ is derived from the spectral intensity by accounting for radiation incident from all directions. Mathematically, this implies integrating over the arbitrary, hypothetical hemisphere centered on dA . The contribution from a differential area dS of this surface is obtained by rearranging Equation (2.1),

$$dG_\lambda(\lambda, \theta, \varphi) = \frac{dQ_{\lambda,i}}{dA d\lambda} = I_{\lambda,i}(\lambda, \theta, \varphi) \cos \theta d\omega \quad (2.3)$$

The solid angle $d\omega$ is defined as the ratio of dS to the square of the hemisphere's radius r ,

$$d\omega = \frac{dS}{r^2} \quad (2.4)$$

From Figure 2.2, that differential area can be formulated as

$$dS = r d\theta \cdot r \sin \theta d\varphi \quad (2.5)$$

Substituting this expression for dS in Equation (2.4), and the result for $d\omega$ in Equation (2.3),

$$dG_\lambda(\lambda, \theta, \varphi) = I_{\lambda,i}(\lambda, \theta, \varphi) \cos \theta \sin \theta d\theta d\varphi \quad (2.6)$$

Integrating over the hemisphere yields the desired spectral irradiance,

$$G_\lambda(\lambda) = \int_0^{2\pi} \int_0^{\pi/2} I_{\lambda,i}(\lambda, \theta, \varphi) \cos \theta \sin \theta d\theta d\varphi \quad (2.7)$$

which represents the radiant energy per unit time received at dA , per unit area, and per interval $d\lambda$ about λ . Its SI units are typically given as watts/square-meter/micrometer ($\text{W}/\text{m}^2\text{-}\mu\text{m}$).

The *total* irradiance G , often called the *flux*, is simply the radiant energy per unit time received by a surface, per unit area. Its SI units are watts/square-meter (W/m^2). As with total intensity, it can be computed from its spectral counterpart by integrating over all wavelengths,

$$G = \int_0^\infty G_\lambda(\lambda) d\lambda \quad (2.8)$$

For the particular case of diffuse irradiation, the incident spectral intensity is independent of direction, and Equation (2.7) becomes

$$G_{\lambda}(\lambda) = I_{\lambda,i}(\lambda) \int_0^{2\pi} \int_0^{\pi/2} \cos \theta \sin \theta d\theta d\varphi = \pi I_{\lambda,i}(\lambda) \quad (2.9)$$

Using Equations (2.8) and (2.2), the total irradiance can then be related directly to the total intensity,

$$G = \pi \int_0^{\infty} I_{\lambda,i}(\lambda) d\lambda = \pi I_i \quad (2.10)$$

2.1.2 Radiosity

Irradiance tends to be the preferred fundamental quantity in describing nearly uniform radiation *arriving* from a distant source, as in the case of the Sun. More generally, the total amount of radiant energy *leaving* a surface constitutes its *radiosity*. This latter concept is typically adopted for sources, such as the Earth, whose outgoing radiation varies spatially. Mathematically, the radiosity J is defined to be

$$J = E + B \quad (2.11)$$

where E and B denote, respectively, the radiant energy per unit time emitted directly and reflected from other sources, by a surface, per unit area. Both have SI units of W/m².

The derivation of each of these radiosity components parallels the one given in the previous section for irradiance. Again using Figure 2.2, but now considering the *outgoing* radiation from the differential area dA , the spectral intensity of the emitted energy is

$$I_{\lambda,e}(\lambda, \theta, \varphi) \equiv \frac{dQ_{\lambda,e}}{dA \cos \theta \cdot d\omega \cdot d\lambda} \quad (2.12)$$

while that of the reflected energy is

$$I_{\lambda,r}(\lambda, \theta, \varphi) \equiv \frac{dQ_{\lambda,r}}{dA \cos \theta \cdot d\omega \cdot d\lambda} \quad (2.13)$$

Specifically, $I_{\lambda,e}$ and $I_{\lambda,r}$ represent, respectively, the electromagnetic energy of wavelength λ per unit time emitted ($dQ_{\lambda,e}$) and reflected ($dQ_{\lambda,r}$) from dA , per interval $d\lambda$ about λ , per unit solid angle about the (θ, φ) direction, and per unit area projected normal to it. Integrating over all wavelengths produces the corresponding total intensities,

$$I_e(\theta, \varphi) = \int_0^\infty I_{\lambda,e}(\lambda, \theta, \varphi) d\lambda \quad (2.14)$$

and

$$I_r(\theta, \varphi) = \int_0^\infty I_{\lambda,r}(\lambda, \theta, \varphi) d\lambda \quad (2.15)$$

As with the spectral irradiance of Equation (2.7), the *spectral emissive power* E_λ is defined by considering the contribution from the differential area dS on the hemisphere surrounding dA . Rearranging Equation (2.12),

$$dE_\lambda(\lambda, \theta, \varphi) = \frac{dQ_{\lambda,e}}{dA d\lambda} = I_{\lambda,e}(\lambda, \theta, \varphi) \cos \theta d\omega \quad (2.16)$$

Making the substitutions of Equations (2.4) and (2.5), and integrating over the hemisphere,

$$E_\lambda(\lambda) = \int_0^{2\pi} \int_0^{\pi/2} I_{\lambda,e}(\lambda, \theta, \varphi) \cos \theta \sin \theta d\theta d\varphi \quad (2.17)$$

The *total* emissive power appearing in Equation (2.11) is then obtained by integrating over all wavelengths,

$$E = \int_0^\infty E_\lambda(\lambda) d\lambda \quad (2.18)$$

The *spectral reflected irradiance* B_λ is similarly defined. From Equation (2.13), the corresponding contribution of dS is

$$dB_\lambda(\lambda, \theta, \varphi) = \frac{dQ_{\lambda,r}}{dA d\lambda} = I_{\lambda,r}(\lambda, \theta, \varphi) \cos \theta d\omega \quad (2.19)$$

Again, substituting the expressions in Equations (2.4) and (2.5), and integrating over the hemisphere,

$$B_\lambda(\lambda) = \int_0^{2\pi} \int_0^{\pi/2} I_{\lambda,r}(\lambda, \theta, \varphi) \cos \theta \sin \theta d\theta d\varphi \quad (2.20)$$

Integrating over all wavelengths yields

$$B = \int_0^\infty B_\lambda(\lambda) d\lambda \quad (2.21)$$

which is the *total* reflected irradiance in Equation (2.11).

For the particular case of diffuse emission, the outgoing spectral intensity is independent of direction, and Equation (2.17) becomes

$$E_\lambda(\lambda) = I_{\lambda,e}(\lambda) \int_0^{2\pi} \int_0^{\pi/2} \cos \theta \sin \theta d\theta d\varphi = \pi I_{\lambda,e}(\lambda) \quad (2.22)$$

and, in turn,

$$E = \pi \int_0^\infty I_{\lambda,e}(\lambda) d\lambda = \pi I_e \quad (2.23)$$

Likewise, for diffuse reflection, the outgoing spectral intensity is independent of direction, and Equation (2.20) becomes

$$B_{\lambda}(\lambda) = I_{\lambda,r}(\lambda) \int_0^{2\pi} \int_0^{\pi/2} \cos \theta \sin \theta d\theta d\varphi = \pi I_{\lambda,r}(\lambda) \quad (2.24)$$

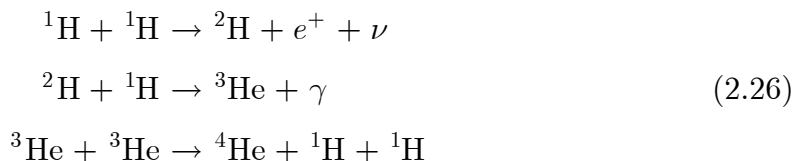
which leads to

$$B = \pi \int_0^{\infty} I_{\lambda,r}(\lambda) d\lambda = \pi I_r \quad (2.25)$$

In general, a surface that emits radiation diffusely does not necessarily reflect incident energy in the same manner, and vice versa, although such assumptions are commonly made in thermal analyses.

2.2 Direct Solar Radiation

Most of the electromagnetic energy incident on the surfaces of a satellite in orbit about the Earth begins its journey at the core of the Sun. There, under intense pressure and at extraordinary temperatures, the hydrogen atoms that comprise its bulk fuse with one another to produce helium, a “transmutation” first suggested by Eddington (1920). Familiar with the then-recent discovery that the mass of a helium atom is slightly less than the combined mass of its four constituent hydrogen atoms, he theorized that significant energy would be liberated in the conversion. Nearly twenty years later, Bethe (1939) confirmed this conjecture, when he identified the specific series of thermonuclear reactions powering main-sequence stars. In the Sun, this energy-production process is dominated by the proton-proton chain reaction (Naur, 1954):



It derives its name from the first reaction, in which two hydrogen nuclei, or protons, denoted ${}^1\text{H}$, combine to produce the hydrogen isotope ${}^2\text{H}$, known as deuterium, releasing a positron e^+ and a neutrino ν . The deuterium subsequently captures another proton, yielding the light isotope of helium ${}^3\text{He}$, and emitting a gamma-ray photon γ . Finally, two of these helium-3 isotopes combine to produce the other stable helium isotope ${}^4\text{He}$, also known as an α -particle, and two protons, which are then available to participate in the first reaction of a subsequent chain. The positron created in the first reaction immediately annihilates with a free electron, stripped from the ionized hydrogen, creating two additional gamma-ray photons. Accounting for the energy lost to the neutrino, which leaves the Sun unimpeded, Salpeter (1952) determined that a single, complete proton-proton chain produces 26.2×10^6 electron volts, or 4.20×10^{-12} J.

Collisions among the gamma-ray photons, within the extremely dense, ionized core, lower their energies, transforming them almost immediately into X-ray photons. Gradually, over *millions* of years, they make their way toward the surface, repeatedly absorbed and re-emitted by the atoms that they encounter, in a diffusion process dictated by the opacity of the Sun. As a result, they progressively lose additional energy, and ultimately, emerge largely as visible-wavelength photons before being conveyed to the photosphere via convection (Shu, 1982). It is from this outer layer of the Sun that they are emitted into

space, with a small fraction, but nevertheless vital number, reaching the Earth — and the satellites in orbit about it.

Direct measurements of this incident radiation, the total solar irradiance (TSI), have been made since 1978, using a series of satellite-based instruments (Willson and Mordvinov, 2003). Although frequently dubbed the “solar constant,” the TSI actually exhibits long-term variations of $\sim 0.1\%$ in concert with the solar magnetic cycle, and smaller, shorter-period fluctuations associated with sunspots and faculae (Willson and Hudson, 1991; Fröhlich and Lean, 1998). Nonetheless, it can be regarded as constant for most aerospace applications. Typically normalized to a distance of one astronomical unit (AU) from the Sun, this reference TSI has an adopted standard value of $S_{\odot} = 1366.1 \text{ W/m}^2$ (American Society for Testing and Materials (ASTM), 2000). At an arbitrary distance r , the local TSI, denoted G_{\odot} , can be obtained by scaling S_{\odot} ,

$$G_{\odot}(r) = \frac{4\pi R^2 \cdot S_{\odot}}{4\pi r^2} = S_{\odot} \left(\frac{R}{r} \right)^2 \quad (2.27)$$

where R represents one AU, 1.49598×10^{11} meters. Figure 2.3 illustrates this variation at the distance of the Earth, over the course of a year, as it moves through its elliptical orbit about the Sun. The numerator of the middle expression in Equation (2.27) constitutes the Sun’s total radiance, or luminosity, approximately $3.84 \times 10^{26} \text{ W}$. To produce energy at this rate, nearly 9×10^{37} proton-proton chain reactions in the core must be completed each second.

As Equation (2.8) suggests, the TSI should correspond to the integration of the solar *spectral* irradiance. In fact, early efforts to define the “solar constant” often used this very method (see, for example, Labs and Neckel, 1968). With that

value now precisely and independently monitored, however, recent standards calibrate the spectral irradiance data so that the integration recovers S_{\odot} . Plotted in Figure 2.4, the ASTM E-490 extraterrestrial reference spectrum incorporates observations from ground-based solar telescopes, high-altitude aircraft, rocket soundings, satellites, and even Space Shuttle missions (ASTM, 2000). It shows that the Sun emits nearly all of its radiation at wavelengths between 0.2 and 4.0 μm , with the peak occurring within the visible region, at about 0.5 μm .

This spectral distribution can be closely approximated by that emitted from a blackbody with a temperature of 5800 K. As given by Planck's law, the spectral emissive power for such a body is

$$E_{\lambda,b}(\lambda, T) = \frac{2\pi hc^2}{\lambda^5 \left(e^{hc/k\lambda T} - 1 \right)} \quad (2.28)$$

where λ and T represent wavelength and temperature, respectively. The other parameters are fundamental constants: c , the speed of light; h , Planck's constant; and k , Boltzmann's constant. Integrating over all wavelengths yields the total emissive power for a blackbody, and the Stefan-Boltzmann law,

$$E_b(T) = \int_0^{\infty} E_{\lambda,b}(\lambda, T) d\lambda = \sigma T^4 \quad (2.29)$$

where σ is the Stefan-Boltzmann constant. As with the reference spectrum, the blackbody curve in Figure 2.4 has been normalized to yield an integrated total irradiance equal to S_{\odot} .

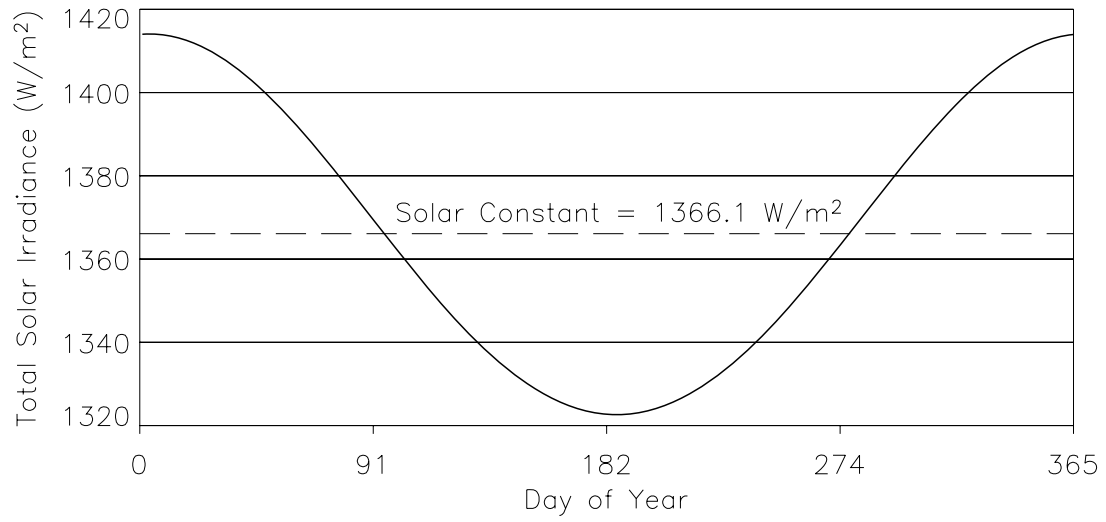


Figure 2.3. Variations in Total Solar Irradiance at the Earth

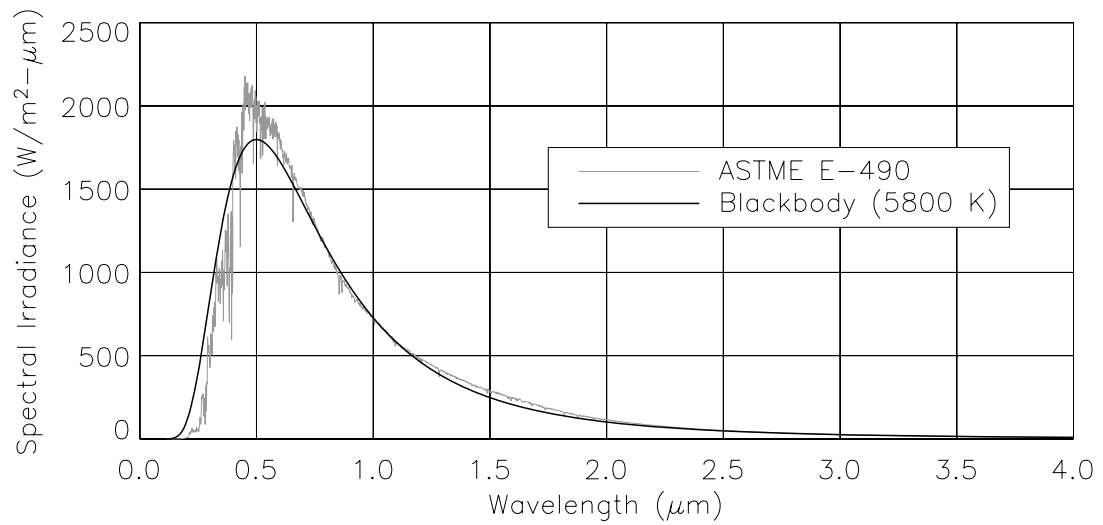


Figure 2.4. Spectral Distribution of Solar Irradiance at the Earth

2.3 Earth Albedo and Emissivity

The Earth reflects, on average, about 30% of the radiation that it intercepts from the Sun, and absorbs the remainder, emitting it later at infrared wavelengths (de Pater and Lissauer, 2001). The fraction of normally incident solar radiation reflected from a differential Earth element dA_{\oplus} is defined to be its Bond, or planetary, albedo a ,

$$a = \frac{B_{\oplus}}{G_{\odot} \cos \psi_{\oplus}^{\odot}} \quad (2.30)$$

where B_{\oplus} represents the total reflected irradiance. In the denominator of Equation (2.30), the cosine of the solar zenith angle ψ_{\oplus}^{\odot} scales the total solar irradiance G_{\odot} , obtained from Equation (2.27), to yield the normal component of the incoming radiation. Illustrated in Figure 2.5, this angle lies between \hat{n}_{\oplus} , the normal to dA_{\oplus} , and \hat{R}_{\odot} , the geocentric unit vector to the Sun. Thus,

$$\cos \psi_{\oplus}^{\odot} = \hat{n}_{\oplus} \cdot \hat{R}_{\odot} \quad (2.31)$$

In contrast, the emissivity e of dA_{\oplus} describes the total emissive power E_{\oplus} of the infrared energy that it emits — often called outgoing longwave radiation (OLR) — as a fraction of the equivalent blackbody total emissive power E_b ,

$$e = \frac{E_{\oplus}}{E_b} \quad (2.32)$$

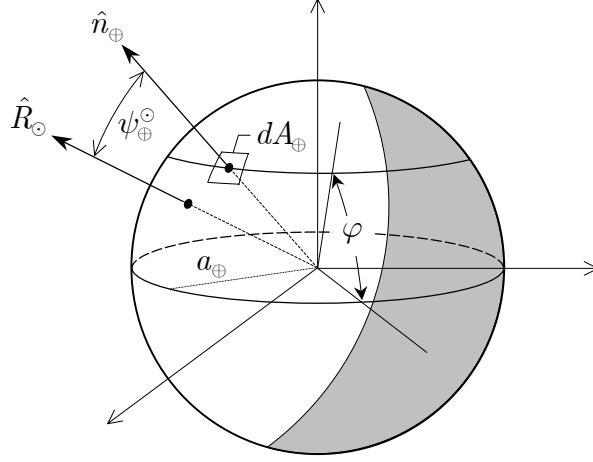


Figure 2.5. Earth Radiation Geometry

If the Earth were, in fact, a blackbody, it would absorb and emit *all* of the solar radiation that it intercepted. Integrating that incident radiation over the hemisphere H facing the Sun provides the total energy absorbed per unit time by a blackbody Earth,

$$Q_{\oplus,b} = \int_H G_{\odot} \cos \psi_{\oplus}^{\odot} dA_{\oplus} = \pi G_{\odot} a_{\oplus}^2 \quad (2.33)$$

where a_{\oplus} denotes the radius of the Earth. The complete emission of this energy occurs uniformly across the entire surface area of the blackbody Earth, yielding

$$E_b = \frac{Q_{\oplus,b}}{A_{\oplus}} = \frac{\pi G_{\odot} a_{\oplus}^2}{4\pi a_{\oplus}^2} = \frac{G_{\odot}}{4} \quad (2.34)$$

Substituting this result into Equation (2.32) relates the emissivity to the incident solar radiation,

$$e = \frac{4E_{\oplus}}{G_{\odot}} \quad (2.35)$$

The various land, water and ice surfaces on the Earth, along with the aerosols and clouds in its atmosphere, drive the reflection and absorption of incoming radiation from the Sun. Early estimates of a globally averaged albedo were inferred from limited observations made by Danjon (1954) of *earthshine* — the sunlight reflected from the Earth to the Moon’s surface — between 1926 and 1935. In general, however, terrestrial measurements of either albedo or emissivity for the Earth have been, and continue to be, inherently difficult to make. Only with the launch of meteorological satellites, in the early 1960s, did it become possible to determine either quantity more or less directly.

From the first Television and Infrared Observation Satellites (TIROS) to the current Aqua and Terra missions, radiometers have been carried into orbit to investigate the link between the net radiation balance of the planet and its climate. Although these instruments evolved significantly over the intervening decades, each was designed to measure the spectral intensity of the reflected solar and emitted infrared energy reaching its sensors. Deriving albedo and emissivity from such observations requires several additional computations to account for their intrinsic spectral, directional and temporal properties¹ (see, for example, for example, Raschke et al., 1973). The resulting values represent conditions at the top of the Earth’s atmosphere, the boundary where radiation balance is typically evaluated in climate studies.

¹ Interestingly, the earthshine technique, abandoned at the onset of the satellite era, has resurfaced as an independent means of calibrating the assumptions and models used to infer globally averaged albedo from satellite measurements of reflected radiation (Qiu et al., 2003).

In his work regarding the orbital perturbations induced by Earth radiation, Lochry (1966) confirmed that both albedo and emissivity (more accurately, OLR) exhibited strong latitude dependencies, and virtually no longitude ones. Using the TIROS-derived data sets of Bandeen et al. (1965), he compared least-squares fits for various mathematical models based exclusively on latitude. This remains the most common approach, even for data subsequently collected by later satellites, although others have been developed. For example, Sehnal (1979) performed a full spherical harmonic analysis — to degree and order 12 — of the albedo data computed by Lála et al. (1978) from the accelerometer onboard the French D5B (Castor) satellite. Knocke et al. (1988) incorporated the observed periodic trends into their models, after concluding that both albedo and emissivity could be represented effectively using only two-degree zonal harmonic expansions in terms of the geocentric latitude φ_c :

$$\begin{aligned} a &= a_0 + a_1 P_1(\sin \varphi_c) + a_2 P_2(\sin \varphi_c) \\ a_1 &= c_0 + c_1 \cos[\omega_{\oplus}(t - t_0)] + c_2 \sin[\omega_{\oplus}(t - t_0)] \end{aligned} \tag{2.36}$$

$$\begin{aligned} e &= e_0 + e_1 P_1(\sin \varphi_c) + e_2 P_2(\sin \varphi_c) \\ e_1 &= k_0 + k_1 \cos[\omega_{\oplus}(t - t_0)] + k_2 \sin[\omega_{\oplus}(t - t_0)] \end{aligned} \tag{2.37}$$

where P_1 and P_2 are the first- and second-degree Legendre polynomials, respectively. The time-dependent $a_1(t)$ and $e_1(t)$ coefficients reflect the seasonal variations, with a frequency of $\omega_{\oplus} = 2\pi/365.25$ rad/day. They obtained values for the constant coefficients in Equations (2.36) and (2.37) from least-squares fits to the Earth radiation budgets of Stephens et al. (1981), using an initial epoch t_0 of December 22, 1981. Table 2.1 summarizes those results, which were adopted for this study.

Albedo		Emissivity	
a_0	0.34	e_0	0.68
c_0	0	k_0	0
c_1	0.10	k_1	-0.07
c_2	0	k_2	0
a_2	0.29	e_2	-0.18

Table 2.1. Earth Albedo and Emissivity Model Coefficients

2.4 Eclipsing

Depending on the size, shape and orientation of its orbit, a satellite may periodically pass through the shadow cast by the Earth. During such eclipse intervals, the planet obscures the Sun, blocking its incoming radiation. The determination of whether, and when, these transits occur is critical to the management of power and thermal systems onboard most satellites. It also factors directly into algorithms designed to compute the orbit perturbations induced by solar radiation pressure. To address these various concerns, two different models of the Earth's shadow have traditionally been considered: (1) a cylinder and (2) a cone. The choice to use one or the other depends on the specific application, particularly the accuracy required and the computational resources available.

In the first model, a spherical Earth of radius a_{\oplus} lies at an infinite distance from the Sun. Under this assumption, the rays of electromagnetic energy arriving from the latter appear to be parallel, as if from a point source. They

produce a right-cylindrical shadow that extends indefinitely beyond the planet, its axis along the Earth-Sun line. Figure 2.6 illustrates this geometry, drawn in the plane defined by the satellite position vector \vec{r} and the unit vector \hat{R}_\odot from the Earth to the Sun. Within this theoretical cylinder, the Sun is completely eclipsed, and a satellite traveling through it encounters no solar radiation.

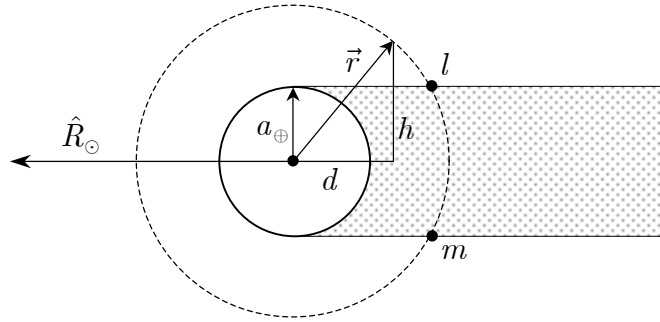


Figure 2.6. Cylindrical Shadow Model

Using this model, the conditions for eclipse can be established by examining the horizontal and vertical components of \vec{r} , resolved, respectively, along the Earth-Sun line,

$$d = \vec{r} \cdot \hat{R}_\odot \quad (2.38)$$

and perpendicular to it,

$$h = \sqrt{r^2 - d^2} \quad (2.39)$$

where $r = |\vec{r}|$. If $d > 0$, the satellite is sunward of the planet and, clearly, unshadowed. Otherwise, and if $h < a_\oplus$, the satellite is within the cylinder and, by definition, shadowed. The intersections of the orbit with the surface of the

cylinder — points l and m , in Figure 2.6 — occur where $d < 0$ and $h = a_{\oplus}$. Marking the entry to and the exit from eclipse, these terminators can be found analytically in the two-body problem (Escobal, 1962) or numerically for an integrated ephemeris (see, for example, Neta and Vallado, 1998).

To overcome some of the limiting assumptions made in the cylindrical approach, the second model accounts for the finite size and distance of the Sun. In this formulation, a spherical Earth of radius a_{\oplus} intercepts the variously oriented rays of radiant energy emitted isotropically by a spherical Sun of radius a_{\odot} . They produce a conical shadow behind the Earth with two discernible regions, the penumbra and the umbra. Figure 2.7 depicts each as a cone with its axis along the Earth-Sun line, projected onto the plane defined by \vec{r} and \vec{R}_{\odot} . The larger penumbral cone begins sunward of the planet, at a theoretical vertex V , and continues indefinitely beyond it. Oppositely oriented, the smaller umbral cone extends a finite distance into the penumbra, converging at the vertex W . Only within the umbra is the Sun completely eclipsed. In the surrounding penumbra, the Earth partially obscures the Sun, reducing, but not eliminating, the solar irradiance encountered by a satellite traveling through it.

Often referred to as the “dual-cone” or “umbra-penumbra” shadow model, it establishes conditions for eclipse that depend on the apparent sizes, and the relative separation, of the Sun and the Earth, as viewed from the satellite’s position. Each has an apparent angular radius α defined to be its linear radius divided by the distance from the satellite to its center. Thus, for the Sun and the Earth, respectively,

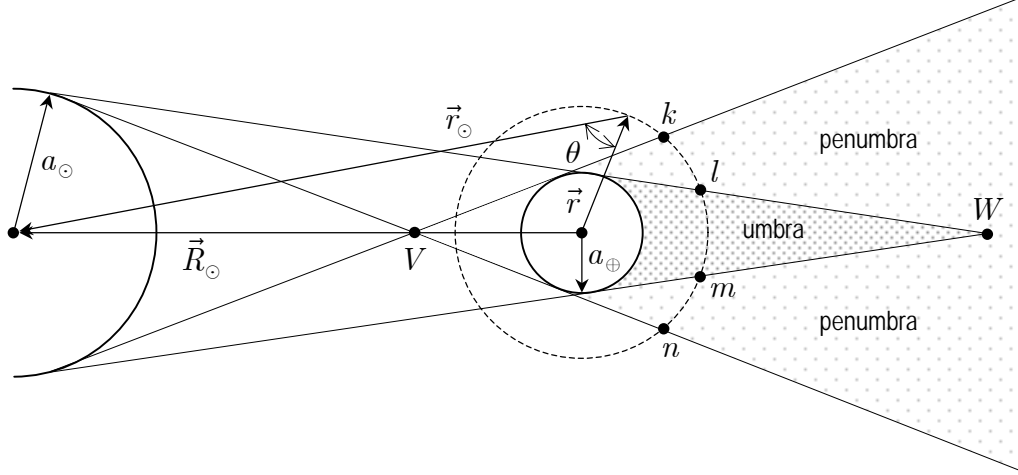


Figure 2.7. Conical Shadow Model

$$\alpha_\odot = \frac{a_\odot}{r_\odot} \quad \alpha_\oplus = \frac{a_\oplus}{r} \quad (2.40)$$

where $r_\odot = |\vec{R}_\odot - \vec{r}|$ and $r = |\vec{r}|$. Their relative separation can be quantified by θ , the angle between $-\vec{r}$ and \vec{r}_\odot ,

$$\theta = \cos^{-1} \left(\frac{-\vec{r} \cdot \vec{r}_\odot}{r r_\odot} \right) \quad (2.41)$$

If $\theta \geq \alpha_\odot + \alpha_\oplus$, the Sun and the Earth are sufficiently far apart that no eclipsing occurs, leaving the satellite entirely unshadowed. Alternatively, if $\theta \leq \alpha_\oplus - \alpha_\odot$, the Earth completely obscures the Sun, placing the satellite within the umbra, fully shadowed.

The penumbra lies between these two limiting conditions, where $\alpha_\odot + \alpha_\oplus > \theta > \alpha_\oplus - \alpha_\odot$. There, the partial occultation of the Sun effectively scales the solar irradiance of Equation (2.27) by a factor f ,

$$G_{\odot}(r_{\odot}) = f S_{\odot} \left(\frac{R}{r_{\odot}} \right)^2 \quad (2.42)$$

Typically, at a given position, the value of f is determined either by assuming a linear transition across the penumbra, from full sun to full shadow, or through proportional shadowing. In the latter method, the solar irradiance varies directly with the apparent area of the unobstructed portion of the Sun. Both the Sun and the Earth have total apparent areas derived using the angular radii of Equation (2.40),

$$A_{\odot} = \pi \alpha_{\odot}^2 \quad A_{\oplus} = \pi \alpha_{\oplus}^2 \quad (2.43)$$

Illustrated in Figure 2.8, their intersection represents the obstructed portion of the Sun, shown by Gibson (1977) to be

$$A_{\oplus} \cap A_{\odot} = \alpha_{\odot}^2 \cos^{-1} \left(\frac{\zeta}{\alpha_{\odot}} \right) + \alpha_{\oplus}^2 \cos^{-1} \left(\frac{\theta - \zeta}{\alpha_{\oplus}} \right) - \theta \sqrt{\alpha_{\odot}^2 - \zeta^2} \quad (2.44)$$

where

$$\zeta = \frac{\theta^2 + \alpha_{\odot}^2 - \alpha_{\oplus}^2}{2\theta} \quad (2.45)$$

Consequently, the desired scale factor, defined as the ratio of the apparent area of the unobstructed Sun to its total apparent area, can be expressed as

$$f = \frac{A_{\odot} - (A_{\oplus} \cap A_{\odot})}{A_{\odot}} = 1 - \frac{A_{\oplus} \cap A_{\odot}}{A_{\odot}} \quad (2.46)$$

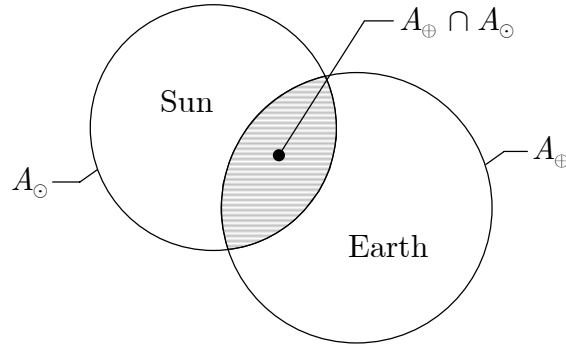


Figure 2.8. Partial Eclipse of the Sun by the Earth

The four terminators identified in Figure 2.7 correspond to the intersections of the orbit with the two cones in the model. Those on the surface of the penumbra — points k and n — occur where $\theta = \alpha_{\odot} + \alpha_{\oplus}$. Similarly, points l and m lie on the surface of the umbra, where $\theta = \alpha_{\oplus} - \alpha_{\odot}$. They are typically found numerically, even in the two-body problem, although extremely cumbersome analytical solutions do exist there (Mullins, 1991).

At the cost of increased computational intensity, this conical model provides a more accurate representation of the shadow cast by the Earth. It avoids the discontinuities that occur at the surface of the cylinder, where the satellite moves instantaneously between full sun and full shadow. Still, other models have been developed to account for secondary factors, such as the refraction of light through the Earth's atmosphere (Haley, 1973), the ellipticity of the Earth (Khatib and Sturms, 1970), and additional shadowing introduced by the Moon (Gibson, 1977).

Chapter 3

Radiation Pressure Modeling

3.1 Existence of Radiation Pressure

It would be difficult to overstate the impact that inquiries into the nature of light have had on the development of scientific thought. On the centenary of James Clerk Maxwell's birth, Planck (1931) wrote that the former's theory of electromagnetism "must remain for all time one of the greatest triumphs of human intellectual endeavour." Three decades later, and amidst the quantum revolution in physics, Feynman et al. (1964) went so far as to assert that,

From a long view of the history of mankind — seen from, say, ten thousand years from now — there can be little doubt that the most significant event of the 19th century will be judged as Maxwell's discovery of the laws of electrodynamics. The American Civil War will pale into provincial insignificance in comparison with this important scientific event of the same decade.

Although speculation about the properties of light dates back to Aristotle, modern optical theories trace their origins to René Descartes, who first suggested that light is only a mechanical property of the emitting object and the intervening medium (Sabra, 1967). Over the ensuing four centuries, eminent natural philosophers from around the world debated nearly every aspect of this idea. The most contentious and protracted arguments concerned the composition

and the transmission of light — namely, whether it consists of particles or waves, and whether it requires a medium in which to travel.

Without articulating a specific mechanism, Johannes Kepler first surmised that light also exerts a pressure. Based on his observations of the comet of 1607, subsequently named for Edmund Halley, he posited that the rays of the Sun expel material from its head, producing the characteristic tail in the anti-solar direction (Hellman, 1975). Isaac Newton (1726) acknowledged the plausibility of Kepler’s hypothesis in the *Principia*, noting

...it is not altogether unreasonable to suppose that in very free [or empty] spaces, the extremely thin upper air should yield to the action of the rays, despite the fact that gross substances in the very obstructed regions here on earth cannot be sensibly propelled by the rays of the sun.

Despite this concession, Newton did not believe it to be the most likely explanation for the formation of comet tails. Instead, he theorized that solar heating rarefied the surrounding ether, which he supposed to occupy the space between celestial bodies, allowing a comet’s tail to ascend away from the Sun in a buoyant fashion.

The more general question of whether light exerts a pressure remained unresolved well into the nineteenth century. Most proponents of an emission theory of light recognized that if it were material in nature, the constituent particles would possess, and thus transfer, momentum. Consequently, the repeated failures to observe the anticipated effects through experiment provided impetus to the increasingly popular wave theories of light, which did not appear

to predict any associated pressure (Schagrin, 1974; Worrall, 1982). In his seminal work on electricity and magnetism, Maxwell (1873), however, derived the electrostatic and electrokinetic energies stored in the waves that make up light under his theory, and concluded:

Hence in a medium in which [electromagnetic] waves are propagated there is a pressure in the direction normal to the waves, and numerically equal to the energy in unit of volume.

Shortly thereafter, and independently of Maxwell's work, Bartoli (1876) devised a thought experiment to consider the existence of light pressure from a thermodynamic perspective. Using a system of concentric shells, he was able to demonstrate that radiant heat could be transferred from the outer to the inner one, although the latter was at higher temperature. This appeared to violate the Clausius statement of the second law, which requires that work be done in such a process. Bartoli suggested that this work could be done by radiation pressure. Although Boltzmann (1884a) and Galitzine (1892) catalogued significant flaws in Bartoli's reasoning, they reached the same conclusion after reformulating the thought experiment, and correctly determined the pressure associated with the radiation. Boltzmann (1884b) used this same approach to derive Equation (2.29) — then known only as Stefan's law — finally giving that empirical relationship a theoretical foundation. Ironically, Bartoli himself ultimately abandoned his work on light pressure, convinced that his hypothesis was incorrect (Carazza and Kragh, 1989).

As with other aspects of Maxwell's electromagnetic theory, experimental evidence of radiation pressure remained elusive. The issue was complicated for some time by the misinterpretation of results obtained by Crookes (1874) with his radiometer. In his experiment, he placed a freely rotating vane, one side coated with polished silver and the other painted black, inside a partially evacuated glass bulb. When exposed to light or heat, the vane rotated. Crookes initially claimed that radiation pressure produced this motion, but numerous objections swiftly followed, with nearly all noting that the observed effects were several orders of magnitude greater than those predicted by theory. Furthermore, Schuster (1876) demonstrated that the responsible force was internal to the radiometer, and thus was not being induced by the external light source. Reynolds (1879) ultimately attributed the motion to a process he called "thermal transpiration," in which the residual gas molecules (present even in near-vacuum conditions) drive the vane in response to the thermal gradient existing between the reflective, silvered side and the absorptive, blackened one.

Overcoming these and many other challenges in the design of his apparatus, Lebedev (1901) succeeded in isolating the effects of radiation pressure and, within the limits of his observational errors, became the first to validate the predictions of Maxwell and Bartoli experimentally. These results appeared to be confirmed independently, and with greater precision, a few months later, by Nichols and Hull (1901). Their work, however, was later shown to be plagued by calculation errors (Bell and Green, 1933). Nonetheless, radiation pressure became an accepted fact within the scientific community, surviving even the quantum revolution in physics. Mulser (1985) provides a comprehensive and modern

derivation of the Maxwell-Bartoli formula, which, using the notation and terminology of this study, can be expressed as

$$p_r = \frac{G}{c}(1 + \eta) \quad (3.1)$$

The radiation pressure p_r is directly proportional to the energy density — the normally incident irradiance G divided by the speed of light c . The coefficient η varies between 0, for a perfectly absorptive surface, and 1, for a perfectly reflective one. In the case of the former, the numerical equivalence of pressure and energy density, first articulated by Maxwell, is obtained.

Although radiation pressure continued to have little significance for terrestrial applications, it was soon acknowledged to play an important role in various celestial phenomena. Resurrecting Kepler’s hypothesis, Arrhenius (1900) again suggested that light from the Sun causes the deflection of comet tails in the anti-solar direction. Schwarzschild (1901), in response, computed the effects of electromagnetic energy on small particles of different sizes, thus providing a theoretical foundation for this assertion. Ultimately, though, the comet tails extending radially away from the Sun were found to consist of ionized gas molecules whose deflection results from their interaction with the charged particles of the solar wind (Biermann, 1951). Nonetheless, radiation pressure does act on the larger dust particles released from the nucleus as it heats up during its approach toward the Sun, but this produces a tail typically observed along the comet’s trajectory (Festou et al., 1993).

Perhaps most significantly, Eddington (1916) determined that radiation pressure contributes to the internal equilibrium of stars, particularly those larger

than the Sun. The stability of any star depends on counteracting the enormous force of gravitational self-attraction that would otherwise cause it to collapse. Eddington suggested that this resistance stems from the pressure generated by the kinetic motion of gas molecules in the interior, as well as that associated with the outward flow of radiant energy. Furthermore, he asserted that their relative contributions in a given star depend on its mass, with the former dominating in smaller stars and the latter in larger ones. This realization eventually led him to uncover the relationship between mass and luminosity (Eddington, 1924), which explains the stellar main sequence observed empirically by Hertzsprung (1905) and Russell (1910).

Finally, Poynting (1904) was the first to consider the impact of radiation pressure on the motion of objects in orbit. His paper has often been cited for its novel discussion of the non-uniform emission of radiant energy absorbed by small bodies, an effect further investigated by Robertson (1937) and now referred to as Poynting-Robertson drag. In the latter half, however, Poynting discussed the action of radiation pressure on dust particles in orbit about the Sun, and speculated that it may also play a role in maintaining the rings of Saturn, which he supposed to be a net emitter of radiation. Based on this work, Plummer (1905, 1906) suggested that this pressure might explain the discrepancies between the observed and predicted orbits of comets. Remarkably, aside from Robertson's paper, little more was published regarding its perturbative effects until the advent of the space age, when the need arose to account for solar, and eventually terrestrial, radiation in the motion of artificial satellites.

3.2 Surface Reflection

As Equation (3.1) suggests, the radiation pressure exerted on an object depends on the extent to which its surface reflects incident energy. Under the classical formulation, electromagnetic waves possess momentum due to their time-varying electric and magnetic fields. Within quantum electrodynamics, an individual photon possesses momentum p proportional to its frequency ν ,

$$p = \frac{h\nu}{c} \quad (3.2)$$

where c and h are, respectively, the speed of light and Planck's constant. From either perspective, conservation of momentum dictates that an intercepting object acquire the momentum of any radiation that it absorbs, and twice that amount for any that it completely reflects. Thus, in Equation (3.1), as η varies from 0 to 1, the radiation pressure p_r varies from G/c to $2G/c$.

Generally, intercepted electromagnetic energy is neither entirely absorbed nor entirely reflected. Some is usually reflected at, or near, the surface, while the remainder passes into the object. In turn, some of that portion may be transmitted entirely through, but the rest is absorbed, raising the internal temperature. These reflected, transmitted and absorbed quantities are often described as fractions of the total irradiance G of the incident radiation. For example, the reflectivity ρ of a surface can be defined such that

$$B = \rho G \quad (3.3)$$

where B is the total reflected irradiance of Equation (2.21). Its transmissivity τ and absorptivity α can be similarly defined for the transmitted and absorbed components, respectively.

In addition to momentum, energy must be conserved in the interaction at the surface, which requires

$$\alpha G + \tau G + \rho G = G \quad (3.4)$$

Furthermore, if the object is opaque, no energy will be transmitted entirely through it. Setting $\tau = 0$ for such cases, and dividing through by G , leaves

$$\alpha + \rho = 1 \quad (3.5)$$

The precise behavior of the intercepted energy depends on its wavelength relative to the dimensions of the material's internal atomic structure, and on various conditions at the surface. In the ideal case of a pure substance, with an optically smooth surface, these radiative characteristics can be derived from its optical and electrical properties, using electromagnetic theory (see, for example, Siegel and Howell, 2002). Frequently, however, the values measured for real surfaces deviate from these theoretical predictions due to less-than-ideal conditions, such as surface roughness or contamination.

Measuring reflectivity directly can be especially difficult, since reflection is inherently bidirectional. Figure 3.1 illustrates the most general circumstance, in which radiation of wavelength λ from a (θ, φ) direction is reflected into an arbitrary (θ_r, φ_r) direction. Accordingly, a bidirectional spectral reflectivity can be defined,

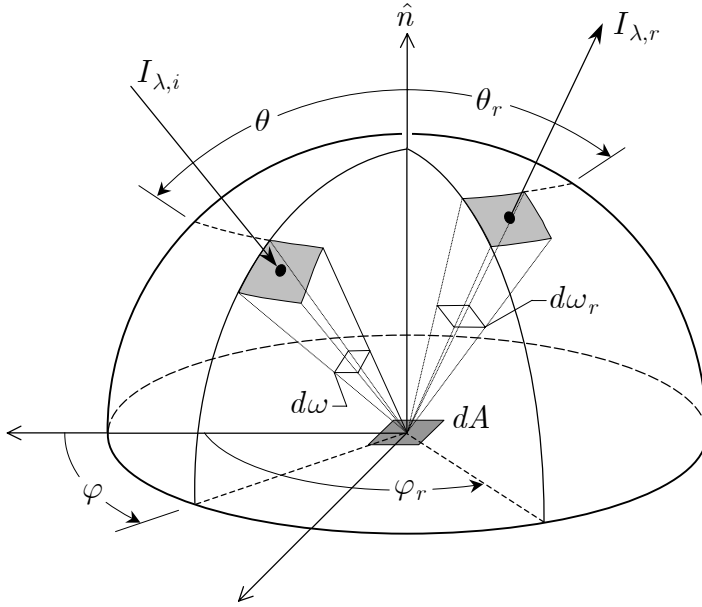


Figure 3.1. Bidirectional Reflection

$$\rho_{\lambda}(\lambda, \theta_r, \varphi_r, \theta, \varphi) = \frac{I_{\lambda,r}(\lambda, \theta_r, \varphi_r, \theta, \varphi)}{I_{\lambda,i}(\lambda, \theta, \varphi) \cos \theta d\omega} \quad (3.6)$$

Notably, this is a ratio of the reflected spectral *intensity* $I_{\lambda,r}$ to the incident spectral *irradiance* $I_{\lambda,i} \cos \theta d\omega$, the latter being the right-hand side of Equation (2.3). Therefore, it is not a dimensionless parameter, instead retaining units of sr^{-1} . Theoretically, ρ_{λ} could be integrated over all incident and reflected directions, and then over all wavelengths, to obtain the dimensionless, total reflectivity ρ that appears in Equation (3.5).

In practice, however, it has been observed that reflection from real surfaces generally resembles a combination of two limiting cases: diffuse and specular reflection. This is represented schematically, for the plane of incidence, in Figure 3.2. As noted in Chapter 2, the spectral intensity of diffusely reflected radiation is independent of direction. Thus, Equation (2.19) can be written as

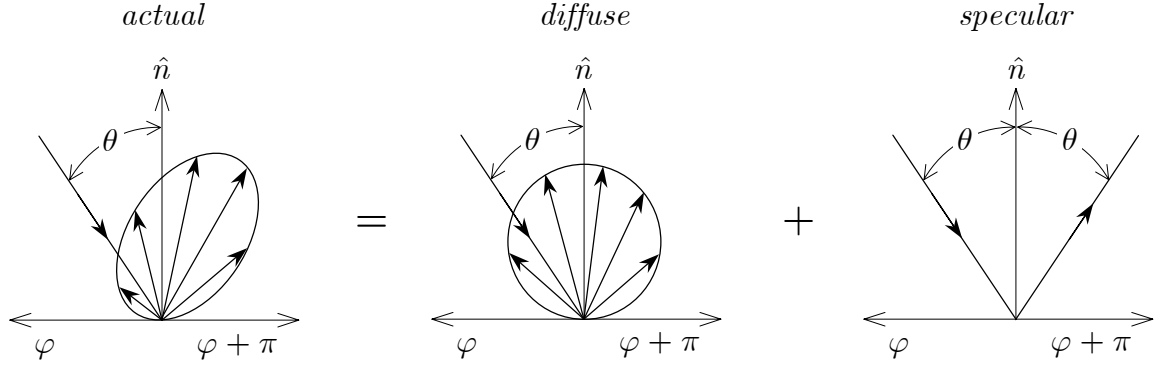


Figure 3.2. Combined Diffuse and Specular Reflection

$$dB_{\lambda}(\lambda, \theta_r, \varphi_r) = I_{\lambda, r}(\lambda) \cos \theta_r d\omega_r \quad (3.7)$$

where the r subscripts have been added to be consistent with Figure 3.1. Integrating this result over all wavelengths yields a *directional* total reflected irradiance,

$$dB(\theta_r, \varphi_r) = I_r \cos \theta_r d\omega_r \quad (3.8)$$

which remains a differential quantity because only the contribution within the solid angle $d\omega_r$ is being considered. Ideally diffuse surfaces reflect energy according to Equation (3.8) — a form of Lambert’s cosine law — and therefore, are often called *Lambertian* surfaces. Specular reflection, on the other hand, takes place within a plane containing the incident direction vector and the surface normal. As shown in the last illustration of Figure 3.2, radiation from a (θ, φ) direction is reflected with the same intensity into a single (θ_r, φ_r) direction, where $\theta_r = \theta$ and $\varphi_r = \varphi + \pi$.

To facilitate the modeling of real reflection as a combination of these two extremes, a linear transition from diffuse to specular reflection is assumed. The degree to which it resembles the latter for a given surface can be characterized by a specularity ξ , which varies from 0 (completely diffuse) to 1 (completely specular). Consequently, the reflectivity ρ can be resolved into a specular component,

$$\rho_s = \xi\rho \quad (3.9)$$

and a diffuse one,

$$\rho_d = (1 - \xi)\rho \quad (3.10)$$

Besides the challenges associated with measuring reflectivity directly, thermal analyses are generally concerned with the rates at which objects absorb and emit energy. As a result, absorptivity and emissivity data are more readily available for various engineering materials, including those used in space applications. Defined like that for the Earth in Equation (2.32), the emissivity of a satellite surface is the ratio of its total emissive power E , obtained from Equation (2.18), to the equivalent blackbody total emissive power E_b ,

$$\varepsilon = \frac{E}{E_b} \quad (3.11)$$

The denominator can be determined using the Stefan-Boltzmann law of Equation (2.29), based on the temperature at the surface. From Equation (3.5),

$$\rho = 1 - \alpha \quad (3.12)$$

This provides a straightforward way to obtain the specular and diffuse reflectivities from the absorptivity of a surface. Dropping the s subscript from Equation (3.9), and replacing ρ_d with δ in Equation (3.10), they become

$$\rho = \xi(1 - \alpha) \quad \delta = (1 - \xi)(1 - \alpha) \quad (3.13)$$

Both α and ε may vary with wavelength, and thus, they typically have values for solar radiation (including terrestrial albedo) different from those for the infrared radiation emitted by the Earth. In the case of the latter, the radiant energy incident at the satellite surface is essentially diffuse, and accordingly, Kirchoff's law states that $\alpha = \varepsilon$ within this spectral band. Therefore, the specular and diffuse reflectivities associated with infrared radiation can be expressed alternatively as

$$\rho = \xi(1 - \varepsilon) \quad \delta = (1 - \xi)(1 - \varepsilon) \quad (3.14)$$

3.3 Early Orbit Determination Models

Many of the techniques of classical celestial mechanics were initially adopted for the study of artificial satellites. As Shapiro (1963) notes, however, work in this area was rapidly influenced by “the availability of high-speed digital computers and the necessity of considering orbital behavior over many thousands of revolutions.” Consequently, analytical methods gave way to semi-analytical, and eventually, entirely numerical techniques. Although the integration methods of both Encke and Cowell were formulated long before the satellite era, they became practical only with the introduction of modern computers, in which the

numerous, repetitive steps could be automated. Furthermore, these two methods also became the preferred approaches to modeling satellite motion, especially when considering the various, often non-conservative perturbations associated with low-Earth orbits. In particular, the dynamic method of orbit determination described in Chapter 1 relies on the Cowell formulation, which involves a straightforward numerical integration of Equation (1.12).

Early studies of radiation pressure perturbations, however, employed various analytical techniques, including the Lagrange planetary equations, either in their original form, using a disturbing function, or in the Gaussian form, using a disturbing force (see, for example, Kozai, 1961). Typically, they required some very simple assumptions about the nature of the incident radiation and the satellite geometry. These same assumptions were often carried over to numerical methods, even though they could, in principle, accommodate more elaborate models. As the complexity of satellites and knowledge of the radiation environment in low-Earth orbit have increased, though, the computation of these forces has become significantly more intensive. As a result, they are frequently calculated offline, outside of the orbit determination algorithm, and then fit, using a mathematical series or a simplified model. The following sections summarize the various solar and Earth radiation pressure models that served as heritage for those developed for ICESat precision orbit determination (POD).

3.3.1 Solar Radiation Pressure

Launched in 1958, Vanguard I revealed the critical influence of J_3 — the third zonal harmonic of the Earth’s gravitational field — in the orbital motion of

an artificial satellite (O’Keefe et al., 1959). After considering its effects and those of luni-solar gravity, Musen et al. (1960) continued to observe disparities between the perigee heights predicted by their models and the values obtained from reductions of tracking data. Suspecting incident solar radiation to be perturbing the orbit, they computed a constant acceleration, using an effective cross-sectional area for the satellite and assuming only specular reflection from its surface. The addition of this simple model significantly improved the agreement between the predicted and observed perigee heights.

Parkinson et al. (1960) undertook a more general investigation of the solar radiation pressure perturbation prior to the launch of the Echo I balloon. Using a disturbing force similar to the one employed in the Vanguard I analysis, they numerically integrated the Lagrange equations in their Gaussian form, allowing them to evaluate the effects of the Earth’s shadow. Based on the resulting evolution of the perigee height, they were able to estimate how long a satellite would remain in orbit. Their prediction of the decay rate for Echo I was validated after launch by Muhleman et al. (1960), who determined the orbit of the satellite from tracking data. The latter group also generated accurate predictions of the perigee height by incorporating the same constant-acceleration model into an Encke integration method.

All of these models consider the satellite to be a sphere, or cannonball, that has a constant projected area A_c with respect to the Sun. The Multi-Satellite Orbit Determination Program (MSODP) uses this approach in its Radiation Pressure (RADPR) subroutine, modeling the solar radiation force per unit mass of Equation (1.12) as

$$\vec{S} = -f \frac{S_{\odot}}{c} \left(\frac{R}{r_{\odot}} \right)^2 \frac{A_c}{m} (1 + \eta_{\odot}) \hat{r}_{\odot} \quad (3.15)$$

where c represents the speed of light, and m denotes the mass of the satellite. Lochry (1966) argued that the $1 + \eta_{\odot}$ “augmentation factor” should account not only for reflected radiation, as suggested by Equation (3.1), but also for any radiation initially absorbed and later re-emitted. Nonetheless, η_{\odot} is often still referred to as the satellite reflectivity, with the subscript indicating that it applies to the visible portion of the spectrum that characterizes solar radiation. The force produced by this model acts along $-\hat{r}_{\odot}$, the unit vector from the Sun to the satellite. Although scaled by the distance r_{\odot} along this direction, according to Equation (2.27), the solar constant S_{\odot} in the MSODP implementation assumes a value of 1367.2 W/m², derived earlier by Willson (1978).

The additional scale factor f accounts for any shadowing of the satellite that may occur during the orbit. For the cylindrical model of radius a_{\oplus} , described in Section 2.4, the eclipse conditions yield

$$f = \begin{cases} 0, & d \leq 0 \text{ and } h \leq a_{\oplus} \\ 1, & \text{otherwise} \end{cases} \quad (3.16)$$

where d and h are defined, respectively, by Equations (2.38) and (2.39). Likewise, for the conical shadow model

$$f = \begin{cases} 0, & \theta \leq \alpha_{\oplus} - \alpha_{\odot} \\ 1, & \theta \geq \alpha_{\odot} + \alpha_{\oplus} \\ \text{Equation (2.46)}, & \text{otherwise} \end{cases} \quad (3.17)$$

where α_{\odot} and α_{\oplus} are defined by Equations (2.40), and θ , by Equation (2.41). The discontinuities associated with the shadow boundaries in both models can introduce errors into the numerical integration of the equation of motion. Although MSODP does not attempt to mitigate these errors, they can be reduced by the application of modified back differences (Lundberg et al., 1991) or local Encke corrections (Woodburn, 2001).

Due to its simplicity and generality, the cannonball model remains common in orbit determination algorithms, although alternative approaches have been developed for specific applications. To prepare for the Pioneer 10 and 11 missions to the outer solar system, Georgevic (1971) derived the solar radiation forces acting on the large parabolic high-gain antenna reflector during the cruise phase. He compared these results to those predicted by a standard cannonball model, and found the errors to be as large as 25%. Consequently, he designed an analytical model for the trajectory software in terms of the Sun-spacecraft-Earth angle, based on fits made to his detailed results. He used this same method for the Mariner 9 mission to Mars (Georgevic, 1973), and then extended it for the Mariner 10 mission to Venus and Mercury, in light of the increased magnitude of the solar radiation perturbation in the inner solar system (Georgevic, 1974).

A similar strategy was eventually adopted for the Global Positioning System (GPS) satellites. The original ROCK4 model for Block I (Fliegel et al., 1985), and the original ROCK42 model for Block II (Fliegel and Gallini, 1989), divided each satellite into flat and cylindrical surfaces to determine the net solar radiation force acting. In addition to being computationally intensive from an orbit determination perspective, these models failed to consider visible radiation

that is absorbed and later emitted as heat. Fliegel et al. (1992) subsequently enhanced both models to include such thermal radiation effects, but then used high-fidelity Fourier series to fit the resulting output, producing the more efficient, analytical T10 and T20 models. Beutler et al. (1994) extended these models by including satellite-specific empirical parameters, which they estimated during GPS data processing at the Center for Orbit Determination in Europe (CODE). Through an analysis of 5.5 years of CODE-generated ephemerides, Springer et al. (1998) obtained order-of-magnitude improvements in both orbit determination and prediction accuracy using a considerably expanded empirical model. Given the significance of the solar radiation pressure perturbation for the GPS satellites, ongoing efforts to improve the overall quality of the orbit solutions continue to focus on refining these models (see, for example, Bar-Sever and Kuang, 2004).

3.3.2 Earth Radiation Pressure

As mentioned in Section 2.3, empirical data regarding the radiation reflected and emitted by the Earth only became available with the launch of meteorological satellites in the early 1960s. This lack of knowledge, combined with the geometrical complexity of the Earth-radiation problem, led some early investigators to ignore the potential effects on orbiting satellites. Others, using simplified models to make their analyses mathematically tractable, concluded that such effects were negligible, particularly in the presence of more dominant perturbations. Shapiro and Jones (1960), for example, adopted a uniform, specular model for Earth albedo, and asserted that its effects on the Echo I orbit

amounted to only 1% of those induced by direct solar radiation pressure. Later, Shapiro (1963) also argued that the radiation absorbed and re-emitted by the Earth was likely uniformly distributed, acting only to reduce the planet's gravitational constant by an insignificant amount.

Despite this dearth of evidence as to the spatial and temporal characteristics of terrestrial radiation, Wyatt (1963) explored the perturbations arising from several hypothetical models of varying complexity. In doing so, he correctly ascertained that the diffuse component of the radiation reflected from the Earth constitutes a more substantial perturbing force than the more readily modeled specular one. As a result, his general-perturbation analysis concluded that the associated secular changes in orbit period and eccentricity were nearly 10% of those induced by direct solar radiation. Although limiting his work to constant, diffuse albedo, Sehnal (1966a) nonetheless produced “the most detailed study of the orbital perturbations of Earth-radiation pressure” during this period, according to Smith (1970). Using the Gaussian form of the Lagrange equations, he derived the theoretical change in each of the Keplerian orbit elements in response to an albedo disturbing force that he formulated in an earlier paper (Sehnal, 1966b).

Suggesting that special perturbations represented a more suitable technique for studying the effects of Earth radiation, Baker (1966) derived detailed expressions for the components of the forces associated with both reflected and emitted radiation. Lochry (1966) subsequently refined these results, and combined them with the data collected by the Television and Infrared Observation Satellites (TIROS), as reported by Bandeen et al. (1965), to obtain

the secular variations in the orbital elements. Adopting Lochry's equations for the force components in the case of uniform albedo, Lautman (1977a) developed analytic expressions for the orbital perturbations as series in the true anomaly. He applied the same approach in a later paper for one of the latitude-dependent albedo models with which Lochry had fit the TIROS observations (Lautman, 1977b).

The increased orbit determination accuracy afforded by ground-based laser ranging to geodetic satellites renewed interest in improving numerical models for Earth-radiation forces (Knocke, 1989). In addition, observations obtained from the accelerometer onboard the French D5B (Castor) satellite led Sehnal (1981) to revisit the perturbations induced by the emitted infrared radiation. Perhaps the most significant impetus for investigations in this area, however, came with the revelation of an unexplained, secular decrease in the semi-major axis of the Laser Geodynamic Satellite (LAGEOS), first reported by Smith and Dunn (1980). This produced a remarkable series of papers attempting to identify or to dismiss a variety of potential causes, including several that investigated terrestrial radiation, such as Rubincam (1982), Anselmo et al. (1983), Rubincam and Weiss (1986), and Rubincam et al. (1987). Ultimately, Rubincam (1987, 1988) attributed the majority of the decrease to thermal drag, in which the onboard anisotropic re-emission of infrared radiation absorbed from the Earth creates a temperature gradient that, in turn, produces a net acceleration opposite the direction of motion due to the orientation of the LAGEOS spin axis.

As part of the effort to determine the source of the anomalous behavior of LAGEOS, Knocke et al. (1988) adapted and extended a model for Earth radiation developed earlier by McCarthy and Martin (1977). The latter divides the portion of the planet visible to the satellite, at any given time, into a cap, centered at the subsatellite point, and two concentric rings, each with six area elements. The albedo and infrared contributions from these surfaces are summed to yield the net pressure acting on the satellite. The updated model follows a similar approach, but divides the outer ring into 12 elements. Furthermore, whereas the original model creates elements with identical projected areas, the new algorithm defines the ring boundaries such that the each element has the same projected, *attenuated* area:

$$A' = \frac{2(1 - \cos \theta_{max})}{N} \quad (3.18)$$

where $N (= 19)$ is the total number of elements. As illustrated in Figure 3.3, θ_{max} represents the half-angle of the cone bounding the surface visible to the satellite, and can be expressed in terms of the radius of a spherical Earth a_{\oplus} and the geocentric satellite distance r ,

$$\theta_{max} = \sin^{-1} \left(\frac{a_{\oplus}}{r} \right) \quad (3.19)$$

Rearranging Equation (2.30) provides the total reflected irradiance of the i -th element,

$$B_{\oplus}^i = a_i G_{\odot} \cos \psi_{\oplus,i}^{\odot} = a_i G_{\odot} \left(\hat{n}_{\oplus}^i \cdot \hat{R}_{\odot} \right) \quad (3.20)$$

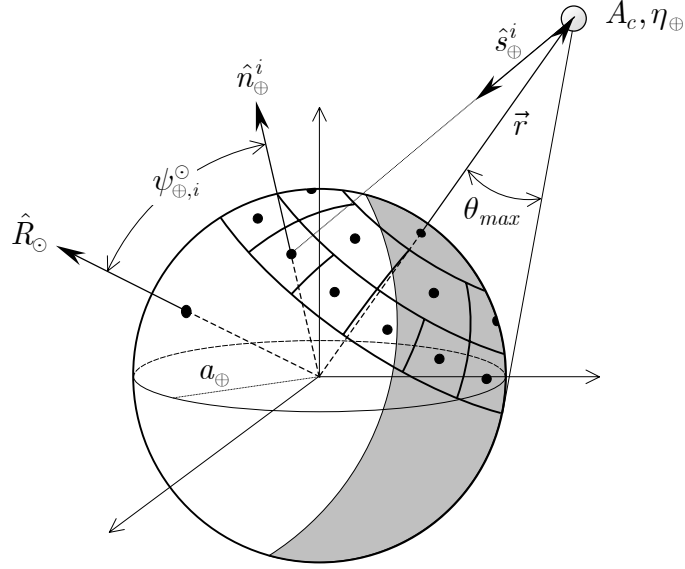


Figure 3.3. Earth Radiation Pressure Geometry

Here, the total solar irradiance G_\odot is calculated from Equation (2.27), using the distance R_\odot between the Sun and the Earth, and further scaled by the cosine of the solar zenith angle $\psi_{\oplus,i}^\odot$ — defined as the dot product of the normal to the element \hat{n}_\oplus^i and the geocentric unit vector to the Sun \hat{R}_\odot . Similarly, the total emissive power of the i -th element is obtained from Equation (2.35),

$$E_\oplus^i = \frac{e_i G_\odot}{4} \quad (3.21)$$

Together, these two quantities constitute the radiosity of the element.

The satellite is again assumed to be a cannonball, with a constant projected area A_c and mass m . For the Earth radiation pressure perturbation of Equation (1.12), summing over all of the area elements yields the net force per unit mass,

$$\vec{E} = -\frac{1}{c} \left[A' \sum_{i=1}^N (B_{\oplus}^i + E_{\oplus}^i) \right] \frac{A_c}{m} (1 + \eta_{\oplus}) \hat{s}_{\oplus}^i \quad (3.22)$$

While this result resembles Equation (3.15), the coefficient η_{\oplus} , used for both the reflected visible radiation and the emitted infrared radiation, may differ from η_{\odot} . The quantity in brackets represents the total irradiance from the Earth incident at the satellite, and the resulting force is directed along the $-\hat{s}_{\oplus}^i$ unit vector, from the center of the i -th element to the satellite. Substituting Equations (3.18), (3.20) and (3.21), along with the appropriate expression for G_{\odot} , yields the model implemented in the MSODP Earth Radiation Pressure (ERADP) subroutine:

$$\begin{aligned} \vec{E} = & -\frac{2(1 - \cos \theta_{max})}{N} \frac{S_{\odot}}{c} \left(\frac{R}{R_{\odot}} \right)^2 \frac{A_c}{m} (1 + \eta_{\oplus}) \\ & \times \sum_{i=1}^N \left[a_i (\hat{n}_{\oplus}^i \cdot \hat{R}_{\odot}) + \frac{e_i}{4} \right] \hat{s}_{\oplus}^i \end{aligned} \quad (3.23)$$

The albedo a_i and the emissivity e_i of each element are based on the latitude at its center, and computed using Equations (2.36) and (2.37), respectively, in conjunction with the constants of Table 2.1.

3.3.3 TOPEX/Poseidon Macro-Model

Faced with the previously unprecedented orbit accuracy requirements of the TOPEX/Poseidon oceanographic mission, Marshall et al. (1991) proposed the development of a satellite *macro-model* to compute solar and Earth radiation forces. Illustrated in Figure 3.4, this model consists of a six-sided “box”, representing the satellite bus, and a two-sided “wing”, representing the single solar array. Each of these eight surfaces is a flat plate that reflects both diffusely

and specularly. Baker (1966) first noted that the force acting on such an illuminated surface is not aligned with the direction of the incoming radiation. He derived the resulting force per unit mass, which, using the notation of this study, can be expressed as

$$\ddot{\vec{r}} = -\frac{G}{c}(\hat{n} \cdot \hat{s})\frac{A}{m}\left\{(1-\rho)\hat{s} + 2\left[\frac{\delta}{3} + \rho(\hat{n} \cdot \hat{s})\right]\hat{n}\right\} \quad (3.24)$$

for a surface with an area A , a diffuse reflectivity δ , and a specular reflectivity ρ . The direction of the force produced by the total irradiance G is a linear combination of $-\hat{s}$, the unit vector from the arbitrary source to the surface, and $-\hat{n}$, the opposite of the unit surface normal.

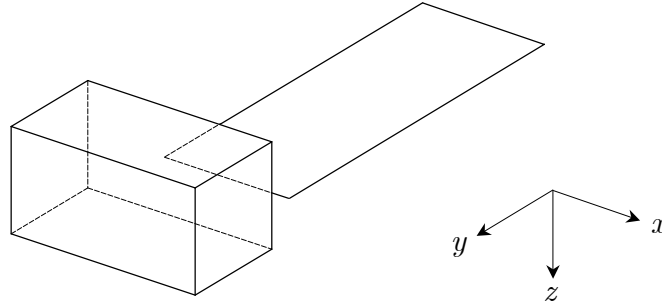


Figure 3.4. TOPEX/Poseidon Macro-Model

Marshall and Luthcke (1994a) determined the parameters for the surfaces of the TOPEX/Poseidon macro-model (A_k, δ_k, ρ_k) prior to launch, based on a Bayesian least-squares fit to solar radiation forces *only*, as predicted by the micro-model simulation of Antreasian (1992). Although these values were subsequently used by the Goddard Space Flight Center (GSFC) to compute both solar *and* Earth radiation forces in their generation of precision orbit ephemerides

(POEs), the ERADP model of Equation (3.23) was retained to determine the latter in MSODP. A new Box-Wing Solar Radiation Pressure (BWSRP) subroutine, however, was implemented to calculate the \vec{S} perturbation of Equation (1.12) using the estimated macro-model parameters. The force acting on each plate is computed independently, ignoring any potential shadowing of one surface by another, and the results are then summed to obtain the net force per unit mass,

$$\vec{S} = -f\gamma_{\odot} \frac{S_{\odot}}{c} \left(\frac{R}{r_{\odot}} \right)^2 \frac{1}{m} \times \sum_{k=1}^K A_k (\hat{n}_k \cdot \hat{s}_{\odot}) \left\{ (1 - \rho_k) \hat{s}_{\odot} + 2 \left[\frac{\delta_k}{3} + \rho_k (\hat{n}_k \cdot \hat{s}_{\odot}) \right] \hat{n}_k \right\} \quad (3.25)$$

where $K (= 8)$ denotes the total number of satellite surfaces. As in the RADPR model of Equation (3.15), the solar constant S_{\odot} of Willson (1978) is scaled, per Equation (2.27), by the distance r_{\odot} from the Sun to the satellite, along the incident $-\hat{s}_{\odot}$ direction. The scale factor f is determined from Equation (3.17) using the eclipse conditions of the conical shadow model (Ries, 1990). To compensate for errors in the magnitude of the net force, an additional scale factor γ_{\odot} was introduced, which can also be estimated. The success of the macro-model in helping to meet the TOPEX/Poseidon orbit accuracy requirements led to the adoption of similar approaches for other missions, including those of the Tracking and Data Relay Satellites (TDRS) (Luthcke et al., 1997), the Geosat Follow-On (GFO) (Lemoine et al., 1999a), and even the Mars Global Surveyor (MGS) (Lemoine et al., 1999b).

3.4 ICESat Modeling

In preparation for the launch of ICESat, modifications to MSODP were made to ensure that Equation (1.12) would adequately represent the motion of the satellite in orbit. First, the TOPEX/Poseidon macro-model was extended to 10 surfaces to accommodate the two solar arrays. Shown in Figure 3.5, this ICESat version includes a six-sided “box” and two two-sided “wings”, which are used in conjunction with the BWSRP model of Equation (3.25) to compute the solar radiation pressure perturbation \vec{S} . Furthermore, projections of the individual surface areas in this model are combined to yield the overall cross-sectional area needed to evaluate the atmospheric drag perturbation \vec{D} . Second, at its nominal altitude of 600 km, ICESat experiences Earth radiation forces 35% greater than those encountered at the 1336-km altitude of TOPEX/Poseidon. In light of this increased significance, a more detailed model for the Earth radiation pressure perturbation \vec{E} was developed by substituting the extended macro-model for the cannonball geometry in the ERADP model of Equation (3.23).

To orient these box and wing surfaces accurately, additional changes were made in MSODP to allow the input of data from precision attitude determination (PAD), and solar array orientation data from telemetry. In the event that these are unavailable, or have large gaps, nominal models for both were developed in accordance with planned mission operations. A unique aspect of these pre-launch plans involved the inhibition of solar array articulation during the acquisition of data along the reference ground tracks in the polar regions or from other targets of opportunity (TOOs) around the orbit. Although several options were

implemented to reflect such operations, a recurring undervoltage condition early in the mission resulted in severe restrictions being placed on any solar array inhibition. Nonetheless, this functionality remains in MSODP, and is presented here, along with the other changes made to support the ICESat mission.

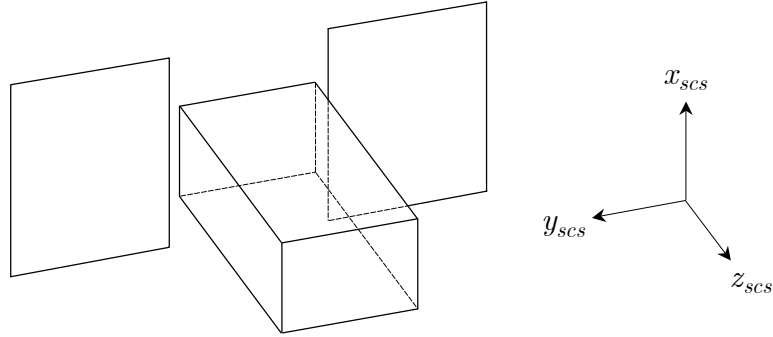


Figure 3.5. ICESat Macro-Model

3.4.1 Earth Radiation Pressure

To model the Earth radiation pressure perturbation for ICESat POD, the macro-model parameters of Equation (3.25) were combined with the ERADP model of Equation (3.23). Implemented in MSODP as the Box-Wing Earth Radiation Pressure (BWERP) subroutine, this new model requires a double-summation over the N Earth area elements and the K satellite macro-model surfaces:

$$\begin{aligned}
\vec{E} = & -\frac{2(1 - \cos \theta_{max})}{N} \frac{S_{\odot}}{c} \left(\frac{R}{R_{\odot}} \right)^2 \frac{1}{m} \\
& \times \sum_{i=1}^N \sum_{k=1}^K \left\{ A_k \left(\hat{n}_k \cdot \hat{s}_{\oplus}^i \right) \right. \\
& \times \left[\gamma_{\oplus}^a a_i \left(\hat{n}_{\oplus}^i \cdot \hat{R}_{\odot} \right) + \gamma_{\oplus}^e \frac{e_i}{4} \right] \\
& \times \left\{ (1 - \rho_k) \hat{s}_{\oplus}^i + 2 \left[\frac{\delta_k}{3} + \rho_k \left(\hat{n}_k \cdot \hat{s}_{\oplus}^i \right) \right] \hat{n}_k \right\} \left. \right\}
\end{aligned} \tag{3.26}$$

An albedo scale factor γ_{\oplus}^a and an emissivity scale factor γ_{\oplus}^e were introduced, similar to the solar radiation pressure scale factor γ_{\odot} in Equation (3.25). These allow Earth radiation pressure errors, other than variations in the solar constant S_{\odot} , to be considered. The partial derivatives required to estimate the state vector components, including those related to the Earth radiation model and the satellite macro-model parameters, are detailed in Appendix B. The Fortran 90 code developed for the entire model is provided in Appendix C.

3.4.2 Satellite Attitude

Nominally, the ICESat attitude determination and control subsystem (ADCS) maintains the satellite bus in a near-geodetic-nadir-pointing orientation. This default attitude incorporates a 5-mrad pitch bias to avoid specular returns of the laser pulses from the Earth's surface to the telescope of the Geoscience Laser Altimeter System (GLAS) instrument. In addition, to manage the onboard thermal environment and to ensure sufficient illumination of the solar arrays, the satellite operates in one of four possible yaw orientations, or control frames, depending on the relative geometry of the Sun and the orbit plane. As shown in

Figure 3.6, the angle β lies between the orbit normal \hat{h} and the geocentric unit vector to the Sun \hat{R}_{\odot} . Thus,

$$\cos \beta = \hat{h} \cdot \hat{R}_{\odot} \quad (3.27)$$

The complement of this angle effectively describes the inclination of the Sun with respect to the orbit plane and is often used instead,

$$\beta' = \frac{\pi}{2} - \beta \quad (3.28)$$

Figure 3.7 plots the anticipated evolution of the β' angle for ICESat, from launch through the five years of its planned mission.

The four nominal control frames, numbered 0 through 3, are illustrated in Figure 3.8, where \vec{n} represents the geodetic-nadir vector. In each, the pitch bias φ_b is implemented such that the satellite always looks “up”, pointing ahead, along the direction of motion. Table 3.1 provides the yaw angles that define the control frames, and the corresponding β' ranges to which they apply. For control frames 0 and 2, the solar array rotation axis, $+y_{scs}$, is perpendicular to the direction of motion. In such orientations, the arrays resemble wings, and the two frames constitute an “airplane” mode. Control frames 1 and 3, on the other hand, make up a “sailboat” mode, in which the $+y_{scs}$ axis lies opposite (or along) the direction of motion, and thus, the arrays resemble sails.

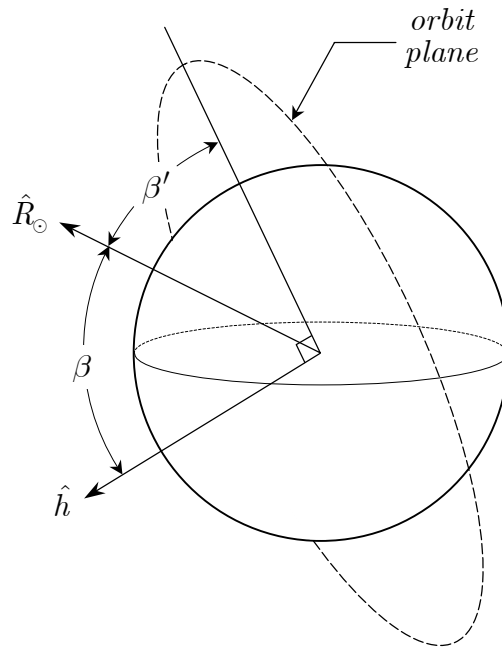


Figure 3.6. Definition of β' Angle

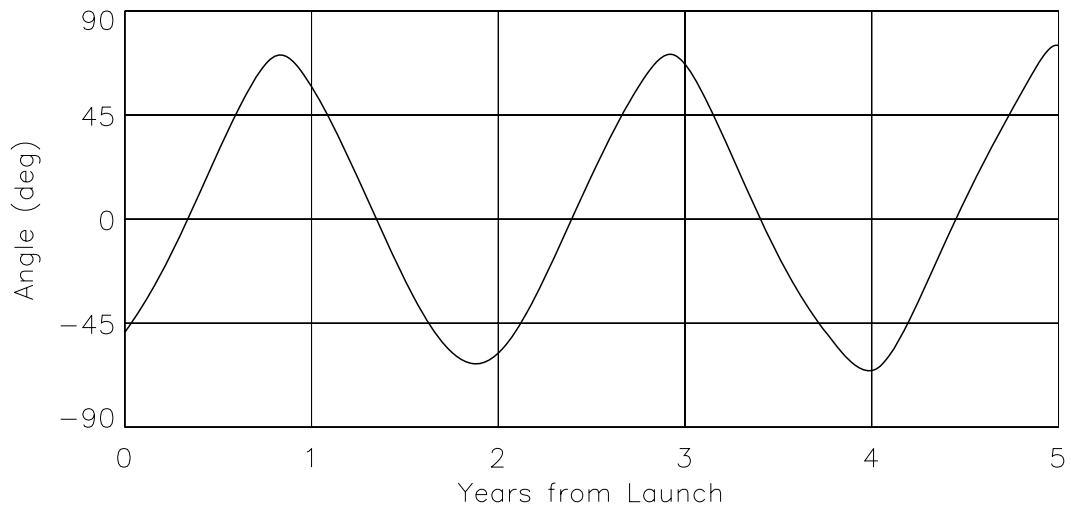
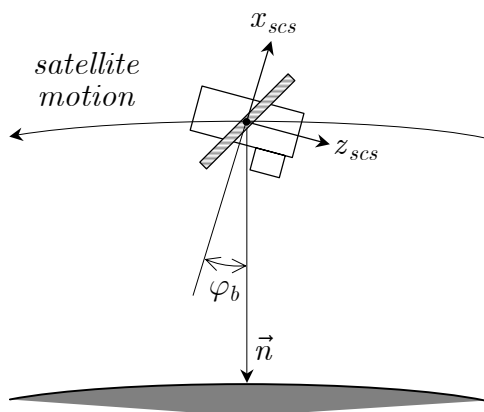
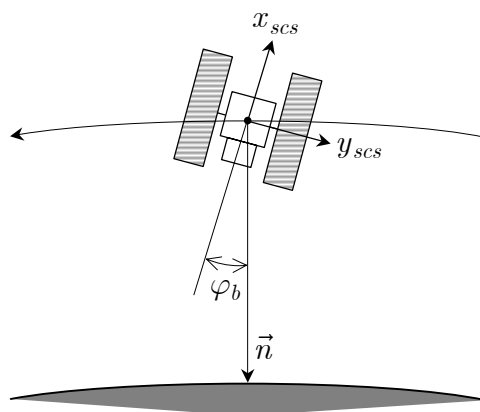


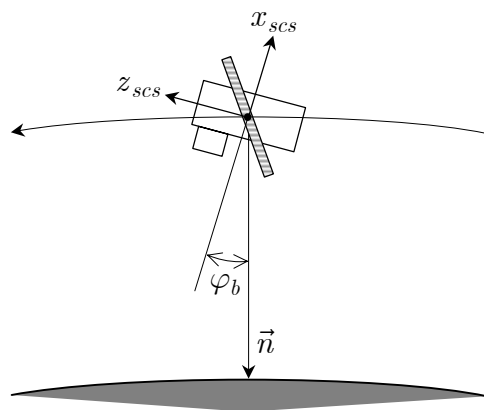
Figure 3.7. Projected β' Angle During ICESat Mission



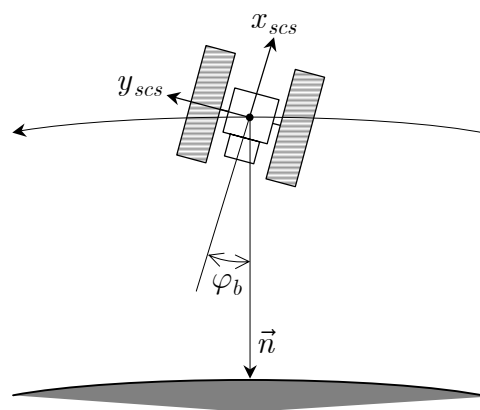
Control Frame 0



Control Frame 1



Control Frame 2



Control Frame 3

Figure 3.8. ICESat Nominal Attitude Control Frames

Control Frame	Operational Mode	Yaw Angle	β' Limits	
			Lower	Upper
0	Airplane	180°	0°	33°
1	Sailboat	90°	33°	90°
2	Airplane	0°	-33°	0°
3	Sailboat	270°	-90°	-33°

Table 3.1. β' Constraints for Nominal Attitude Control Frames

To accommodate these various attitudes, a nominal model for ICESat was developed and implemented in MSODP. First, a local-vertical local-horizontal (LVLH) frame is defined such that

$$T_{icrf}^{lvlh}(t) = \begin{bmatrix} \hat{r}' & -\hat{h} & -\hat{r}' \times \hat{h} \end{bmatrix}^T \quad (3.29)$$

which represents its orientation with respect to the International Celestial Reference Frame (ICRF) at time t . The instantaneous $+\hat{x}_{lvlh}$ axis coincides with the unit geodetic-zenith vector,

$$+\hat{x}_{lvlh} = \hat{r}' = -\frac{\vec{n}}{|\vec{n}|} \quad (3.30)$$

where $\vec{n} = \vec{r}_{sub} - \vec{r}$, extending from the satellite's ICRF position \vec{r} to its subsatellite point \vec{r}_{sub} on the TOPEX reference ellipsoid (Tapley et al., 1994). The $+\hat{y}_{lvlh}$ axis lies opposite the normal to the orbit plane, defined by \vec{r} and the ICRF velocity \vec{v} ,

$$+\hat{y}_{lwh} = -\hat{h} = -\frac{\vec{r} \times \vec{v}}{|\vec{r} \times \vec{v}|} \quad (3.31)$$

The $+\hat{z}_{lwh}$ axis completes the orthonormal triad,

$$+\hat{z}_{lwh} = \hat{x}_{lwh} \times \hat{y}_{lwh} = -\hat{r}' \times \hat{h} \quad (3.32)$$

Applying the pitch bias to the LVLH frame produces a pitched LVLH' frame. The transformation from the former to the latter consists of a single rotation φ_b about the $+\hat{y}_{lwh}$ axis,

$$T_{lwh}^{lwh'}(\varphi_b) = \begin{bmatrix} \cos \varphi_b & 0 & -\sin \varphi_b \\ 0 & 1 & 0 \\ \sin \varphi_b & 0 & \cos \varphi_b \end{bmatrix} \quad (3.33)$$

Dictated by the β' constraints of Table 3.1, the yaw angle ψ is measured about the $-x_{lwh'}$ axis, with a value of 0° assigned to the orientation of control frame 2. The resulting transformation orients the body-fixed Spacecraft Coordinate System (SCS) axes of Figure 3.5 with respect to the LVLH' frame,

$$T_{lwh'}^{scs}(\psi) = \begin{bmatrix} 1 & 0 & 0 \\ 0 & \cos \psi & -\sin \psi \\ 0 & \sin \psi & \cos \psi \end{bmatrix} \quad (3.34)$$

Thus, the ICRF attitude of the satellite for any of the nominal control frames can be obtained by combining Equations (3.29), (3.33) and (3.34):

$$T_{icrf}^{scs}(\psi, \varphi_b, t) = T_{lwh'}^{scs}(\psi) \cdot T_{lwh}^{lwh'}(\varphi_b) \cdot T_{icrf}^{lwh}(t) \quad (3.35)$$

During its mission, however, ICESat routinely deviates from these near-nadir orientations to point at reference ground tracks in the polar regions and selected TOOs located around the orbit. In anticipation of this, MSODP was also modified to use the attitude solutions generated by ground-based PAD. In the course of computing the laser-pointing direction, this processing uses the onboard star-tracker and gyro data to estimate the ICRF orientation of the GLAS instrument $T_{icrf}^{gcs}(t)$, at a 10-Hz rate (Bae and Schutz, 2002). This transformation represents the rotation from the ICRF to the GLAS coordinate system (GCS) at time t . The concurrent attitude of the satellite bus $T_{icrf}^{scs}(t)$ can be approximated from these precise solutions, using the idealized alignment of the GCS and SCS axes,

$$T_{icrf}^{scs}(t) = T_{gcs}^{scs} \cdot T_{icrf}^{gcs}(t) = \begin{bmatrix} 0 & 0 & 1 \\ 0 & -1 & 0 \\ 1 & 0 & 0 \end{bmatrix} \cdot T_{icrf}^{gcs}(t) \quad (3.36)$$

As discussed in Appendix A, the errors introduced by this assumption are negligible in a POD context. Tables produced by applying Equation (3.36) to the daily time series of PAD solutions capture the actual orientation of the satellite at all times. Consequently, for ICESat POD, MSODP typically interpolates these external tables to obtain $T_{icrf}^{scs}(t)$, using the nominal model of Equation (3.35) only in the event of large data gaps.

3.4.3 Solar Array Articulation

To ensure adequate power generation onboard the satellite, its two solar arrays were designed to articulate, tracking the Sun when visible and following a fictitious Sun during eclipse. Each array includes three interconnected and deployable panels, composed of aluminum honeycomb and graphite epoxy face sheets. Triple-junction gallium arsenide (GaAs) solar cells, mounted to one side of each panel, convert incident solar energy into usable electricity. Although intended to rotate in unison, the two arrays are driven independently by separate stepper motors. As shown in Figure 3.9, the resulting orientation of either array can be described by an angle ζ , measured from the $-z_{scs}$ axis of the satellite to its cell-side surface normal \hat{n} . These angles range from -180° to $+180^\circ$ and, for both arrays, take on positive values for positive right-hand rotations about the $+y_{scs}$ axis. Used to orient the corresponding macro-model surfaces in ICESat POD, they are downlinked with the X-band science telemetry, extracted by the ICESat Science Investigator-led Processing System (I-SIPS), and transferred to the University of Texas Center for Space Research (UT/CSR).

For those times when this onboard orientation data is unavailable or contains long gaps, a nominal articulation model was developed and implemented in MSODP. It assigns the same angle to both arrays, pointing them toward the Sun, insofar as they are constrained to rotate about the $+y_{scs}$ axis. Determining this angle begins with the interpolation of the Jet Propulsion Laboratory (JPL) DE-405 planetary ephemeris to obtain the ICRF position of the Sun \vec{R}_{\odot}^{icrf} at the desired time t . Subtracting \vec{r}_{com}^{icrf} , the concurrent position vector of the satellite center of mass (COM), yields

$$\vec{r}_{\odot}^{icrf}(t) = \vec{R}_{\odot}^{icrf}(t) - \vec{r}_{com}^{icrf}(t) \quad (3.37)$$

which is the vector from the satellite to the Sun in the ICRF. It can be rotated to the SCS by applying the transformation from either Equation (3.35) or (3.36),

$$\vec{r}_{\odot}^{scs}(t) = T_{icrf}^{scs}(t) \cdot \vec{r}_{\odot}^{icrf}(t) \quad (3.38)$$

Designating the components of this vector to be $(x_{\odot}^{scs}, y_{\odot}^{scs}, z_{\odot}^{scs})$, the nominal orientation for both arrays is defined to be

$$\zeta(t) = \tan^{-1} \left[\frac{-x_{\odot}^{scs}(t)}{-z_{\odot}^{scs}(t)} \right] \quad (3.39)$$

Post-launch comparisons have verified that the angles obtained from this model typically agree with those recorded onboard to within 0.3° .

The ICRF satellite-to-Sun vector, defined by Equation (3.37), changes slowly due to the gradual motion of the Earth about the Sun and the comparatively small magnitude of the more rapidly varying satellite position vector. Consequently, the ICRF orientation of the arrays, dictated by \vec{r}_{\odot}^{icrf} , remains virtually unchanged over an orbit revolution. As reflected in Equation (3.38), however, they rotate with respect to the SCS during that interval to compensate for the changing ICRF attitude of the satellite, $T_{icrf}^{scs}(t)$. Chapter 4 examines the resulting variations in ζ for several particular cases, but in general, they depend on whether the satellite is operating in an airplane or a sailboat mode. In the former, the arrays rotate through 360° each orbit, while in the latter, they oscillate between two β' -dependent limits.

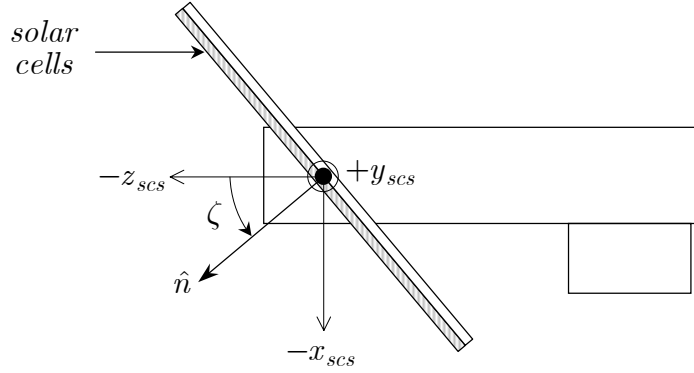


Figure 3.9. Solar Array Orientation Angle

3.4.4 Solar Array Inhibition

Pre-launch mission operations plans called for inhibiting the articulation of the solar arrays during all passes over the Greenland and Antarctic ice sheets to minimize the impact of jitter on the altimeter measurements. Although any such inhibition would be reflected in the onboard orientation angles, changes to the nominal articulation model in MSODP were also made to accommodate this requirement. Specifically, when the satellite reaches 60° N latitude on an ascending pass, or 60° S on a descending pass, the enhanced algorithm advances the requisite macro-model surfaces by an angle $\Delta\zeta$ to a fixed orientation with respect to the SCS. The desired stop angle ζ_{stop} corresponds to that which the arrays would have attained at the midpoint of the pass, had they been allowed to articulate, as illustrated in Figure 3.10. This strategy reduces the time needed for the arrays to catch up to the Sun after the satellite exits a polar region.

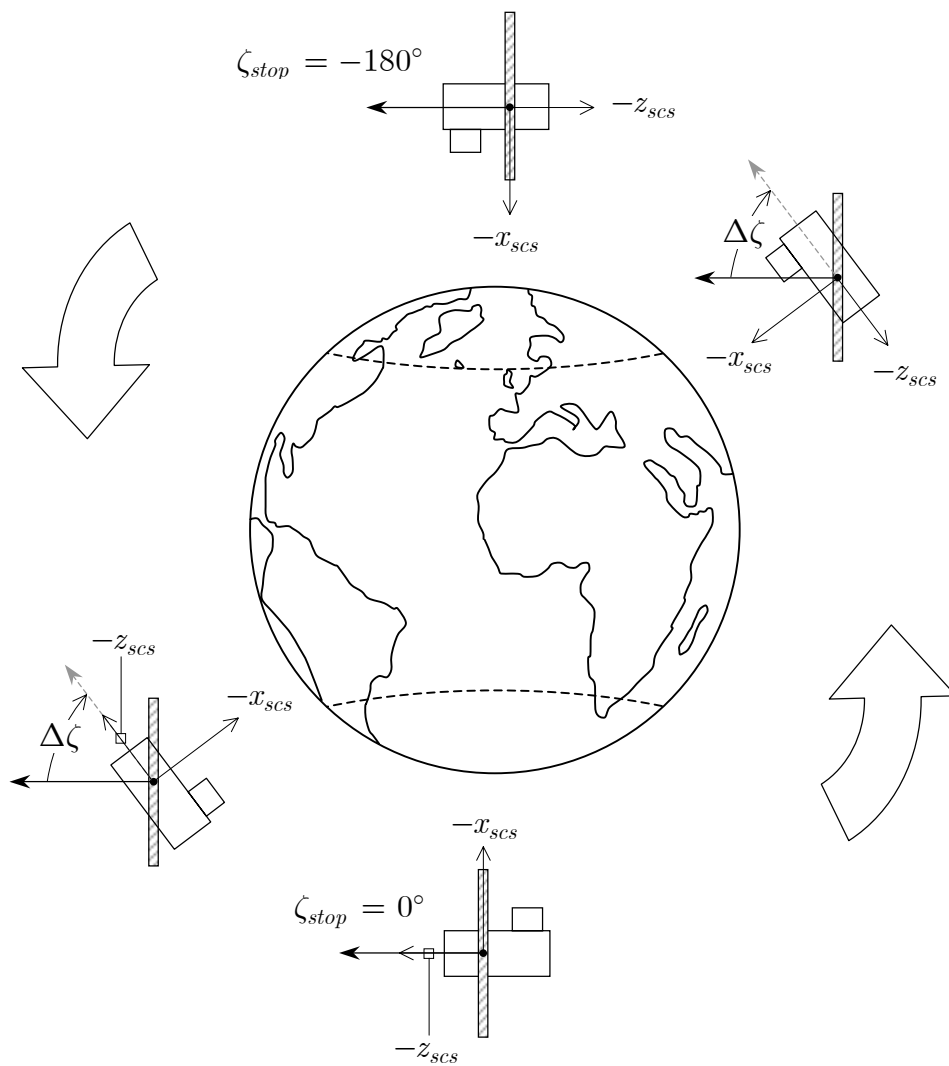


Figure 3.10. Stop Angle for Solar Array Inhibition

Conceptually, the simplest approach would be to integrate the state vector forward to the midpoint, apply Equations (3.37) through (3.39) to determine ζ there, and then fix this value for the duration of the pass. The computational costs introduced by the additional integrations, along with the challenges posed by the frequent stopping and restarting of the integrator, however, proved to be prohibitive. As a result, an alternate method was developed to approximate ζ_{stop} at time t_0 , when the satellite initially exceeds $\pm 60^\circ$ latitude on each polar pass. Since the arrays begin articulating again at the same latitude after the satellite traverses the pole, the midpoint coincides with the apex — the point of maximum latitude. The time at which this occurs is predicted to be

$$t_{apx} = t_0 + \frac{u_{apx} - u_0}{n_0} \quad (3.40)$$

where $n_0 = n(t_0)$ and $u_0 = u(t_0)$, representing the Keplerian mean motion and the argument of latitude, respectively, at t_0 . The argument of latitude at the apex, denoted u_{apx} , is 90° for a northern pass and 270° for a southern one.

Assuming the inclination i and the right ascension of the ascending node Ω change little over the interval between t_0 and t_{apx} , the ICRF unit direction vector of the satellite COM at the apex is given by

$$\hat{r}_{com}^{icrf}(t_{apx}) = \begin{bmatrix} \cos \Omega_0 \cos u_{apx} - \sin \Omega_0 \sin u_{apx} \cos i_0 \\ \sin \Omega_0 \cos u_{apx} + \cos \Omega_0 \sin u_{apx} \cos i_0 \\ \sin u_{apx} \sin i_0 \end{bmatrix} \quad (3.41)$$

where $i_0 = i(t_0)$ and $\Omega_0 = \Omega(t_0)$. Making a similar assumption about the semi-major axis a , Equation (3.41) is then scaled by $a_0 = a(t_0)$ to obtain the corresponding position vector,

$$\vec{r}_{com}^{icrf}(t_{apx}) = a_0 \cdot \hat{r}_{com}^{icrf}(t_{apx}) \quad (3.42)$$

Subtracting this result from the concurrent ICRF position of the Sun \vec{R}_{\odot}^{icrf} , interpolated from the JPL DE-405 planetary ephemeris at t_{apx} , yields

$$\vec{r}_{\odot}^{icrf}(t_{apx}) = \vec{R}_{\odot}^{icrf}(t_{apx}) - \vec{r}_{com}^{icrf}(t_{apx}) \quad (3.43)$$

This satellite-to-Sun vector can be rotated from the ICRF to the SCS using $\tilde{T}_{icrf}^{scs}(t_{apx})$, an approximation of the satellite attitude at the apex,

$$\vec{r}_{\odot}^{scs}(t_{apx}) = \tilde{T}_{icrf}^{scs}(t_{apx}) \cdot \vec{r}_{\odot}^{icrf}(t_{apx}) \quad (3.44)$$

To derive this simplified orientation, Equation (3.41) is first substituted for \hat{r}' in Equation (3.29), producing a geocentric, rather than geodetic, nadir-pointing attitude. Then, under the assumptions previously made for i and Ω , the required orbit normal is rendered by

$$\hat{h}(t_{apx}) = \begin{bmatrix} \sin i_0 \sin \Omega_0 \\ -\sin i_0 \cos \Omega_0 \\ \cos i_0 \end{bmatrix} \quad (3.45)$$

Designating the components of Equation (3.44) to be $(x_{\odot}^{scs}, y_{\odot}^{scs}, z_{\odot}^{scs})$, the predicted stop angle becomes

$$\zeta_{stop} = \zeta(t_{apx}) = \tan^{-1} \left[\frac{-x_{\odot}^{scs}(t_{apx})}{-z_{\odot}^{scs}(t_{apx})} \right] \quad (3.46)$$

The angles generated using this method agree with those computed by the nominal articulation model at the midpoint of a polar pass to within 0.1° .

In addition to these periods of reference ground-track pointing, the articulation of the solar arrays was to be inhibited during passes involving TOOs. Since these path targets are significantly shorter than polar passes, the array motion was simply to be stopped prior to the initiation of the off-nadir pointing, and restarted upon its completion. Although TOOs can be arbitrarily scheduled, their start and end times are known in advance. Thus, an option was added in MSODP to read these times from a Sequence-of-Events (SOE) file, and to orient the appropriate macro-model surfaces accordingly.

Finally, as $|\beta'|$ increases, the Earth-Sun line becomes more perpendicular to the orbit plane, requiring the solar arrays to articulate less in both of the sailboat-mode attitudes associated with this geometry. Maintaining the articulation yields diminishing marginal increases in power, so the arrays were to be fixed in their $\zeta = 0^\circ$ orientation when $|\beta'| \geq 55^\circ$. To reflect this requirement, a β' check was implemented in MSODP to distinguish between articulating and fixed-array operations. Together, the nominal articulation model, described in the previous section, and the inhibition options, outlined here, constitute the GLAS Solar Array (GLASSA) subroutine developed for MSODP, and provided in Appendix D.

Chapter 4

Micro-Model Force History Generation

4.1 Thermal Synthesizer System

To support ICESat component and system-level thermal analyses, engineers at the Ball Aerospace and Technologies Corporation (BATC) and the Goddard Space Flight Center (GSFC) created detailed models of the spacecraft bus and the Geoscience Laser Altimeter System (GLAS), respectively, using the Thermal Synthesizer System (TSS). As designed, the TSS software computes a variety of related quantities for an object in orbit or on the surface of a planet, including radiation conductors, view factors, and heating rates. Typically, this data is input to other programs, such as the Systems Improved Numerical Differencing Analyzer (SINDA), that then characterize the thermal response of the object. This process allows engineers to verify whether an individual component will meet its temperature requirements when operated as part of a complex system within the anticipated environment.

Although similar in functionality, TSS differs in fundamental ways from its predecessor, the Thermal Radiation Analysis System (TRASYS), which had emerged from the Space Shuttle design effort in the early 1970s as the industry standard in a wide range of thermal applications. In 1985, at the outset of the design phase for the International Space Station, the theoretical and computational limitations of TRASYS prompted the Johnson Space Center (JSC) to initiate the development of a new generation of thermal-analysis

software (Panczak et al., 1991). The contracted developers at the Lockheed Missiles and Space Company adopted a methodology that reflected advances in both software design and computing hardware. Notably, they elected to use the C programming language, rather than the more traditional Fortran, which allowed them to follow a modular approach in the development of individual applications. It also enabled them to implement a graphical user interface that facilitates the creation of models in a computer-aided-design-like manner, and supports the mapping of results back to the input geometry for visual verification and evaluation. As a result, they were able to address the nearly universal complaints that TRASYS was cryptic to use and laborious to maintain.

For the purposes of this study, the most important difference between TRASYS and TSS concerned the formulation of the radiation exchange problem that both were designed to solve. TRASYS relies on a conventional gray-body approach, first proposed by Gebhart (1957), in which surfaces emit and receive radiation diffusely and uniformly. TSS avoids these limiting assumptions by adopting a Monte Carlo Ray Tracing (MCRT) technique to compute incident and absorbed heating rates directly. Consequently, the TRASYS-based force algorithms that Antreasian (1992) developed for the TOPEX/Poseidon micro-model simulation could not be adapted for use in TSS. Instead, the existing TSS Heat Rate application was augmented to calculate the forces induced by both solar and Earth radiation. The following sections describe the basic incident heat rate problem, the corresponding MCRT formulation for a satellite in low-Earth orbit, and the modifications made within TSS to support the ICESat radiation-force simulation.

4.1.1 Incident Heat Rate Problem

The general “heat rate” problem involves determining the rate at which electromagnetic energy emitted (or reflected) from a source is *absorbed* at an object’s surface. The difference between this input and the loss of heat through emission dictates its internal temperature. As Equation (3.1) suggests, however, the pressure acting on a surface that intercepts such energy depends on its irradiance, the rate at which it is *incident*. This somewhat simpler problem can be formulated by considering the two surfaces in Figure 4.1, where A_1 represents the source of radiant energy and A_2 represents the surface intercepting it. For the arbitrary differential areas shown, the total energy per unit time emitted from dA_1 , and incident at dA_2 , is obtained by rearranging Equation (2.16) and integrating over all wavelengths,

$$dQ_{1,e \rightarrow 2} = I_{1,e} \cos \theta_1 dA_1 d\omega_{2-1} \quad (4.1)$$

The subscripts have been added for clarity. $I_{1,e}$ denotes the total intensity of the radiation emitted in the θ_1 direction, within the solid angle subtended by the projected area of dA_2 at a distance s ,

$$d\omega_{2-1} = \frac{dA_2 \cos \theta_2}{s^2} \quad (4.2)$$

Substituting this expression into Equation (4.1) yields

$$dQ_{1,e \rightarrow 2} = \frac{I_{1,e} \cos \theta_1 \cos \theta_2}{s^2} dA_1 dA_2 \quad (4.3)$$

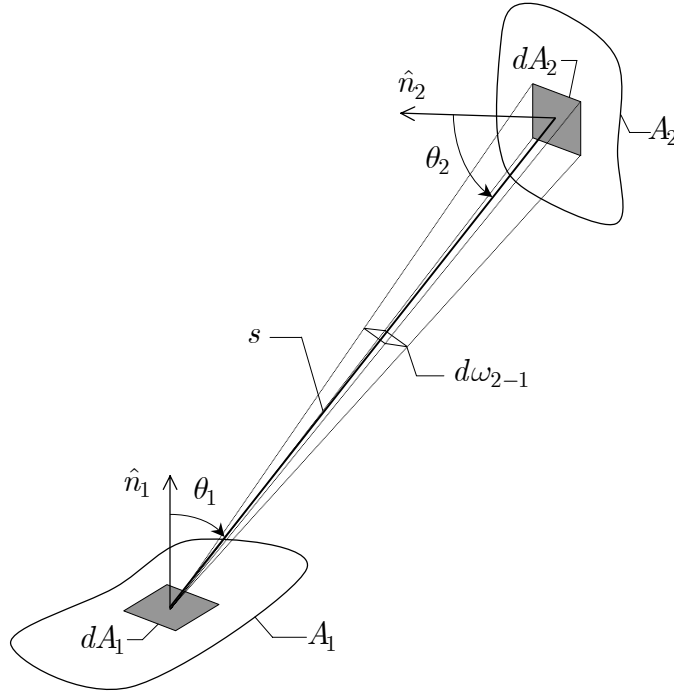


Figure 4.1. General Incident Radiation Geometry

For a diffusely emitting source, the total intensity of the outgoing radiation is independent of direction. Thus, from Equation (2.23), $I_{1,e} = E_1/\pi$, and

$$dQ_{1,e \rightarrow 2} = \frac{E_1 \cos \theta_1 \cos \theta_2}{\pi s^2} dA_1 dA_2 \quad (4.4)$$

where E_1 is the total emissive power. A similar result is obtained for radiation diffusely reflected by a source to the intercepting surface,

$$dQ_{1,r \rightarrow 2} = \frac{B_1 \cos \theta_1 \cos \theta_2}{\pi s^2} dA_1 dA_2 \quad (4.5)$$

where B_1 is the total reflected irradiance.

4.1.2 Monte Carlo Ray Tracing Formulation

Conceptually, applying either Equation (4.4) or (4.5) to any finite problem requires integrating over the areas of both the source and the intercepting surface. Obtaining an analytical solution, however, is usually possible only for relatively simple geometries. To contend with the complex shapes — and often, the directional- and wavelength-dependent radiative properties — of surfaces in practical heat transfer applications, a wide range of numerical methods have been developed or adapted, including numerical integration, finite differences and finite elements (see, for example, Siegel and Howell, 2002). These approaches can be used to determine heat rates directly from Equation (4.4) or (4.5), but more often, they effectively integrate a differential view, or configuration, factor between the two surfaces,

$$dF_{1 \rightarrow 2} = \frac{\cos \theta_1 \cos \theta_2}{\pi s^2} dA_2 \quad (4.6)$$

which represents the fraction of energy leaving dA_1 incident at dA_2 . The integrated factors are often parameterized in terms of the size, distance and orientation of the surfaces involved, and tabulated for reference (see, for example, Howell, 1982).

In the heat transfer literature, and in commercial software like TSS, however, problems of radiation exchange are increasingly being solved with MCRT. Metropolis and Ulam (1949) first introduced Monte Carlo methods to address various problems in mathematical physics that could not be solved using either classical or statistical mechanics. Drawing upon games of chance, they asserted that a combination of deterministic and stochastic techniques could be

used to predict the likely outcome of a given physical process, by averaging a large, but finite, number of “plays.” Since then, the use of Monte Carlo methods has expanded well beyond the scope for which they were designed, finding applications in fields as diverse as cellular biology (see, for example, Graner and Glazier, 1992) and mathematical finance (see, for example, Boyle, 1977). Howell and Perlmutter (1964) were the first to apply them to the solution of radiant heat transfer problems. The ray-tracing component of MCRT emerged later, when Whitted (1980) proposed a method to improve the illumination of objects in computer-generated graphics. Unlike earlier ray-casting techniques, which considered only incident light, this enhanced approach uses geometric optics to trace individual rays through multiple interactions with a model’s surfaces, accounting for reflection, refraction and shadowing.

As described by Siegel and Howell (2002), the most robust MCRT formulation of the heat rate problem stochastically simulates the emission of discrete energy bundles from a surface, based on its temperature and probabilistic assumptions regarding its emissive properties. Similarly, each time a bundle strikes another surface, it is randomly absorbed or reflected, depending on its direction of incidence and the surface’s absorptivity, also characterized by a probability density function. If reflected, the bundle continues on, until it is absorbed or leaves the system. The total energy transferred to a surface — its heat rate — is simply the number of bundles it has absorbed multiplied by the average energy per bundle, defined to be the total energy emitted divided by the number of bundles emitted. By tracking a sufficiently large number of bundles, this heat rate can be computed to an arbitrary accuracy.

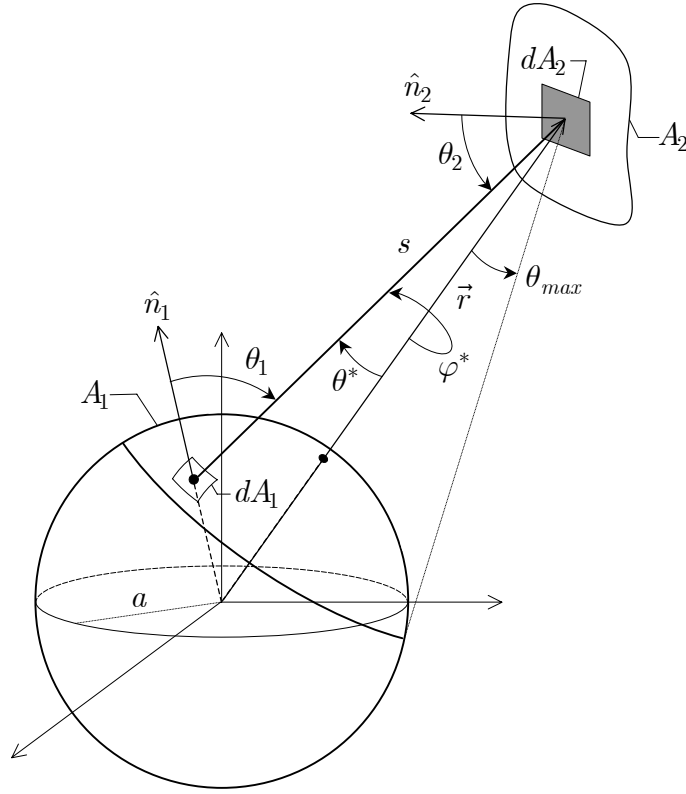


Figure 4.2. Incident Radiation Geometry in Low-Earth Orbit

Such a generalized approach to MCRT can be simplified considerably to calculate *incident* heat rates for a satellite in orbit. Both the Sun and the Earth have well-defined, analytical radiation models, as described in Chapter 2, which eliminate the need to simulate emission (or reflection, in the case of albedo) stochastically. Considering the geometry depicted in Figure 4.2, the total energy per unit time emitted from the differential area dA_1 on the surface of a spherical source, and incident at dA_2 , is given by Equation (4.4), which can be rewritten in a slightly different form,

$$dQ_{1,e \rightarrow 2} = E_1 \left(\frac{dA_1 \cos \theta_1}{\pi s^2} \right) dA_2 \cos \theta_2 \quad (4.7)$$

The term in parentheses represents the projected, attenuated area of dA_1 . Its numerator can also be expressed as

$$dA_1 \cos \theta_1 = s d\theta^* \cdot s \sin \theta^* d\varphi^* \quad (4.8)$$

where the local angles θ^* and φ^* are measured from and about the position vector \vec{r} , respectively. Thus,

$$\frac{dA_1 \cos \theta_1}{\pi s^2} = \frac{\sin \theta^*}{\pi} d\theta^* d\varphi^* \quad (4.9)$$

Integrating over the area of the source visible to dA_2 yields the projected, attenuated area of A_1 :

$$\begin{aligned} \int_{A_1} \frac{dA_1 \cos \theta_1}{\pi s^2} &= \frac{1}{\pi} \int_0^{2\pi} \int_0^{\theta_{max}} \sin \theta^* d\theta^* d\varphi^* \\ &= 2(1 - \cos \theta_{max}) \end{aligned} \quad (4.10)$$

Using this result, Equation (4.7) can be integrated stochastically with MCRT. In place of the differential dA_2 , the intercepting surface A_2 is divided into a finite number of nodes, each with finite area A_j and normal \hat{n}_j , as shown in Figure 4.3. The visible surface of the source is then sampled by sending N rays to A_1 , with each \vec{s}^i initiated at a random location on A_j , and randomly oriented $(\theta_i^*, \varphi_i^*)$ within the bounding cone defined by

$$\theta_{max} = \sin^{-1} \left(\frac{a}{r} \right) \quad (4.11)$$

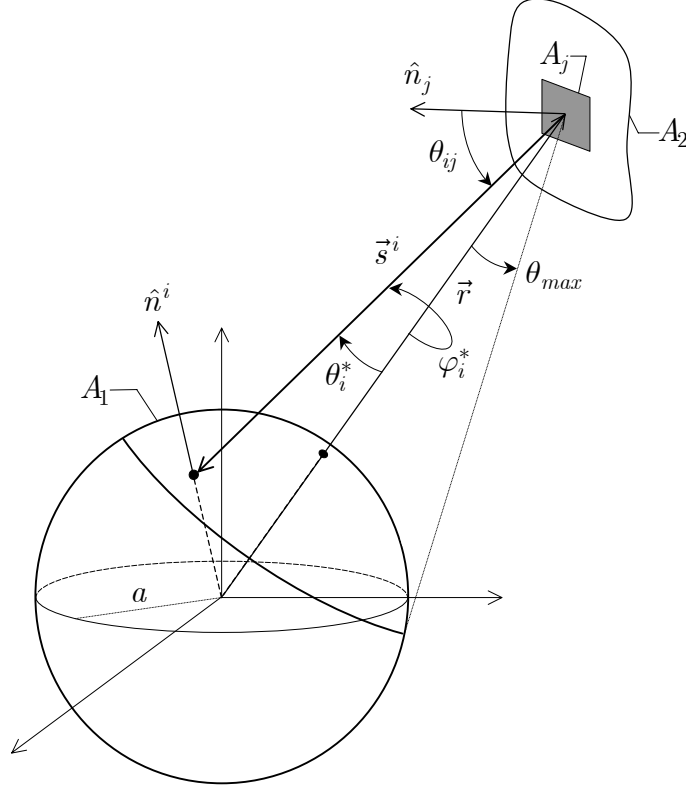


Figure 4.3. MCRT Geometry for Incident Radiation

where $r = |\vec{r}|$ and a denotes the mean radius of the source. Each outgoing ray makes an angle θ_{ij} with the surface normal \hat{n}_j , such that

$$\cos \theta_{ij} = \hat{n}_j \cdot \hat{s}^i \quad (4.12)$$

where $\hat{s}^i = \vec{s}^i / |\vec{s}^i|$. Provided that it does not encounter another surface in the satellite model before reaching the source, its intersection with A_1 is assigned a projected, attenuated area,

$$A'_i = \frac{2(1 - \cos \theta_{max})}{N} \quad (4.13)$$

which replaces the differential form in Equation (4.7). With a total emissive power E^i , the ray is then returned to A_j and the incident heat rate for that node is accumulated:

$$Q^j = \frac{2(1 - \cos \theta_{max})}{N} A_j \sum_{i=1}^N E^i (\hat{n}_j \cdot \hat{s}^i) \quad (4.14)$$

On the other hand, if the outgoing ray does strike another surface in the satellite model, it does not reach the source. Thus, no ray is returned to A_j and no accumulation is made — although i is incremented. This implicitly accounts for shadowing within the model. Since each node is assumed to be a flat, relatively small area, summing Q^j for all nodes of a given surface effectively completes the integration of Equation (4.7) and yields the total incident heat rate. While these features make MCRT both versatile and easy to implement, Whitted (1980) realized that checking for ray intersections within the model can consume as much as 95% of the computation time. Glassner (1984) addressed this concern by subdividing models spatially into small cubes, called voxels, and then checking first for intersections with the comparatively few surfaces in the voxel in which a ray originated. In extending this approach, Panczak (1989) proposed an adaptive technique to create voxels of different sizes, each with approximately the same number of surfaces in it. He demonstrated that this method — ultimately implemented in TSS — reduced the computation time by a factor of 30, relative to the original method.

Since MCRT employs random sampling, the heat rate computed by Equation (4.14) is only an estimate \hat{Q} of the true value Q . To determine whether the solution has converged, TSS first computes the standard error σ_s/\sqrt{N} associated with \hat{Q} , based on the sample standard deviation σ_s and the number of samples N . Sampling continues for a given node until a weighted percentage error (WPE) falls below a user-defined limit, with the desired confidence interval, or until the number of rays reaches a user-defined maximum. According to the Central Limit Theorem, the standard error approximates the standard deviation σ of the normal distribution about Q . Consequently, the 90% confidence interval, for example, is

$$\hat{Q} - 1.645 \frac{\sigma_s}{\sqrt{N}} < Q < \hat{Q} + 1.645 \frac{\sigma_s}{\sqrt{N}} \quad (4.15)$$

The WPE, in this case, is simply the error term in Equation (4.15) divided by the estimate \hat{Q} ,

$$\text{WPE} = \frac{1.645 \sigma_s}{\hat{Q} \sqrt{N}} \quad (4.16)$$

Taken together, Equations (4.15) and (4.16) can be interpreted to mean that there is a 90% probability that the true value Q lies within the WPE of the estimate \hat{Q} . If the WPE is less than the limit input by the user, the solution has converged, and the sampling process ends. Alternatively, if the maximum number of rays is reached, the final WPE represents the residual uncertainty in \hat{Q} with a 90% confidence interval.

4.1.3 Incident Heat Rates for Solar and Earth Radiation

The incident heat rate for a node receiving solar radiation can be computed using Equation (4.14),

$$Q_{\odot}^j = f \frac{2(1 - \cos \theta_{max})}{N} A_j \sum_{i=1}^N E_{\odot}^i (\hat{n}_j \cdot \hat{s}_{\odot}^i) \quad (4.17)$$

where the \odot subscript has been added for clarity, and the factor f has been introduced to account for satellite eclipse, based on the conditions set forth in Equation (3.16) for the cylindrical shadow model. Assuming that the Sun emits its energy uniformly, Equation (4.17) reduces to

$$Q_{\odot}^j = f \frac{2(1 - \cos \theta_{max})}{N} E_{\odot} A_j \sum_{i=1}^N (\hat{n}_j \cdot \hat{s}_{\odot}^i) \quad (4.18)$$

The constant total emissive power E_{\odot} can also be expressed in terms of the solar irradiance G_{\odot} at the satellite's distance r_{\odot} ,

$$E_{\odot} = G_{\odot} \left(\frac{4\pi r_{\odot}^2}{4\pi a_{\odot}^2} \right) = G_{\odot} \left(\frac{r_{\odot}}{a_{\odot}} \right)^2 \quad (4.19)$$

where a_{\odot} represents the mean radius of the Sun, and $a_{\odot}/r_{\odot} = \sin \theta_{max}$, from Equation (4.11). Thus,

$$E_{\odot} = \frac{G_{\odot}}{\sin^2 \theta_{max}} \quad (4.20)$$

Substituting this expression into Equation (4.18), and simplifying, yields

$$Q_{\odot}^j = f \frac{2}{N(1 + \cos \theta_{max})} G_{\odot} A_j \sum_{i=1}^N (\hat{n}_j \cdot \hat{s}_{\odot}^i) \quad (4.21)$$

Furthermore, if the Sun is considered to be a point source, $\theta_{max} = 0^\circ$ and Equation (4.21) reduces to

$$Q_{\odot}^j = f \frac{G_{\odot} A_j}{N} \sum_{i=1}^N (\hat{n}_j \cdot \hat{s}_{\odot}^i) \quad (4.22)$$

Within its Heat Rate application, TSS allows the user to define θ_{max} (including 0°), and to input a constant value for G_{\odot} .

Similarly, for a node receiving radiation emitted by the Earth, the incident heat rate can be obtained from Equation (4.14),

$$Q_{\oplus,e}^j = \frac{2(1 - \cos \theta_{max})}{N} A_j \sum_{i=1}^N E_{\oplus}^i (\hat{n}_j \cdot \hat{s}_{\oplus}^i) \quad (4.23)$$

where the \oplus and e subscripts have been added for clarity. The existing TSS Heat Rate application allows the user to input a *planetshine* table, which assigns a total emissive power E_{\oplus}^i to a ray based on the latitude of its intersection with the Earth. If, instead, the user assumes the energy to be emitted uniformly, Equation (4.23) reduces to

$$Q_{\oplus,e}^j = \frac{2(1 - \cos \theta_{max})}{N} E_{\oplus} A_j \sum_{i=1}^N (\hat{n}_j \cdot \hat{s}_{\oplus}^i) \quad (4.24)$$

For this study, the current TSS vendor, Space Design, Inc., in consultation with the University of Texas Center for Space Research (UT/CSR), implemented an

additional option. Rearranging Equation (2.35), the total emissive power in Equation (4.23) can be expressed as

$$E_{\oplus}^i = \frac{e_i G_{\odot}}{4} \quad (4.25)$$

where G_{\odot} now represents the solar irradiance at the Earth's distance from the Sun. The emissivity e_i is obtained from the two-degree zonal harmonic model of Equation (2.37), based on the latitude of the intersection. Substituting Equation (4.25) into Equation (4.23) yields

$$Q_{\oplus,e}^j = \frac{2(1 - \cos \theta_{max})}{N} \frac{G_{\odot}}{4} A_j \sum_{i=1}^N e_i (\hat{n}_j \cdot \hat{s}_{\oplus}^i) \quad (4.26)$$

For a node receiving radiation reflected from the Earth, the total reflected irradiance B_{\oplus}^i can be substituted for E^i in Equation (4.14) to determine the incident heat rate,

$$Q_{\oplus,a}^j = \frac{2(1 - \cos \theta_{max})}{N} A_j \sum_{i=1}^N B_{\oplus}^i (\hat{n}_j \cdot \hat{s}^i) \quad (4.27)$$

where the \oplus and a subscripts have been added for clarity. Rearranging Equation (2.30), the total reflected irradiance can be expressed as

$$B_{\oplus}^i = a_i G_{\odot} \cos \psi_{\oplus,i}^{\odot} = a_i G_{\odot} (\hat{n}_{\oplus}^i \cdot \hat{R}_{\odot}) \quad (4.28)$$

where G_{\odot} again represents the solar irradiance at the Earth's distance from the Sun. The cosine of the solar zenith angle $\psi_{\oplus,i}^{\odot}$ has been replaced by the dot product of \hat{n}_{\oplus}^i , the normal to the Earth at the intersection, and \hat{R}_{\odot} , the geocentric unit vector to the Sun. As with planetshine, the existing TSS Heat

Rate application allows the user to input an albedo table, which assigns a_i to a ray based on the latitude of its intersection. Substituting Equation (4.28) into Equation (4.27) yields

$$Q_{\oplus,a}^j = \frac{2(1 - \cos \theta_{max})}{N} G_{\odot} A_j \sum_{i=1}^N a_i (\hat{n}_j \cdot \hat{s}_{\oplus}^i) (\hat{n}_{\oplus}^i \cdot \hat{R}_{\odot}) \quad (4.29)$$

If, instead, the user assumes the energy to be reflected from the Earth uniformly, this reduces to

$$Q_{\oplus,a}^j = \frac{2(1 - \cos \theta_{max})}{N} a G_{\odot} A_j \sum_{i=1}^N (\hat{n}_j \cdot \hat{s}_{\oplus}^i) (\hat{n}_{\oplus}^i \cdot \hat{R}_{\odot}) \quad (4.30)$$

As with emissivity, another option was added for this study that allows a_i to be computed for Equation (4.29), using the two-degree zonal harmonic model of Equation (2.36) and the latitude of the intersection.

4.1.4 Solar and Earth Radiation Forces

Since it involves the same physical process, the MCRT formulation for radiation forces is developed here by analogy with the one described for incident heat rates in the preceding sections. In Figure 4.3, the contribution of a single ray \vec{s}^i to the force acting on the nodal area A_j can be described using the form derived by Baker (1966), and presented earlier as Equation (3.24). Multiplying both sides by the mass m ,

$$\vec{F}^{ij} = m\ddot{\vec{r}} = -\frac{1}{c} [G^i (\hat{n}_j \cdot \hat{s}^i) A_j] \left\{ (1 - \rho^j) \hat{s}^i + 2 \left[\frac{\delta^j}{3} + \rho^j (\hat{n}_j \cdot \hat{s}^i) \right] \hat{n}_j \right\} \quad (4.31)$$

where c represents the speed of light, and $\hat{s}^i = \vec{s}^i / |\vec{s}^i|$. Again, the node has a normal \hat{n}_j , but also a specular reflectivity ρ^j and a diffuse reflectivity δ^j . Since G^i denotes the ray's irradiance, the quantity in the first set of brackets constitutes its contribution to the incident heat rate. From Equation (4.14), this can be represented equivalently by

$$Q^{ij} = \frac{2(1 - \cos \theta_{max})}{N} A_j E^i (\hat{n}_j \cdot \hat{s}^i) \quad (4.32)$$

Substituting this expression into Equation (4.31), and summing the result for the N rays, yields

$$\begin{aligned} \vec{F}^j = & -\frac{2(1 - \cos \theta_{max})}{N} \frac{A_j}{c} \\ & \times \sum_{i=1}^N E^i (\hat{n}_j \cdot \hat{s}^i) \left\{ (1 - \rho_j) \hat{s}^i + 2 \left[\frac{\delta_j}{3} + \rho_j (\hat{n}_j \cdot \hat{s}^i) \right] \hat{n}_j \right\} \end{aligned} \quad (4.33)$$

Assuming that the Sun emits its energy uniformly, the force acting on a node receiving solar radiation is

$$\begin{aligned} \vec{F}_{\odot}^j = & -f \frac{2(1 - \cos \theta_{max})}{N} \frac{E_{\odot}}{c} A_j \\ & \times \sum_{i=1}^N (\hat{n}_j \cdot \hat{s}_{\odot}^i) \left\{ (1 - \rho_{\odot}^j) \hat{s}_{\odot}^i + 2 \left[\frac{\delta_{\odot}^j}{3} + \rho_{\odot}^j (\hat{n}_j \cdot \hat{s}_{\odot}^i) \right] \hat{n}_j \right\} \end{aligned} \quad (4.34)$$

The specular and diffuse reflectivities for the incident solar radiation are obtained from the corresponding absorptivity α_j , using Equation (3.13):

$$\rho_{\odot}^j = \xi_j (1 - \alpha_j) \quad \delta_{\odot}^j = (1 - \xi_j) (1 - \alpha_j) \quad (4.35)$$

where ξ_j is the specularity. Substituting Equation (4.20) into Equation (4.34), and simplifying, yields

$$\begin{aligned} \vec{F}_{\odot}^j = & -f \frac{2}{N(1 + \cos \theta_{max})} \frac{G_{\odot}}{c} A_j \\ & \times \sum_{i=1}^N (\hat{n}_j \cdot \hat{s}_{\odot}^i) \left\{ (1 - \rho_{\odot}^j) \hat{s}_{\odot}^i + 2 \left[\frac{\delta_{\odot}^j}{3} + \rho_{\odot}^j (\hat{n}_j \cdot \hat{s}_{\odot}^i) \right] \hat{n}_j \right\} \end{aligned} \quad (4.36)$$

If the Sun is considered to be a point source (i.e., $\theta_{max} = 0^\circ$), this reduces to

$$\begin{aligned} \vec{F}_{\odot}^j = & -f \frac{G_{\odot} A_j}{N c} \\ & \times \sum_{i=1}^N (\hat{n}_j \cdot \hat{s}_{\odot}^i) \left\{ (1 - \rho_{\odot}^j) \hat{s}_{\odot}^i + 2 \left[\frac{\delta_{\odot}^j}{3} + \rho_{\odot}^j (\hat{n}_j \cdot \hat{s}_{\odot}^i) \right] \hat{n}_j \right\} \end{aligned} \quad (4.37)$$

The force acting on a node receiving radiation emitted by the Earth can also be obtained using Equation (4.33),

$$\begin{aligned} \vec{F}_{\oplus,e}^j = & - \frac{2(1 - \cos \theta_{max})}{N} \frac{A_j}{c} \\ & \times \sum_{i=1}^N E_{\oplus}^i (\hat{n}_j \cdot \hat{s}_{\oplus}^i) \left\{ (1 - \rho_{\oplus}^j) \hat{s}_{\oplus}^i + 2 \left[\frac{\delta_{\oplus}^j}{3} + \rho_{\oplus}^j (\hat{n}_j \cdot \hat{s}_{\oplus}^i) \right] \hat{n}_j \right\} \end{aligned} \quad (4.38)$$

The specular and diffuse reflectivities for the incident *infrared* radiation can be expressed in terms of the corresponding emissivity ε_j , using Equation (3.14):

$$\rho_{\oplus}^j = \xi_j (1 - \varepsilon_j) \quad \delta_{\oplus}^j = (1 - \xi_j) (1 - \varepsilon_j) \quad (4.39)$$

Substituting Equation (4.25) into Equation (4.38), and simplifying, yields

$$\begin{aligned} \vec{F}_{\oplus,e}^j = & -\frac{(1 - \cos \theta_{max})}{2N} \frac{G_{\odot}}{c} A_j \\ & \times \sum_{i=1}^N e_i (\hat{n}_j \cdot \hat{s}_{\oplus}^i) \left\{ (1 - \rho_{\oplus}^j) \hat{s}_{\oplus}^i + 2 \left[\frac{\delta_{\oplus}^j}{3} + \rho_{\oplus}^j (\hat{n}_j \cdot \hat{s}_{\oplus}^i) \right] \hat{n}_j \right\} \end{aligned} \quad (4.40)$$

As for the incident heat rate, the emissivity e_i is obtained from Equation (2.37), based on the latitude of the ray's intersection with the Earth.

To determine the force acting on a node receiving radiation reflected by the Earth, the total reflected irradiance B_{\oplus}^i can be substituted for E^i in Equation (4.33),

$$\begin{aligned} \vec{F}_{\oplus,a}^j = & -\frac{2(1 - \cos \theta_{max})}{N} \frac{A_j}{c} \\ & \times \sum_{i=1}^N B_{\oplus}^i (\hat{n}_j \cdot \hat{s}_{\oplus}^i) \left\{ (1 - \rho_{\odot}^j) \hat{s}_{\oplus}^i + 2 \left[\frac{\delta_{\odot}^j}{3} + \rho_{\odot}^j (\hat{n}_j \cdot \hat{s}_{\oplus}^i) \right] \hat{n}_j \right\} \end{aligned} \quad (4.41)$$

The specular and diffuse reflectivities are the same as those given for incident solar radiation in Equation (4.35). Substituting Equation (4.28) into Equation (4.41), and simplifying, yields

$$\begin{aligned} \vec{F}_{\oplus,a}^j = & -\frac{2(1 - \cos \theta_{max})}{N} \frac{G_{\odot}}{c} A_j \\ & \times \sum_{i=1}^N a_i (\hat{n}_j \cdot \hat{s}_{\oplus}^i) (\hat{n}_{\oplus}^i \cdot \hat{R}_{\odot}) \left\{ (1 - \rho_{\odot}^j) \hat{s}_{\oplus}^i + 2 \left[\frac{\delta_{\odot}^j}{3} + \rho_{\odot}^j (\hat{n}_j \cdot \hat{s}_{\oplus}^i) \right] \hat{n}_j \right\} \end{aligned} \quad (4.42)$$

As for the incident heat rate, the albedo a_i is obtained from Equation (2.36), based on the latitude of the intersection. For this study, Space Design, Inc., implemented an option to compute radiation forces using Equations (4.36), (4.40) and (4.42) within the TSS Heat Rate application.

4.2 Simulation Methodology

Prior to the launch of ICESat, the micro-model simulation offered the most accurate characterization of the satellite’s response to the anticipated radiation environment. Specifically, it produced a series of predicted forces, as a function of position within the orbit and the relative location of the Sun. This force history served as a “truth” data set, from which the macro-model parameters were derived, and against which their performance was assessed. Had these been the only objectives, this simulation could have been structured in any number of ways to maximize the observability of those parameters. Instead, it also presented an opportunity to explore the potential for updating them, once the satellite was in orbit. Consequently, the actual simulation represented a compromise, reflecting the planned mission operations as accurately as possible, but at the same time, providing *sufficient* observability of the macro-model parameters.

Its methodology included four distinct steps within TSS, which are discussed in the following sections. The first involved the construction of a satellite model, detailing both the geometric and radiative properties of its surfaces. Next, individual orbit revolutions were generated for different Sun geometries, and in each case, the satellite was oriented according to the constraints outlined in Section 3.4.2. The third step animated the surfaces of the two solar arrays to meet the articulation requirements of Section 3.4.3. Finally, at discrete points around the orbit, the solar and Earth radiation forces were calculated for each node in the satellite model. In addition to these results, the

orbit and attitude data used in the computations were output, so that the same values could be accessed in the determination of the macro-model parameters. At the end of each TSS simulation, an external, post-processing step summed the nodal body-fixed forces at a given orbit position, and rotated the resulting total-force vector to an orbit frame.

4.2.1 Satellite Model

BATC engineers developed a model of the ICESat bus using the TSS Geometry application. They incorporated the salient features of the GLAS instrument from a separate model developed at GSFC. Illustrated in Figure 4.4, the composite pre-launch version consists of 950 surfaces, including flat plates, cones and cylinders. Each of these was oriented within the body-fixed Vehicle Coordinate System (VCS) — also shown — that was defined to coincide with the Spacecraft Coordinate System (SCS) of Figure 1.2. Many of the larger surfaces were further subdivided, yielding 2058 individual nodes, of which 1124 receive external radiation.

Associated with each node are a surface area and a user-defined surface type. Typically, the latter is the component to which the node belongs (e.g., separation ring), its constitutive material (e.g., stainless steel), or a surface coating that fundamentally alters its radiative properties (e.g., white paint). Table 4.1 lists each surface type used in the ICESat model, along with its absorptivity α , emissivity ε and specularity ξ . The corresponding specular and diffuse reflectivities, needed in the force computations, were derived for each node from these parameters, using Equations (4.35) and (4.39). The values for

absorptivity and emissivity were compiled by BATC from industry standards and vendor-supplied data. They represent the expected surface characteristics at launch, often referred to as the beginning of life (BOL). The degradation of these properties during the mission is considered in Section 4.3.2, with an examination of the estimated end-of-life (EOL) values.

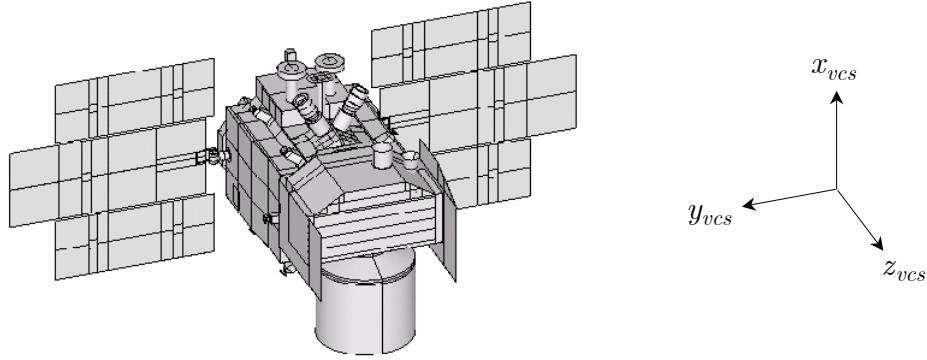


Figure 4.4. ICESat Micro-Model and Vehicle Coordinate System (VCS)

Significantly less data is available regarding the specularity of various surface types, as its role in heat transfer contexts is limited. For the TOPEX/Poseidon micro-model simulation, Antreasian (1992) assumed a uniform value of 0.2 for all surfaces, implying that 20% of any reflected radiation was specular in nature, with the remainder being diffuse. The same assumption has been made in this study, except for two surface types: “Black” and “Gallium Arsenide Solar Cells”. The former has the characteristics of a blackbody, absorbing all incoming radiation ($\alpha = 1$) and reflecting none; thus, $\xi = 0$. For the solar cells, the array vendor, Spectrolab, determined that diffuse reflection constitutes $\sim 1\%$ of the total reflection from their surfaces, yielding an estimated specularity of 0.99 (Granata, 2001).

	α	ϵ	ξ
Black	1.0000	1.0000	0.00
Black Anodize	0.7300	0.8600	0.20
Black Kapton	0.9300	0.7800	0.20
Black Nylon	0.8500	0.8500	0.20
Black Paint	0.9000	0.9200	0.20
Black Paint (Z306)	0.9000	0.9200	0.20
Black Titanium Anodize	0.8000	0.8000	0.20
Bracket, back (RSS)	0.6032	0.3867	0.20
Bracket, front (RSS)	0.7956	0.6406	0.20
Chromacoat	0.3400	0.0370	0.20
Clear Anodize	0.4600	0.8300	0.20
Copper-Tinned	0.6800	0.5600	0.20
Desoto Black Paint	0.9600	0.9200	0.20
GPS Antenna	0.9000	0.9000	0.20
GPS Kapton	0.4000	0.6500	0.20
Inconel	0.4000	0.3000	0.20
Indium-Tin-Oxide Silver Teflon	0.1000	0.7600	0.20
Kapton	0.4400	0.8000	0.20
Optical Surface Reflector	0.0700	0.7600	0.20
Separation Ring	0.6100	0.6700	0.20
Silver Teflon	0.0900	0.8000	0.20
Gallium Arsenide Solar Cells	0.6700	0.7900	0.99
Stainless Steel (C455)	0.3900	0.1100	0.20
Titanium (6AL4V)	0.5500	0.1700	0.20
Vacuum Deposited Aluminum	0.0800	0.0300	0.20
White Paint (Z93)	0.1600	0.9200	0.20

Table 4.1. Micro-Model BOL Radiative Properties

4.2.2 Orbit Generation

As indicated in Section 3.4.2, the relative geometry of the orbit and the Sun can be characterized by the β' angle. Although the TSS Orbit application has a “Basic” option to establish a fixed orbit with a designated β' , the Earth-radiation model of Section 2.3 requires date information to compute the seasonal variations in albedo and emissivity. Consequently, this study employed the “Date-Dependent” option, which allows the user to associate a specific epoch with an initial state. In determining subsequent states, this option also accounts for the apsidal rotation and nodal precession induced by the J_2 term of the geopotential. No other perturbations were considered, including those arising from the radiation pressure forces being investigated. Table 4.2 identifies the values of the orbit parameters used in the simulation, along with the geophysical constants adopted for the dynamic model.

Epoch, $\beta' \leq 0^\circ$	9/12/2001 00:42:00
Epoch, $\beta' \geq 0^\circ$	10/3/2001 19:46:00
Maximum altitude	600 km
Eccentricity	0
Inclination	94°
Argument of perigee	90°
Right ascension of ascending node	β' – dependent
Earth radius, a_\oplus	6378.137 km
Earth gravity, g	9.79828547 m/s^2
Earth J_2	$1.08263602 \times 10^{-3}$

Table 4.2. TSS Orbit Simulation Parameters

Since the β' angle can vary, theoretically, between -90° and $+90^\circ$, single orbit revolutions were generated at 5° increments within this range by adjusting the right ascension of the ascending node at the initial epoch. Additionally, this node was placed sunward of the Earth's terminator (i.e., the plane perpendicular to the Earth-Sun line) for $\beta' \geq 0^\circ$, and on the opposite side for $\beta' \leq 0^\circ$. The 94° inclination of the orbit precluded the use of a single epoch to span the full β' interval. Consequently, two different dates — included in Table 4.2 — were selected, one associated with $\beta' \leq 0^\circ$ and the other with $\beta' \geq 0^\circ$. Although this strategy introduced a discontinuity in the radiation characteristics of the Earth, due to the temporal variations in albedo and emissivity, its effects were limited for two reasons. First, the proximity of the two epochs, and their symmetry with respect to the autumnal equinox, minimized the differences in the cosine terms of the a_1 and e_1 coefficients in Equations (2.36) and (2.37), respectively. The resulting albedo and emissivity for both data sets are plotted in Figure 4.5. Second, the residual disparities had no impact on the estimated macro-model parameters, as their determination relied on the same dates for the β' sub-intervals, producing albedo and emissivity characteristics identical to those calculated here.

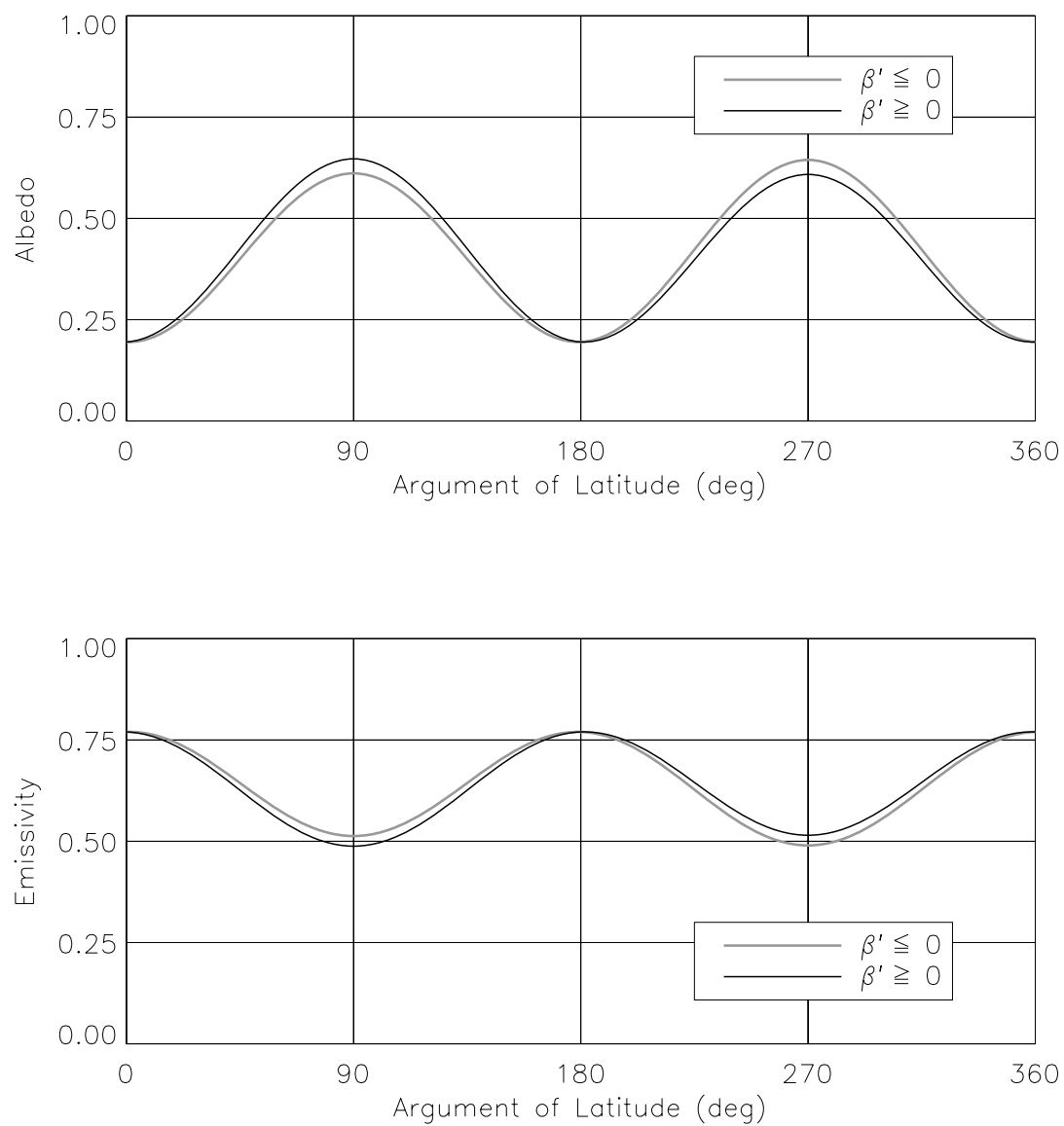


Figure 4.5. Earth Albedo and Emissivity for $\beta' \leq 0^\circ$ and $\beta' \geq 0^\circ$

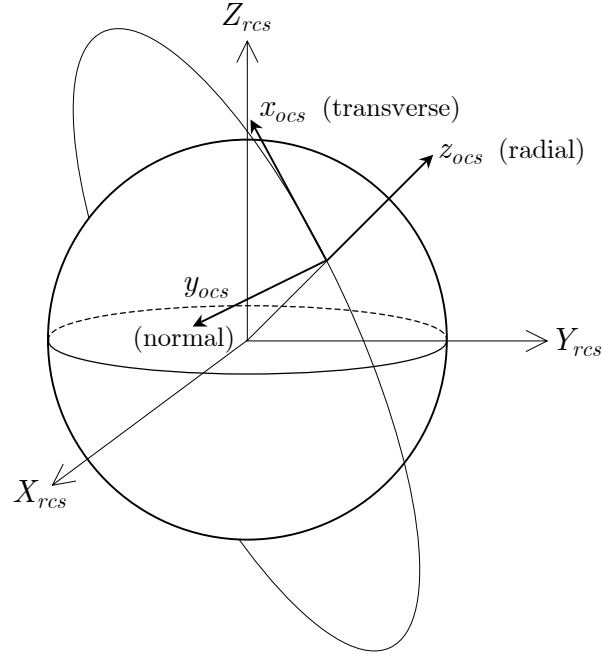


Figure 4.6. TSS Reference and Orbit Coordinate Systems (RCS, OCS)

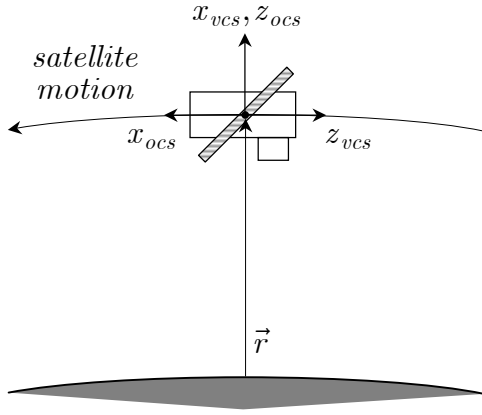
For each β' case, the position and velocity of the satellite with respect to the Reference Coordinate System (RCS) were computed and output every 15° around the orbit, yielding 24 unique points per revolution. Illustrated in Figure 4.6, the RCS is a non-rotating Earth-centered frame, with the $+X_{rcs}$ axis pointing toward the vernal equinox, the $+Z_{rcs}$ axis aligned with the mean pole, and the $+Y_{rcs}$ axis completing the orthonormal triad. It was at these points that the radiation forces were subsequently calculated. For each orbit that experienced an eclipse, the entry and exit terminators provided two additional points for evaluation. Their locations were determined using a cylindrical shadow model comparable to that of Section 2.4.

4.2.3 Satellite Attitude and Solar Array Articulation

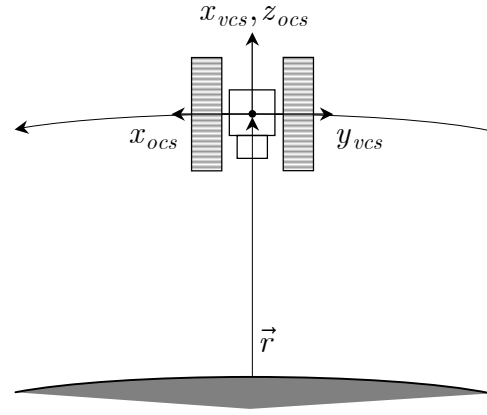
The TSS Orbit application allows the user to input a series of Euler angle rotations to orient the satellite's body-fixed VCS axes with respect to the Orbit Coordinate System (OCS). Juxtaposed with the RCS in Figure 4.6, the OCS is a locally derived Radial-Transverse-Normal (RTN) frame, with the $+z_{ocs}$ axis pointing radially outward from the Earth, the $+y_{ocs}$ axis aligned with the orbit normal, and the $+x_{ocs}$ axis completing the orthonormal triad, in the direction of motion. In this simulation, four different sequences were employed, corresponding to the four control frames (CF) defined in Table 3.2. Identified in Table 4.3, each one included only two rotations, the first about the $+y_{ocs}$ axis, and the second about the $+x_{ocs}$ axis. Taken together, they rotate the OCS axes to the VCS orientation associated with a particular control frame, as illustrated in Figure 4.7. It should be noted that these sequences produced satellite orientations based on radial, rather than ellipsoid-normal, pointing, and that each neglected the small pitch bias discussed in Section 3.4.2.

Control Frame	β' Limits		Euler Rotations			
	Lower	Upper	1st		2nd	
0	0°	33°	y	270°	x	0°
1	33°	90°	y	270°	x	90°
2	-33°	0°	y	270°	x	180°
3	-90°	-33°	y	270°	x	270°

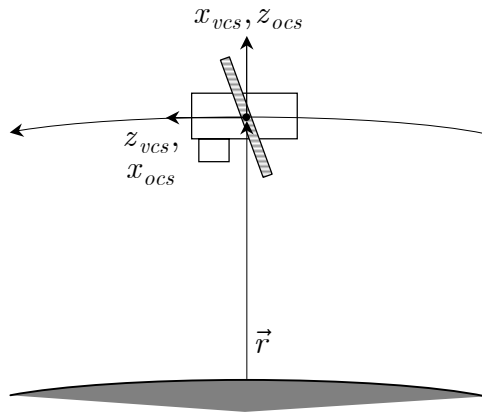
Table 4.3. TSS Attitude Model Euler Rotation Sequences



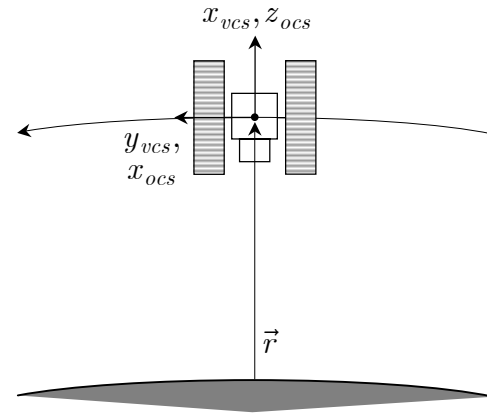
Control Frame 0



Control Frame 1



Control Frame 2



Control Frame 3

Figure 4.7. Micro-Model Simulation Attitude Control Frames

An individual surface, or a collection of surfaces called an assembly, can be oriented kinematically with the TSS Animation application. To facilitate the articulation of the two solar arrays in the ICESat model, they were defined as assemblies, one rotating about the $+y_{vcs}$ axis, and the other about the $-y_{vcs}$ axis. For the simulation, when $|\beta'| \leq 55^\circ$, both arrays tracked the Sun (or a fictitious Sun, during eclipse). Specifically, using the Auto-Orbit Track option, the normal to the solar-cell side of each array pointed toward the Sun, insofar as possible, given its constraint to rotate about the required axis. No inhibition of the array motion, during any part of the orbit, was considered, and the resulting orientation angles were identical to those obtained from Equation (3.39). For cases in which $|\beta'| \geq 55^\circ$, the arrays were fixed in the neutral $\zeta = 0^\circ$ orientation, with the cell-side normal along the $-z_{vcs}$ (i.e., the $-z_{scs}$ axis in Figure 3.9).

4.2.4 Force History Generation

The micro-model simulation produced a comprehensive radiation force history from 40 separate simulations made with the modified version of the TSS Heat Rate application. Each one reflected a unique combination of β' , satellite attitude, and solar array motion, as summarized in Tables 4.4 and 4.5. In addition to the 37 different β' angles considered, other cases were included to distinguish between the two attitudes at $\beta' = 0^\circ$, and between fixed and articulating solar arrays at $\beta' = \pm 55^\circ$. Furthermore, the cases listed in Table 4.4 used the first epoch given in Table 4.2, while those from Table 4.5 used the second. Several supplemental cases were generated to facilitate the interpolation

of the modeled forces through the attitude transitions at the β' limits of Table 4.3, as part of the pre-launch precision orbit determination (POD) simulation discussed in Chapter 5. Tables 4.6 and 4.7 summarize those for $\beta' \leq 0^\circ$ and $\beta' \geq 0^\circ$, respectively. These cases were not used in the determination of the macro-model parameters.

Although TSS features a graphical user interface in its component applications, it also provides a Command-Language mode, which allows groups of commands to be submitted via script, helping to standardize and to automate the execution of large numbers of cases. Using this approach, the individual Heat Rate simulations calculated the solar and Earth radiation forces acting on each of the 1124 active nodes in the satellite model, at each of the 24 (or 26) distinct points around the respective orbit. As discussed in Section 4.1.2, the computations for a given node and radiation source terminated either when a WPE below the user-defined limit (1% with a 90% confidence interval) had been achieved, or when the number of rays generated reached the specified maximum (10,000). Running on a dedicated 1-GHz Pentium-3 PC platform, a single execution — *one* orbit revolution — required 2.5 hours to complete.

Epoch: September 12, 2001 00:42:00				
Case	β'	Satellite Attitude	Solar Arrays	Orbit Eclipse
1	-90°	Sailboat Yaw = 270° CF 3	Fixed	No
2	-85°			
3	-80°			
4	-75°			
5	-70°			
6	-65°			
7	-60°			
8	-55°			
9	-55°		Articulating	Yes
10	-50°			
11	-45°			
12	-40°			
13	-35°			
14	-30°	Airplane Yaw = 0° CF 2		
15	-25°			
16	-20°			
17	-15°			
18	-10°			
19	-5°			
20	0°			

Table 4.4. Nominal Radiation Force Simulation Cases: $\beta' \leq 0^\circ$

Epoch: October 3, 2001 19:46:00				
Case	β'	Satellite Attitude	Solar Arrays	Orbit Eclipse
21	0°	Airplane Yaw = 180° CF 0	Articulating	Yes
22	5°			
23	10°			
24	15°			
25	20°			
26	25°			
27	30°			
28	35°	Sailboat Yaw = 90° CF 1	Fixed	
29	40°			
30	45°			
31	50°			
32	55°			
33	55°			
34	60°			
35	65°			
36	70°		No	
37	75°			
38	80°			
39	85°			
40	90°			

Table 4.5. Nominal Radiation Force Simulation Cases: $\beta' \geq 0^\circ$

Epoch: September 12, 2001 00:42:00				
Case	β'	Satellite Attitude	Solar Arrays	Orbit Eclipse
41	-33°	Sailboat Yaw = 270° CF 3	Articulating	Yes
42	-33°	Airplane Yaw = 0° CF 2	Articulating	Yes

Table 4.6. Supplemental Radiation Force Simulation Cases: $\beta' \leq 0^\circ$

Epoch: October 3, 2001 19:46:00				
Case	β'	Satellite Attitude	Solar Arrays	Orbit Eclipse
43	33°	Airplane Yaw = 180° CF 0	Articulating	Yes
44	33°	Sailboat Yaw = 90° CF 1	Articulating	Yes
45	0°	Airplane Yaw = 0° CF 2	Articulating	Yes

Table 4.7. Supplemental Radiation Force Simulation Cases: $\beta' \geq 0^\circ$

Each simulation output the predicted forces to two files, one for direct solar radiation, and the other for the separate albedo and emissivity components of Earth radiation. A post-processing program was written to extract and to sum these nodal forces at each orbit position for each type of radiation. Initially computed in the VCS, the net forces acting on the satellite were subsequently rotated to the OCS. At a given orbit position, the net solar radiation force can be expressed as

$$\left[\vec{F}_{\odot} \right]_{ocs} = T_{vcs}^{ocs} \sum_{j=1}^M \left[\vec{F}_{\odot}^j \right]_{vcs} \quad (4.43)$$

where M represents the 1124 active nodes in the satellite model. Similarly, the net force arising from Earth emission is

$$\left[\vec{F}_{\oplus,e} \right]_{ocs} = T_{vcs}^{ocs} \sum_{j=1}^M \left[\vec{F}_{\oplus,e}^j \right]_{vcs} \quad (4.44)$$

while that due to Earth albedo is

$$\left[\vec{F}_{\oplus,a} \right]_{ocs} = T_{vcs}^{ocs} \sum_{j=1}^M \left[\vec{F}_{\oplus,a}^j \right]_{vcs} \quad (4.45)$$

The transformation T_{vcs}^{ocs} from the VCS to the OCS was derived, for a given control frame, from the corresponding pair of Euler angle rotations in Table 4.3,

$$T_{vcs}^{ocs} = R_y(\vartheta_1) R_x(\vartheta_2) \quad (4.46)$$

The elementary rotation matrices are defined to be

$$\begin{aligned}
 R_y(\vartheta_1) &= \begin{bmatrix} \cos \vartheta_1 & 0 & \sin \vartheta_1 \\ 0 & 1 & 0 \\ -\sin \vartheta_1 & 0 & \cos \vartheta_1 \end{bmatrix} \\
 R_x(\vartheta_2) &= \begin{bmatrix} 1 & 0 & 0 \\ 0 & \cos \vartheta_2 & -\sin \vartheta_2 \\ 0 & \sin \vartheta_2 & \cos \vartheta_2 \end{bmatrix}
 \end{aligned} \tag{4.47}$$

Two additional output files were created at the end of each Heat Rate simulation, containing the specific orbit and attitude data applied in its calculations. These files were later used in the determination of the macro-model parameters, to avoid errors introduced by potential dynamic model differences. For each orbit position, this data included:

- Time tag, seconds from epoch
- True anomaly, degrees
- Shadow flag: 0 = full shadow, 1 = full sun
- Position vector (RCS), meters
- Velocity vector (RCS), normalized
- Right ascension of the Sun (RCS), degrees
- Declination of the Sun (RCS), degrees
- OCS-to-VCS Euler angle rotations, degrees
- RCS-to-VCS transformation matrix
- Satellite-to-Sun unit vector (VCS)

4.3 Simulation Results

Using the procedure outlined in the preceding section, solar and Earth radiation forces were generated for each of the 40 cases in Tables 4.4 and 4.5. Four of those cases, summarized in Table 4.8, were chosen to illustrate the behavior observed in the four attitude control frames. Figures 4.8 through 4.11 plot the resulting solar, Earth albedo, Earth emission, and total radiation forces over one orbital revolution. Each reflects the combined influence of the orbit-Sun geometry (β'), the orientation of the satellite (Mode/Yaw), the motion of the solar arrays (Articulate/Fixed) and the occurrence of eclipses (Yes/No).

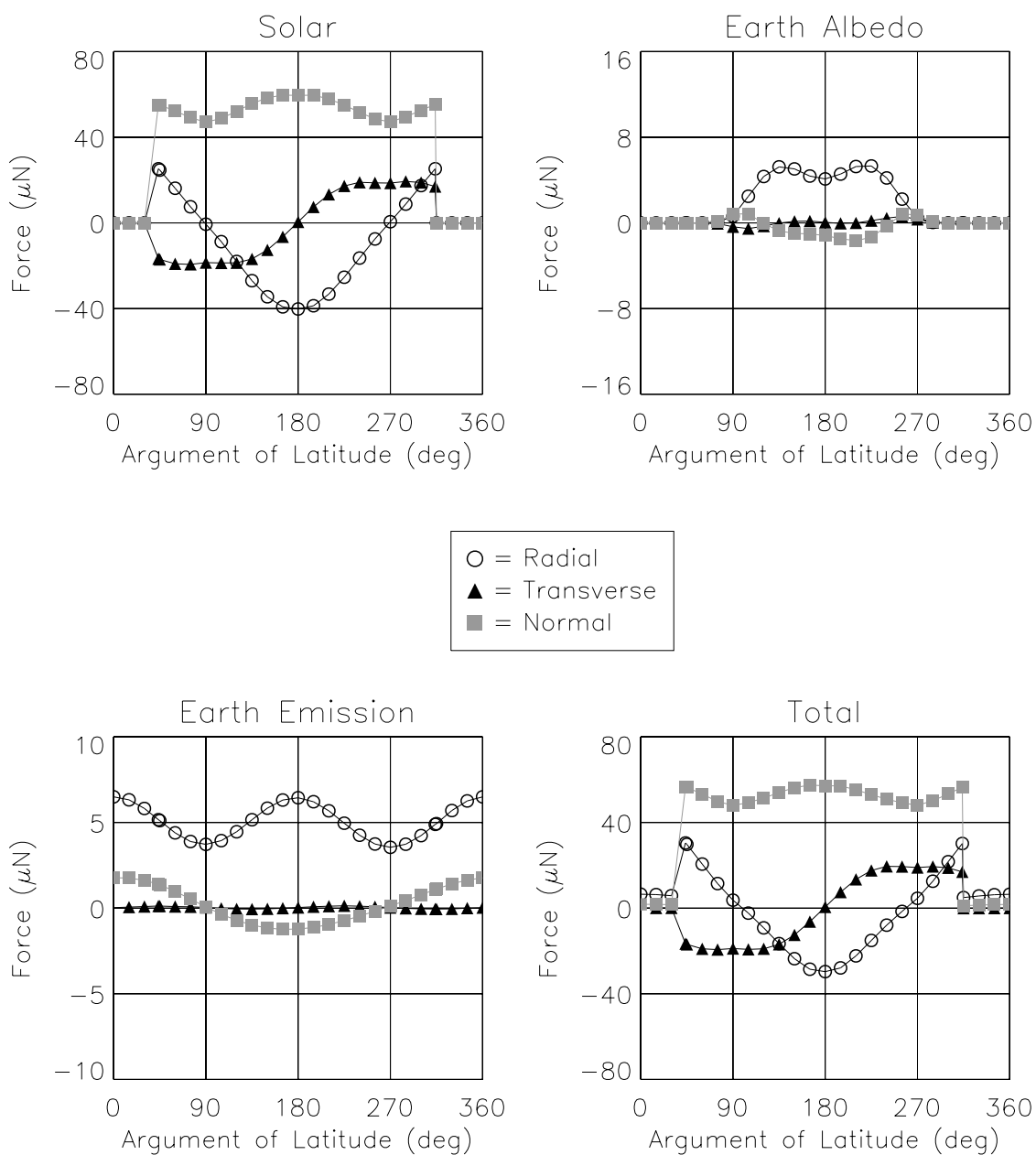
Case	Control Frame	β'	Mode	Yaw	Solar Arrays	Eclipse
9	3	-55°	Sailboat	270°	Articulate	Yes
14	2	-30°	Airplane	0°	Articulate	Yes
21	0	0°	Airplane	180°	Articulate	Yes
37	1	$+75^\circ$	Sailboat	90°	Fixed	No

Table 4.8. Representative Force History Cases

Some general observations can be made from these plots. In all cases, the solar radiation forces were significantly larger than those induced by Earth radiation, and thus dominated the total force histories. They were largely radial and transverse in character for the airplane mode, due to the proximity of the Sun to the orbit plane. In the sailboat mode, as $|\beta'|$ increased, the orbit plane became more perpendicular to the Earth-Sun line, and the solar radiation forces

grew to be principally normal. They dissipated rapidly when the satellite entered eclipse, but quickly materialized again upon its exit, as evidenced in the solar plots for the first three cases.

Whereas the solar radiation forces were driven by the orbit-Sun geometry, those due to Earth albedo and emission were governed, generally, by the spatial variations of Figure 4.5. Chiefly radial in direction, they were also modulated by the articulation of the solar arrays. Although the albedo forces disappeared when the satellite entered eclipse, the emission forces were unaffected. Even when the satellite did not experience an eclipse, as in Case 37, the albedo forces dropped nearly to zero as it viewed the dark side of the planet, near the descending node in Figure 4.11. The following sections examine these and additional cases in more detail, to underscore the influence of solar array articulation in the generation of the micro-model forces, and to consider the degradation of surface radiative properties over the life of the mission.



**Figure 4.8. Case 9 Radiation Forces: $\beta' = -55^\circ$, Yaw = 270° (Sailboat),
Articulating Arrays, Eclipsing Orbit**

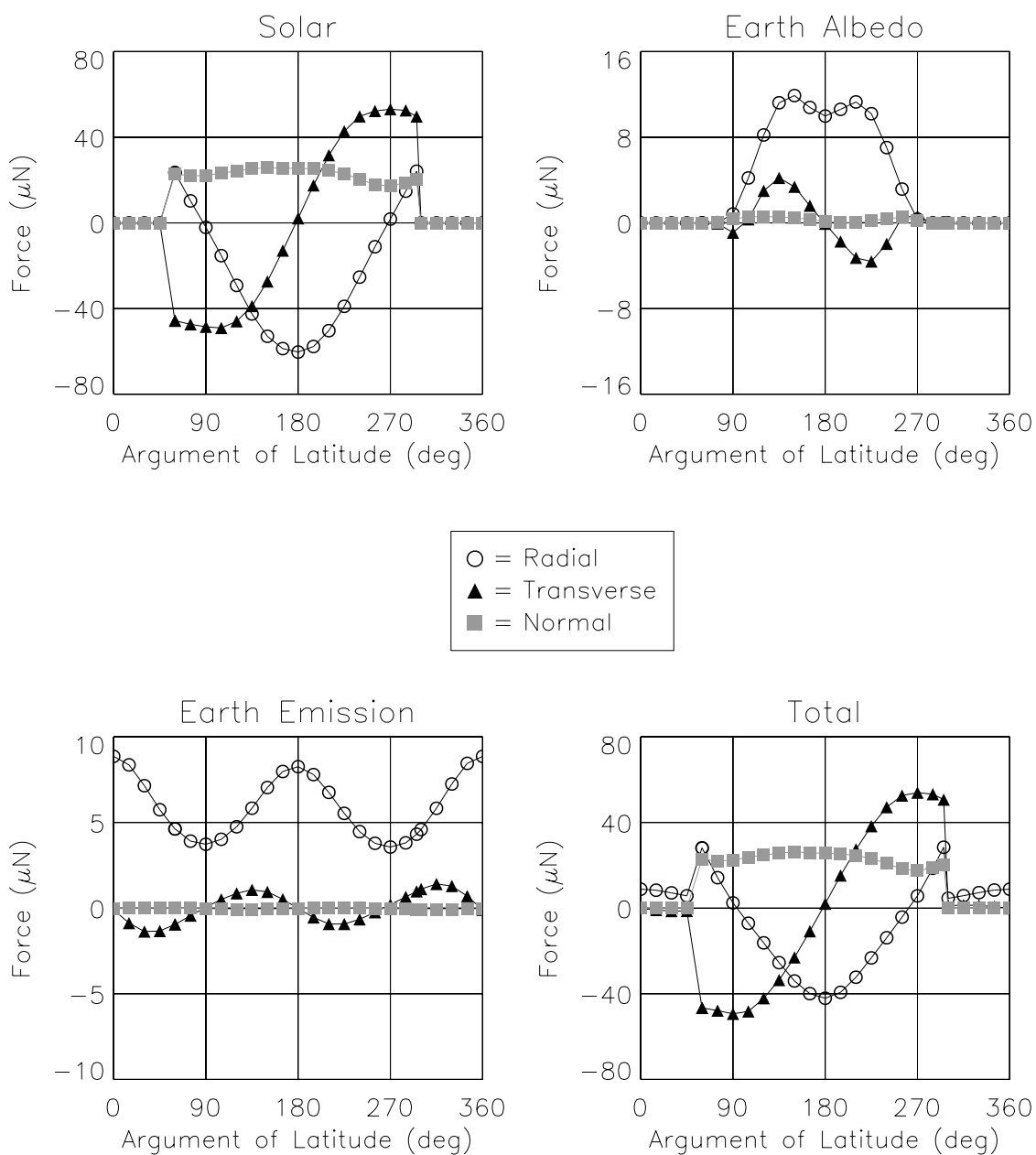
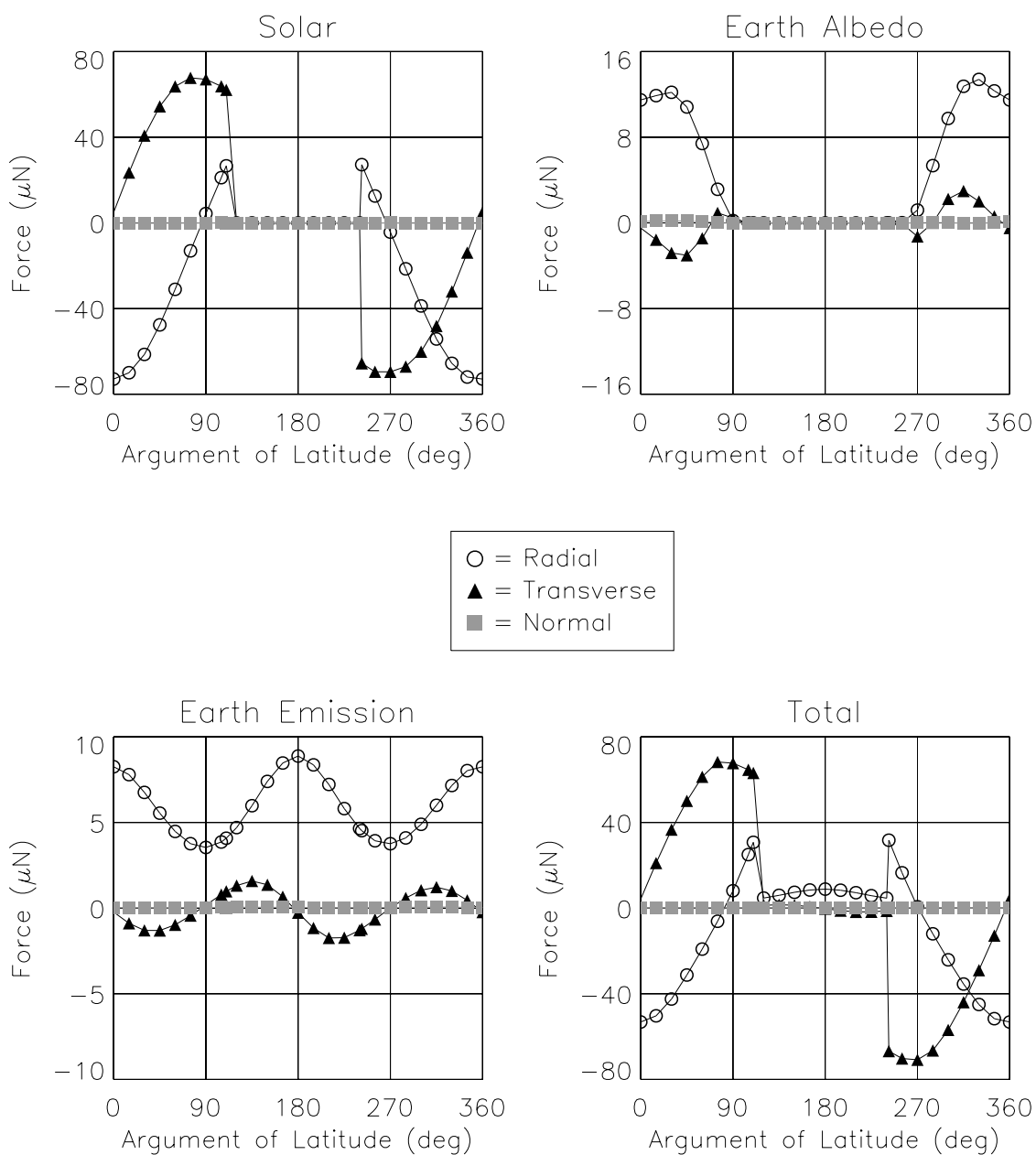


Figure 4.9. Case 14 Radiation Forces: $\beta' = -30^\circ$, Yaw = 0° (Airplane), Articulating Arrays, Eclipsing Orbit



**Figure 4.10. Case 21 Radiation Forces: $\beta' = 0^\circ$, Yaw = 180° (Airplane),
Articulating Arrays, Eclipsing Orbit**

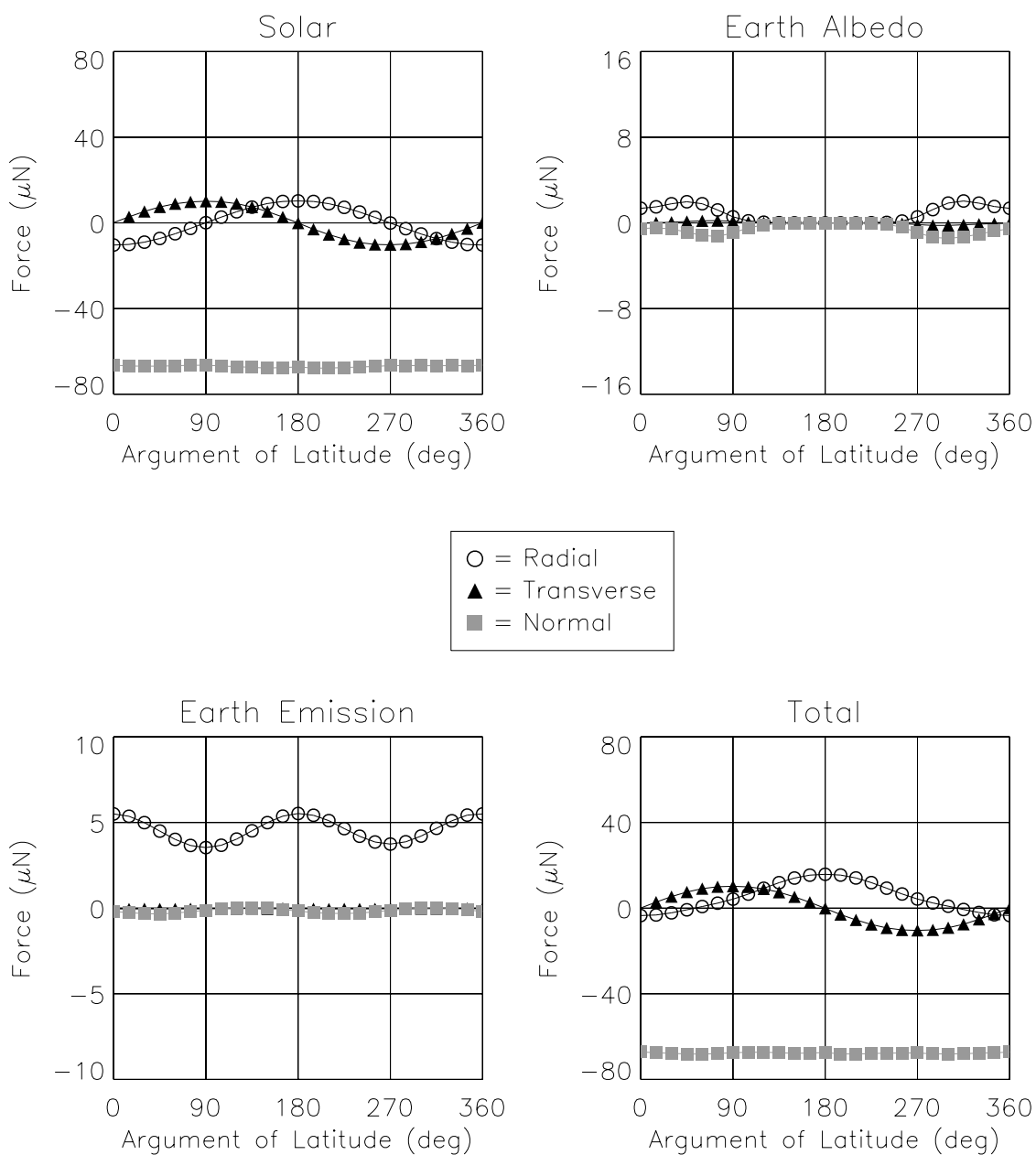


Figure 4.11. Case 37 Radiation Forces: $\beta' = 75^\circ$, Yaw = 90° (Sailboat), Fixed Arrays, Non-Eclipsing Orbit

4.3.1 Solar Array Articulation

As described in Section 4.2.3, the solar arrays articulated when $|\beta'| \leq 55^\circ$, and were fixed in the $\zeta = 0^\circ$ orientation otherwise. The TSS Auto-Track option used in the simulation produced the angles plotted in Figure 4.12 for each of the four representative cases in Table 4.8. When the solar arrays were fixed, as in Case 37, the Earth albedo and emission forces nonetheless exhibited periodic trends, like those observed in Figure 4.11. Their similarities to the plots of Figure 4.5 indicate that the spatial variations in Earth albedo and emissivity significantly influence the resulting forces.

These same trends are also evident in Figures 4.8 through 4.10, but for each, the solar arrays played an additional, modulating role. In the sailboat mode, they wobbled back and forth, between two β' -dependent limits (e.g., $\pm 35^\circ$ for Case 9, in Figure 4.12). Since the arrays were essentially edge-on to the direction of motion, as depicted in Figure 4.7, this motion yielded a small sinusoidal variation in the area exposed to the planet, which augmented the underlying spatial trend in the Earth radiation forces. It also introduced the small normal components observed in Figure 4.8.

These articulation effects were even more pronounced for the airplane mode, in which the solar arrays rotated 360° each revolution (e.g., Cases 14 and 21, in Figure 4.12). As a result, they exposed their entire surface areas to the planet twice per orbit. This comparatively larger sinusoidal area variation amplified the spatial trend in the Earth radiation forces more than for the sailboat mode. It also introduced the small transverse components seen in Figures 4.9 and 4.10.

The impact of the solar arrays can be observed directly by comparing Cases 32 and 33 from Table 4.5, plotted in Figures 4.13 and 4.14, respectively. Both were generated at $\beta' = +55^\circ$, in the same sailboat-mode attitude, but the former allowed the arrays to articulate, while the latter fixed them in the $\zeta = 0^\circ$ orientation. The solar radiation force had a larger amplitude in Case 32, particularly for the radial and normal components. There, the tracking of the Sun by the arrays presented a larger projected area to the incident solar radiation than when they were fixed in Case 33, increasing the magnitude of the resulting force. Furthermore, the amplification effects for Earth albedo and emission, discussed above, are clear when comparing Figure 4.13 to Figure 4.14. The larger amplitudes of these forces in Case 32 reflect the area variation introduced by the small wobbling motion of the arrays.

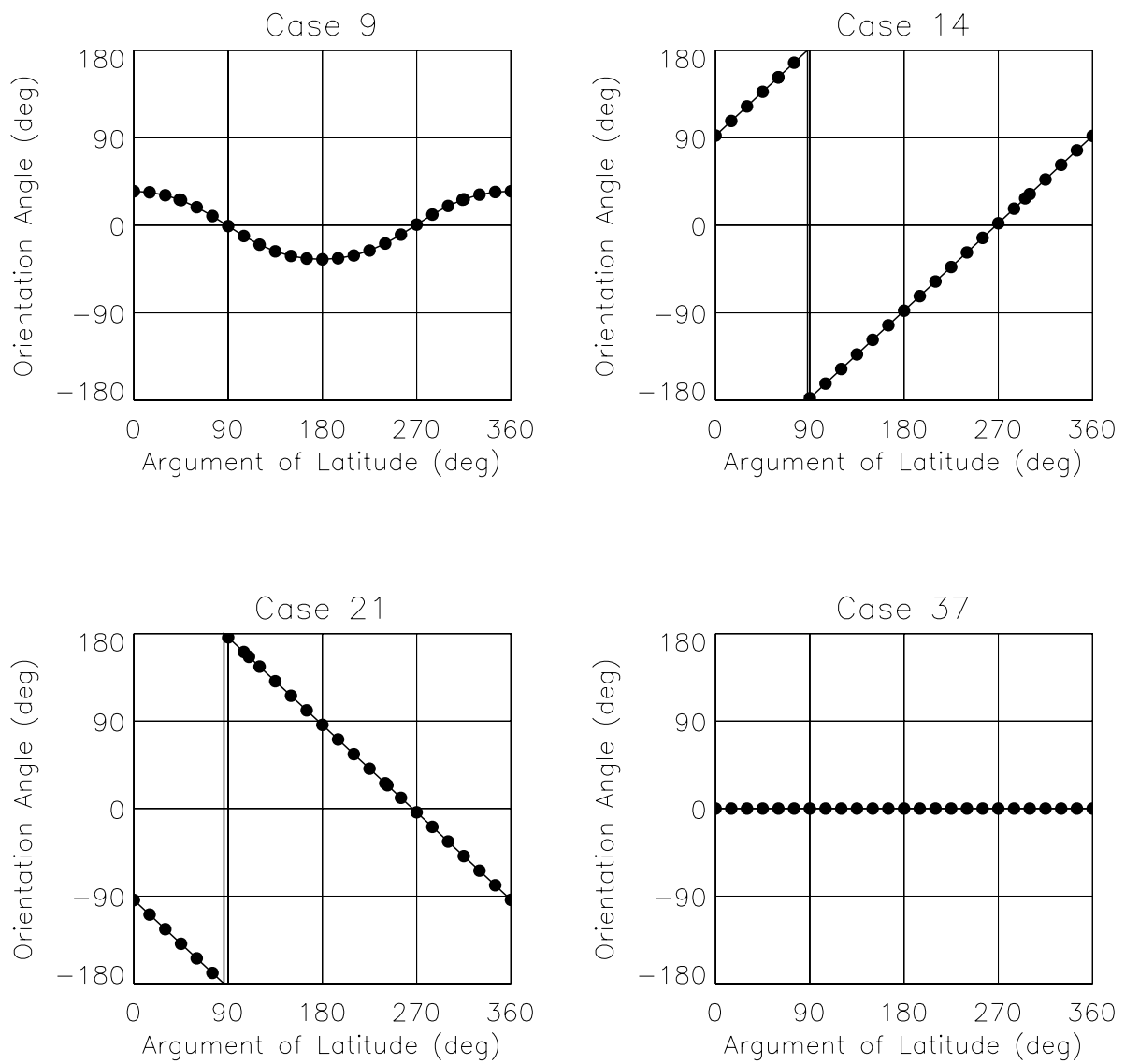


Figure 4.12. Solar Array Orientation Angles

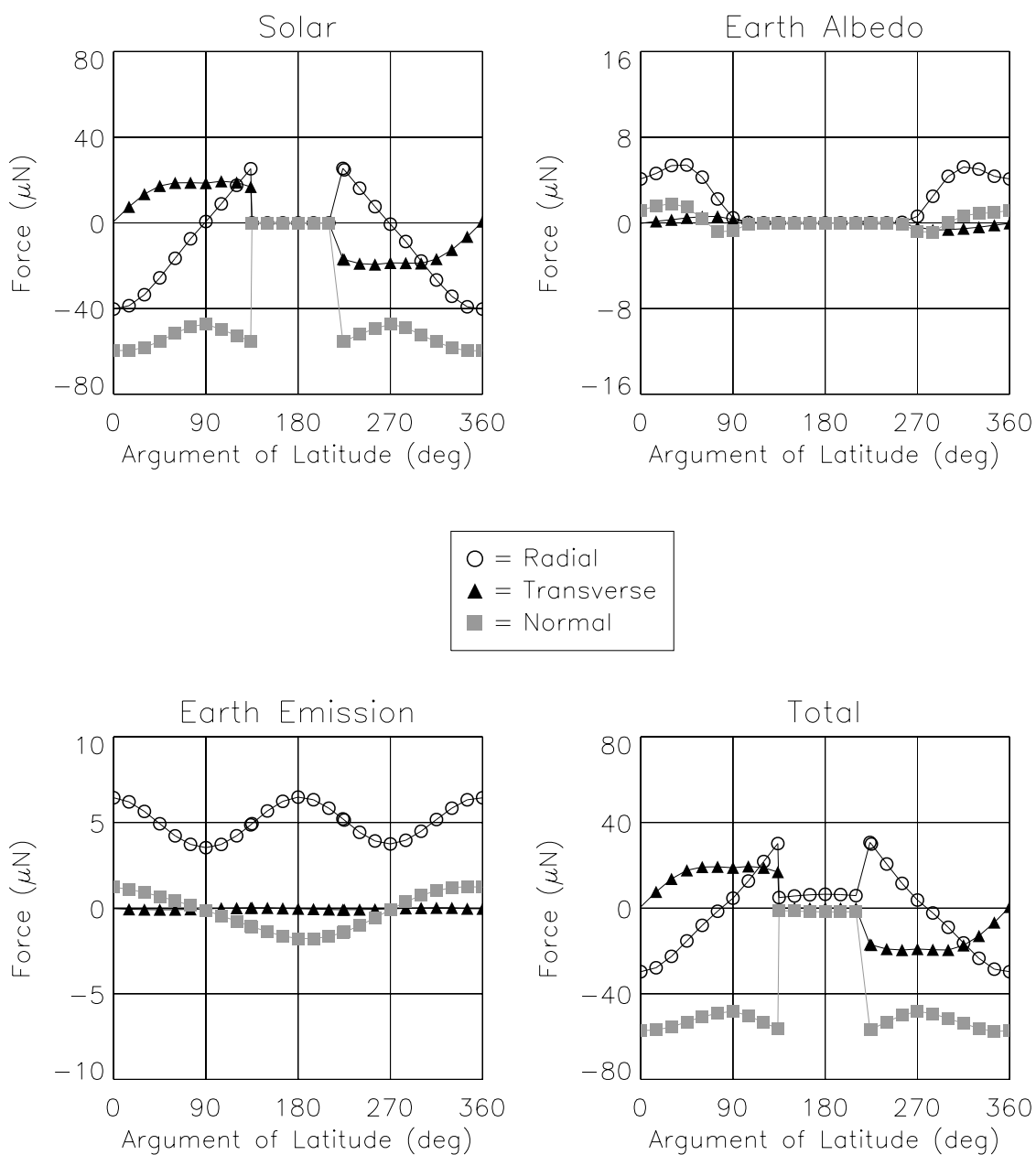


Figure 4.13. Case 32 Radiation Forces: $\beta' = 55^\circ$, Yaw = 90° (Sailboat), Articulating Arrays, Eclipsing Orbit

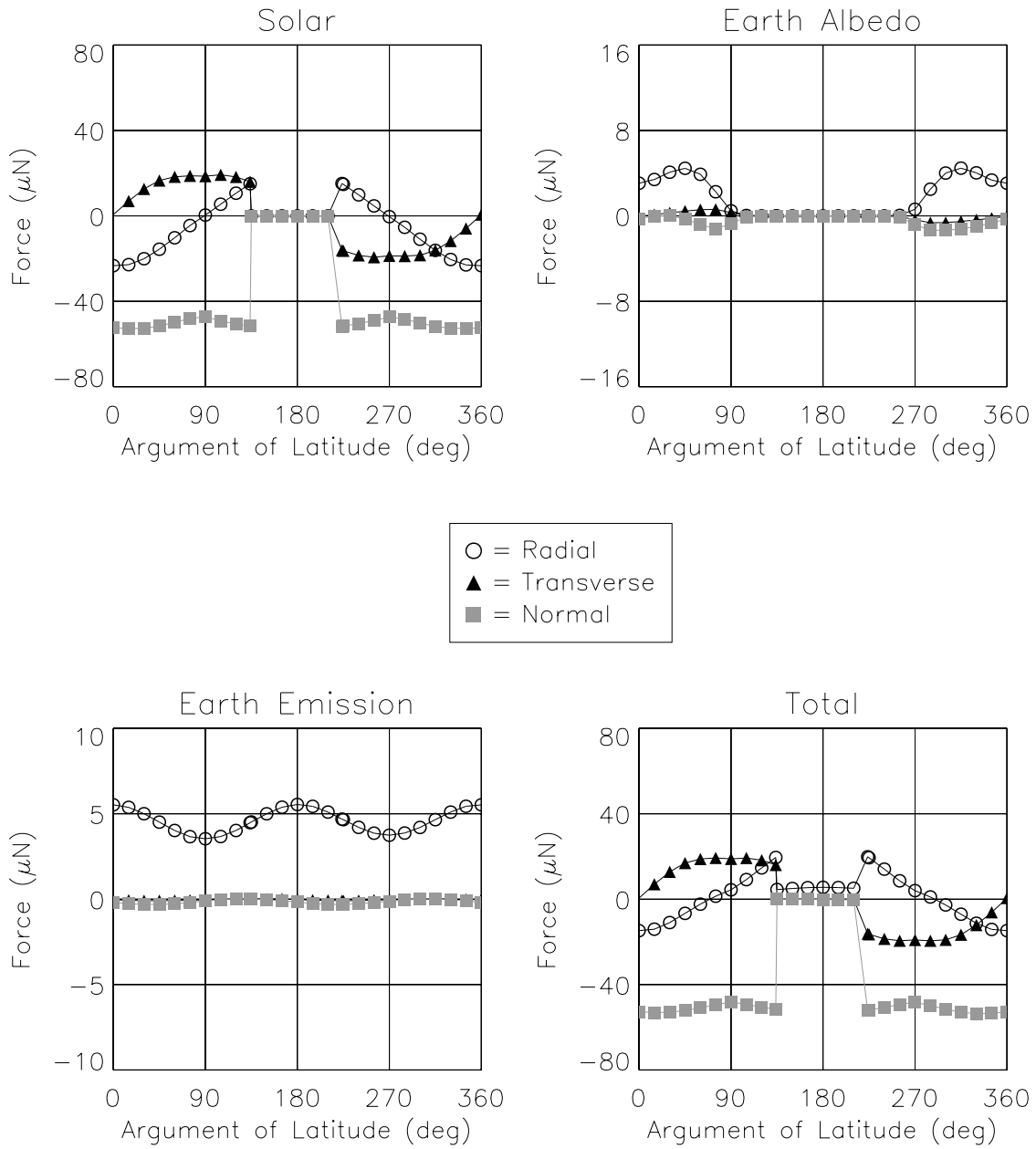


Figure 4.14. Case 33 Radiation Forces: $\beta' = 55^\circ$, Yaw = 90° (Sailboat), Fixed Arrays, Eclipsing Orbit

4.3.2 Surface Property Degradation

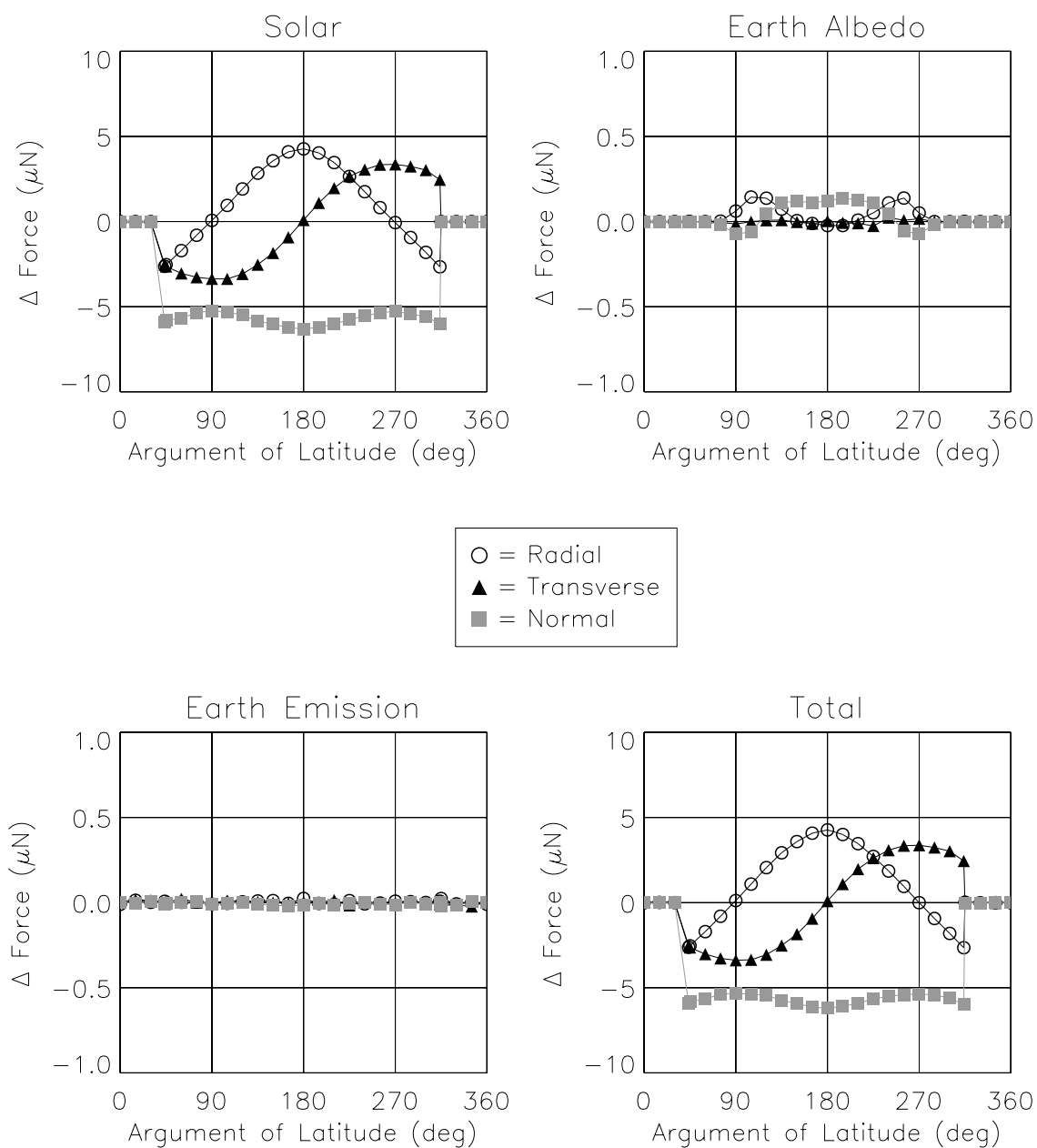
Over time, exposure to the space environment leads to changes in the radiative properties of a surface. As part of the design effort for the International Space Station, Silverman (1995) compiled an exhaustive survey of its effects on various materials, discerned from both short-term and long-term space flight experiments, as well as laboratory simulation. The causes for the degradation experienced by a particular satellite depend on its altitude and inclination. For highly inclined, low-Earth orbits, such as that of ICESat, they include ultraviolet radiation from the Sun, cosmic and trapped particle radiation, atomic oxygen, and micrometeoroids. In general, a surface's absorptivity, in the solar spectrum, increases the longer it remains in orbit, but its emissivity is largely unaffected. Thermal analyses are particularly concerned with increases in the ratio of absorptivity to emissivity, since greater absorption, or less emission, produces higher temperatures.

Table 4.9 lists the EOL absorptivity α and emissivity ε for each surface type in the ICESat model, as compiled by BATC. Those that differ from the BOL values in Table 4.1 are shown in bold. The specularities ξ values reflect the assumptions previously discussed in Section 4.2.1. As expected, the absorptivity increased for several of the surfaces, but most notably for the gallium arsenide (GaAs) cells on the solar arrays. This increase, from 0.67 to 0.86, is especially significant given the large surface area that the cells cover. The emissivity, on the other hand, showed only small decreases for a few of the surfaces, and no change at all for the others.

A separate radiation force history was generated using these EOL properties in the 40 cases from Tables 4.4 and 4.5. In general, the resulting forces differed little from those computed using the BOL properties, but Figures 4.15 through 4.18 plot the EOL–BOL differences for the representative cases of Table 4.8. The solar radiation forces showed the greatest differences due to the change in absorptivity for the solar cells. As Equation (4.35) suggests, that increase produced a lower specular reflectivity ρ_{\odot} , but actually increased the magnitude of the force, due to the $(1 - \rho_{\odot})$ term in Equation (4.37) and the high specularity of the cells ($\xi = 0.99$). This effect was largest when the Sun most directly illuminated the solar arrays, as in the $\beta' = 0^{\circ}$ case in Figure 4.17 and the $\beta' = 75^{\circ}$ case in Figure 4.18. A similar, but significantly smaller, increase occurred in the Earth albedo forces, while virtually none was observed for the Earth emission forces.

	α	ϵ	ξ
Black	1.0000	1.0000	0.00
Black Anodize	0.8800	0.8184	0.20
Black Kapton	0.9300	0.7800	0.20
Black Nylon	0.8500	0.8500	0.20
Black Paint	0.9000	0.9200	0.20
Black Paint (Z306)	0.9600	0.8700	0.20
Black Titanium Anodize	0.8000	0.8000	0.20
Bracket, back (RSS)	0.6032	0.3867	0.20
Bracket, front (RSS)	0.7956	0.6406	0.20
Chromacoat	0.3400	0.0370	0.20
Clear Anodize	0.4600	0.8300	0.20
Copper-Tinned	0.6800	0.5600	0.20
Desoto Black Paint	0.9600	0.9200	0.20
GPS Antenna	0.9000	0.9000	0.20
GPS Kapton	0.4000	0.6500	0.20
Inconel	0.5200	0.1000	0.20
Indium-Tin-Oxide Silver Teflon	0.2100	0.7600	0.20
Kapton	0.5500	0.7600	0.20
Optical Surface Reflector	0.1200	0.7300	0.20
Separation Ring	0.6100	0.6700	0.20
Silver Teflon	0.1600	0.8000	0.20
Gallium Arsenide Solar Cells	0.8600	0.7900	0.99
Stainless Steel (C455)	0.3900	0.1100	0.20
Titanium (6AL4V)	0.5500	0.1700	0.20
Vacuum Deposited Aluminum	0.1500	0.0200	0.20
White Paint (Z93)	0.2500	0.9200	0.20

Table 4.9. Micro-Model EOL Radiative Properties
(Values changed from BOL noted in bold)



**Figure 4.15. Case 9 EOL-BOL Radiation Force Differences: $\beta' = -55^\circ$,
Yaw = 270° (Sailboat), Articulating Arrays, Eclipsing Orbit**

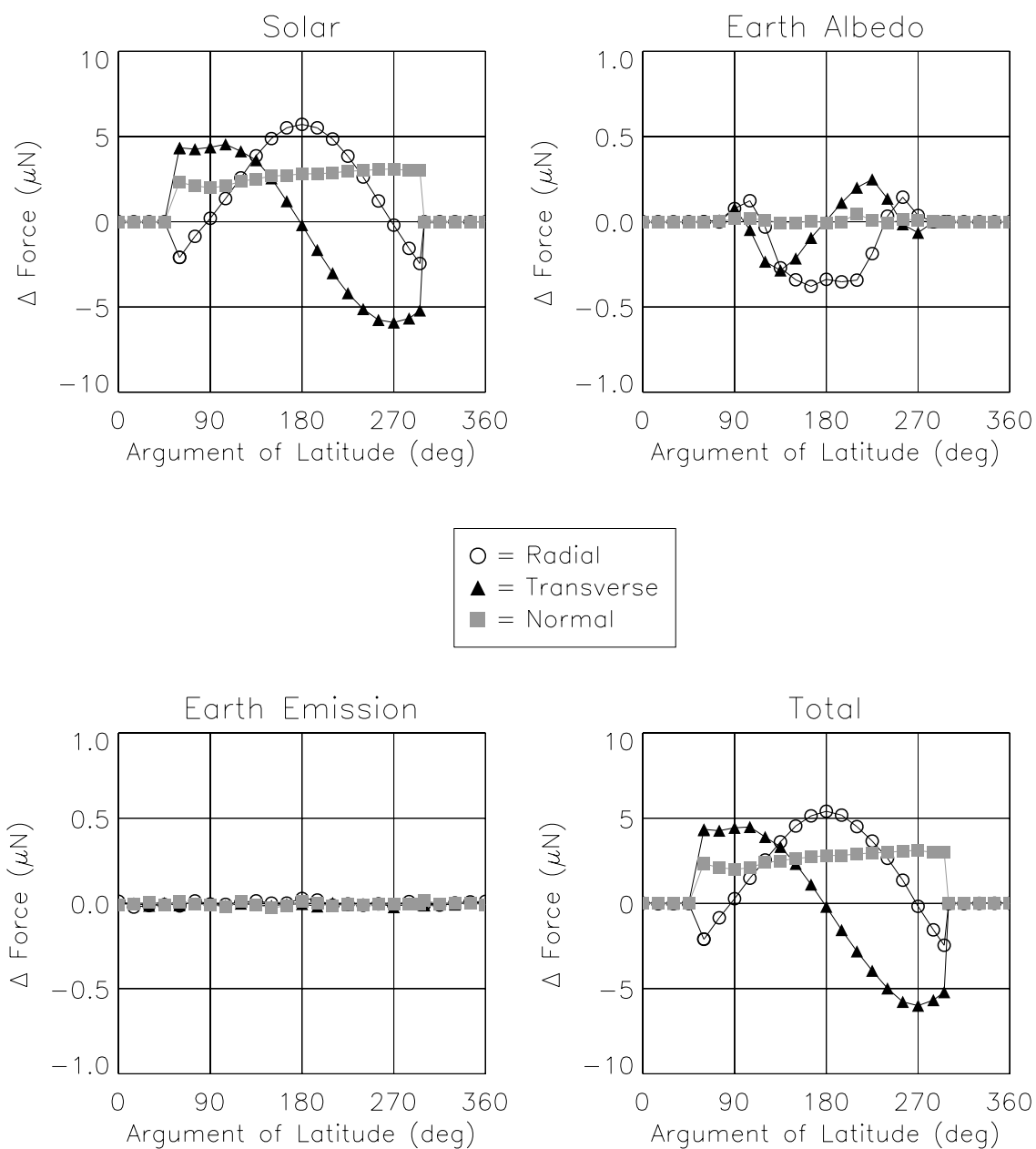


Figure 4.16. Case 14 EOL–BOL Radiation Force Differences: $\beta' = -30^\circ$, Yaw = 0° (Airplane), Articulating Arrays, Eclipsing Orbit

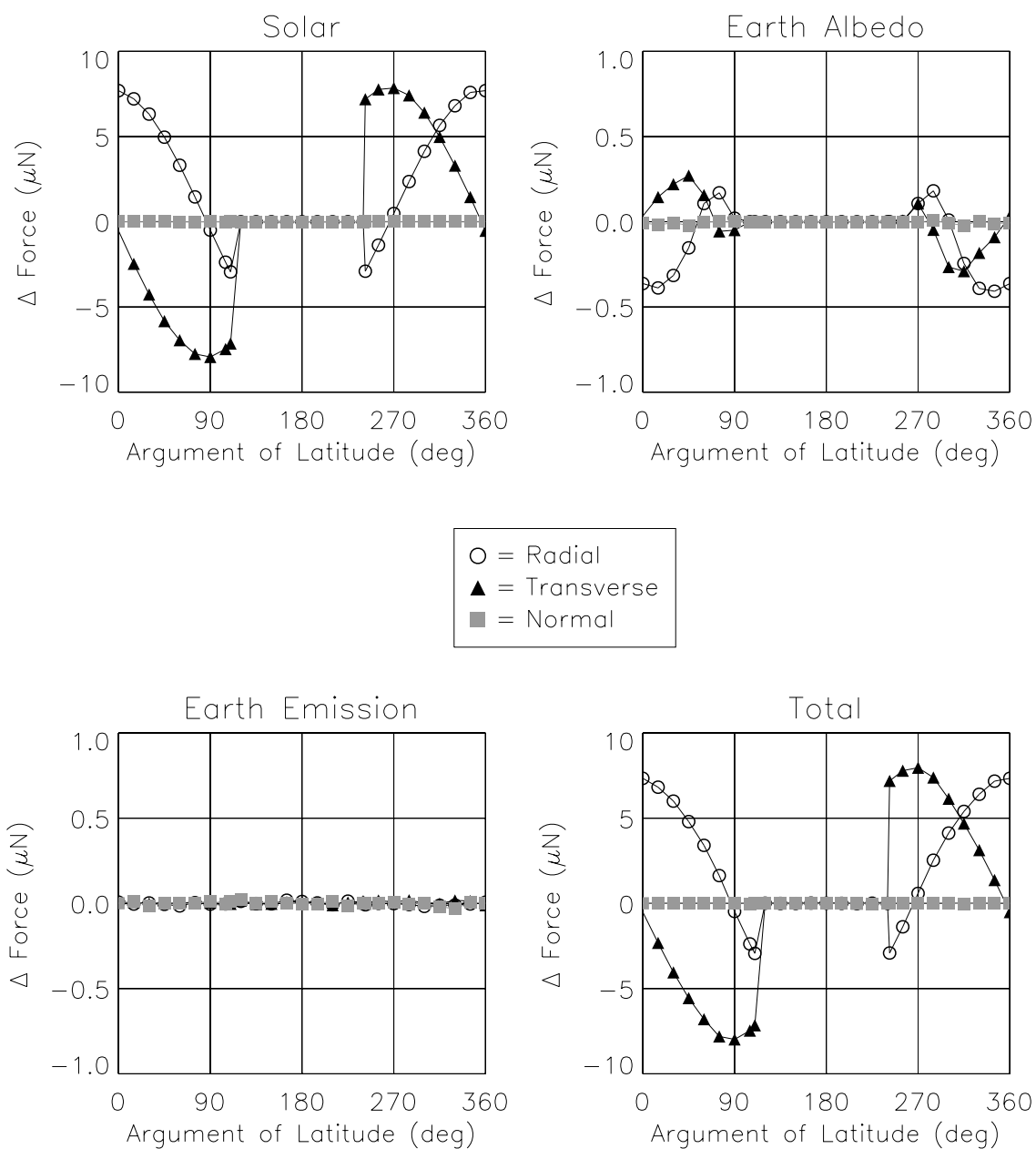
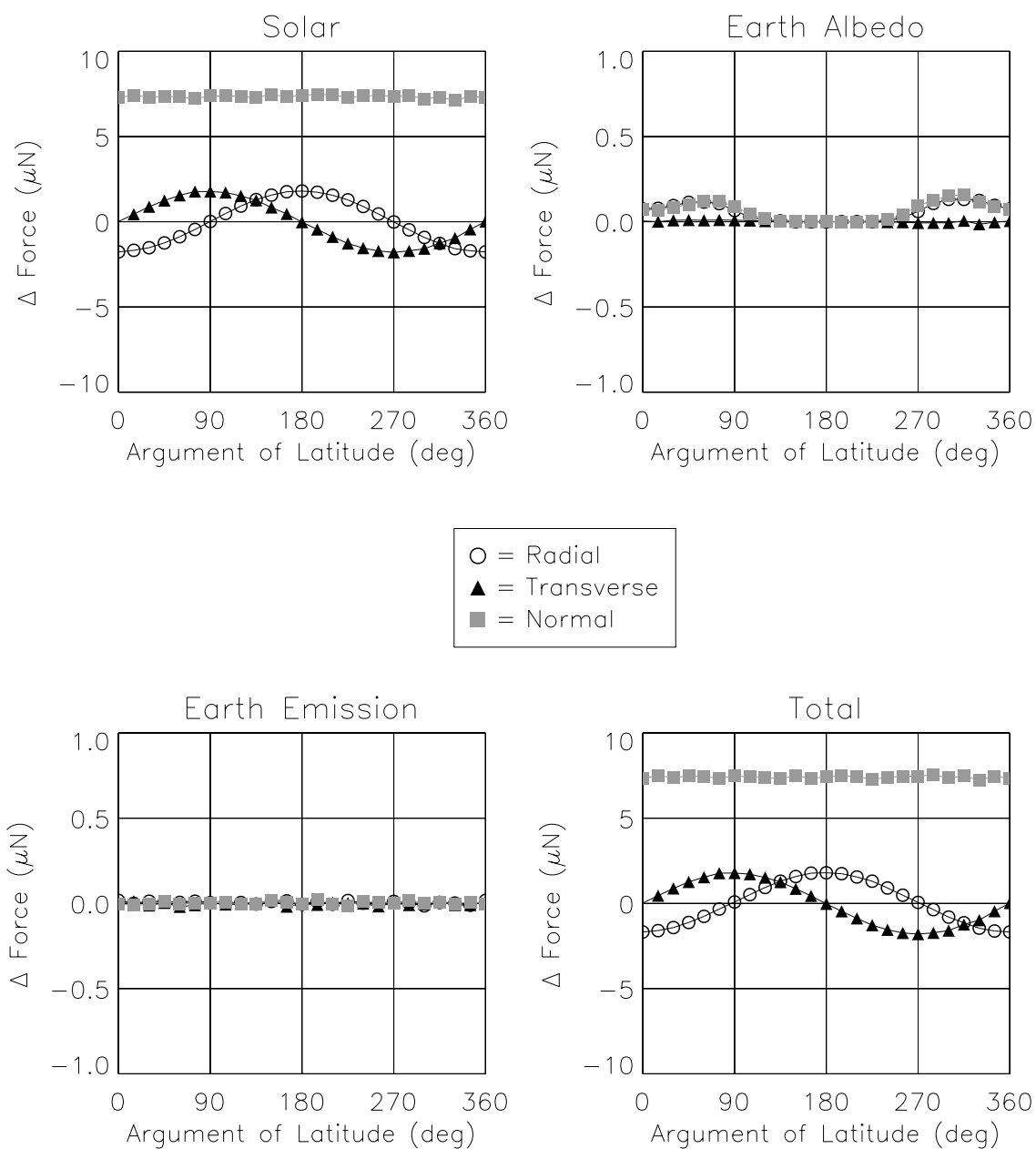


Figure 4.17. Case 21 EOL–BOL Radiation Force Differences: $\beta' = 0^\circ$, Yaw = 180° (Airplane), Articulating Arrays, Eclipsing Orbit



**Figure 4.18. Case 37 EOL-BOL Radiation Force Differences: $\beta' = 75^\circ$,
Yaw = 90° (Sailboat), Fixed Arrays, Non-Eclipsing Orbit**

Chapter 5

Macro-Model Parameter Determination

5.1 Direct Determination of Parameters

To compute the solar radiation pressure perturbation \vec{S} in Equation (1.12), ICESat precision orbit determination (POD) adopted the Box-Wing Solar Radiation Pressure (BWSRP) model of Equation (3.25), which yields the net force per unit mass:

$$\vec{S} = -f\gamma_{\odot} \frac{S_{\odot}}{c} \left(\frac{R}{r_{\odot}} \right)^2 \frac{1}{m} \times \sum_{k=1}^K A_k (\hat{n}_k \cdot \hat{s}_{\odot}) \left\{ (1 - \rho_k) \hat{s}_{\odot} + 2 \left[\frac{\delta_k}{3} + \rho_k (\hat{n}_k \cdot \hat{s}_{\odot}) \right] \hat{n}_k \right\} \quad (5.1)$$

where c represents the speed of light, and m denotes the mass of the satellite. Each of the K ($= 10$) surfaces of the satellite macro-model, illustrated in Figure 3.5, has an area A_k , a diffuse reflectivity δ_k , a specular reflectivity ρ_k , and a unit normal vector \hat{n}_k . Per Equation (2.27), the solar constant S_{\odot} — the total solar irradiance at the reference distance R — is scaled by the distance r_{\odot} , from the satellite to the Sun, along the incident $-\hat{s}_{\odot}$ direction. Based on the eclipse conditions for the conical shadow model described in Section 2.4, the scale factor f is obtained from Equation (3.17). An additional scale factor γ_{\odot} allows the resulting force to be adjusted, either by user input or through estimation.

The Earth radiation pressure perturbation \vec{E} in Equation (1.12) includes the effects of solar radiation reflected from the planet (i.e., albedo) and infrared

radiation emitted by it. To compute the combined net force per unit mass, ICESat POD adopted the Box-Wing Earth Radiation Pressure (BWERP) model of Equation (3.26):

$$\begin{aligned}
\vec{E} = & -\frac{2(1 - \cos \theta_{max})}{N} \frac{S_{\odot}}{c} \left(\frac{R}{R_{\odot}} \right)^2 \frac{1}{m} \\
& \times \sum_{i=1}^N \sum_{k=1}^K \left\{ A_k (\hat{n}_k \cdot \hat{s}_{\oplus}^i) \right. \\
& \times \left[\gamma_{\oplus}^a a_i (\hat{n}_{\oplus}^i \cdot \hat{R}_{\odot}) + \gamma_{\oplus}^e \frac{e_i}{4} \right] \\
& \times \left\{ (1 - \rho_k) \hat{s}_{\oplus}^i + 2 \left[\frac{\delta_k}{3} + \rho_k (\hat{n}_k \cdot \hat{s}_{\oplus}^i) \right] \hat{n}_k \right\} \Bigg\}
\end{aligned} \tag{5.2}$$

The parameters for each macro-model surface have the same values as those used in the BWSRP model. As described in Section 3.3.2, the additional summation over $N (= 19)$ Earth elements approximates the integral over its visible surface, which is bounded by θ_{max} . The reflected and the emitted radiation are both incident along the $-\hat{s}_{\oplus}^i$ direction, which extends from the center of the i -th element to the satellite. Using Equations (3.20) and (3.21), both can be expressed in terms of the incident solar radiation, scaled from the solar constant S_{\odot} by the distance R_{\odot} from the Earth to the Sun. The albedo a_i and the emissivity e_i of each element are obtained from Equations (2.36) and (2.37), respectively, based on the latitude of its center. The reflected radiation is further scaled by the dot product of the unit vector normal to the element \hat{n}_{\oplus}^i and the geocentric unit vector to the Sun \hat{R}_{\odot} . The two contributions to the resulting force can be adjusted separately, either by user input, or through estimation, of an albedo scale factor γ_{\oplus}^a or an emissivity scale factor γ_{\oplus}^e .

In both radiation pressure models, the axes of the Spacecraft Coordinate System (SCS), shown in Figure 3.5, define the body-fixed unit vectors \hat{n}_k normal to each face of the “box” in the macro-model. Those normal to the solar array “wings” are derived from the orientation angles described in Section 3.4.3, which can be obtained from either onboard telemetry or the nominal articulation model. This chapter concerns the determination of the remaining macro-model parameters — A_k , δ_k , and ρ_k . The first method calculates averaged values using data from the ICESat micro-model directly, while the second method estimates them based on a least-squares fit to the force history produced by the micro-model simulation discussed in Chapter 4.

5.1.1 Surface Areas

Conceptually, the area of each macro-model surface represents the combined, projected areas of the various components along the corresponding Vehicle Coordinate System (VCS) axis in the ICESat micro-model, depicted in Figure 4.4. Computing these projections for the complex shapes in the micro-model, and accounting for the overlap among them, however, is non-trivial. Antreasian (1992) proposed an alternate method for determining the surface areas in the TOPEX/Poseidon macro-model. Using the Thermal Radiation Analysis System (TRASYS), he oriented the Sun along each axis of the TOPEX/Poseidon micro-model, and simulated the incident heat rates. Summing over the nodes receiving radiation in a particular orientation, and dividing by the constant solar irradiance, produced the effective area of the desired macro-model surface.

This study applied the same approach to ICESat, first using the “Basic” option in the Orbit module of the Thermal Synthesizer System (TSS) to generate a 600-km circular orbit. After choosing a β' angle — defined in Section 3.4.2 — of 0° , to align the Sun with the orbit plane, the satellite micro-model was placed at the ascending node. Its attitude was then adjusted to point each of the body-fixed VCS axes, in turn, directly toward the Sun. Figures 5.1 through 5.6 illustrate these orientations, along with the coincident macro-model surfaces. With the Sun defined to be a point source of constant irradiance G_\odot , the TSS Heat Rate application computed the incident heat rate Q_\odot^j for each node, using Equation (4.22). The effective area for the k -th surface of the macro-model is given by

$$A_k = \frac{1}{G_\odot} \sum_{j=1}^{M_k} Q_\odot^j \quad (5.3)$$

where M_k denotes the number of nodes receiving radiation in a given orientation. The nodes that make up the surfaces in Figures 5.5 and 5.6 were separated to compute the individual areas of the $\pm z_{scs}$ faces and the solar array wings ($\pm y_{scs}$ SA, front/back). Table 5.1 summarizes the results for all of the macro-model surfaces.

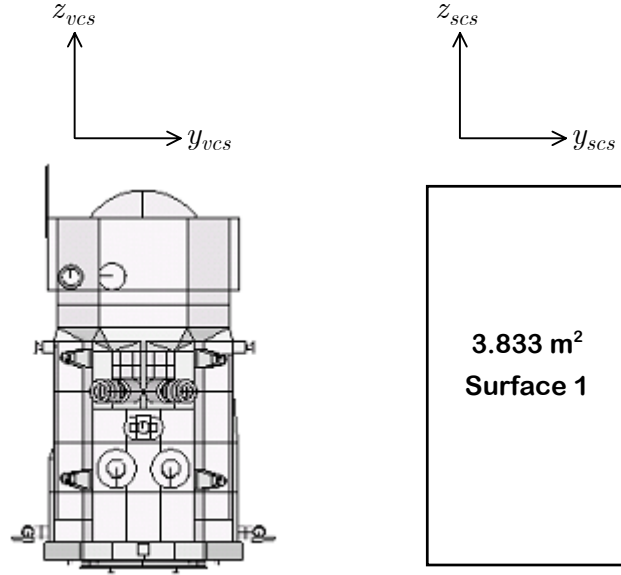


Figure 5.1. $+x$ Orientation: Micro-Model (left) and Macro-Model (right)

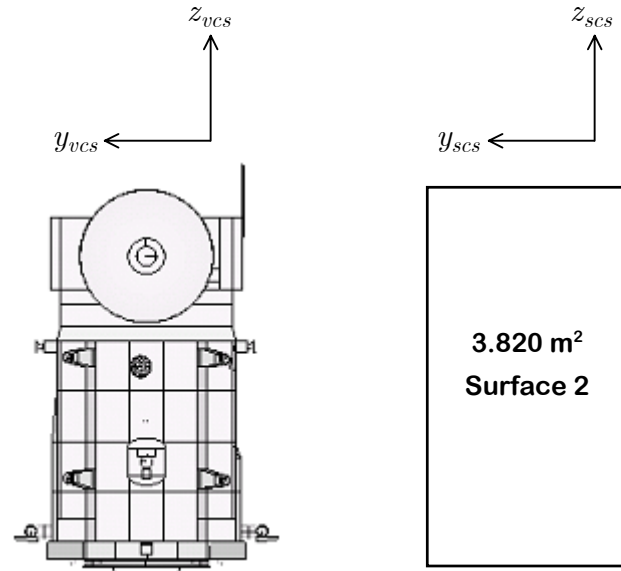


Figure 5.2. $-x$ Orientation: Micro-Model (left) and Macro-Model (right)

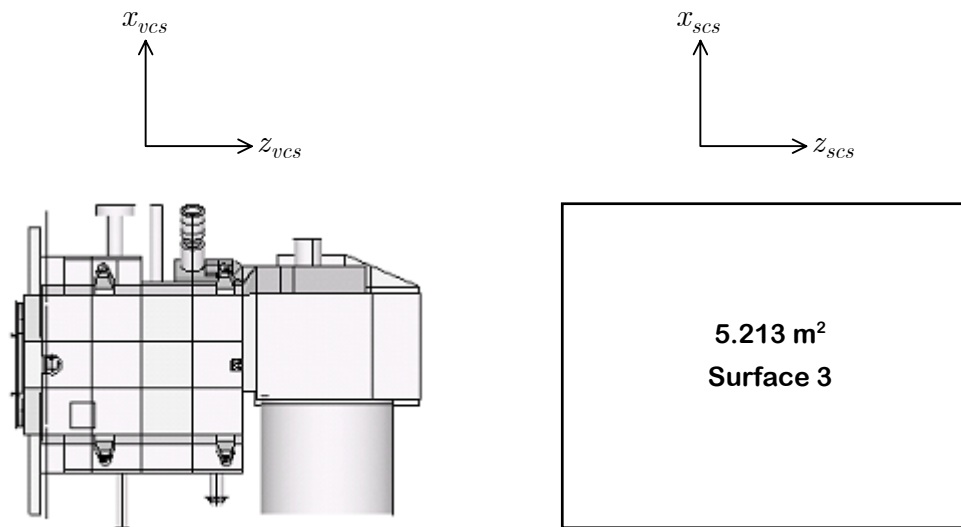


Figure 5.3. +y Orientation: Micro-Model (left) and Macro-Model (right)

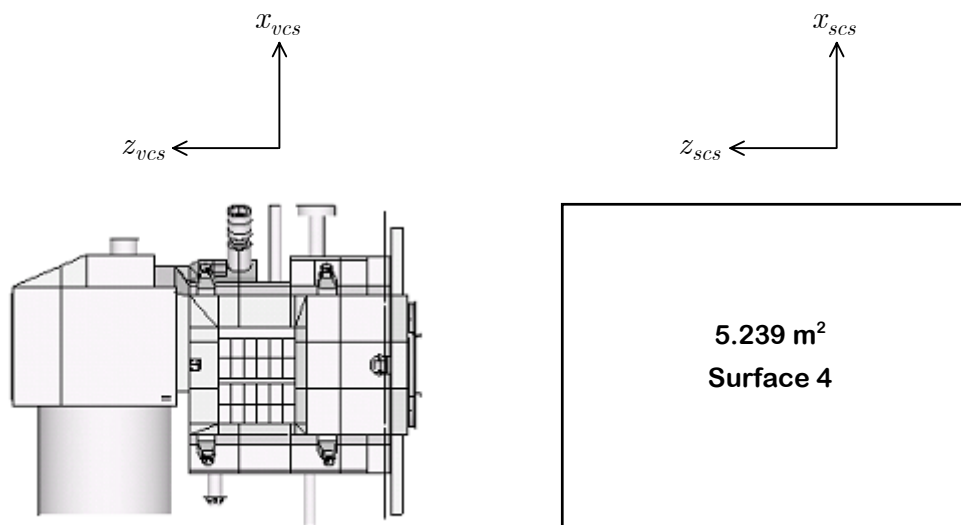


Figure 5.4. -y Orientation: Micro-Model (left) and Macro-Model (right)

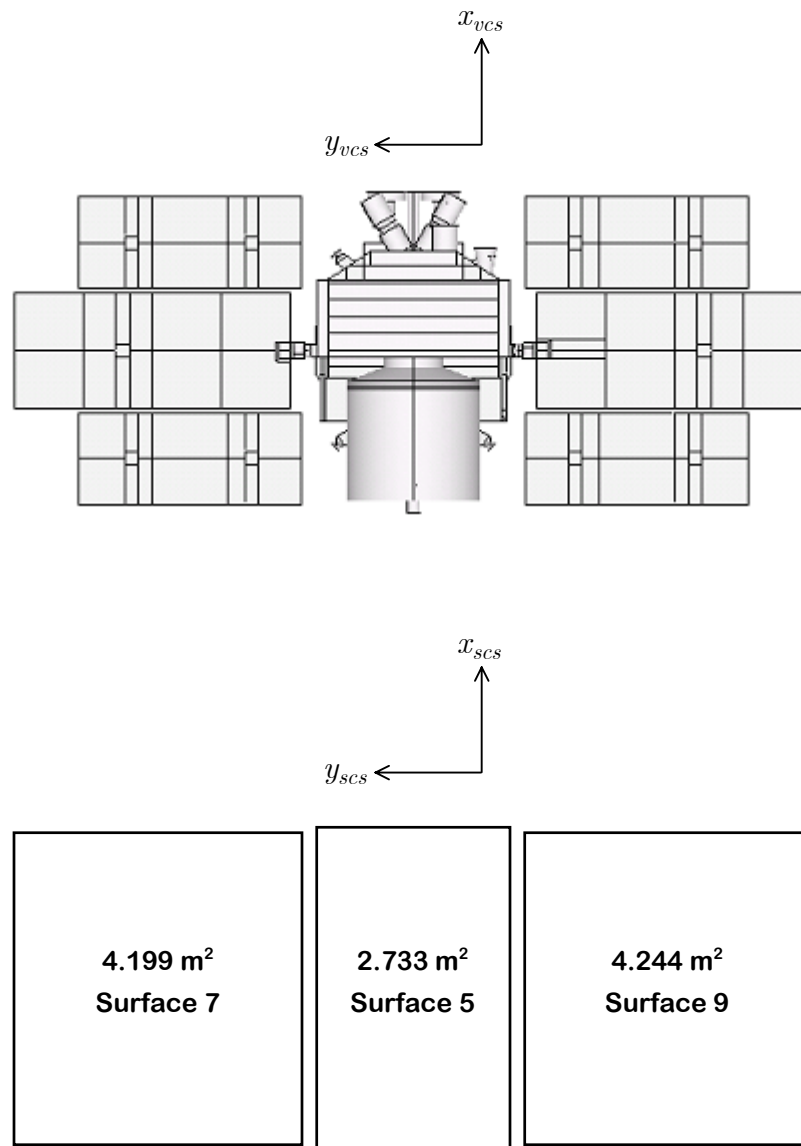


Figure 5.5. $+z$ Orientation: Micro-Model (top) and Macro-Model (bottom)

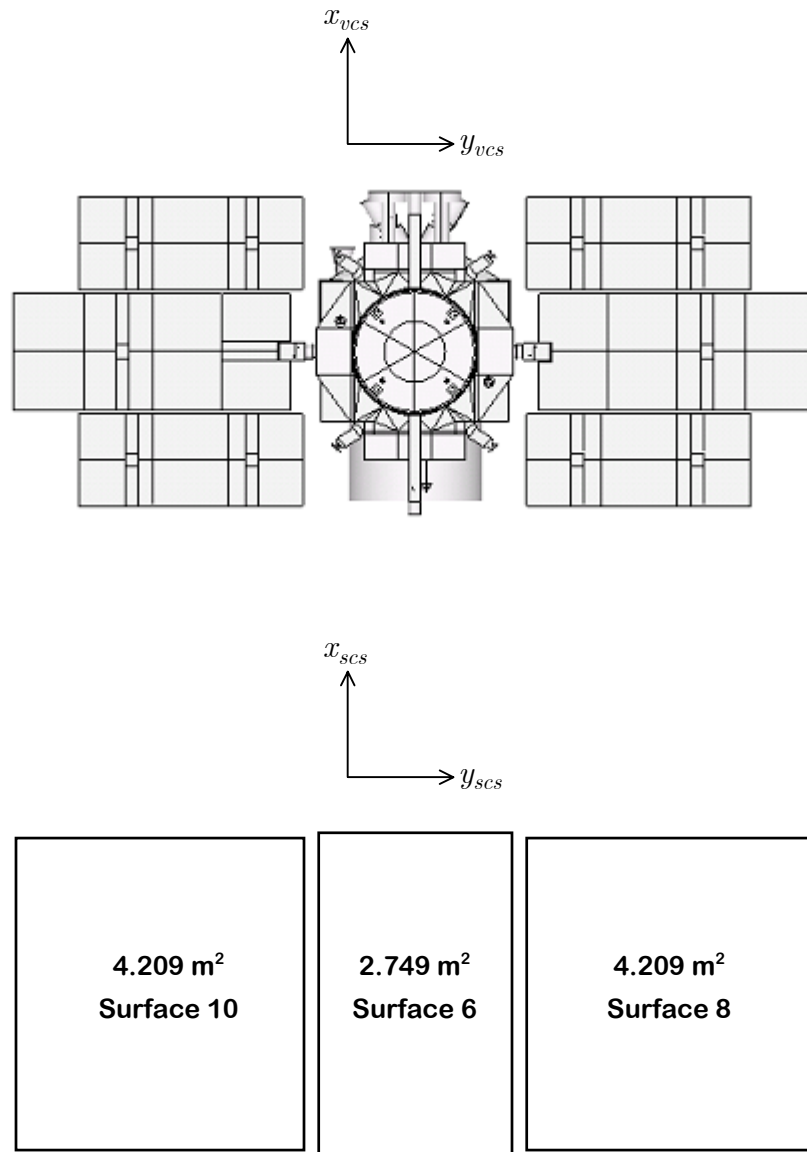


Figure 5.6. $-z$ Orientation: Micro-Model (top) and Macro-Model (bottom)

Surface k	Nodes M_k	Face (SCS)	A_k (m ²)
1	222	$+x$	3.833
2	176	$-x$	3.819
3	170	$+y$	5.212
4	205	$-y$	5.239
5	98	$+z$	2.733
6	193	$-z$	2.749
7	49	$+y$ SA (front)	4.199
8	45	$+y$ SA (back)	4.209
9	49	$-y$ SA (front)	4.244
10	45	$-y$ SA (back)	4.209

Table 5.1. Macro-Model Surface Areas

5.1.2 Surface Reflectivities

As discussed in the next section, Marshall and Luthcke (1994a) applied a least-squares fit to the solar radiation forces generated in a micro-model simulation to estimate the reflectivities for the TOPEX/Posidon macro-model. Although subsequent missions also developed macro-models for radiation pressure perturbations, they adopted simpler strategies for determining the reflectivities. For the Tracking and Data Relay Satellites (TDRS), Luthcke et al. (1997) derived them from area-weighted averages of the component absorptivities. Lemoine et al. (1999a) used a similar method for the Geosat Follow-On (GFO) mission, as did Lemoine et al. (1999b) for the Mars Global Surveyor (MGS) mission.

Under this approach, reflectivities for the ICESat macro-model surfaces were obtained from area-weighted averages of the nodal reflectivities in the micro-model. For solar radiation, including albedo, the specular and diffuse reflectivities for the k -th surface are

$$\rho_{\odot}^k = \frac{\sum_{j=1}^{M_k} A_j \xi_j (1 - \alpha_j)}{\sum_{j=1}^{M_k} A_j} \quad \delta_{\odot}^k = \frac{\sum_{j=1}^{M_k} A_j (1 - \xi_j) (1 - \alpha_j)}{\sum_{j=1}^{M_k} A_j} \quad (5.4)$$

where A_j represents the nodal area, and M_k retains the same value for each surface as shown in Table 5.1. Using Equations (4.35), the specular reflectivity ρ_{\odot}^j and the diffuse reflectivity δ_{\odot}^j of each node have been expressed in terms of its absorptivity α_j and specularity ξ_j , from which they were originally derived.

Similarly, for the infrared radiation emitted by the Earth, the specular and diffuse reflectivities for the k -th surface are

$$\rho_{\oplus}^k = \frac{\sum_{j=1}^{M_k} A_j \xi_j (1 - \varepsilon_j)}{\sum_{j=1}^{M_k} A_j} \quad \delta_{\oplus}^k = \frac{\sum_{j=1}^{M_k} A_j (1 - \xi_j) (1 - \varepsilon_j)}{\sum_{j=1}^{M_k} A_j} \quad (5.5)$$

In this case, Equations (4.39) have been used to express the specular reflectivity ρ_{\oplus}^j and the diffuse reflectivity δ_{\oplus}^j of each node in terms of its emissivity ε_j and specularity ξ_j , from which they were originally derived.

Surface k	Face (SCS)	Solar		Infrared	
		ρ_{\odot}^k	δ_{\odot}^k	ρ_{\oplus}^k	δ_{\oplus}^k
1	$+x$	0.040	0.160	0.075	0.299
2	$-x$	0.066	0.263	0.096	0.385
3	$+y$	0.043	0.172	0.094	0.378
4	$-y$	0.043	0.173	0.099	0.396
5	$+z$	0.042	0.168	0.090	0.359
6	$-z$	0.045	0.180	0.114	0.458
7	$+y$ SA (front)	0.206	0.006	0.323	0.005
8	$+y$ SA (back)	0.017	0.069	0.167	0.668
9	$-y$ SA (front)	0.206	0.006	0.323	0.005
10	$-y$ SA (back)	0.017	0.069	0.167	0.668

Table 5.2. Area-Weighted Average Reflectivities

Table 5.2 summarizes the results for all of the macro-model surfaces. Neither Equation (5.1) nor (5.2), however, distinguishes between solar and infrared reflectivities. Therefore, the values obtained from Equations (5.4) and (5.5) must be combined to yield a single specular reflectivity and a single diffuse reflectivity for each surface,

$$\rho^k = \chi \rho_{\odot}^k + (1 - \chi) \rho_{\oplus}^k \quad \delta^k = \chi \delta_{\odot}^k + (1 - \chi) \delta_{\oplus}^k \quad (5.6)$$

The parameter χ may be arbitrarily chosen, but is defined such that $0 \leq \chi \leq 1$. Chapter 6 examines three particular cases in its evaluation of the post-launch macro-model performance: (1) $\chi = 0$, which returns the infrared values in Table 5.2; (2) $\chi = 1$, which returns the solar values; and (3) $\chi = 0.5$, which yields a numerical average of the solar and infrared values.

5.2 Estimation of Parameters

Prior to the launch of TOPEX/Poseidon, Marshall and Luthcke (1994a) obtained values for its macro-model parameters from a Bayesian least-squares fit to the solar radiation forces predicted by the micro-model simulation of Antreasian (1992). This method makes use of an *a priori* covariance to constrain estimated parameters that may not be observable independently, or that would otherwise assume physically unrealistic values. In an earlier study for ICESat, Webb et al. (2001) employed a similar strategy, although the fit included both solar and Earth radiation forces. Rather than relying on this indirect manipulation of the *a priori* covariance to achieve a feasible solution, the current study incorporates linear equality and inequality constraints directly into the least-squares formulation.

The following three sections detail the radiation force model adapted from Equations (5.1) and (5.2), its linearization, and the constraints imposed on the macro-model parameters. The remaining three sections outline the solution to the consequent least-squares problem, as proposed by Haskell and Hanson (1981), beginning with the elimination of the equality constraints. The reduced problem is then converted to an equivalent least distance problem, and ultimately, solved using a dual approach.

5.2.1 Radiation Force Model

Within the Multi-Satellite Orbit Determination Program (MSODP), the models of Equations (5.1) and (5.2) produce net forces (per unit mass) in the International Celestial Reference Frame (ICRF). In each case, however, the coordinate system of the resultant force depends only on the one used to express the unit normal vectors \hat{n}_k , and the applicable unit source vector(s): \hat{s}_\odot , in Equation (5.1), and \hat{s}_\oplus^i , in Equation (5.2). As described in Chapter 4, the micro-model simulation initially computed and summed the nodal radiation forces in the TSS body-fixed VCS. These net forces were then rotated to the TSS Orbit Coordinate System (OCS), a Radial-Transverse-Normal (RTN) frame shown in Figure 4.6.

To fit the “observed” micro-model forces, the unit normal vectors of the macro-model and the unit source vectors are expressed with respect to the TSS VCS, which is identical to the SCS. Assuming the scale factor γ_\odot to be 1 in Equation (5.1) and multiplying both sides by the satellite mass m , the solar radiation force acting on the macro-model becomes

$$\vec{F}_\odot = -f \frac{G_\odot}{c} \sum_{k=1}^{K'} A_k (\hat{n}_k \cdot \hat{s}_\odot) \left\{ (1 - \rho_k) \hat{s}_\odot + 2 \left[\frac{\delta_k}{3} + \rho_k (\hat{n}_k \cdot \hat{s}_\odot) \right] \hat{n}_k \right\} \quad (5.7)$$

A constant solar irradiance G_\odot replaces the seasonal one from Equation (2.27). The scale factor f and the VCS satellite-to-Sun vector \hat{s}_\odot are both obtained from the micro-model simulation output. Referred to as the shadow factor in TSS, the former was determined from the eclipse conditions for the cylindrical shadow model given by Equation (3.16), and applied during the computation of Equation

(4.37). Lastly, as the solar array wings share the same orientation at all times, their parameters are not independently observable. Thus, for the purposes of this estimation algorithm *only*, the number of macro-model surfaces is reduced from K ($= 10$) to K' ($= 8$), by combining the two arrays into one two-sided surface.

Isolating the emissivity contribution in Equation (5.2) and multiplying both sides by m , the total Earth emission force acting on the macro-model becomes

$$\begin{aligned} \vec{F}_{\oplus,e} = & -\frac{(1 - \cos \theta_{max}) G_{\odot}}{2N} \frac{1}{c} \\ & \times \sum_{i=1}^N \sum_{k=1}^{K'} e_i A_k (\hat{n}_k \cdot \hat{s}_{\oplus}^i) \left\{ (1 - \rho_k) \hat{s}_{\oplus}^i + 2 \left[\frac{\delta_k}{3} + \rho_k (\hat{n}_k \cdot \hat{s}_{\oplus}^i) \right] \hat{n}_k \right\} \end{aligned} \quad (5.8)$$

The scale factor γ_{\oplus}^e is assumed to be 1, and again, a constant solar irradiance G_{\odot} is introduced. Using the method developed by Knocke (1989), the satellite-to-segment unit vectors \hat{s}_{\oplus}^i are first defined in the TSS Reference Coordinate System (RCS) of Figure 4.6, which is essentially identical to the ICRF. They are then rotated to the VCS by applying the appropriate transformation from the micro-model simulation output.

Similarly, isolating the albedo contribution in Equation (5.2) and multiplying both sides by m , the total Earth albedo force acting on the macro-model becomes

$$\begin{aligned} \vec{F}_{\oplus,a} = & -\frac{2(1 - \cos \theta_{max}) G_{\odot}}{N} \frac{1}{c} \\ & \times \sum_{i=1}^N \sum_{k=1}^{K'} a_i A_k (\hat{n}_k \cdot \hat{s}_{\oplus}^i) (\hat{n}_{\oplus}^i \cdot \hat{R}_{\odot}) \left\{ (1 - \rho_k) \hat{s}_{\oplus}^i + 2 \left[\frac{\delta_k}{3} + \rho_k (\hat{n}_k \cdot \hat{s}_{\oplus}^i) \right] \hat{n}_k \right\} \end{aligned} \quad (5.9)$$

The scale factor γ_{\oplus}^a is assumed to be 1, and as before, a constant solar irradiance G_{\odot} is used. As part of the computation of the satellite-to-segment unit vectors \hat{s}_{\oplus}^i , the method developed by Knocke (1989) also defines the unit vectors normal to the Earth elements \hat{n}_{\oplus}^i in the RCS. The unit vector to the Sun \hat{R}_{\odot} is derived in the same frame, from the right ascension and declination output by the micro-model simulation.

Summing the solar and Earth contributions in the VCS, and rotating the result to the OCS, yields the total radiation force acting on the macro-model,

$$\vec{F}_{ocs} = T_{ocs}^{ocs} \left(\vec{F}_{\odot} + \vec{F}_{\oplus,e} + \vec{F}_{\oplus,a} \right) \quad (5.10)$$

After substituting Equations (5.7), (5.8), and (5.9), this can be expressed as

$$\vec{F}_{ocs} = -T_{ocs}^{ocs} \frac{G_{\odot}}{c} \sum_{k=1}^{K'} A_k \left(\vec{P}_k + \vec{Q}_k \delta_k + \vec{R}_k \rho_k \right) \quad (5.11)$$

where \vec{P}_k represents the absorbed component, which acts along a linear combination of the \hat{s}_{\odot} and \hat{s}_{\oplus}^i source vectors,

$$\begin{aligned} \vec{P}_k &= f(\hat{n}_k \cdot \hat{s}_{\odot}) \hat{s}_{\odot} \\ &+ \frac{2(1 - \cos \theta_{max})}{N} \sum_{i=1}^N (\hat{n}_k \cdot \hat{s}_{\oplus}^i) \left[a_i (\hat{n}_{\oplus}^i \cdot \hat{r}_{\odot}) + \frac{e_i}{4} \right] \hat{s}_{\oplus}^i \end{aligned} \quad (5.12)$$

Additionally, in Equation (5.11), \vec{Q}_k represents the diffuse component, which acts along the surface normal vector \hat{n}_k ,

$$\begin{aligned}\vec{Q}_k &= \frac{2}{3} \left\{ f(\hat{n}_k \cdot \hat{s}_\odot) \right. \\ &\quad \left. + \frac{2(1 - \cos \theta_{max})}{N} \sum_{i=1}^N (\hat{n}_k \cdot \hat{s}_\oplus^i) \left[a_i (\hat{n}_\oplus^i \cdot \hat{r}_\odot) + \frac{e_i}{4} \right] \right\} \hat{n}_k\end{aligned}\tag{5.13}$$

Finally, in Equation (5.11), \vec{R}_k represents the specular component, which acts along a linear combination of the surface normal vector \hat{n}_k , and the \hat{s}_\odot and \hat{s}_\oplus^i source vectors,

$$\begin{aligned}\vec{R}_k &= 2f(\hat{n}_k \cdot \hat{s}_\odot) \left[(\hat{n}_k \cdot \hat{s}_\odot) \hat{n}_k - \hat{s}_\odot \right] \\ &\quad + \frac{2(1 - \cos \theta_{max})}{N} \sum_{i=1}^N (\hat{n}_k \cdot \hat{s}_\oplus^i) \left[a_i (\hat{n}_\oplus^i \cdot \hat{r}_\odot) + \frac{e_i}{4} \right] \left[2(\hat{n}_k \cdot \hat{s}_\oplus^i) \hat{n}_k - \hat{s}_\oplus^i \right]\end{aligned}\tag{5.14}$$

5.2.2 Linearized Radiation Force Model

Equation (5.11) represents a system of non-linear scalar equations for the three components of the total radiation force. Dropping the *ocs* subscript, it can be expressed, functionally, as

$$\vec{F} = \vec{F}(A_k, \delta_k, \rho_k)\tag{5.15}$$

Expanding the right-hand side of this expression in a Taylor series about a set of *a priori* macro-model parameters $(A_k^*, \delta_k^*, \rho_k^*)$ yields

$$\begin{aligned}\vec{F} &= \underbrace{\vec{F}(A_k^*, \delta_k^*, \rho_k^*)}_{\vec{F}^*} + \sum_{k=1}^{K'} \left[\frac{\partial \vec{F}}{\partial A_k} \right]^* \underbrace{(A_k - A_k^*)}_{\Delta A_k} \\ &\quad + \sum_{k=1}^{K'} \left[\frac{\partial \vec{F}}{\partial \delta_k} \right]^* \underbrace{(\delta_k - \delta_k^*)}_{\Delta \delta_k} + \sum_{k=1}^{K'} \left[\frac{\partial \vec{F}}{\partial \rho_k} \right]^* \underbrace{(\rho_k - \rho_k^*)}_{\Delta \rho_k} + \dots\end{aligned}\tag{5.16}$$

Neglecting the higher-order terms, and allowing \vec{F}_l and \vec{F}_l^* to denote, respectively, the l -th “observed” micro-model force and the corresponding “computed” macro-model force, a system of three *linear* scalar equations can be obtained:

$$\vec{f}_l = \vec{F}_l - \vec{F}_l^* = H_l \vec{x} \quad (5.17)$$

The state vector \vec{x} in this linearized problem consists of the corrections to be estimated and applied to the *a priori* macro-model parameters. From Equation (5.16),

$$\vec{x} = \left[\Delta A_1 \quad \Delta \delta_1 \quad \Delta \rho_1 \quad \cdots \quad \Delta A_{K'} \quad \Delta \delta_{K'} \quad \Delta \rho_{K'} \right]^T \quad (5.18)$$

As each macro-model surface has three parameters, the total number of state vector components is $n = 3 \times K' = 3 \times 8 = 24$. The 3×24 H_l matrix in Equation (5.17) contains the partial derivatives appearing in Equation (5.16), evaluated using the *a priori* macro-model parameters,

$$H_l = \left[\frac{\partial \vec{F}_l^*}{\partial A_1} \quad \frac{\partial \vec{F}_l^*}{\partial \delta_1} \quad \frac{\partial \vec{F}_l^*}{\partial \rho_1} \quad \cdots \quad \frac{\partial \vec{F}_l^*}{\partial A_{K'}} \quad \frac{\partial \vec{F}_l^*}{\partial \delta_{K'}} \quad \frac{\partial \vec{F}_l^*}{\partial \rho_{K'}} \right] \quad (5.19)$$

Differentiating Equation (5.11) with respect to each surface area A_k yields

$$\frac{\partial \vec{F}}{\partial A_k} = -T_{vcs}^{ocs} \frac{G_\odot}{c} \left(\vec{P}_k + \vec{Q}_k \delta_k + \vec{R}_k \rho_k \right) \quad (5.20)$$

Similarly, the derivatives with respect to each diffuse reflectivity δ_k , and each specular reflectivity ρ_k , are

$$\frac{\partial \vec{F}}{\partial \delta_k} = -T_{vcs}^{ocs} \frac{G_{\odot}}{c} A_k \vec{Q}_k \quad \frac{\partial \vec{F}}{\partial \rho_k} = -T_{vcs}^{ocs} \frac{G_{\odot}}{c} A_k \vec{R}_k \quad (5.21)$$

The \vec{P}_k , \vec{Q}_k , and \vec{R}_k vectors in Equations (5.20) and (5.21) are obtained from Equations (5.12), (5.13), and (5.14), respectively.

5.2.3 Equality and Inequality Constraints

Applying Equation (5.17) to each of the m vector observations from the micro-model simulation yields

$$\begin{aligned} \vec{f}_1 &= H_1 \vec{x} \\ \vec{f}_2 &= H_2 \vec{x} \\ &\vdots \\ \vec{f}_m &= H_m \vec{x} \end{aligned} \quad (5.22)$$

Defining

$$\vec{f} = \begin{bmatrix} \vec{f}_1 \\ \vec{f}_2 \\ \vdots \\ \vec{f}_m \end{bmatrix} \quad H = \begin{bmatrix} H_1 \\ H_2 \\ \vdots \\ H_m \end{bmatrix} \quad (5.23)$$

Equation (5.22) can be written as

$$\vec{f} = H \vec{x} \quad (5.24)$$

Given that each observation has three scalar components, \vec{f} is a $3m \times 1$ vector, and H is a $3m \times 24$ matrix. Due to the omission of the higher-order terms in Equation (5.16), however, the linear system on the right-hand side of Equation

(5.24) only approximates the observation on the left-hand side. The basic linear least-squares problem seeks to determine the estimate \hat{x} that minimizes the magnitude of the residual vector for Equation (5.24), defined to be $\vec{f} - H\vec{x}$. Mathematically, this can be expressed as

$$\min \left| \vec{f} - H\vec{x} \right| \quad (5.25)$$

In the absence of restrictions on \vec{x} , however, the macro-model parameters can assume physically unrealistic, or simply undesirable, values. This section details the equality and inequality constraints on the macro-model parameters that define a feasible solution, and derives the corresponding constraints on the components of \vec{x} in the linearized problem.

Equality Constraints

Table 5.1 shows that the $+x$ and $-x$ faces in the macro-model have slightly different areas, as obtained from the heat-rate simulation. Geometrically, however, the area projected along these opposing axes should be the same. Therefore, it is desired that $A_1 = A_2$, or

$$A_1 - A_2 = 0 \quad (5.26)$$

The same holds true for the other faces, along the $\pm y$ and $\pm z$ axes, in the box portion of the macro-model, as well as for the front and back of the single wing. Noting that Equation (5.16) defines $\Delta A_k = A_k - A_k^*$, Equation (5.26) can be written as

$$A_1^* + \Delta A_1 - (A_2^* + \Delta A_2) = 0 \quad (5.27)$$

Rearranging Equation (5.27) yields

$$\Delta A_1 - \Delta A_2 = A_2^* - A_1^* \quad (5.28)$$

which constitutes a constraint on ΔA_1 and ΔA_2 , in the linearized problem, equivalent to the original constraint on A_1 and A_2 , given in Equation (5.26). Applying the same approach to the other pairs of areas leads to a set of four equality constraints for the K' ($= 8$) surfaces,

$$B\vec{x} = \vec{d} \quad (5.29)$$

Based on the ordering of the state vector in Equation (5.18), the 4×24 matrix B and the 4×1 vector \vec{d} are defined to be

$$B = \begin{bmatrix} B_1 & 0 & 0 & 0 \\ 0 & B_2 & 0 & 0 \\ 0 & 0 & B_3 & 0 \\ 0 & 0 & 0 & B_4 \end{bmatrix} \quad \vec{d} = \begin{bmatrix} A_2^* - A_1^* \\ A_4^* - A_3^* \\ A_6^* - A_5^* \\ A_8^* - A_7^* \end{bmatrix} \quad (5.30)$$

where

$$B_1 = B_2 = B_3 = B_4 = \begin{bmatrix} 1 & 0 & 0 & -1 & 0 & 0 \end{bmatrix} \quad (5.31)$$

Inequality Constraints

The inequality constraints are imposed for two different reasons. First, since the macro-model surface areas are also used to compute the atmospheric drag perturbation \vec{D} , in Equation (1.12), they should not lose their physical

significance. Consequently, in addition to the equality constraints, each must satisfy

$$A_k^{min} \leq A_k \leq A_k^{max} \quad (5.32)$$

Through the values chosen for the limits, the area of each surface can be constrained so that it remains within a desired tolerance of the *a priori* value. Separating the upper and lower constraints in Equation (5.32),

$$A_k \geq A_k^{min} \quad A_k \leq A_k^{max} \quad (5.33)$$

As noted before, Equation (5.16) defines $\Delta A_k = A_k - A_k^*$, so the inequalities become

$$A_k^* + \Delta A_k \geq A_k^{min} \quad A_k^* + \Delta A_k \leq A_k^{max} \quad (5.34)$$

Rearranging yields

$$\Delta A_k \geq A_k^{min} - A_k^* \quad -\Delta A_k \geq A_k^* - A_k^{max} \quad (5.35)$$

which are the constraints on ΔA_k , in the linearized problem, equivalent to the original constraints on A_k , given in Equation (5.33).

Second, by definition, the diffuse and specular reflectivities for each macro-model surface must have values between 0 and 1,

$$0 \leq \delta_k \leq 1 \quad 0 \leq \rho_k \leq 1 \quad (5.36)$$

Separating the upper and lower constraints,

$$\delta_k \geq 0 \quad \delta_k \leq 1 \quad \rho_k \geq 0 \quad \rho_k \leq 1 \quad (5.37)$$

Equation (5.16) defines $\Delta\delta_k = \delta_k - \delta_k^*$, which allows the inequalities for the diffuse reflectivities to be written as

$$\delta_k^* + \Delta\delta_k \geq 0 \quad \delta_k^* + \Delta\delta_k \leq 1 \quad (5.38)$$

Rearranging yields

$$\Delta\delta_k \geq -\delta_k^* \quad -\Delta\delta_k \geq \delta_k^* - 1 \quad (5.39)$$

which are the constraints on $\Delta\delta_k$, in the linearized problem, equivalent to the original constraints on δ_k , given in Equation (5.37). Since Equation (5.16) also defines $\Delta\rho_k = \rho_k - \rho_k^*$, the inequalities for the specular reflectivities, in Equation (5.37), can be written as

$$\rho_k^* + \Delta\rho_k \geq 0 \quad \rho_k^* + \Delta\rho_k \leq 1 \quad (5.40)$$

Rearranging yields

$$\Delta\rho_k \geq -\rho_k^* \quad -\Delta\rho_k \geq \rho_k^* - 1 \quad (5.41)$$

which are the constraints on $\Delta\rho_k$, in the linearized problem, equivalent to the original constraints on ρ_k , given in Equation (5.37). Furthermore, the total reflectivity for each macro-model surface must also lie between 0 and 1,

$$0 \leq \delta_k + \rho_k \leq 1 \quad (5.42)$$

The lower inequality is automatically satisfied provided that the constraints of Equation (5.37) are met. The remaining constraint is

$$\delta_k + \rho_k \leq 1 \quad (5.43)$$

which, based on the definitions in Equation (5.16), can be written as

$$\delta_k^* + \Delta\delta_k + \rho_k^* + \Delta\rho_k \leq 1 \quad (5.44)$$

Rearranging yields

$$-\Delta\delta_k - \Delta\rho_k \geq \delta_k^* + \rho_k^* - 1 \quad (5.45)$$

which is the final, combined constraint on $\Delta\delta_k$ and $\Delta\rho_k$, in the linearized problem, equivalent to the constraint on δ_k and ρ_k , given in Equation (5.43).

Together, Equations (5.35), (5.39), (5.41), and (5.45) include seven inequality constraints for each of the K' ($= 8$) macro-model surfaces, yielding a total set of 56 to be satisfied,

$$C\vec{x} \geq \vec{h} \quad (5.46)$$

Based on the ordering of the state vector in Equation (5.18), the 56×24 matrix C and the 56×1 vector \vec{h} are defined to be

$$C = \begin{bmatrix} C_1 & 0 & 0 \\ 0 & \ddots & 0 \\ 0 & 0 & C_8 \end{bmatrix} \quad \vec{h} = \begin{bmatrix} \vec{h}_1 \\ \vdots \\ \vec{h}_8 \end{bmatrix} \quad (5.47)$$

where

$$C_k = \begin{bmatrix} 1 & 0 & 0 \\ -1 & 0 & 0 \\ 0 & 1 & 0 \\ 0 & -1 & 0 \\ 0 & 0 & 1 \\ 0 & 0 & -1 \\ 0 & -1 & -1 \end{bmatrix} \quad \vec{h}_k = \begin{bmatrix} A_k^{min} - A_k^* \\ A_k^* - A_k^{max} \\ -\delta_k^* \\ \delta_k^* - 1 \\ -\rho_k^* \\ \rho_k^* - 1 \\ \delta_k^* + \rho_k^* - 1 \end{bmatrix} \quad k = 1, \dots, 8 \quad (5.48)$$

5.2.4 Elimination of Equality Constraints

Combined, Equations (5.25), (5.29), and (5.46) form a least-squares problem with equality and inequality constraints, a problem designated “LSEI” by Haskell and Hanson (1981):

$$\begin{aligned} \min \quad & \left| \vec{f} - H\vec{x} \right| \\ & B\vec{x} = \vec{d} \\ & C\vec{x} \geq \vec{h} \end{aligned} \quad (5.49)$$

Their solution begins with the elimination of the equality constraints. First, they computed an orthogonal decomposition of B ,

$$B = Q\Lambda V^T \quad (5.50)$$

Based on Equations (5.30) and (5.31), Q and V are 4×4 and 24×24 orthogonal matrices, respectively. The 4×24 matrix Λ has the form

$$\Lambda = \begin{bmatrix} L & 0 \\ 0 & 0 \end{bmatrix} \quad (5.51)$$

where L is an 4×4 lower triangular matrix. Substituting Equation (5.50) into the equality constraint in Equation (5.49), and pre-multiplying both sides by Q^T , yields

$$\Lambda V^T \vec{x} = Q^T \vec{d} \quad (5.52)$$

Defining

$$V^T \vec{x} = \vec{y} = \begin{bmatrix} \vec{y}_1 \\ \vec{y}_2 \end{bmatrix} \quad Q^T \vec{d} = \vec{g} = \begin{bmatrix} \vec{g}_1 \\ \vec{g}_2 \end{bmatrix} \quad (5.53)$$

and substituting Equation (5.51) for Λ , Equation (5.52) becomes

$$\begin{bmatrix} L & 0 \\ 0 & 0 \end{bmatrix} \begin{bmatrix} \vec{y}_1 \\ \vec{y}_2 \end{bmatrix} = \begin{bmatrix} \vec{g}_1 \\ \vec{g}_2 \end{bmatrix} \quad (5.54)$$

While the 20×1 vector \vec{y}_2 is arbitrary, a unique solution \hat{y}_1 is found by solving

$$L \vec{y}_1 = \vec{g}_1 \quad (5.55)$$

where both \vec{y}_1 and \vec{g}_1 are 4×1 vectors. From Equation (5.53), $\vec{x} = V \vec{y}$. Thus, all solutions to the original minimization problem have the form

$$\hat{x} = V \begin{bmatrix} \hat{y}_1 \\ \vec{y}_2 \end{bmatrix} \quad (5.56)$$

Partitioning V into a 24×4 matrix V_1 and a 24×20 matrix V_2 , and expanding, yields

$$\hat{x} = \begin{bmatrix} V_1 & V_2 \end{bmatrix} \begin{bmatrix} \hat{y}_1 \\ \vec{y}_2 \end{bmatrix} = V_1 \hat{y}_1 + V_2 \vec{y}_2 \quad (5.57)$$

Substituting this expression for \hat{x} in Equation (5.49) confirms that the equality constraints have been satisfied, leaving a reduced least-squares problem, now with 20 unknowns, subject only to inequality constraints:

$$\begin{aligned} \min \quad & \left| \vec{f}_r - \tilde{H} \vec{y}_2 \right| \\ & \tilde{C} \vec{y}_2 \geq \vec{h}_r \end{aligned} \quad (5.58)$$

where the $3m \times 20$ matrix $\tilde{H} = HV_2$; the $3m \times 1$ vector $\vec{f}_r = \vec{f} - HV_1 \hat{y}_1$; the 56×20 matrix $\tilde{C} = CV_2$; and the 56×1 vector $\vec{h}_r = \vec{h} - CV_1 \hat{y}_1$.

5.2.5 Transformation to Least Distance Problem

Haskell and Hanson (1981) next converted the problem posed by Equation (5.58), which they denoted “LSI”, into the least distance problem. This transformation begins with the orthogonal decomposition of \tilde{H} ,

$$\tilde{H} = R\Gamma W^T \quad (5.59)$$

where R and W are $3m \times 3m$ and 20×20 orthogonal matrices, respectively. The $3m \times 20$ matrix Γ has the form

$$\Gamma = \begin{bmatrix} U & 0 \\ 0 & 0 \end{bmatrix} \quad (5.60)$$

where U is a 20×20 upper-triangular matrix. Substituting Equation (5.59) for \tilde{H} , the residual vector in Equation (5.58) becomes

$$\vec{f}_r - R\Gamma W^T \vec{y}_2 \quad (5.61)$$

Since R is an orthogonal matrix, pre-multiplying both terms of this vector by R^T does not change its magnitude,

$$R^T \vec{f}_r - \Gamma W^T \vec{y}_2 \quad (5.62)$$

Substituting Equation (5.60) for Γ ,

$$\begin{bmatrix} R_1^T \\ R_2^T \end{bmatrix} \vec{f}_r - \begin{bmatrix} U & 0 \\ 0 & 0 \end{bmatrix} \begin{bmatrix} W_1^T \\ W_2^T \end{bmatrix} \vec{y}_2 \quad (5.63)$$

where R^T and W^T have been partitioned by rows. After expanding the resulting vector in Equation (5.63), the square of its magnitude can be expressed as

$$\left| R_1^T \vec{f}_r - U W_1^T \vec{y}_2 \right|^2 + \left| R_2^T \vec{f}_r \right|^2 \quad (5.64)$$

Defining

$$\vec{z} = U W_1^T \vec{y}_2 - R_1^T \vec{f}_r \quad (5.65)$$

Equation (5.64) becomes

$$|\vec{z}|^2 + \left| R_1^T \vec{f}_r \right|^2 \quad (5.66)$$

Since the second term is only an additive constant, the overall minimum is achieved by minimizing $|\vec{z}|^2$, or equivalently, $|\vec{z}|$. Solving Equation (5.65) for \vec{y}_2 , and substituting the result into the inequality constraint of Equation (5.58), yields the least distance problem:

$$\begin{aligned} \min \quad & |\vec{z}| \\ & \tilde{C}'\vec{z} \geq \vec{h}'_r \end{aligned} \tag{5.67}$$

Like \vec{y}_2 , \vec{z} is a 20×1 vector. The 56×20 matrix $\tilde{C}' = \tilde{C}W_1U^{-1}$, and the 56×1 vector $\vec{h}'_r = \vec{h}_r - \tilde{C}W_1U^{-1}R_1^T\vec{f}_r$.

5.2.6 Solution in Dual Form

To solve the least distance problem of Equation (5.67), Haskell and Hanson (1981) adopted the dual approach advocated by Lawson and Hanson (1974). The latter proved that the correct solution for \vec{z} can be obtained by solving an equivalent non-negative least-squares (NNLS) problem:

$$\begin{aligned} \min \quad & |P\vec{u} - \vec{q}| \\ & \vec{u} \geq 0 \end{aligned} \tag{5.68}$$

In the current problem, P and \vec{q} are defined, respectively, to be an augmented $(20 + 1) \times 56$ matrix and an augmented $(20 + 1) \times 1$ vector,

$$P = \begin{bmatrix} (\tilde{C}')^T \\ (\vec{h}'_r)^T \end{bmatrix} \quad \vec{q} = \begin{bmatrix} 0 \\ \vdots \\ 1 \end{bmatrix} \tag{5.69}$$

The solution \hat{u} is determined using an active-set algorithm from Lawson and Hanson (1974), which partitions the unknown variables into two sets, based on whether they assume positive or zero values under the non-negativity constraints. From the residual vector in the NNLS problem,

$$\vec{r} = P\hat{u} - \vec{q} \tag{5.70}$$

the solution to the least distance problem is found,

$$\hat{z} = \begin{bmatrix} \frac{r_1}{r_{20+1}} \\ \vdots \\ \frac{r_{20}}{r_{20+1}} \end{bmatrix} \quad (5.71)$$

where the r_i are the $20 + 1$ components of \vec{r} in Equation (5.70). This result is then transformed back to the previous coordinates by substituting \vec{z} into Equation (5.65) and solving for \vec{y}_2 . Finally, \vec{y}_2 is combined with the previously determined \hat{y}_1 , and transformed per Equation (5.56), to yield \hat{x} , the complete solution to the LSEI problem in Equation (5.49).

5.3 Pre-Launch Solutions and Assessment

Hanson and Haskell (1982) subsequently published a Fortran-based “LSEI” subroutine that implemented the solution outlined in Sections 5.2.4 through 5.2.6. Later, they also made the complete source code available through the on-line Netlib repository (www.netlib.org). For this study, a new program was written around the LSEI subroutine to estimate the macro-model parameters. As Figure 5.7 illustrates, the algorithm begins by reading their *a priori* values. The initial area for each surface was taken from Table 5.1. Those for surfaces 7 and 9 were combined to yield a single value (8.443 m²) for the front of the one wing used in the linearized force model of Section 5.2.2. Likewise, the areas for surfaces 8 and 10 were combined to yield a single value (8.418 m²) for the back. The initial specular and diffuse reflectivities for all eight surfaces were set to zero.

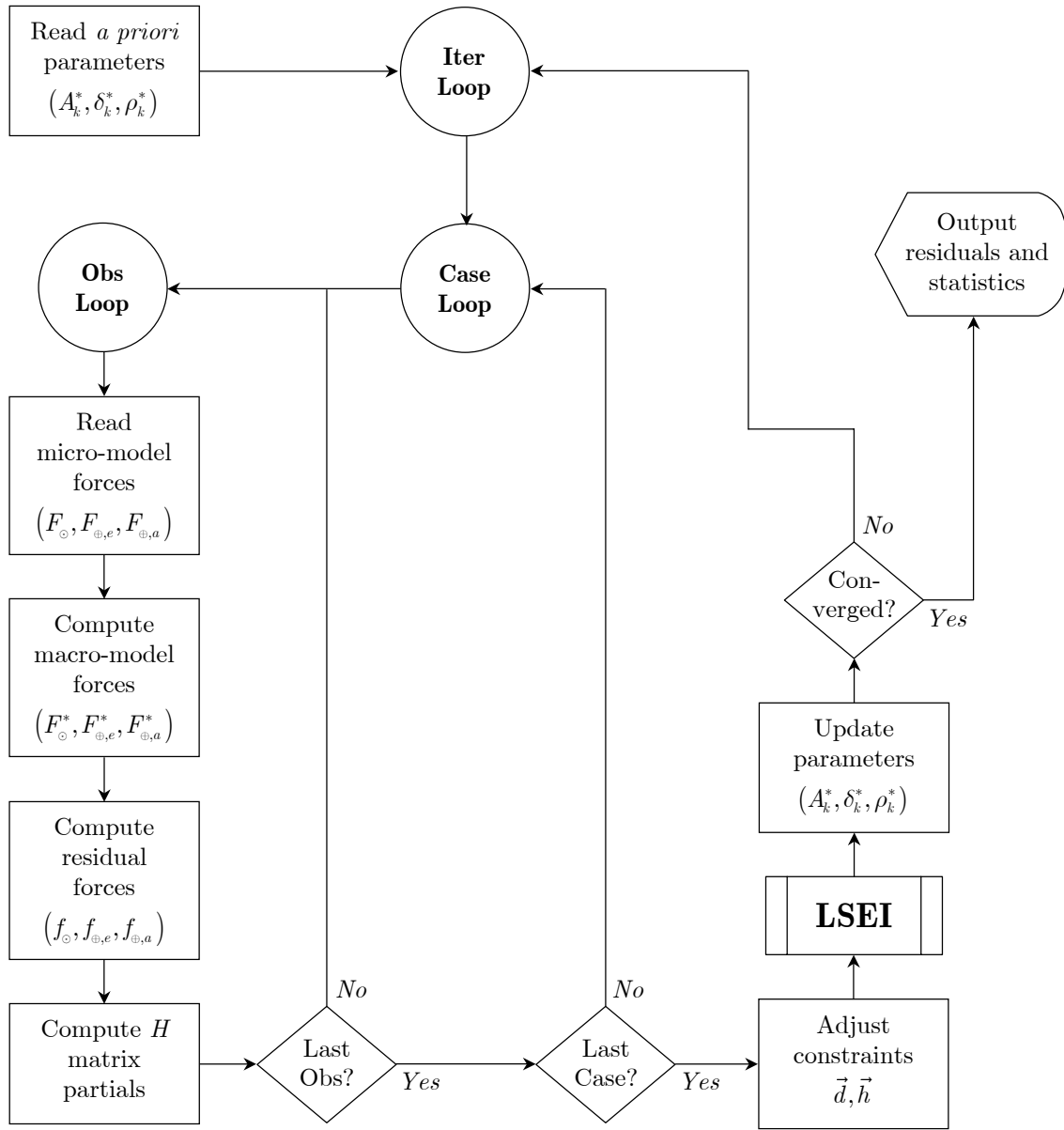


Figure 5.7. Macro-Model Parameter Estimation Algorithm

For each iteration, the micro-model simulation cases selected from Tables 4.4 and 4.5 are processed to construct the matrices and vectors needed in Equation (5.49). For each case, the solar and Earth radiation forces at a given

point in the orbit are read from the micro-model simulation output file. The corresponding macro-model forces are computed from Equations (5.7) through (5.10), using the current *a priori* parameters, along with the orbit and attitude data generated by the micro-model simulation. Differencing the micro-model and macro-model forces yields the “observation” vector \vec{f} in the linearized problem. In addition, the concomitant partial derivatives of Equations (5.20) and (5.21) are calculated to populate the H matrix per Equation (5.19).

Although the B and C matrices in the equality and inequality constraints, respectively, are fixed, the \vec{d} and \vec{h} vectors must be updated each iteration, based on the current macro-model parameters, and the definitions of Equations (5.30) and (5.48). In the latter equation, the minimum and maximum areas for each surface k were set to the smaller and larger areas, respectively, for each pair of surfaces in Table 5.1. For example, the equality constraints require that $A_1 = A_2$, so the lower limits A_1^{min} and A_2^{min} were both set to 3.819 m², while the upper limits A_1^{max} and A_2^{max} were both set to 3.833 m². This restriction limits the estimated areas to the range predicted by the heat-rate simulation. After all of the necessary matrices and vectors have been established, the LSEI subroutine generates a solution \hat{x}_i in the linearized problem, for the i -th iteration, the components of which are then applied to update the macro-model parameters:

$$\begin{aligned} A_{k,i+1}^* &= A_{k,i}^* + \Delta A_{k,i} \\ \delta_{k,i+1}^* &= \delta_{k,i}^* + \Delta \delta_{k,i} \\ \rho_{k,i+1}^* &= \rho_{k,i}^* + \Delta \rho_{k,i} \end{aligned} \tag{5.72}$$

Finally, the processing ends when the number of iterations exceeds a user-defined maximum value (10), or if the root-mean-square (RMS) of the residual force

differences changes by less than a user-specified tolerance (1×10^{-6} μN) during the current iteration.

The following sections present and discuss three different solutions. The first was obtained by fitting the beginning-of-life (BOL) micro-model forces from all 40 cases in Tables 4.4 and 4.5. The second actually encompasses four separate solutions, one for each attitude control frame, generated by fitting the subset of BOL micro-model cases with the corresponding satellite orientation. The third solution again fit forces from all 40 cases, but used, instead, the end-of-life (EOL) micro-model force histories. As described in this chapter, area and reflectivity parameters were estimated for an eight-surface model. The solutions shown in the following sections, however, have been expanded to the full 10-surface model used in ICESat POD. The areas estimated for the front and the back of the single solar array in the linearized model were divided in two, with equal areas assigned, respectively, to surfaces 7 and 9, and surfaces 8 and 10. The estimated diffuse and specular reflectivities remain unchanged, with their values being assigned, accordingly, to both of the two smaller arrays. In addition, the mean and RMS of the residual forces for each solution have been computed and tabulated. Finally, to illustrate the quality of the fits, the individual residual forces for each solution have been plotted for the four representative cases of Table 4.8.

5.3.1 Nominal BOL Solution

Fitting all 40 micro-model simulation cases from Tables 4.4 and 4.5, the nominal BOL solution reflects all planned orbit and satellite attitude geometries. Summarized in Table 5.3a, it thus constitutes the most general set of BOL

macro-model parameters. The effects of the constraints on the solution are evident. All of the inequality constraints imposed on the surface areas were active, with each of the estimates equal to its lower limit in Equation (5.32). Most of the estimated diffuse reflectivities were similarly constrained, with their values set to 0, except those for the $+x_{scs}$ face and the back sides of the solar arrays. None of the inequality constraints associated with the specular reflectivities, however, were active, as each of the estimates lies between 0 and 1.

At first glance, these results are surprising. The relatively low specularity of 0.2, adopted in Section 4.2.1 for nearly all of the surfaces in the micro-model simulation, suggested that the macro-model surfaces would also exhibit chiefly diffuse reflective behavior. Clearly, that is not the case, which implies that some of the differences between the underlying radiation models were absorbed by the estimated specular reflectivities. As detailed in Section 5.2.1, the total radiation force acts on an individual macro-model surface along a direction that is a linear combination of its surface normal, and the unit direction vectors to the Sun and the Earth segments. The total radiation force acting on a micro-model node, however, accounts for the directions of as many as 10,000 rays from each source. The macro-model appears to have compensated for this disparity through the multi-directional paths associated with specular reflection. Only the front sides of the solar arrays produced estimated reflectivities resembling those implemented in the micro-model simulation: $(\rho, \delta) = (0.257, 0.000)$ from Table 5.3a, versus $(\rho, \delta) = (0.265, 0.006)$, the averages of the solar and infrared values in Table 5.1.

The cost of the constraints can be observed directly by comparing the residual statistics from the nominal BOL solution, in Table 5.3b, with those from

the unconstrained solution, in Table 5.4b. The root-sum-square (RSS) of the residual RMS values for the RTN components of the total radiation force increased by a factor of three in the constrained case, from $1.245 \mu\text{N}$ to $3.789 \mu\text{N}$. This was due almost entirely to an increase in the solar radiation force residuals. Although the same statistic for the Earth emission force increased by a factor of two in the constrained case, that for the Earth albedo force actually decreased by nearly the same factor. A quick inspection of the unconstrained solution in Table 5.4a, however, reveals that almost all of the estimated reflectivities are infeasible, except those for the $+y_{scs}$ face and the front sides of the solar arrays. All of the unconstrained surface areas estimated for the box portion of the macro-model are lower with respect to the nominal BOL solution, but those for the front sides of the arrays are higher.

In their determination of the TOPEX/Poseidon macro-model parameters, Marshall and Luthcke (1994a) computed similar statistics for their fit to the solar radiation forces generated by an earlier micro-model simulation. They chose, however, to present these results as forces per unit mass, with units of acceleration (nm/s^2). To compare these with the statistics from the nominal BOL solution, in Table 5.3b, the latter were divided by the BOL satellite mass, 958 kg. The results are shown in Table 5.5a, while those for TOPEX/Poseidon are shown in Table 5.5b. The RSS of the residual RMS values for the RTN components of the solar radiation force was better for ICESat by a factor of two, but the same statistics for Earth albedo and emission were slightly higher. This latter result is surprising, as Marshall and Luthcke (1994a) used only the micro-model solar forces to compute the macro-model parameters. It suggests that, despite the

inclusion of Earth radiation in the ICESat modeling, the estimated macro-model parameters were dictated primarily by solar radiation.

Figures 5.8 through 5.11 illustrate the residual radiation forces for the four representative cases in Table 4.8. The relatively large and systematic variation in the solar force residuals results from shadowing within the micro-model, which was ignored by the macro-model. Figure 5.12 plots the number of nodes in the micro-model illuminated by solar radiation throughout the orbit, for each of these four cases. In Case 9, for example, the magnitudes of the transverse and normal components from the micro-model were smaller than those from the macro-model, at arguments of latitude 90° and 270° . These clearly correspond to drops in the number of illuminated micro-model nodes at these positions in Figure 5.12. Similar, but smaller, effects are observed for the other three cases.

Although the residual Earth radiation forces were smaller than their solar counterparts, two factors influenced the observed patterns. First, for Earth albedo, the sampling associated with the micro-model Monte Carlo Ray Tracing (MCRT) method better renders the Earth's terminator than the limited number of Earth segments used in the macro-model approach. As a result, depending on the orbit geometry, the micro-model forces were slightly larger or smaller than the macro-model forces at the eclipse boundaries. Second, the estimated reflectivities for the back sides of the solar arrays are significantly different from those implemented in the micro-model simulation: $(\rho, \delta) = (0.545, 0.095)$ from Table 5.3a, versus $(\rho, \delta) = (0.092, 0.369)$, the averages of the solar and infrared values in Table 5.1. This disparity produced the larger Earth emission residuals observed when these surfaces were most directly exposed to the planet.

Surface k	Face (SCS)	A_k (m ²)	ρ_k	δ_k
1	$+x$	3.819	0.460	0.179
2	$-x$	3.819	0.987	0.000
3	$+y$	5.212	0.433	0.000
4	$-y$	5.212	0.396	0.000
5	$+z$	2.733	0.472	0.000
6	$-z$	2.733	0.727	0.000
7	$+y$ SA (front)	4.209	0.257	0.000
8	$+y$ SA (back)	4.209	0.545	0.095
9	$-y$ SA (front)	4.209	0.257	0.000
10	$-y$ SA (back)	4.209	0.545	0.095

Table 5.3a. Nominal BOL Solution (Cases 1-40)

		Radial	Trans	Normal	3D RSS
Solar	Mean RMS	0.050 1.093	0.009 2.849	-0.002 1.954	— 3.623
Earth Albedo	Mean RMS	-0.069 0.221	-0.032 0.365	0.004 0.334	— 0.542
Earth Emission	Mean RMS	-0.445 0.683	-0.081 0.382	0.004 0.544	— 0.953
Total	Mean RMS	-0.463 1.042	-0.104 3.024	0.006 2.032	— 3.789

Table 5.3b. Nominal BOL Residual Statistics (μN)

Surface k	Face (SCS)	A_k (m ²)	ρ_k	δ_k
1	$+x$	1.697	-0.417	1.417
2	$-x$	4.634	0.475	-0.320
3	$+y$	1.233	0.751	0.249
4	$-y$	1.527	0.715	-0.035
5	$+z$	-0.017	-15.655	-5.195
6	$-z$	0.601	2.572	-1.981
7	$+y$ SA (front)	5.207	0.153	0.261
8	$+y$ SA (back)	3.871	-1.163	2.163
9	$-y$ SA (front)	5.207	0.153	0.261
10	$-y$ SA (back)	3.871	-1.163	2.163

Table 5.4a. Unconstrained Solution (Cases 1-40)

		Radial	Trans	Normal	3D RSS
Solar	Mean RMS	-0.094 0.725	-0.005 0.803	-0.002 0.670	— 1.273
Earth Albedo	Mean RMS	0.231 0.668	-0.031 0.426	0.004 0.454	— 0.913
Earth Emission	Mean RMS	-0.068 0.222	-0.083 0.240	0.005 0.271	— 0.425
Total	Mean RMS	0.069 0.578	-0.119 0.883	0.007 0.660	— 1.245

Table 5.4b. Unconstrained Residual Statistics (μN)

		Radial	Trans	Normal	3D RSS
Solar	Mean	0.052	0.009	−0.002	—
	RMS	1.141	2.974	2.040	3.782
Earth Albedo	Mean	−0.072	−0.033	0.004	—
	RMS	0.231	0.381	0.349	0.566
Earth Emission	Mean	−0.465	−0.085	0.004	—
	RMS	0.713	0.399	0.568	0.995

Table 5.5a. ICESat Nominal BOL Residual Statistics (nm/s²)

		Radial	Trans	Normal	3D RSS
Solar	Mean	1.300	−0.038	1.700	—
	RMS	4.900	4.300	4.300	7.810
Earth Albedo	Mean	—	—	—	—
	RMS	0.240	0.230	0.330	0.468
Earth Emission	Mean	—	—	—	—
	RMS	0.540	0.540	0.530	0.930

Table 5.5b. TOPEX/Poseidon Residual Statistics (nm/s²)
(Marshall and Luthcke, 1994a)

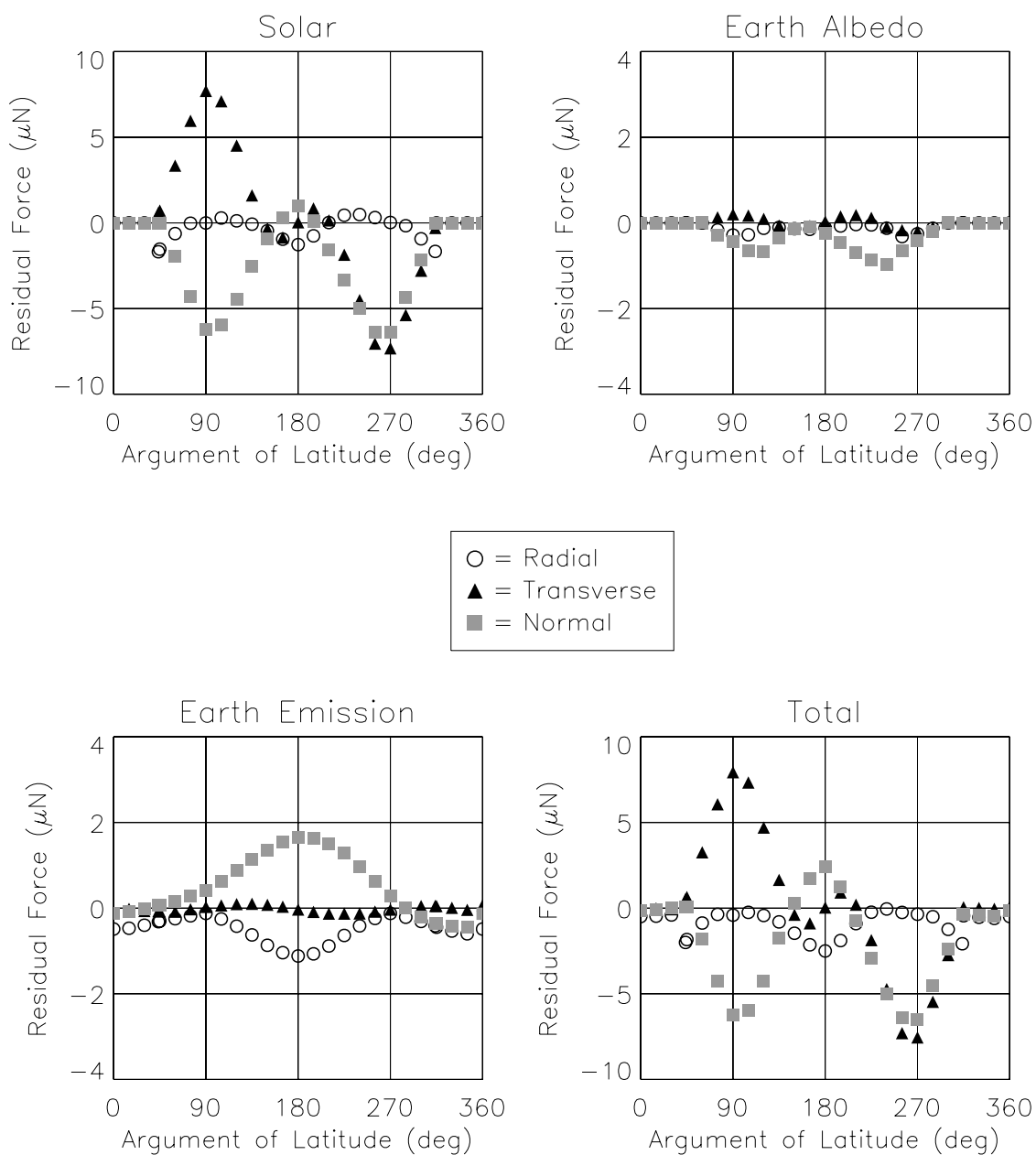


Figure 5.8. Case 9 Nominal BOL Residual Forces: $\beta' = -55^\circ$, Yaw = 270° (Sailboat), Articulating Arrays, Eclipsing Orbit

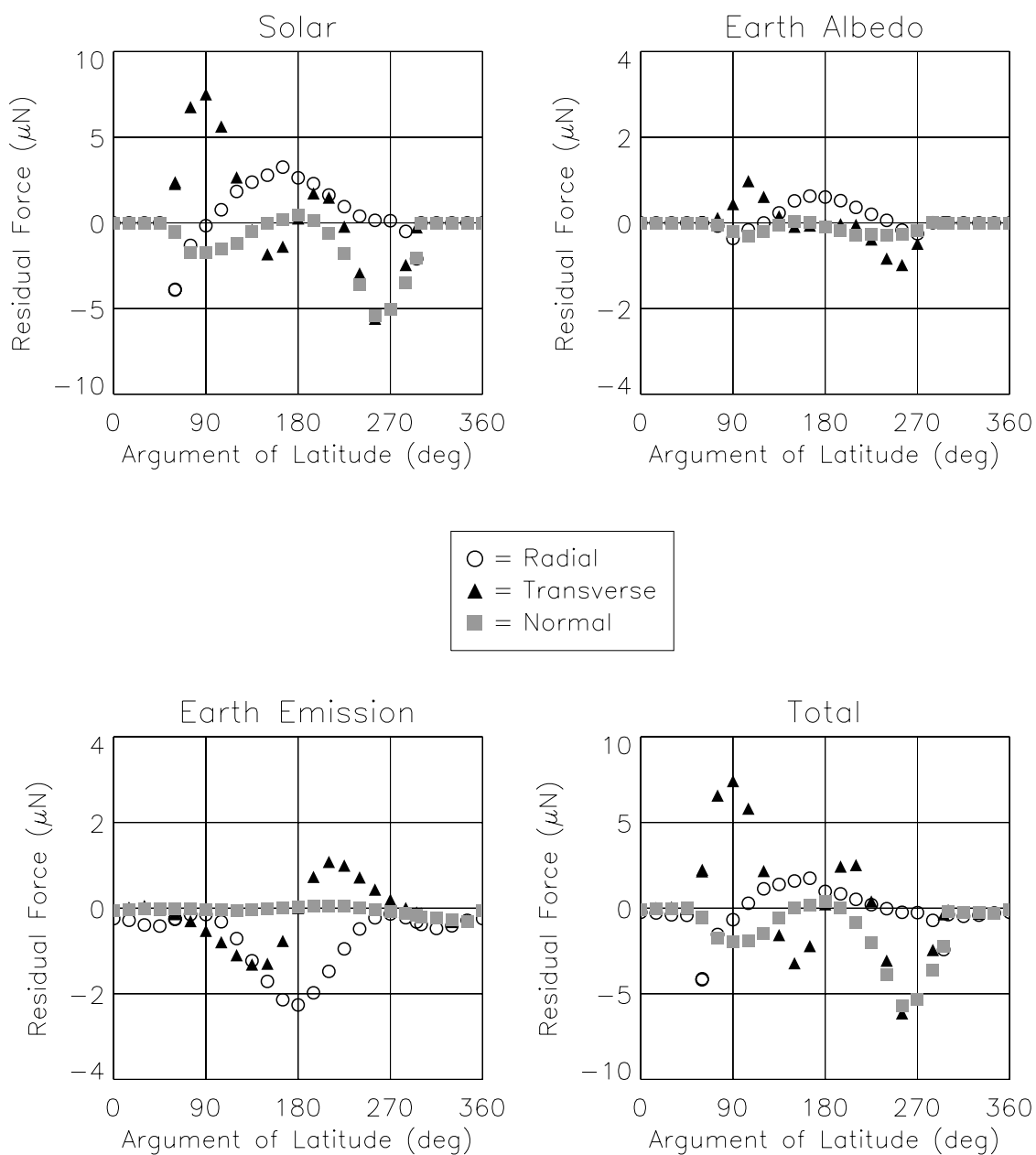


Figure 5.9. Case 14 Nominal BOL Residual Forces: $\beta' = -30^\circ$, Yaw = 0° (Airplane), Articulating Arrays, Eclipsing Orbit

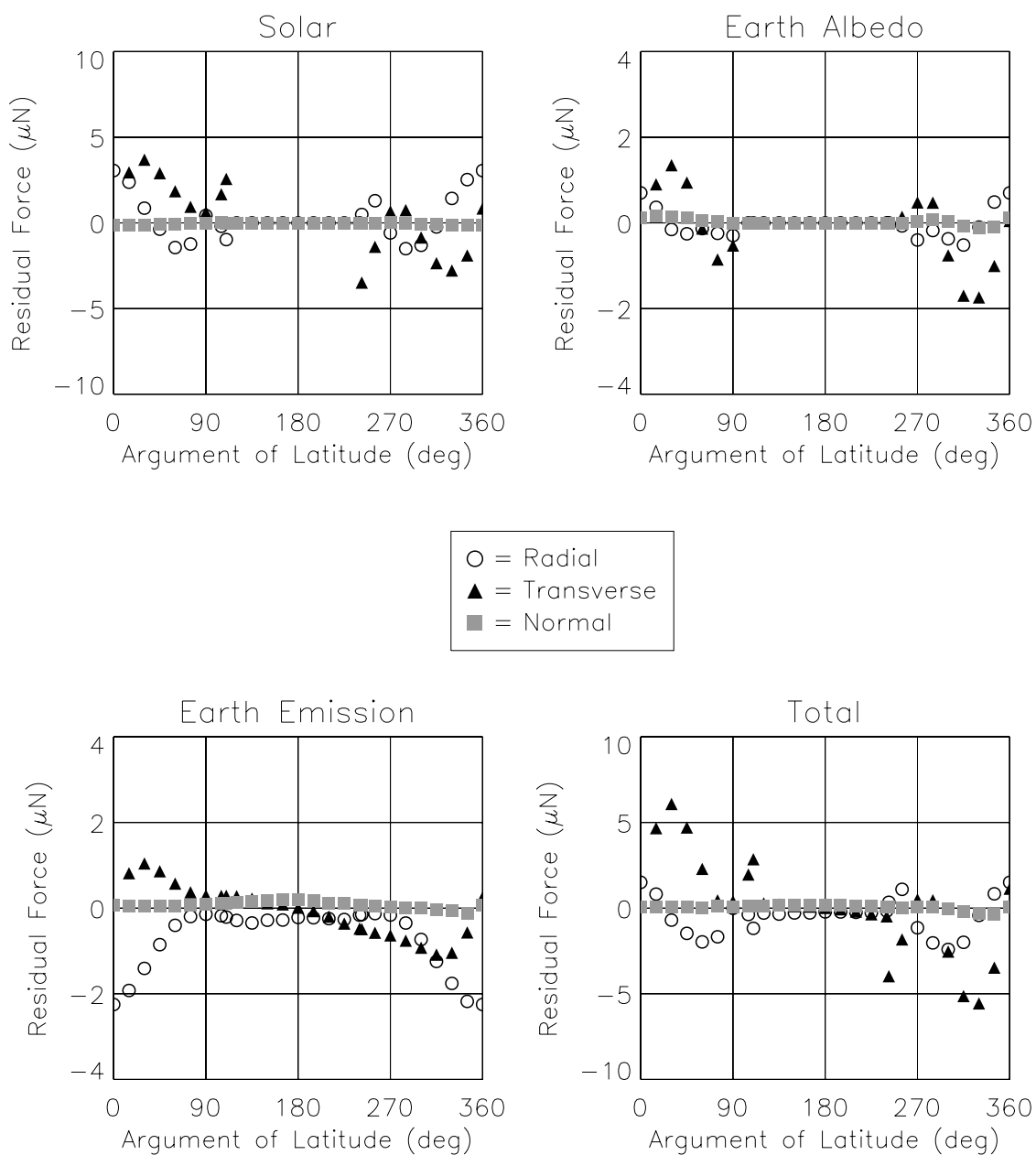


Figure 5.10. Case 21 Nominal BOL Residual Forces: $\beta' = 0^\circ$, Yaw = 180° (Airplane), Articulating Arrays, Eclipsing Orbit

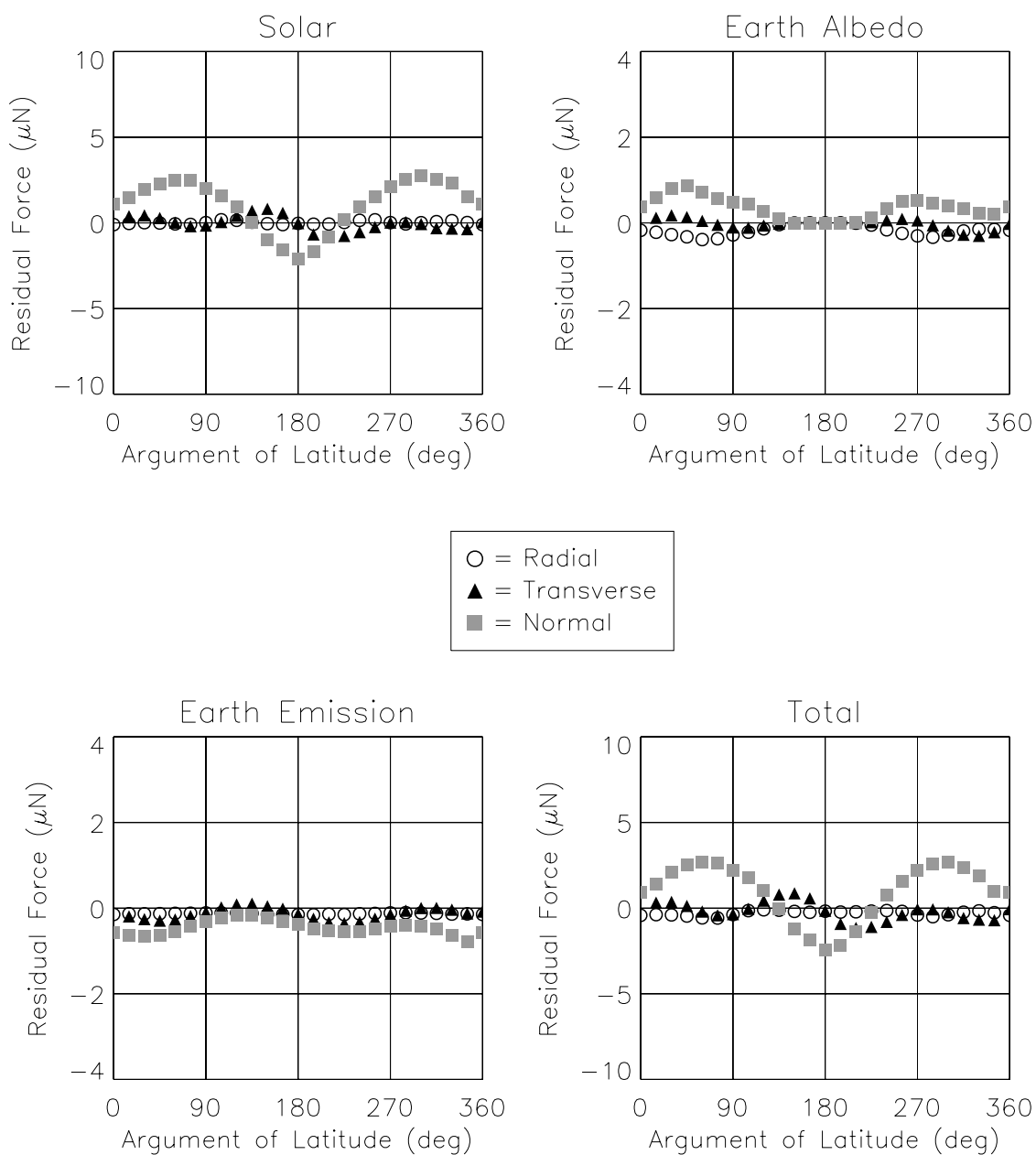


Figure 5.11. Case 37 Nominal BOL Residual Forces: $\beta' = 75^\circ$, Yaw = 90° (Sailboat), Fixed Arrays, Non-Eclipsing Orbit

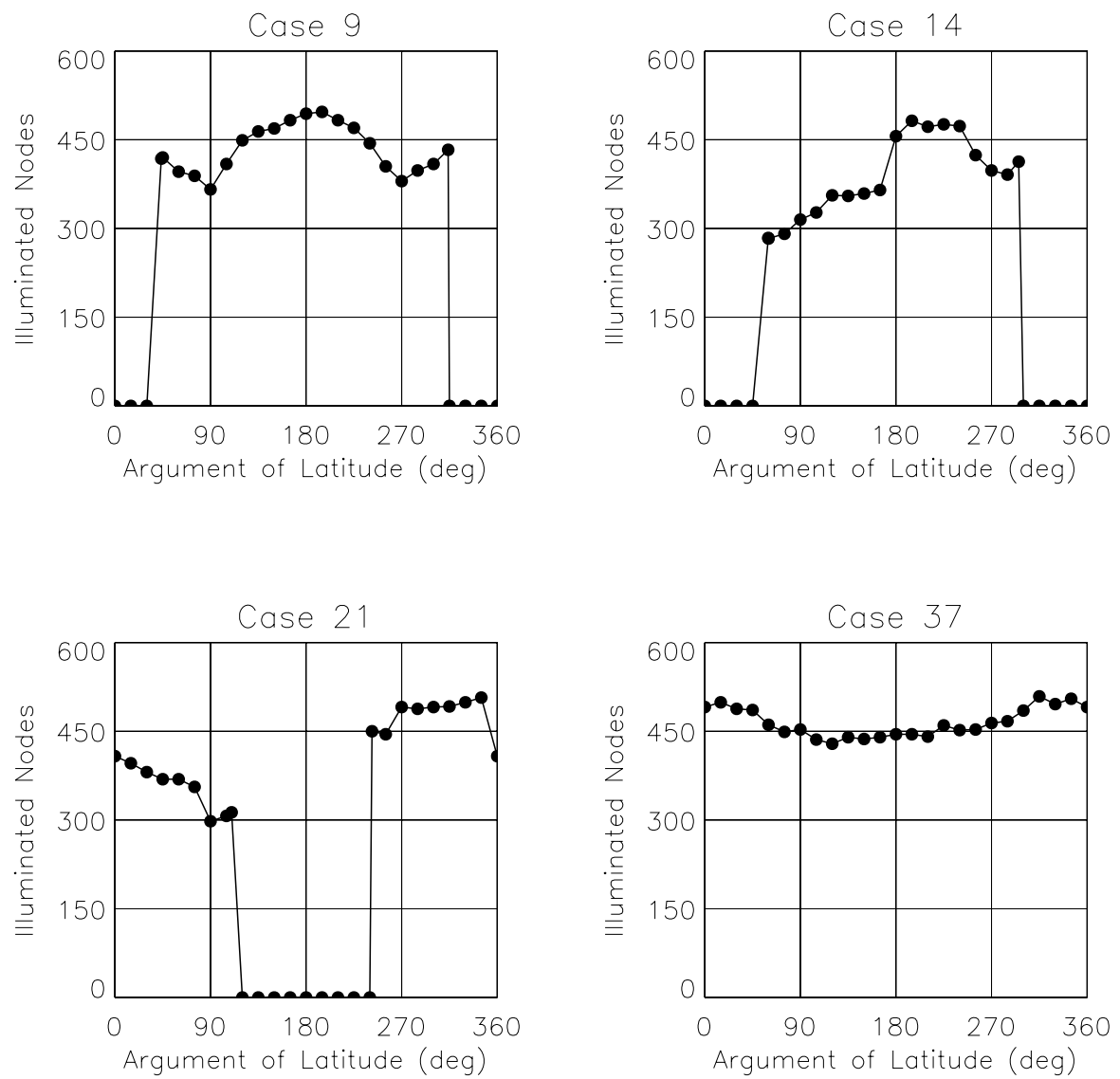


Figure 5.12. Micro-Model Nodes Illuminated by Solar Radiation

5.3.2 Attitude-Specific Solutions

Instead of fitting all 40 cases from Tables 4.4 and 4.5, a solution for each attitude control frame in Table 5.6 was obtained by fitting only the BOL micro-model simulation cases shown. These attitude-specific solutions are summarized in Tables 5.7a through 5.10a. The two solutions for the sailboat mode are similar to each other and, generally, resemble the nominal BOL solution, with the exception of the estimated reflectivities for the back sides of the solar arrays: $(\rho, \delta) = (0.228, 0.727)$ and $(\rho, \delta) = (0.237, 0.741)$, from Tables 5.7a and 5.10a, respectively, versus $(\rho, \delta) = (0.545, 0.095)$, from Table 5.3a. For both solutions, all of the inequality constraints imposed on the surface areas were active, with each of the estimates equal to its lower limit in Equation (5.32). Most of the estimated diffuse reflectivities were similarly constrained, with their values set to 0, except those for the $+x_{scs}$ face and the back sides of the solar arrays. Unlike in the nominal BOL solution, two of the inequality constraints associated with the specular reflectivities were active, yielding upper-limit estimates of 1 for both the $-x_{scs}$ and $+z_{scs}$ faces.

Control Frame	Mode	Yaw	Cases Used in Fit	Example Case
3	Sailboat	270°	1–13	9
2	Airplane	0°	14–20	14
0	Airplane	180°	21–27	21
1	Sailboat	90°	28–40	37

Table 5.6. Micro-Model Cases for Attitude-Specific Solutions

The two airplane-mode solutions, in Tables 5.8a and 5.9a, also resemble each other, but they differ noticeably from the nominal BOL solution. For both, all of the inequality constraints imposed on the surface areas were again active, with each of the estimates equal to its lower limit in Equation (5.32). The estimated diffuse reflectivities were similarly constrained for control frame 0, with all of their values set to 0. For control frame 2, most of the estimated diffuse reflectivities were also 0, except those for the back sides of the solar arrays. In both solutions, only one of the inequality constraints associated with the specular reflectivities was active, yielding an upper-limit estimate of 1 for the $-y_{scs}$ face.

The residual statistics for each solution are provided in Tables 5.7b through 5.10b. The RSS of the residual RMS values for the RTN components of the total radiation force was nearly 40% lower for each of the airplane-mode solutions than for the nominal BOL solution. The same statistic, however, was almost 7% higher for each of the sailboat-mode cases. The significantly better fit achieved in the airplane mode stems mainly from an improvement in the solar radiation force residuals, a consequence of the more direct exposure that the arrays have to the Sun. For Earth albedo, the RSS of the RMS values for the residual force components was higher in the airplane mode, while the same statistic for Earth emission was lower, as compared to the nominal BOL solution. These results were reversed for the sailboat mode. Figures 5.13 through 5.16 plot the residuals for the four representative cases of Table 4.8. The patterns resemble those observed for the nominal BOL solution, although, as expected, with slightly smaller amplitudes for solar radiation and Earth albedo in the airplane mode, and slightly higher amplitudes for Earth emission in the sailboat mode.

Surface k	Face (SCS)	A_k (m ²)	ρ_k	δ_k
1	$+x$	3.819	0.654	0.198
2	$-x$	3.819	1.000	0.000
3	$+y$	5.212	0.360	0.000
4	$-y$	5.212	0.380	0.000
5	$+z$	2.733	1.000	0.000
6	$-z$	2.733	0.767	0.000
7	$+y$ SA (front)	4.209	0.263	0.000
8	$+y$ SA (back)	4.209	0.228	0.727
9	$-y$ SA (front)	4.209	0.263	0.000
10	$-y$ SA (back)	4.209	0.228	0.727

Table 5.7a. Yaw = 270° Solution (Cases 1-13)

		Radial	Trans	Normal	3D RSS
Solar	Mean RMS	0.167 1.268	0.014 2.756	-1.514 2.685	— 4.051
Earth Albedo	Mean RMS	-0.222 0.299	-0.006 0.099	-0.197 0.331	— 0.457
Earth Emission	Mean RMS	-0.507 0.704	-0.049 0.092	0.946 1.095	— 1.305
Total	Mean RMS	-0.562 1.110	-0.042 2.844	-0.765 2.665	— 4.052

Table 5.7b. Yaw = 270° Residual Statistics (μN)

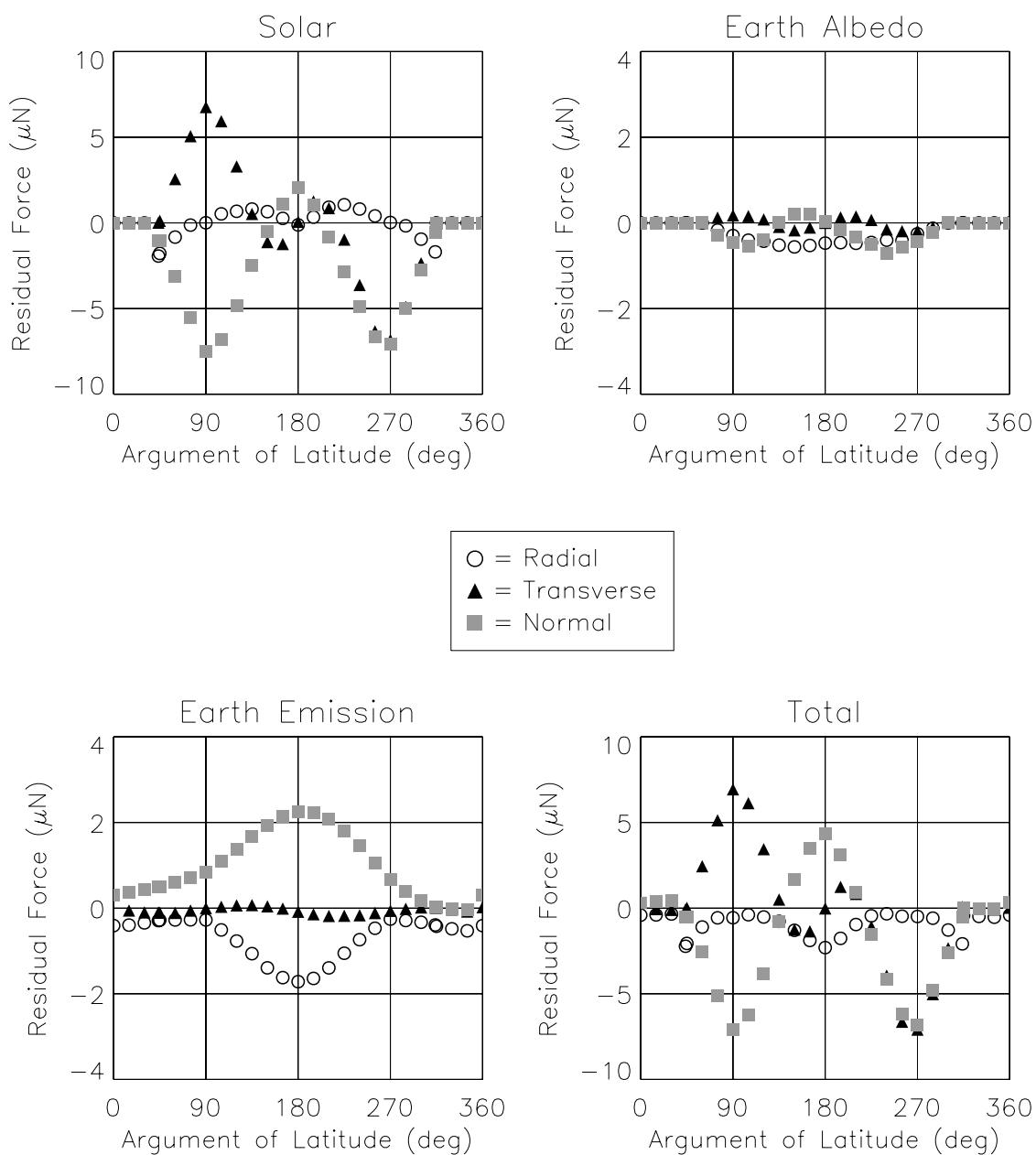


Figure 5.13. Case 9 Attitude-Specific Residual Forces: $\beta' = -55^\circ$, Yaw = 270° (Sailboat), Articulating Arrays, Eclipsing Orbit

Surface k	Face (SCS)	A_k (m ²)	ρ_k	δ_k
1	$+x$	3.819	0.294	0.000
2	$-x$	3.819	0.760	0.000
3	$+y$	5.212	0.640	0.000
4	$-y$	5.212	1.000	0.000
5	$+z$	2.733	0.333	0.000
6	$-z$	2.733	0.585	0.000
7	$+y$ SA (front)	4.209	0.281	0.000
8	$+y$ SA (back)	4.209	0.287	0.130
9	$-y$ SA (front)	4.209	0.281	0.000
10	$-y$ SA (back)	4.209	0.287	0.130

Table 5.8a. Yaw = 0° Solution (Cases 14-20)

		Radial	Trans	Normal	3D RSS
Solar	Mean	−0.756	0.073	−0.539	—
		1.176	1.365	1.546	2.374
Earth Albedo	Mean	0.666	−0.020	0.056	—
		1.178	0.667	0.179	1.366
Earth Emission	Mean	0.050	−0.124	0.196	—
		0.292	0.378	0.229	0.530
Total	Mean	−0.041	−0.071	−0.286	—
		0.675	1.517	1.578	2.291

Table 5.8b. Yaw = 0° Residual Statistics (μN)

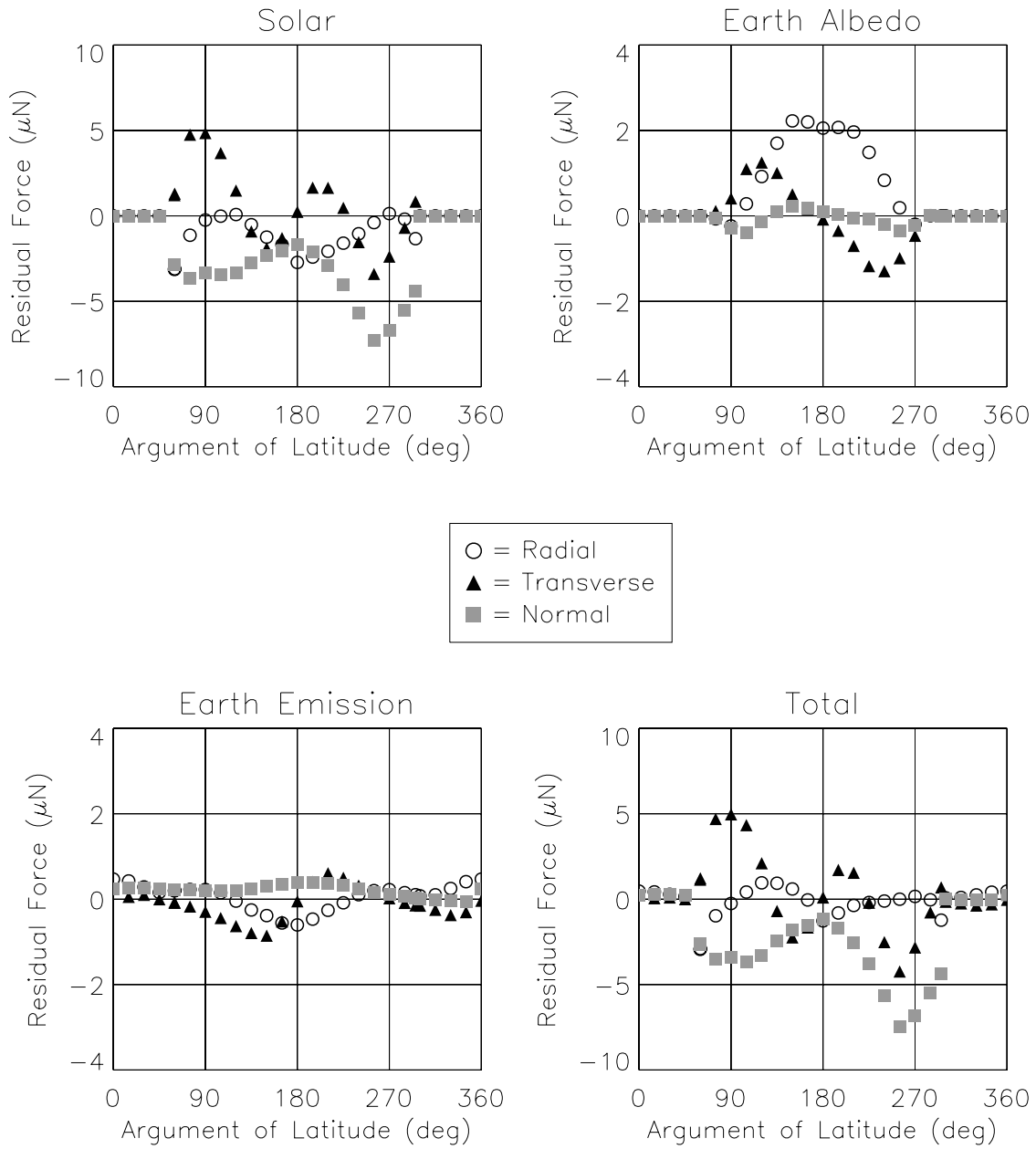


Figure 5.14. Case 14 Attitude-Specific Residual Forces: $\beta' = -30^\circ$, Yaw = 0° (Airplane), Articulating Arrays, Eclipsing Orbit

Surface k	Face (SCS)	A_k (m ²)	ρ_k	δ_k
1	$+x$	3.819	0.225	0.000
2	$-x$	3.819	0.735	0.000
3	$+y$	5.212	0.624	0.000
4	$-y$	5.212	1.000	0.000
5	$+z$	2.733	0.291	0.000
6	$-z$	2.733	0.584	0.000
7	$+y$ SA (front)	4.209	0.287	0.000
8	$+y$ SA (back)	4.209	0.281	0.000
9	$-y$ SA (front)	4.209	0.287	0.000
10	$-y$ SA (back)	4.209	0.281	0.000

Table 5.9a. Yaw = 180° Solution (Cases 21-27)

		Radial	Trans	Normal	3D RSS
Solar	Mean RMS	−0.914 1.399	0.043 1.291	0.594 1.564	— 2.464
Earth Albedo	Mean RMS	0.685 1.229	−0.064 0.392	−0.054 0.218	— 1.308
Earth Emission	Mean RMS	0.202 0.254	−0.045 0.221	−0.197 0.224	— 0.404
Total	Mean RMS	−0.027 0.727	−0.066 1.605	0.343 1.573	— 2.362

Table 5.9b. Yaw = 180° Residual Statistics (μN)

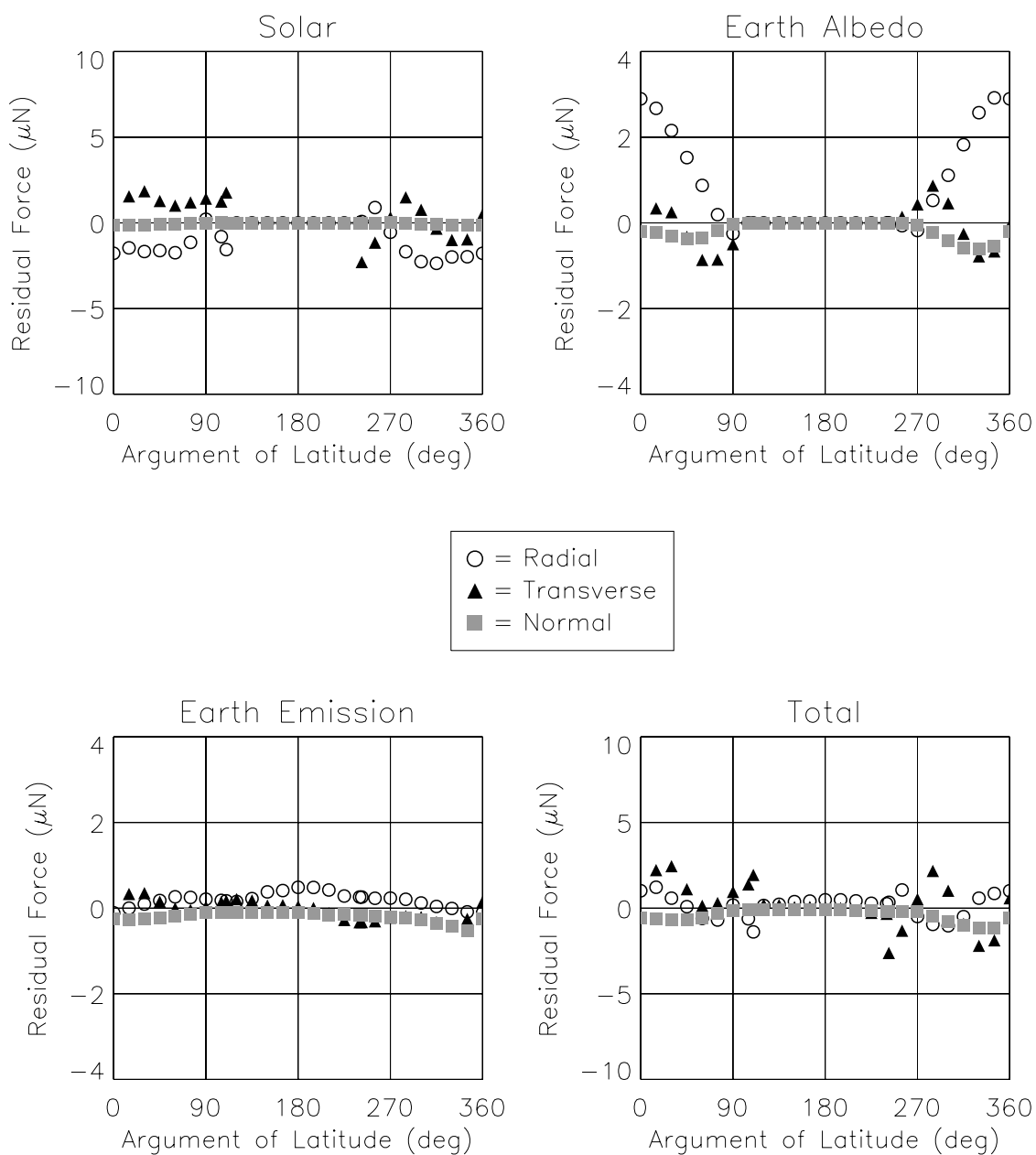


Figure 5.15. Case 21 Attitude-Specific Residual Forces: $\beta' = 0^\circ$, Yaw = 180° (Airplane), Articulating Arrays, Eclipsing Orbit

Surface k	Face (SCS)	A_k (m ²)	ρ_k	δ_k
1	$+x$	3.819	0.622	0.219
2	$-x$	3.819	1.000	0.000
3	$+y$	5.212	0.373	0.000
4	$-y$	5.212	0.377	0.000
5	$+z$	2.733	1.000	0.000
6	$-z$	2.733	0.762	0.000
7	$+y$ SA (front)	4.209	0.263	0.000
8	$+y$ SA (back)	4.209	0.237	0.741
9	$-y$ SA (front)	4.209	0.263	0.000
10	$-y$ SA (back)	4.209	0.237	0.741

Table 5.10a. Yaw = 90° Solution (Cases 28-40)

		Radial	Trans	Normal	3D RSS
Solar	Mean RMS	0.165 1.251	-0.033 2.800	1.499 2.635	— 4.043
Earth Albedo	Mean RMS	-0.213 0.288	-0.036 0.284	0.197 0.371	— 0.549
Earth Emission	Mean RMS	-0.501 0.706	-0.104 0.194	-0.960 1.106	— 1.326
Total	Mean RMS	-0.549 1.101	-0.173 2.853	0.736 2.598	— 4.013

Table 5.10b. Yaw = 90° Residual Statistics (μN)

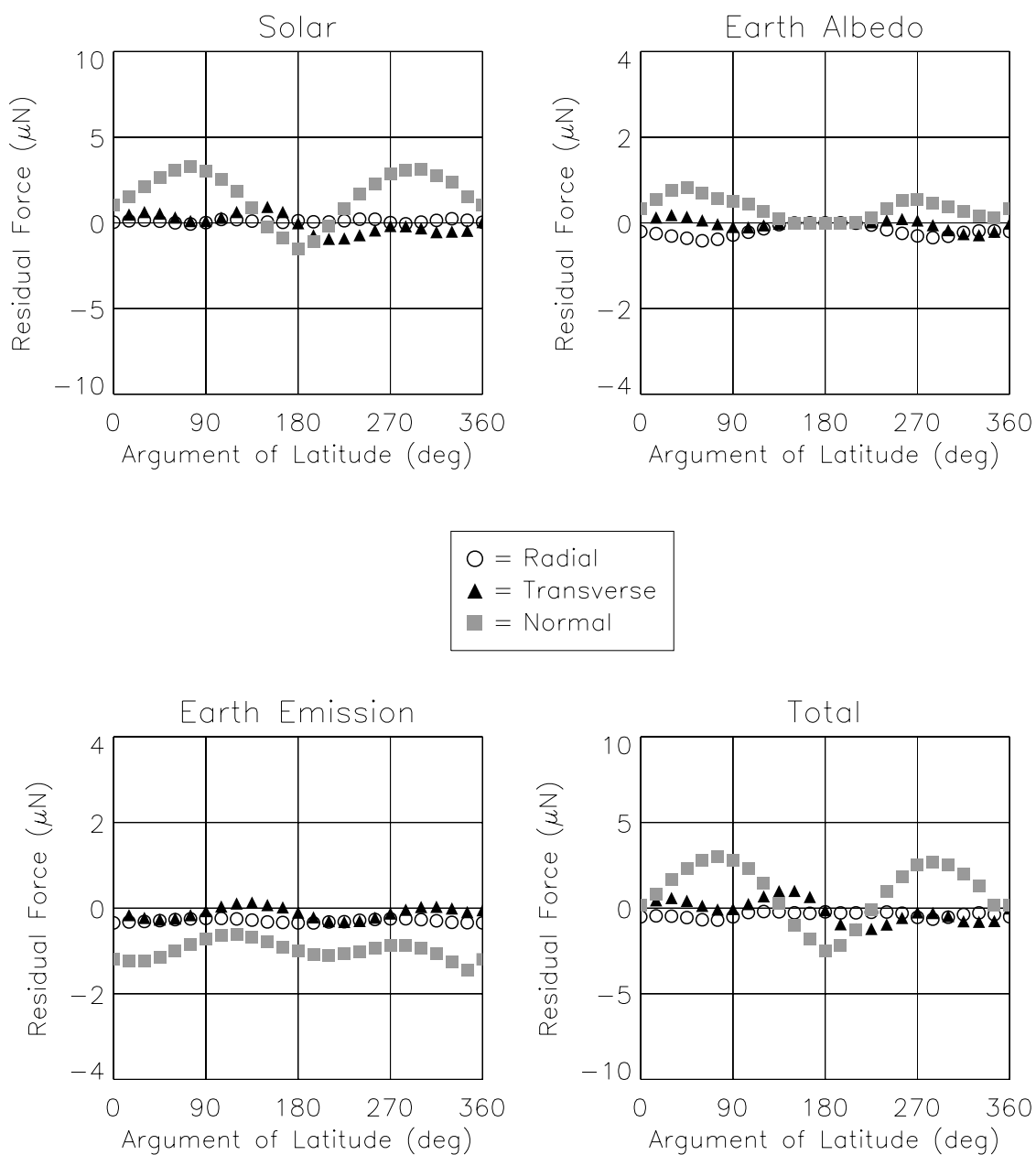


Figure 5.16. Case 37 Attitude-Specific Residual Forces: $\beta' = 75^\circ$, Yaw = 90° (Sailboat), Fixed Arrays, Non-Eclipsing Orbit

5.3.3 Nominal EOL Solution

As described in Section 4.3.2, the radiative properties of satellite surfaces degrade with exposure to the space environment. Consequently, another set of macro-model parameters was obtained by fitting the EOL micro-model forces for all 40 cases in Tables 4.4 and 4.5. Like the nominal BOL solution, this nominal EOL solution, shown in Table 5.11a, reflects all planned orbit and satellite attitude geometries, but also accounts for changes in radiative properties during the mission. All of the inequality constraints imposed on the surface areas were active, with each of the estimates equal to its lower limit in Equation (5.32). Most of the estimated diffuse reflectivities were similarly constrained, with their values set to 0, except those for the $+x_{scs}$ face. Only one of the inequality constraints associated with the specular reflectivities was active, yielding an upper-limit of 1 for the $-x_{scs}$ face.

In general, the solution resembles the nominal BOL solution, with the exception of the estimated specular reflectivities for the front sides of the solar arrays: $\rho = 0.073$, from Table 5.11a, versus $\rho = 0.257$, from Table 5.3a. This decrease resulted from the anticipated increase in absorptivity for the solar cells, making these surfaces less reflective. Table 5.11b summarizes the residual statistics, which were also similar to those produced by the nominal BOL solution. The RSS of the residual RMS values for the RTN components of the total radiation force was 2% greater for the nominal EOL solution. Figures 5.17 through 5.20 plot the residual forces for the four representative cases in Table 4.8, and reveal patterns nearly identical to those for the nominal BOL solution.

Surface k	Face (SCS)	A_k (m ²)	ρ_k	δ_k
1	$+x$	3.819	0.460	0.157
2	$-x$	3.819	1.000	0.000
3	$+y$	5.212	0.409	0.000
4	$-y$	5.212	0.383	0.000
5	$+z$	2.733	0.474	0.000
6	$-z$	2.733	0.684	0.000
7	$+y$ SA (front)	4.209	0.073	0.000
8	$+y$ SA (back)	4.209	0.642	0.000
9	$-y$ SA (front)	4.209	0.073	0.000
10	$-y$ SA (back)	4.209	0.642	0.000

Table 5.11a. Nominal EOL Solution (Cases 1-40)

		Radial	Trans	Normal	3D RSS
Solar	Mean RMS	0.111 1.228	0.007 2.878	-0.003 2.115	— 3.777
Earth Albedo	Mean RMS	-0.134 0.212	-0.032 0.392	0.004 0.290	— 0.532
Earth Emission	Mean RMS	-0.470 0.718	-0.082 0.436	0.004 0.640	— 1.056
Total	Mean RMS	-0.493 1.101	-0.107 3.058	0.004 2.098	— 3.868

Table 5.11b. Nominal EOL Residual Statistics (μN)

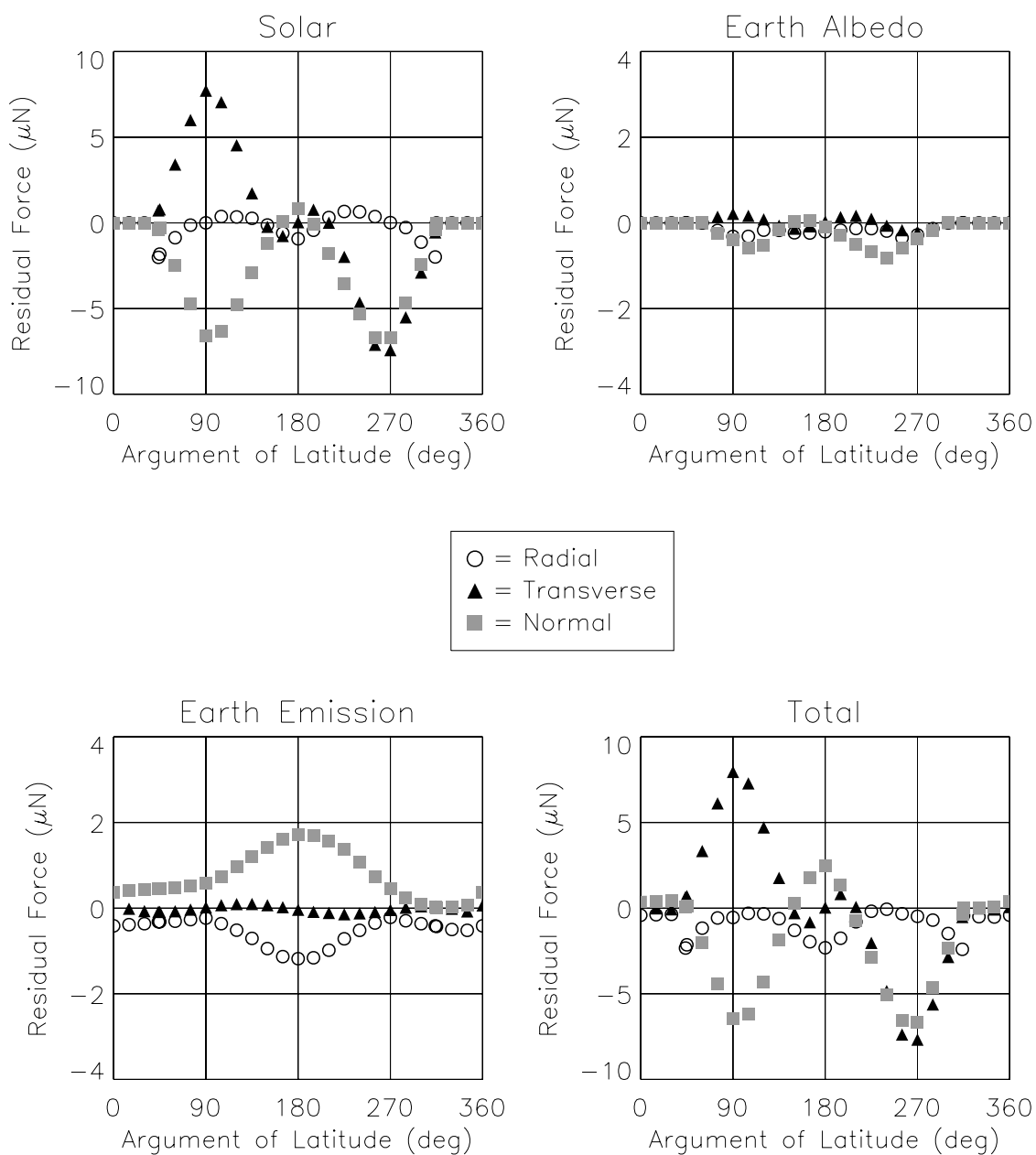


Figure 5.17. Case 9 Nominal EOL Residual Forces: $\beta' = -55^\circ$, Yaw = 270° (Sailboat), Articulating Arrays, Eclipsing Orbit

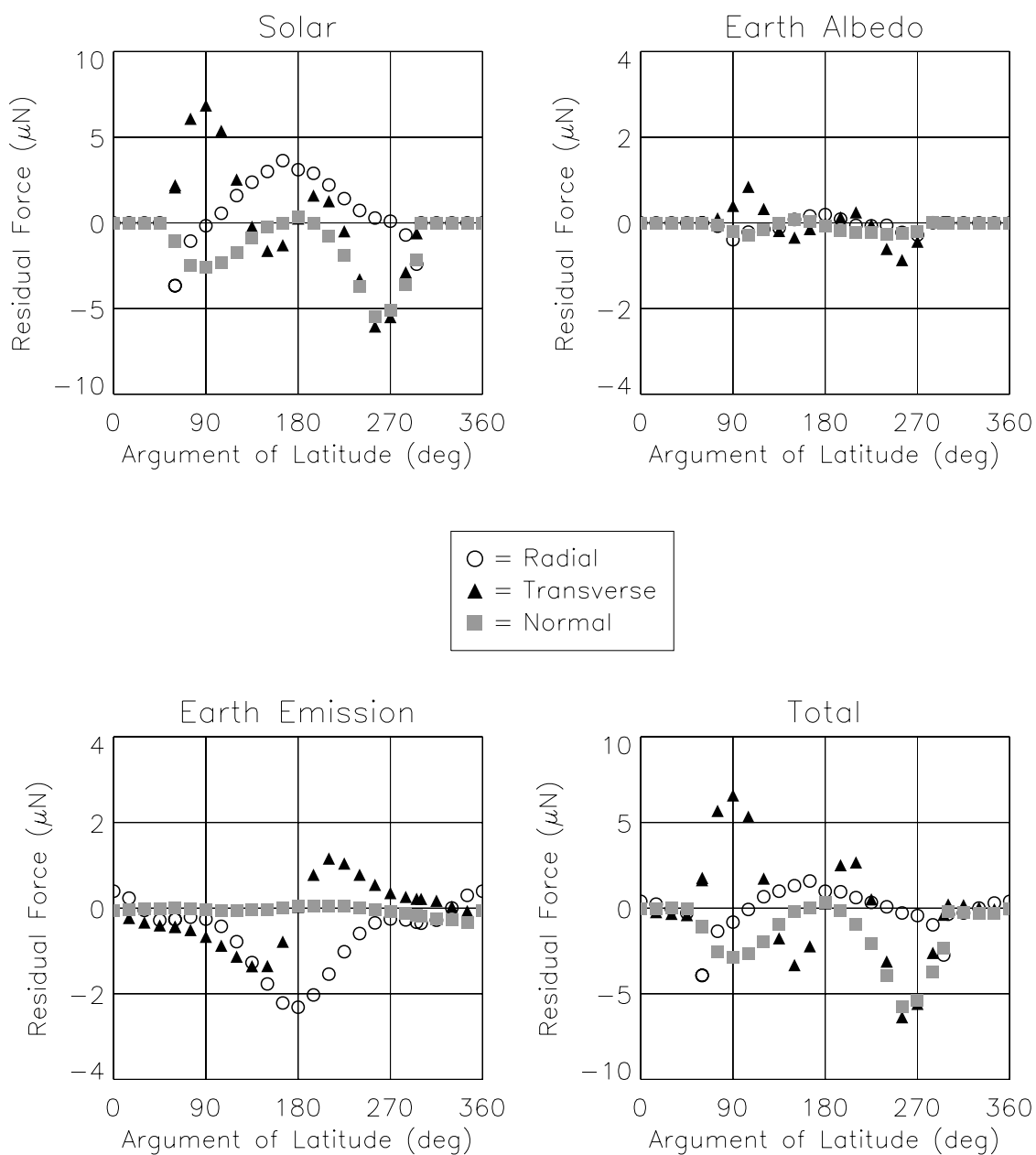


Figure 5.18. Case 14 Nominal EOL Residual Forces: $\beta' = -30^\circ$, Yaw = 0° (Airplane), Articulating Arrays, Eclipsing Orbit

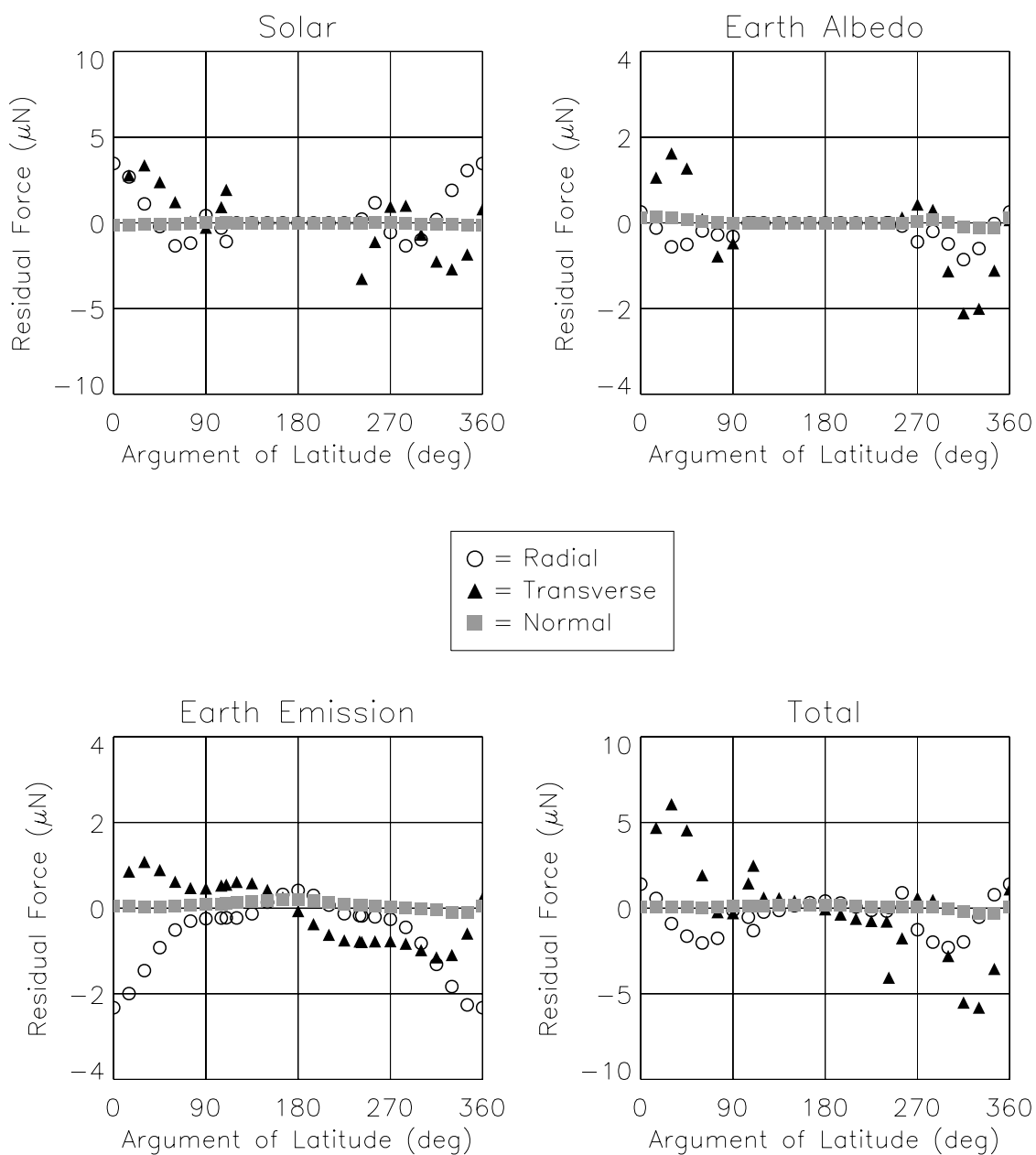


Figure 5.19. Case 21 Nominal EOL Residual Forces: $\beta' = 0^\circ$, Yaw = 180° (Airplane), Articulating Arrays, Eclipsing Orbit

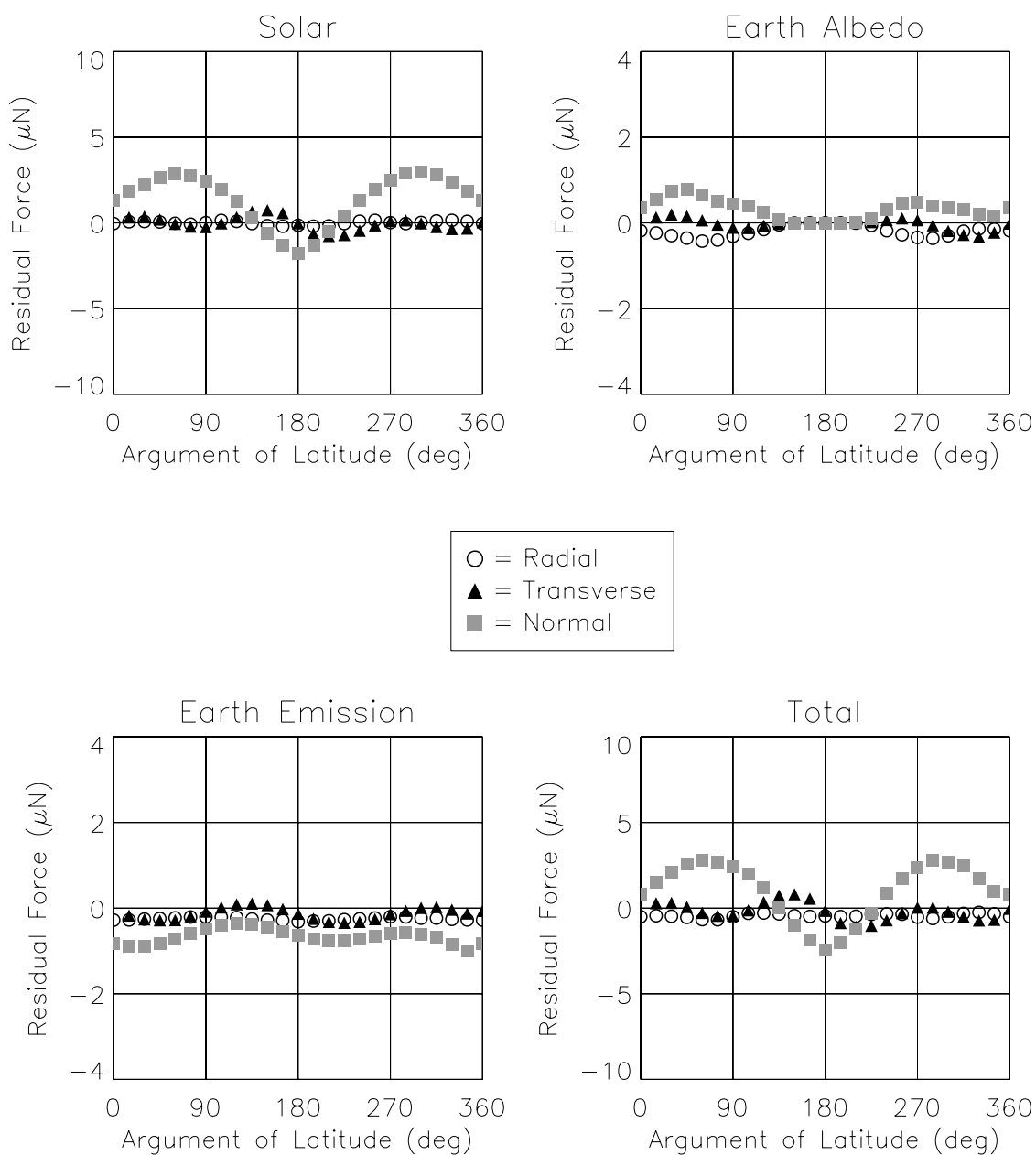


Figure 5.20. Case 37 Nominal EOL Residual Forces: $\beta' = 75^\circ$, Yaw = 90° (Sailboat), Fixed Arrays, Non-Eclipsing Orbit

5.3.4 POD Simulation

In their pre-launch study of the anticipated orbit errors for ICESat, Rim et al. (1999) simulated those from the solar and Earth radiation force models by introducing errors in the macro-model parameters, the alignments of the solar arrays, the Earth albedo and emissivity model parameters, and the eclipse duration. Following their approach, ten days of undifferenced Global Positioning System (GPS) carrier-phase ranges were generated by MSODP, at 60-sec intervals. The nominal BOL macro-model parameters in Table 5.3a were perturbed by applying a $\pm 5\%$ bias to each surface area, and 5% (1σ) random errors to the diffuse and specular reflectivities. Additional errors included:

- 1° (1σ) stochastic errors in the solar array pitch angles, with a 1-hr correlation time
- 1° biases in the alignments of the solar arrays
- 5% (1σ) random errors in the Earth albedo and emissivity model coefficients of Table 2.1
- 5-km (1σ) random error in the Earth shadow radius

Furthermore, the conical Earth shadow model described in Section 2.4 was chosen to determine the satellite eclipses.

After creating the double-difference high-low (DDHL) measurements, POD solutions were obtained for eight overlapping 30-hr arcs, using the unperturbed nominal BOL macro-model parameters in the BWSRP and BWERP models, and the cylindrical Earth shadow model of Section 2.4. The other dynamic models were the same as those used to generate the simulated data. For each arc, the

initial state was estimated, along with an atmospheric drag coefficient for each orbit revolution, and empirical one-cycle-per-revolution (1-cpr) transverse and normal forces (per unit mass) every six hours. Differencing the middle 24 hours of the propagated solution from each arc with the “truth” orbit produced during data generation provides a measure of the orbit errors associated with using the macro-model. Table 5.12 summarizes the RMS for each of the RTN components of these differences, along with their RSS, in six eight-day cases that span the nominal attitude control frames, and various orbit-Sun geometries, as characterized by the β' angle at the midpoint of the interval.

Case	β'	Control Frame	RMS Orbit Differences			
			Radial	Trans	Normal	3D RSS
1	+80°	1	0.2	0.4	1.6	1.7
2	+50°	1	0.2	0.4	0.9	1.0
3	+20°	0	0.5	1.0	0.2	1.1
4	−5°	2	0.5	1.0	0.1	1.1
5	−35°	3	0.3	0.4	0.6	0.8
6	−65°	3	0.2	0.5	1.7	1.8

Table 5.12. Original POD Simulation Orbit Errors (mm)

With the completion of the micro-model simulation and the determination of the macro-model parameters, it became possible, and desirable, to reexamine the orbit errors introduced by using the latter. Instead of perturbing parameters in the BWSRP and BWERP models, an experimental subroutine was developed, and implemented in MSODP, to allow the combined solar and Earth radiation force (per unit mass) to be computed from the total-force history output by the

micro-model simulation. Based on the β' angle and the argument of latitude at a given time, this force is obtained from a bi-linear interpolation of the RTN forces from the 40 cases in Tables 4.4 and 4.5, and the supplemental cases in Tables 4.6 and 4.7. The interpolated force vector is then rotated to the ICRF, divided by the mass of the satellite, and substituted for the \vec{S} and \vec{E} perturbations in Equation (1.12).

Using this force model instead of the BWSRP and BWERP models, ten days of undifferenced GPS carrier-phase ranges were again generated by MSODP, at 60-sec intervals, and combined to yield DDHL measurements. POD solutions were then obtained for eight 30-hr arcs, using the nominal BOL macro-model parameters of Table 5.3a in the BWSRP and BWERP models. The other dynamic models were the same as those used to generate the simulated data. The middle 24 hours of the propagated solution from each arc were again differenced with the “truth” orbit. Table 5.13 summarizes the RMS for each of the RTN components of these differences, and their RSS, for the cases in Table 5.12. For Cases 2-6, the RSS errors in the former are 0.1-1.5 mm larger than those in the latter, suggesting that the original POD simulation slightly underestimated the potential errors in radiation force modeling.

Case	β'	Control Frame	RMS Orbit Differences			
			Radial	Trans	Normal	3D RSS
1	+80°	1	0.2	0.3	0.5	0.7
2	+50°	1	0.6	0.9	1.1	1.5
3	+20°	0	1.1	0.9	1.0	1.8
4	−5°	2	1.2	1.0	0.6	1.6
5	−35°	3	0.9	1.0	1.9	2.3
6	−65°	3	0.6	0.8	1.7	1.9

Table 5.13. Macro–Micro Model Orbit Errors (mm)

Of course, such radiation force modeling errors do not occur in isolation. Rim et al. (1999) also simulated the orbit errors introduced by other dynamic models and by the measurement model:

- Gravitational errors, including solid-Earth and ocean-tide model errors
- Atmospheric drag errors, including density model errors
- DDHL model errors
- GPS ground station position errors
- GPS satellite orbit errors
- Reference frame errors

As before, they introduced these errors by applying random errors and biases to various parameters during the generation of the simulated data, and by using selected dynamic models (e.g., geopotential models) in the estimation of the orbit solutions different from those employed in the data generation. Applying this approach to the six cases in Table 5.12, ten days of undifferenced GPS carrier-phase ranges were first generated by MSODP, at 60-sec intervals, using the

nominal BOL macro-model parameters of Table 5.3a in the BWSRP and BWERP models. After creating the DDHL measurements, POD solutions were obtained for eight 30-hr arcs, using the same macro-model parameters. In this context, differencing the middle 24 hours of the propagated solution from each arc with the “truth” orbit provides a measure of the combined errors associated with these other dynamic and measurement models. Table 5.14 summarizes the RMS for each of the RTN components of these differences, and their RSS, for the cases in Table 5.12. These results do not include any radiation force modeling errors.

Case	β'	Control Frame	RMS Orbit Differences			
			Radial	Trans	Normal	3D RSS
1	+80°	1	147.9	371.6	145.4	425.6
2	+50°	1	133.2	346.2	147.3	399.1
3	+20°	0	125.0	327.8	138.5	377.2
4	−5°	2	143.8	364.4	139.4	415.8
5	−35°	3	131.6	335.9	135.6	385.4
6	−65°	3	144.3	362.8	141.9	415.5

**Table 5.14. Dynamic and Measurement Model Orbit Errors (mm):
No Radiation Force Model Errors**

Finally, the impact of using the macro-model was reconsidered in conjunction with these other dynamic and measurement model errors. Combining the approaches used to generate Tables 5.13 and 5.14, ten days of undifferenced GPS carrier-phase ranges were generated by MSODP, at 60-sec intervals, using the interpolated micro-model radiation forces. After creating the DDHL

measurements, POD solutions were obtained for eight 30-hr arcs, using the nominal BOL macro-model parameters from Table 5.3a. The middle 24 hours of the propagated solution from each arc were differenced with the “truth” orbit. Table 5.15 summarizes the RMS for each of the RTN components of these differences, and their RSS, for the cases in Table 5.12. These results now include the errors associated with using the macro-model, but differ from those in Table 5.14 by no more than ± 0.1 mm. This suggests that any tuning of the macro-model parameters during the mission may prove to be prohibitive, as the requisite error signals were clearly aliased to others and absorbed, presumably by the estimated atmospheric drag coefficients and/or the empirical forces.

Case	β'	Control Frame	RMS Orbit Differences			
			Radial	Trans	Normal	3D RSS
1	+80°	1	147.9	371.6	145.4	425.6
2	+50°	1	133.2	346.2	147.2	399.1
3	+20°	0	125.1	327.8	138.5	377.3
4	−5°	2	143.7	364.4	139.3	415.8
5	−35°	3	131.5	335.9	135.6	385.4
6	−65°	3	144.3	362.8	141.9	415.4

**Table 5.15. Dynamic and Measurement Model Orbit Errors (mm):
Including Macro–Micro Model Errors**

Chapter 6

Post-Launch Performance

6.1 Evaluation Periods

As of May 2007, the Geoscience Laser Altimetry System (GLAS) has completed 12 separate mapping campaigns, each typically lasting about 35 days. To evaluate the performance of the solar and Earth radiation force models in ICESat precision orbit determination (POD), eight-day intervals were selected from four of these campaigns. As shown in Table 6.1, each corresponds to one of the nominal attitude control frames, and to a particular orbit-Sun geometry, as characterized by the β' angle — defined in Section 3.4.2 — at the midpoint of the interval.

Campaign	Year	Days of Year	Control Frame	Mode	Yaw	β'
Laser 3c	2005	158–165	2	Airplane	0°	−9.4°
Laser 3d	2005	299–306	1	Sailboat	90°	+54.0°
Laser 3f	2006	160–167	0	Airplane	180°	+10.3°
Laser 3g	2006	305–312	3	Sailboat	270°	−47.8°

Table 6.1. Post-Launch POD Evaluation Periods

The campaign designation reveals which of the three GLAS lasers was being operated, and its relative order among the campaigns conducted with that laser. For example, Laser 3d denotes the fourth campaign (“d”) to use the third laser.

For each of these evaluation periods, double-difference high-low (DDHL) measurements were first derived from the Global Positioning System (GPS) carrier-phase data collected by the onboard receiver, as discussed in Chapter 1. These measurements were then processed by the Multi-Satellite Orbit Determination Program (MSODP) to obtain orbit solutions for eight overlapping 30-hr arcs in each period. Following the strategy developed by Rim and Schutz (2002) for operational ICESat POD, the initial conditions for each arc were estimated, along with the following parameters:

- An atmospheric drag coefficient for each orbit revolution
- Empirical one-cycle-per-revolution (1-cpr) transverse and normal forces (per unit mass) for each orbit revolution
- Ambiguity parameters for the DDHL measurements
- Zenith-delay parameters for the GPS ground stations
- The radial component of the ICESat GPS antenna offset from the satellite center of mass

The GPS satellite ephemerides were fixed to the final solutions generated by the International GNSS Service (IGS). The dynamic and measurement models used were those defined by Rim and Schutz (2002), with the exception of the geopotential model. Currently, MSODP employs the GRACE Gravity Model 01 (GGM01) (Tapley et al., 2004a) to compute the perturbations associated with the Earth's gravitational field. This study, however, adopted the more recently released GRACE Gravity Model 02 (GGM02) (Tapley et al., 2005) for the post-launch evaluation of the macro-model parameters.

Method	Macro-Model Parameter Set
Micro-Model Fit	Nominal BOL Attitude-Specific Nominal EOL
Area-Weighted Average	Solar Infrared Solar + Infrared

Table 6.2. Macro-Model Parameter Sets

Six POD solutions were produced for each of the evaluation periods in Table 6.1, using the macro-model parameter sets in Table 6.2. The first three of these sets were obtained through least-squares fits to the micro-model forces, as discussed in Section 5.3. They consist of (1) the nominal beginning-of-life (BOL) solution, in Table 5.3a; (2) the attitude-specific solutions, in Tables 5.7a through 5.10a; and (3) the nominal end-of-life (EOL) solution, in Table 5.11a. The remaining three sets in Table 6.2 were derived from the area-weighted average reflectivities in Table 5.2. They consist of (1) the solar spectral values, in the first column; (2) the infrared spectral values, in the second column; and (3) a numerical average of the solar and infrared spectral values. Mathematically, these sets correspond to substituting 1, 0, and 0.5, respectively, for χ in Equation (5.6).

The following sections assess the relative performance of these macro-model parameter sets by comparing the results obtained for various metrics typically used to evaluate POD solutions: (1) DDHL residuals, (2) orbit overlap differences, (3) satellite laser ranging (SLR) residuals, and (4) amplitudes of the estimated 1-cpr transverse and normal forces (per unit mass). The chapter

concludes with a look at the sensitivity of the POD solutions to changes in the macro-model parameters, gauged by differencing those generated with the nominal BOL parameters and those generated using each of the other sets.

6.2 DDHL Residuals

The POD solutions were obtained by processing the DDHL measurements in the MSODP epoch-state batch filter described in Chapter 1. Equation (1.29) furnished the corresponding observation residuals:

$$y_l = Y_l - Y_l^* = \text{DDHL}_{uw}^{pq} - \text{DDHL}_{uw}^{pq*} \quad (6.1)$$

Each “computed” DDHL measurement, denoted by the asterisk, was determined from Equation (1.18), using the fixed GPS satellite positions, the estimated ICESat position, and the estimated DDHL ambiguity. After calculating the root-mean-square (RMS) of these residuals for each arc, those for the eight arcs in each evaluation period of Table 6.1 were averaged to yield a mean RMS. Table 6.3 summarizes these statistics for the POD solutions generated with the various macro-model parameter sets of Table 6.2.

The results within each campaign exhibit only small variations, implying either that the differences among the macro-model sets had little impact on the DDHL residuals, or that the errors signals they produced were absorbed by one or more of the estimated parameters. Laser 3f displayed the most variability, while Laser 3g showed the least. Among the campaigns, the results differ at the sub-millimeter level, with Laser 3c yielding the lowest RMS values, and Laser 3f yielding the highest. Despite the small magnitudes of these differences, the

nominal BOL macro-model parameters performed best in the earlier Laser 3c and Laser 3d campaigns, while the nominal EOL parameters performed best for Laser 3f and Laser 3g (along with the attitude-specific solution). This suggests that the surface radiative properties may have degraded during the mission, moving closer to their EOL values. All of the results in Table 6.3, however, are approaching 10 mm, the noise level of the ICESat DDHL measurements, which, ultimately, limits the ability of this metric to discern the impact of the different macro-model parameter sets.

	Nominal BOL	Attitude Specific	Nominal EOL	Solar	Infrared	Solar + Infrared
Laser 3c	10.193	10.194	10.196	10.195	10.194	10.195
Laser 3d	10.300	10.301	10.303	10.302	10.302	10.302
Laser 3f	10.651	10.652	10.647	10.658	10.657	10.653
Laser 3g	10.204	10.203	10.203	10.204	10.205	10.204

Table 6.3. Mean DDHL Residual RMS (mm)

6.3 Orbit Overlap Differences

Each 30-hr arc in an evaluation period overlaps adjacent arcs, as illustrated in Figure 6.1. The middle 24 hours constitute the daily POD solution, but the three hours before and after this interval create overlaps, which allow the independently determined ephemerides to be compared. Although not a direct indicator of orbit accuracy, these comparisons do provide a measure of the

consistency, and thus, the precision, of the POD solutions. For this study, the ICESat positions, from the two common solutions in each 6-hr overlap, were differenced at their respective 30-sec intervals, and then rotated from the International Celestial Reference Frame (ICRF) to a Radial-Transverse-Normal (RTN) frame, shown in Figure 4.6. After calculating the RMS for each component of the RTN differences in each overlap, those for the seven overlaps in each evaluation period of Table 6.1 were averaged to yield mean RMS values. Table 6.4 summarizes these statistics, along with their root-sum-square (RSS), for the POD solutions generated with the various macro-model parameter sets of Table 6.2

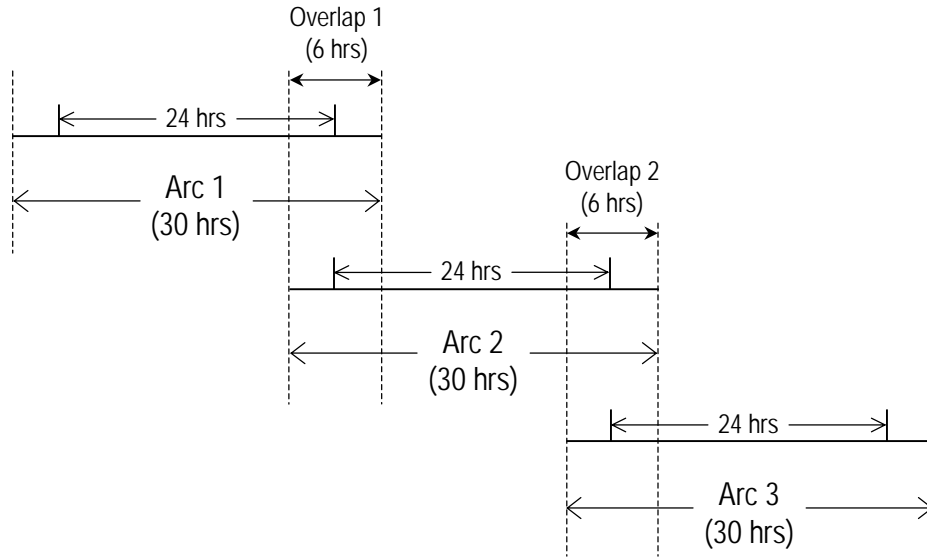


Figure 6.1. Orbit Overlaps

		Nominal BOL	Attitude Specific	Nominal EOL	Solar	Infrared	Solar + Infrared
Laser 3c	R	9.3	9.3	9.3	9.2	9.2	9.2
	T	11.7	11.7	11.7	11.7	11.7	11.6
	N	4.0	4.0	4.0	3.9	3.9	3.9
	3D	15.7	15.7	15.7	15.6	15.6	15.6
Laser 3d	R	5.5	5.4	5.5	5.3	5.2	5.2
	T	10.2	10.1	10.2	10.0	9.8	9.9
	N	5.9	5.9	5.9	5.9	5.9	5.9
	3D	13.2	13.1	13.3	13.0	12.8	12.9
Laser 3f	R	7.5	7.5	7.5	7.6	7.5	7.5
	T	12.7	12.7	12.7	12.9	12.7	12.8
	N	8.1	8.1	8.0	8.2	8.2	8.1
	3D	17.0	17.1	17.1	17.3	17.1	17.1
Laser 3g	R	5.0	5.0	5.0	5.0	5.0	5.0
	T	7.9	7.9	7.9	7.9	7.9	7.9
	N	5.9	5.9	5.9	5.9	5.9	5.9
	3D	11.2	11.3	11.2	11.2	11.3	11.2

**Table 6.4. Mean Orbit Overlap RMS (mm):
Radial (R), Transverse (T), Normal (N), 3D RSS (3D)**

Within each campaign, the results exhibit little to no variation, again implying either that the differences among the macro-model sets had little impact on the precision of the POD solutions, or that the error signals they produced were absorbed by one or more of the estimated parameters. Nonetheless, Laser 3c and Laser 3f, the two airplane-mode campaigns, produced similar results, as did the two sailboat-mode campaigns, Laser 3d and Laser 3g. This suggests that the precision may be influenced by satellite orientation, perhaps as it pertains to other perturbations, such as atmospheric drag, rather than solar and Earth radiation pressure.

6.4 SLR Residuals

Since the ICESat POD solutions are generated exclusively with the GPS data collected by its onboard receiver, any range measurements obtained from ground-based lasers constitute an independent set of observations with which to assess the accuracy of the GPS-derived orbits. Due to the sensitivity of the detectors in the GLAS instrument, such ranging to ICESat has been restricted to a relatively small number of stations in the International Laser Ranging Service (ILRS) network. This group has gradually expanded, as additional stations have demonstrated the ability to observe a 70° elevation limit during ranging, imposed to prevent sending laser energy directly into the GLAS telescope. Now numbering eight, these stations have steadily increased their tracking of ICESat over recent campaigns.

Figure 6.2 illustrates the geometry associated with these SLR observations. Rim and Schutz (2002) define the measurement model for the “computed” range to be

$$\rho_{slr} = |\vec{r} - \vec{r}_s| + \delta\rho_{atm} + \delta\rho_{rel} + \delta\rho_{com} \quad (6.2)$$

where \vec{r} and \vec{r}_s represent, respectively, the GPS-determined position vector of the satellite and the fixed position vector of the ground station. Both are represented in the International Terrestrial Reference Frame 2000 (ITRF2000) (Altamimi et al., 2002). The correction terms $\delta\rho_{atm}$, $\delta\rho_{rel}$, and $\delta\rho_{com}$ account, respectively, for tropospheric delay, general relativity effects, and the offset of the onboard laser retroreflector from the satellite center of mass (COM).

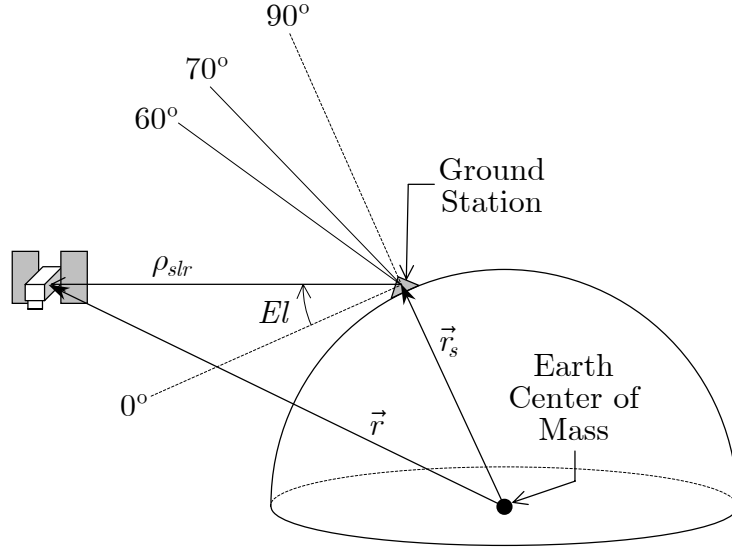


Figure 6.2. SLR Observation Geometry

The differences between the measured, or observed, ranges and those computed from Equation (6.2) represent a set of range residuals that can be determined for each pass over a ground station. For each evaluation period in Table 6.1, the number of observations from all of the ICESat passes was tallied, and the mean and the RMS of the resulting range residuals were computed. Table 6.5 summarizes these statistics for the POD solutions generated with the various macro-model parameter sets of Table 6.2.

		Nominal BOL	Attitude Specific	Nominal EOL	Solar	Infrared	Solar + Infrared
Laser 3c	Obs	379	379	379	379	379	379
	Mean	4.79	4.64	4.94	4.96	4.91	5.05
	RMS	19.17	19.11	19.12	19.19	19.22	19.15
Laser 3d	Obs	1923	1923	1923	1923	1923	1923
	Mean	-12.52	-12.51	-12.15	-12.71	-12.92	-12.62
	RMS	24.62	24.51	24.64	24.60	24.73	24.62
Laser 3f	Obs	3023	3024	3021	3024	3026	3022
	Mean	-7.99	-8.03	-7.69	-8.11	-7.99	-7.90
	RMS	25.99	26.04	26.24	26.12	26.11	26.19
Laser 3g	Obs	3135	3135	3135	3135	3135	3135
	Mean	3.48	3.49	3.37	3.56	3.61	3.55
	RMS	27.54	27.59	27.30	27.71	27.78	27.48

Table 6.5. SLR Residuals (mm): All Passes

Some of these passes are considered to be “high-elevation” passes, in which the satellite approaches zenith, as seen from the ground station. Figure 6.2 shows that, if the satellite passes directly overhead, and thus, attains an elevation (El) of 90° , the range vector from the station is nearly aligned with the satellite’s geocentric position vector. Consequently, the corresponding range residual provides a measure of the radial orbit error. Even with the elevation restrictions for ICESat, the range residuals obtained between 60° and 70° are a good approximation to this metric. The number of observations made at these elevations was tallied for each evaluation period in Table 6.1, and the mean and the RMS of the associated range residuals were computed. Table 6.6 summarizes these statistics for the POD solutions generated with the various macro-model parameter sets of Table 6.2.

		Nominal BOL	Attitude Specific	Nominal EOL	Solar	Infrared	Solar + Infrared
Laser 3c	Obs	9	9	9	9	9	9
	Mean	12.83	12.48	12.85	12.72	12.51	12.78
	RMS	13.30	12.94	13.32	13.18	12.96	13.23
Laser 3d	Obs	76	76	76	76	76	76
	Mean	−12.22	−12.15	−12.11	−12.28	−12.16	−12.22
	RMS	21.70	21.52	22.35	21.46	21.11	21.54
Laser 3f	Obs	105	105	105	105	105	105
	Mean	−7.54	−7.34	−7.72	−7.09	−7.01	−7.18
	RMS	19.92	19.77	20.45	19.79	19.61	19.98
Laser 3g	Obs	83	83	83	83	83	83
	Mean	5.91	5.45	5.95	6.14	6.30	6.12
	RMS	22.33	21.91	22.41	22.64	22.64	22.30

Table 6.6. SLR Residuals (mm): High-Elevation Passes

Although the results within each campaign, in both Tables 6.5 and 6.6, generally exhibit variations at the sub-millimeter level, they do show distinct differences. For Laser 3c and Laser 3d, the attitude-specific macro-model parameters yielded the lowest RMS values in Table 6.5. They only slightly underperformed the nominal BOL parameters in Laser 3f, while those for Laser 3g generated a noticeably higher RMS than the nominal EOL parameters. Considering only the high-elevation passes in Table 6.6, the attitude-specific parameters produced the lowest RMS values for Laser 3c and Laser 3g, implying that they yielded the smallest radial orbit errors. Those for the other two campaigns, however, underperformed the infrared area-weighted reflectivities from Table 5.2 — slightly in Laser 3f, but more significantly in Laser 3d. Still, the maximum improvement obtained from *any* macro-model set with respect to

the nominal BOL parameters, which are currently in use for operational ICESat POD, was 0.24 mm, in Table 6.5, and 0.42 mm, in Table 6.6. Both of these results occurred in Laser 3g, the most recent of the evaluation periods, again suggesting that the surface radiative properties may have degraded during the mission.

6.5 Empirical Forces

In addition to the perturbations represented in Equation (1.12), empirical forces (per unit mass) can be estimated in MSODP to account for unmodeled, or mismodeled, forces within the dynamic model. These can take the form of 1-cpr radial (R), transverse (T), and normal (N) functions:

$$\begin{aligned} f_r &= (R_c \cos u + R_s \sin u) \hat{R} \\ f_t &= (T_c \cos u + T_s \sin u) \hat{T} \\ f_n &= (N_c \cos u + N_s \sin u) \hat{N} \end{aligned} \tag{6.3}$$

where u is the satellite's argument of latitude. For each normalized force f , the subscripts c and s distinguish the coefficients of the cosine and sine components, respectively. Following the approach adopted for operational ICESat POD, only the coefficients for the transverse and normal components were estimated, once per orbit revolution, during each evaluation period in Table 6.1. The amplitudes were then computed from each pair of these coefficients,

$$T = \sqrt{T_c^2 + T_s^2} \quad N = \sqrt{N_c^2 + N_s^2} \tag{6.4}$$

			Nominal BOL	Attitude Specific	Nominal EOL	Solar	Infrared	Solar + Infrared
Laser 3c	T	Mean RMS	6.20 7.34	6.25 7.37	8.28 9.93	6.31 7.42	8.19 8.94	5.92 7.31
	N	Mean RMS	8.70 10.09	8.70 10.07	8.61 9.96	8.61 9.91	8.62 9.94	8.60 9.90
Laser 3d	T	Mean RMS	3.05 3.54	3.02 3.48	3.98 4.49	7.42 7.76	7.58 7.92	7.92 8.24
	N	Mean RMS	9.36 10.51	9.32 10.47	9.17 10.27	9.53 10.68	9.91 11.07	9.33 10.48
Laser 3f	T	Mean RMS	6.77 7.34	7.21 7.76	4.74 5.29	7.22 7.78	10.55 10.98	5.70 6.32
	N	Mean RMS	9.67 11.23	9.63 11.19	9.51 11.06	9.48 11.05	9.49 11.06	9.44 11.01
Laser 3g	T	Mean RMS	3.83 4.27	3.45 3.89	5.42 5.83	9.00 9.30	9.31 9.59	9.50 9.78
	N	Mean RMS	10.41 11.85	10.33 11.81	10.28 11.96	10.74 12.06	11.00 12.26	10.46 11.87

**Table 6.7. Amplitudes of Estimated Empirical Forces (Per Unit Mass) (nm/s²):
Transverse (T) and Normal (N)**

Table 6.7 summarizes the mean and RMS of the derived amplitudes for the POD solutions generated with the various macro-model parameter sets of Table 6.2.

Generally, smaller amplitudes for these empirical forces (per unit mass) indicate that the dynamic models have more accurately represented the forces acting on the satellite. Accordingly, in Table 6.7, a smaller RMS for a particular macro-model set, within a given campaign, suggests that those parameters produced more accurate solar and Earth radiation forces. The RMS of the normal amplitudes, in all of the evaluation periods, displays significantly less variability

than that for the transverse amplitudes, implying that the latter is much more influenced by the macro-model parameters. Thus, considering only the RMS of the transverse amplitudes, the attitude-specific parameter sets outperformed the others in Laser 3d and Laser 3g, and only slightly underperformed the averaged solar and infrared parameter set in Laser 3c. For Laser 3f, however, these parameters produced a significantly lower RMS for the transverse amplitudes than the nominal EOL parameters. Nonetheless, as with the SLR residuals, the maximum improvement in these empirical forces, with respect to the nominal BOL parameters, was generally small — less than 0.1 nm/s^2 , in both Laser 3c and Laser 3d, increasing only to 0.38 nm/s^2 , in Laser 3g. The comparatively dramatic improvement observed in Laser 3f — 2.05 nm/s^2 — clearly stands out, suggesting that errors in the nominal BOL parameters for the more exposed macro-model surfaces in this attitude orientation were larger than in the others.

6.6 Orbit Differences

Finally, to examine their sensitivity to the macro-model parameters, the POD solutions obtained with the nominal BOL set were differenced with those generated using the five other parameter sets in Table 6.2. For each evaluation period of Table 6.1, the middle 24 hours of each arc were extracted and concatenated. The ICESat positions, from the two eight-day solutions being compared, were differenced at their respective 30-sec intervals, and then rotated from the ICRF to the RTN frame. Table 6.8 summarizes the RMS for each component of these RTN differences, along with their RSS, for the POD solutions generated with the corresponding macro-model parameter set in Table 6.2.

Not surprisingly, the nominal EOL parameters, which differ most from the nominal BOL parameters, yielded the largest differences, at least in the first three evaluation periods. The infrared parameters from Table 5.2, however, generated the largest differences in Laser 3g, and substantial differences in Laser 3d. Furthermore, the results from these two sailboat-mode campaigns display more variability than those obtained from the two airplane-mode campaigns, Laser 3c and Laser 3f, which suggests that their POD solutions were more sensitive to the macro-model parameters.

		Attitude Specific	Nominal EOL	Solar	Infrared	Solar + Infrared
Laser 3c	R	0.2	1.4	0.4	0.5	0.6
	T	0.3	1.4	0.8	0.8	0.3
	N	0.1	0.7	1.1	0.9	1.2
	3D	0.4	2.1	1.4	1.3	1.4
Laser 3d	R	0.2	1.0	0.7	1.1	0.5
	T	0.2	1.2	0.7	1.4	0.7
	N	0.1	3.9	0.8	3.3	0.4
	3D	0.3	4.2	1.2	3.8	0.9
Laser 3f	R	0.3	1.5	0.4	0.5	0.7
	T	0.5	1.6	0.8	0.8	0.7
	N	0.1	0.7	1.2	1.0	1.3
	3D	0.6	2.3	1.6	1.4	1.7
Laser 3g	R	0.2	0.7	0.7	0.9	0.5
	T	0.2	0.5	0.9	1.0	0.8
	N	0.2	3.3	1.5	3.4	1.0
	3D	0.3	3.4	1.9	3.7	1.3

**Table 6.8. RMS Orbit Differences from Nominal BOL Solution (mm):
Radial (R), Transverse (T), Normal (N), 3D RSS (3D)**

Chapter 7

Conclusions

7.1 Summary

Prior to the launch of ICESat, Rim et al. (1999) conducted a detailed review of the dynamic models to be used in precision orbit determination (POD), and concluded that the overall orbit error would be dominated by geopotential and atmospheric-drag modeling errors. They estimated that the contributions from solar and Earth radiation force models would be limited to 1 mm in the radial component, and 2 mm overall. These results, however, were obtained by biasing and randomly varying the parameters of existing models, including a simplified representation of the satellite, designated the macro-model. This approach postulated that the actual radiation pressure environment could be characterized as a small perturbation of the modeled one. To evaluate this assumption, this study first developed a high-fidelity simulation of the solar and Earth radiation forces acting on ICESat, using a detailed model of the satellite, called the micro-model.

Although developed by thermal engineers at the Ball Aerospace and Technologies Corporation (BATC), the ICESat micro-model also includes features of the onboard instrument, the Geoscience Laser Altimetry System (GLAS), adapted from a separate model designed by the Goddard Space Flight Center (GSFC). Created with the commercially available Thermal Synthesizer System (TSS), it consists of 950 surfaces, of different shapes and sizes, that have

been subdivided into 2058 nodes, 1124 of which can receive external radiation. The TSS software employs a Monte Carlo Ray Tracing Method (MCRT) method to calculate various quantities related to heat transfer. The current vendor, in consultation with the University of Texas Center for Space Research (UT/CSR), extended this approach to compute solar and Earth radiation forces. Using this modified software, these forces were generated for all of the anticipated ICESat attitude and orbit-Sun geometries.

To model Earth radiation forces with the macro-model, a new subroutine was developed and implemented in the Multi-Satellite Orbit Determination Program (MSODP). Like its predecessor for solar radiation forces, this new model separately calculates, and then sums, the forces acting on each surface of a six-sided box, representing the satellite bus and instrument, and two wings, representing the two ICESat solar arrays. The area, diffuse reflectivity, and specular reflectivity for each of these surfaces were determined through an innovative least-squares method (LSEI), developed by Haskell and Hanson (1981), that incorporates linear equality and inequality constraints directly into the minimization problem. In fitting the forces generated by the micro-model simulation, these constraints ensured that the estimated macro-model parameters were feasible. Two of the solutions obtained spanned all satellite attitude and orbit-Sun geometries, one fitting the micro-model forces computed using the beginning-of-life (BOL) radiative properties, and the other fitting those derived with the end-of-life (EOL) radiative properties. A third solution actually comprised four different solutions, each uniquely determined for one of the

nominal ICESat attitudes, and based on fits to an appropriate subset of the micro-model forces.

Finally, daily POD solutions were generated for selected eight-day intervals in each of four different ICESat campaigns, using these macro-model solutions. Each of these evaluation periods involved a different satellite attitude and orbit-Sun geometry. Three other sets of macro-model parameters were also considered, derived directly from the micro-model through area-weighted averaging of its component reflectivities. One of these sets relied exclusively on the solar spectral reflectivities, while another relied exclusively on the infrared spectral reflectivities. A third set numerically averaged these values. The POD solutions computed with these six macro-model parameter sets were assessed in terms of the Global Positioning System (GPS) double-difference high-low (DDHL) residuals, orbit overlap differences, satellite laser ranging (SLR) residuals, and the amplitudes of estimated empirical forces. In addition, their sensitivity to these parameters was investigated by comparing the orbit determined with the BOL macro-model parameters to those obtained with each of the other parameter sets.

7.2 Conclusions

The MCRT algorithm developed to determine the solar and Earth radiation forces acting on ICESat proved to be a robust and flexible approach. Although prohibitive in its computational intensity, this method allowed for the modeling of arbitrarily complex shapes, and implicitly accounted for the shadowing of surfaces by others within the satellite model. Furthermore, its

random sampling of the Earth, as a distributed radiation source, provided a detailed rendering of the terminator, and enhanced the resolution of the planet's albedo and emissivity. These advantages combined to yield improved predictions of the radiation forces experienced by a satellite in low-Earth orbit, relative to previously available techniques.

The implementation of the LSEI algorithm to determine the ICESat macro-model parameters resulted from frustration with an earlier Bayesian least-squares method, in which the *a priori* covariance required periodic adjustment to achieve a feasible solution. The unambiguous approach offered by this new formulation greatly simplified the search for physically realistic parameters. Despite the mathematical contortions involved with its solution, the algorithm proved to be highly efficient, allowing for rapid parameterization. This, combined with the direct framing of the constraints, significantly increased the number of cases that could be considered.

In the pre-launch assessment, the attitude-specific macro-model solutions produced considerably better fits to the micro-model forces than the nominal BOL solution for the two airplane-mode orientations, but slightly worse fits for the orthogonal sailboat modes. The post-launch analysis, however, revealed that these solutions actually performed better in the latter, at least in terms of the amplitudes of the estimated empirical forces. This incongruity suggests that the micro-model simulation may not have sufficiently characterized the actual solar and Earth radiation forces, most likely due to inaccurate, or incomplete, data regarding the radiative properties of the micro-model surfaces. In particular, the

assumption made regarding specularity, in the absence of available measurements, may have introduced unanticipated errors.

Alternatively, the discrepancy between these pre-launch and post-launch results may indicate that the macro-model parameters were not robust enough to fit the micro-model forces adequately in the sailboat modes. Due to the limited motion of the solar arrays in these orientations, the parameters may simply be less observable than in the airplane-mode attitudes. The post-launch evaluation, however, also revealed that the POD solutions from the sailboat-mode campaigns were more sensitive to changes in the macro-model parameters. This could reflect a deficiency in the structure of the macro-model, perhaps related to the use of a single set of diffuse and specular reflectivities to compute the solar and Earth radiation forces acting on each surface. By not distinguishing between reflective characteristics for solar and infrared radiation, the macro-model reflectivities effectively average, in some sense, both of them. With significantly less area exposed to infrared radiation in the sailboat-mode attitudes, these reflectivities could be significantly biased in favor of solar radiation.

An important question is whether the macro-model parameters obtained by fitting the micro-model forces outperformed those derived through area-weighted averaging of the micro-model reflectivities. Even after discounting the time required to develop the methods needed to simulate the micro-model forces, significant time and resources were expended in the generation of those data sets. The post-launch evaluation indicated that, as a group, the fitted parameters did perform slightly better than the averaged parameters, as measured by the SLR residuals and the amplitudes of the estimated empirical forces. In particular, the

performance of the attitude-specific macro-model sets suggests that unique parameters for each campaign may be optimal, tailoring the modeled solar and Earth radiation forces to a particular satellite attitude and orbit-Sun geometry, while accounting for any degradation in radiative properties with time.

Ultimately, though, the impact of the macro-model parameters on the accuracy of ICESat POD was limited to the sub-millimeter level, as measured by the SLR residuals. The frequent estimation of empirical forces, along with atmospheric drag coefficients, undoubtedly absorbed some of the error signals generated by the different macro-model sets, leading to a relative lack of differentiation in their overall performance. Given that such parameters are necessary to mitigate geopotential and atmospheric drag errors, they will remain an essential feature of ICESat POD. Consequently, any adjustment of the macro-model parameters will likely have only a limited impact on the accuracy of the resulting orbit solutions. Furthermore, since the SLR residuals indicate that that accuracy is currently at the 2-3 cm level, well within the mission requirements, no change to the nominal BOL macro-model parameters is warranted.

7.3 Recommendations

Although tuning the macro-model parameters may do little to improve the accuracy of ICESat POD solutions at present, the process itself provides insight into the factors affecting the observability of those parameters, and their relationships to others within the dynamic model. As orbit accuracy requirements for geodetic satellites increase, such lessons may prove useful for future missions, in which tuning becomes necessary. Marshall and Lutheke (1994b) succeeded in

doing this for a subset of the TOPEX/Poseidon macro-model parameters, using only SLR and Doppler tracking data. Kubitschek and Born (1999) later modified the representation of the solar array in that model to account for thermally induced warping and deployment deflections, further improving its performance.

As discussed in Chapter 1, however, the lower altitude of ICESat significantly increases the geopotential and atmospheric drag perturbations, along with the orbit errors introduced by their models. Despite the availability of global GPS tracking data, simulations prior to launch suggested that the frequent estimation of empirical parameters, required to compensate for such errors, would likely absorb, or corrupt, the comparatively small macro-model error signals, making any tuning of its parameters nearly infeasible. Recently, however, atmospheric drag at the ICESat altitude has declined so dramatically, in response to the periodic cycle of solar activity, that solar radiation now represents the dominant non-gravitational perturbation acting on the satellite. This, combined with the release of the GRACE Gravity Model 02 (GGM02) by Tapley et al. (2005), offers a unique opportunity to revisit the tuning of the ICESat macro-model parameters. A preliminary study by Rim et al. (2007) looked primarily at the reflectivities of the solar arrays, as they were expected to undergo the most significant change during the mission. Their results indicate that such tuning is possible, and could be extended to other macro-model parameters.

Appendix A

GLAS Laser Reference Point

The laser reference point (LRP) of the Geoscience Laser Altimeter System (GLAS) coincides with the origin of the body-fixed GLAS coordinate system (GCS), which is attached to the optical bench of the instrument. Equation (1.11) defines its position in the International Celestial Reference Frame (ICRF) as a function of time, $\vec{r}_{lrp}^{icrf}(t)$. The accuracy of this knowledge depends on errors from several sources:

- Precision orbit determination (POD) of the ICRF position of the satellite center of mass (COM), $\vec{r}_{com}^{icrf}(t)$
- Pre-launch measurement of the position of the LRP in the spacecraft coordinate system (SCS), \vec{r}_{lrp}^{scs}
- Modeling of the SCS position of the COM, $\vec{r}_{com}^{scs}(t)$
- Pre-launch alignment and attitude determination components of the SCS-to-ICRF transformation, $T_{scs}^{icrf}(t)$

The following sections demonstrate that the last three sources have errors that combine to contribute less than 1.3 cm to the total error in the ICRF position of the LRP. Thus, its accuracy is essentially determined by the first source, the POD techniques used to estimate the ICRF position of the satellite COM.

A.1 Laser Reference Point (GCS)

Prior to the launch of ICESat, Sun and Marzouk (2003) measured the position of the SCS origin in the GCS,

$$\vec{r}_{gcs_0 \rightarrow scs_0}^{gcs} = \begin{bmatrix} -2181.71 \\ -0.05 \\ 134.59 \end{bmatrix} \text{mm} \quad (\text{A.1})$$

with an accuracy of ± 0.6 mm in each axis. The vector from the SCS origin to the LRP (i.e., the GCS origin), in the GCS, is the opposite of this vector,

$$\vec{r}_{lrp}^{gcs} = \vec{r}_{scs_0 \rightarrow gcs_0}^{gcs} = \begin{bmatrix} 2181.71 \\ 0.05 \\ -134.59 \end{bmatrix} \text{mm} \quad (\text{A.2})$$

Since the pre-launch range bias of Equation (1.10) was measured with respect to the LRP, any error in its GCS position would produce a residual range bias requiring calibration in orbit.

A.2 Center of Mass (SCS)

Also prior to launch, the Ball Aerospace and Technologies Corporation (BATC) conducted a series of verification tests that included the measurement of the COM for the combined ICESat bus and GLAS instrument configuration, in the SCS. Subsequent error analyses concluded that this measurement had an accuracy of ± 2 mm in the $+x_{scs}$ and the $+y_{scs}$ axes, and ± 3 mm in the $+z_{scs}$ axis (Debevec, 2002). After launch, as orbit maintenance maneuvers are

performed and propellant is expelled, the COM moves gradually, and mainly, along the $+z_{scs}$ axis. Using models developed by BATC, the Laboratory for Atmospheric and Space Physics (LASP) at the University of Colorado at Boulder updates its SCS position following each maneuver. These values are input directly into the Multi-Satellite Orbit Determination Program (MSODP). Iacometti (2002) estimated that these modeled positions have an accuracy of ± 5 mm in each axis, which includes the above uncertainties in the original measurement.

A secondary, periodic motion of the satellite COM in the SCS occurs due to the motion of the solar arrays, whose own centers of mass are offset from their rotation axes. Pre-launch analyses concluded that, at the start of the mission, this effect would be limited to ± 0.68 mm along the $+x_{scs}$ axis and ± 1.36 mm along the $+z_{scs}$ axis. By the end of the mission, they predicted that these values would be ± 0.74 mm along the $+x_{scs}$ axis and ± 1.47 mm along the $+z_{scs}$ axis. Consequently, the solar array contribution was not modeled in MSODP.

A.3 SCS to ICRF Transformation

Equation (1.11) makes use of $T_{icrf}^{scs}(t)$, the transformation from the ICRF to the SCS. This matrix is the transpose of the satellite attitude, which can be decomposed into two separate rotations,

$$T_{scs}^{icrf}(t) = T_{gcs}^{icrf}(t) \cdot T_{scs}^{gcs} \quad (\text{A.3})$$

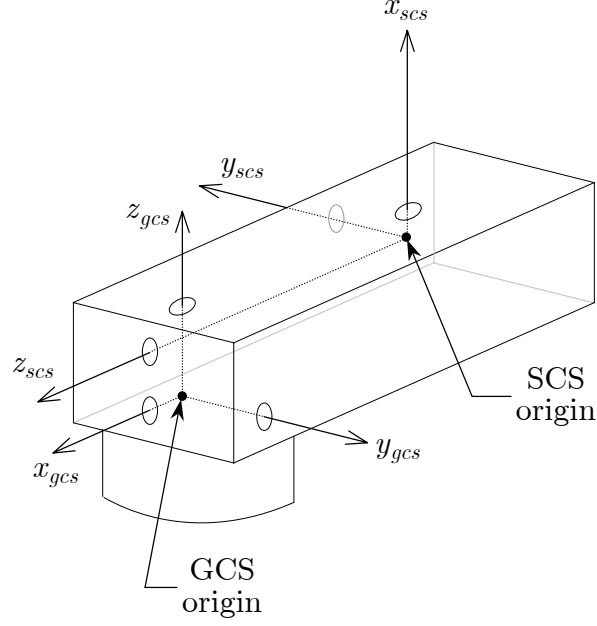


Figure A.1. Relative SCS and GCS Orientations

In Equation (A.3), $T_{gcs}^{icrf}(t)$ represents the time-series of attitude solutions describing the ICRF orientation of the GCS, which are routinely generated through ground-based precision attitude determination (PAD). T_{scs}^{gcs} , on the other hand, is a constant rotation matrix, characterizing the alignment of the SCS and the GCS. The idealized, relative orientation of these two frames are shown in Figure A.1, and the corresponding transformation between them is simply,

$$T_{scs}^{gcs} = \begin{bmatrix} 0 & 0 & 1 \\ 0 & -1 & 0 \\ 1 & 0 & 0 \end{bmatrix} \quad (\text{A.4})$$

In reality, the GCS axes are not precisely parallel to those of the SCS. Expressing Equation (A.4) as a 3-2-3 combination of elementary rotations,

$$T_{scs}^{gcs} = R_z(180^\circ) R_y(-90^\circ) R_z(0^\circ) \quad (\text{A.5})$$

and allowing each of the angles to be perturbed by a small value, the nominal SCS-to-GCS transformation becomes

$$T_{scs}^{gcs} = R_z(180^\circ + \delta\varphi) R_y(-90^\circ + \delta\theta) R_z(0^\circ + \delta\psi) \quad (\text{A.6})$$

where

$$\begin{aligned} R_z(180^\circ + \delta\varphi) &= \begin{bmatrix} \cos(180^\circ + \delta\varphi) & -\sin(180^\circ + \delta\varphi) & 0 \\ \sin(180^\circ + \delta\varphi) & \cos(180^\circ + \delta\varphi) & 0 \\ 0 & 0 & 1 \end{bmatrix} \\ R_y(-90^\circ + \delta\theta) &= \begin{bmatrix} \cos(180^\circ + \delta\theta) & 0 & \sin(180^\circ + \delta\theta) \\ 0 & 1 & 0 \\ -\sin(180^\circ + \delta\theta) & 0 & \cos(180^\circ + \delta\theta) \end{bmatrix} \\ R_z(0^\circ + \delta\psi) &= \begin{bmatrix} \cos \delta\psi & -\sin \delta\psi & 0 \\ \sin \delta\psi & \cos \delta\psi & 0 \\ 0 & 0 & 1 \end{bmatrix} \end{aligned} \quad (\text{A.7})$$

Multiplying these matrices per Equation (A.6), and applying trigonometric reductions, yields

$$T_{scs}^{gcs} = \begin{bmatrix} C\psi S\theta C\varphi - S\psi S\varphi & -S\psi S\theta C\varphi - C\psi S\varphi & C\theta C\varphi \\ -C\psi S\theta S\varphi - S\psi C\varphi & S\psi S\theta S\varphi - C\psi C\varphi & -C\theta S\varphi \\ C\psi C\theta & -S\psi C\theta & -S\theta \end{bmatrix} \quad (\text{A.8})$$

where C and S represent the cosine and sine, respectively, of the associated perturbation angle (e.g., $C\psi = \cos\delta\psi$). Hill et al. (2002) inferred these angles from pre-launch measurements made using alignment cubes placed on the GLAS optical bench and the satellite bus:

$$\begin{aligned}\delta\varphi &= -336'' \\ \delta\theta &= -834'' \\ \delta\psi &= +1578''\end{aligned}\tag{A.9}$$

A.4 Combined Errors

Substituting Equation (A.3) into Equation (1.11), the second term on the right-hand side becomes

$$\vec{r}_{com \rightarrow lrp}^{icrf} = T_{gcs}^{icrf}(t) \cdot T_{scs}^{gcs} [\vec{r}_{lrp}^{scs} - \vec{r}_{com}^{scs}(t)]\tag{A.10}$$

which represents the offset of the LRP from the COM in the ICRF, as computed by MSODP for ICESat POD. In this context, errors introduced by the $T_{gcs}^{icrf}(t)$ matrix in Equation (A.10) are negligible, given the 1.5-arcsec accuracy requirement imposed on — and achieved by — the PAD processing. The remaining terms constitute the LRP offset from the COM in the GCS,

$$\vec{r}_{com \rightarrow lrp}^{gcs} = T_{scs}^{gcs} [\vec{r}_{lrp}^{scs} - \vec{r}_{com}^{scs}(t)]\tag{A.11}$$

For this calculation, MSODP uses the idealized SCS-to-GCS transformation from Equation (A.4). The SCS position of the LRP is obtained by multiplying the GCS vector of Equation (A.2) by the same transformation,

$$\vec{r}_{lrp}^{scs} = \vec{r}_{scs_0 \rightarrow gcs_0}^{scs} = T_{gcs}^{scs} \cdot \vec{r}_{scs_0 \rightarrow gcs_0}^{gcs} = \begin{bmatrix} -134.59 \\ -0.05 \\ 2181.71 \end{bmatrix} \text{mm} \quad (\text{A.12})$$

At the start of the mission, denoted t_0 , the predicted SCS position of the COM is

$$\vec{r}_{com}^{scs}(t_0) = \begin{bmatrix} 51.74 \\ 3.72 \\ 980.29 \end{bmatrix} \text{mm} \quad (\text{A.13})$$

Assuming that the propellant is fully depleted at the end of the mission, denoted t_f , the COM position in the SCS is predicted to move to

$$\vec{r}_{com}^{scs}(t_f) = \begin{bmatrix} 56.20 \\ 4.04 \\ 1049.86 \end{bmatrix} \text{mm} \quad (\text{A.14})$$

Combining the SCS-to-GCS transformation of Equation (A.4), the SCS LRP position of Equation (A.12), and the SCS COM position at t_0 from Equation (A.13), Equation (A.11) yields

$$\vec{r}_{com \rightarrow lrp}^{gcs}(t_0) = \begin{bmatrix} 1201.42 \\ 3.77 \\ -186.33 \end{bmatrix} \text{mm} \quad (\text{A.15})$$

Similarly, for the SCS COM position at t_f from Equation (A.14),

$$\vec{r}_{com \rightarrow lrp}^{gcs}(t_f) = \begin{bmatrix} 1131.85 \\ 4.09 \\ -190.79 \end{bmatrix} \text{mm} \quad (\text{A.16})$$

The errors associated with using the idealized SCS-to-GCS transformation can be determined by comparing the offset from either Equation (A.15) or (A.16) to the result computed with the transformation of Equation (A.8). First, expressing Equation (A.11) as

$$\vec{r}_{com \rightarrow lrp}^{gcs} = \vec{r}_{lrp}^{gcs} - T_{scs}^{gcs} \cdot \vec{r}_{com}^{scs}(t) \quad (\text{A.17})$$

Combining the GCS LRP position of Equation (A.2), the transformation of Equation (A.8), and the SCS COM position at t_0 from Equation (A.13), Equation (A.17) yields

$$\vec{r}_{com \rightarrow lrp}^{gcs}(t_0) = \begin{bmatrix} 1201.23 \\ 5.76 \\ -182.34 \end{bmatrix} \text{mm} \quad (\text{A.18})$$

Similarly, for the SCS COM position at t_f from Equation (A.14),

$$\vec{r}_{com \rightarrow lrp}^{gcs}(t_f) = \begin{bmatrix} 1131.64 \\ 6.23 \\ -186.51 \end{bmatrix} \text{mm} \quad (\text{A.19})$$

Differencing Equations (A.18) and (A.15), and Equations (A.19) and (A.16), yields errors with magnitudes of 4.47 mm at the start of the mission, and 4.79 mm at the end. To assess the impact of other errors in Equation (A.11), all combinations of the uncertainties in the GCS LRP position, and in the modeling of the SCS COM position, were applied, along with the known mismodeling introduced by ignoring the solar array articulation in the latter. In each case, the result from Equation (A.11) was differenced with the corresponding value from

either Equation (A.18) or (A.19). The magnitudes of the largest errors were 11.87 mm at the start of the mission, and 12.19 mm at the end. In both cases, most of this error lies along the $+z_{gs}$ axis, implying that it would contribute to radial orbit error. The estimation of a COM offset along this axis during POD, however, should substantially reduce its impact. As a result, the accuracy of the LRP position in the ICRF is effectively the same as that obtained for the COM.

Appendix B:

Box-Wing Earth Radiation Pressure Partial Derivatives

The need to differentiate the equation of motion with respect to the state vector parameters is implicit in the epoch-state batch filter, described in Section 1.3. Collectively, these partial derivatives constitute the matrix $A(t)$, as defined by Equation (1.25), and through Equation (1.27), they dictate the state transition matrix $\Phi(t, t_0)$. At each observation time t , Φ maps the partial derivatives of the observation equation, defined as the matrix $\tilde{H}(t)$ by Equation (1.31), to the epoch time t_0 , yielding the matrix H in Equation (1.34).

Not all of the state vector parameters of Equation (1.19) appear in each of the perturbation models on the right-hand side of Equation (1.12). Some are common to several, or all, of the models. For these parameters, the corresponding partial derivative must be accumulated from the contributions made by the relevant models. Others are limited to a single model, so the partial derivatives do not need to be accumulated at a given observation time. This appendix provides the equations for the contributions from the Multi-Satellite Orbit Determination Program (MSODP) Box-Wing Earth Radiation Pressure (BWERP) model, including derivatives with respect to the satellite position, the macro-model surface properties, the Earth radiation scale factors, and the coefficients that appear in the albedo and emissivity models.

B.1 Satellite Position

Following the approach adopted by Knocke (1989) in the implementation of the MSODP Earth Radiation Pressure (ERADP) model of Equation (3.23), several simplifications were made in the BWERP subroutine to compute the Earth radiation contribution to the partial derivative of the equation of motion with respect to the satellite position. For this calculation *only*, the visible portion of the Earth is treated as a single surface, rather than divided into area elements. The subsatellite point lies at the center, and through Equations (2.36) and (2.37), its latitude dictates the albedo a and the emissivity e , which are then assumed to be uniform. Consequently, for $N = 1$ in Equation (3.26), the force per unit mass reduces to

$$\begin{aligned} \vec{E} = & -2(1 - \cos \theta_{max}) \frac{S_{\odot}}{c} \left(\frac{R}{R_{\odot}} \right)^2 \frac{1}{m} \left[\gamma_{\oplus}^a a (\hat{r} \cdot \hat{R}_{\odot}) + \gamma_{\oplus}^e \frac{e}{4} \right] \\ & \times \sum_{k=1}^K A_k \cos \theta_k (t_1^k \hat{n}_k - t_2^k \hat{r}) \end{aligned} \quad (\text{B.1})$$

where

$$t_1^k = 2 \left(\frac{\delta_k}{3} + \rho_k \cos \theta_k \right) \quad t_2^k = 1 - \rho_k \quad (\text{B.2})$$

In this modified geometry, the normal to the single Earth element \hat{n}_{\oplus}^i is the geocentric unit position vector \hat{r} , and the unit source vector \hat{s}_{\oplus}^i , from the satellite to the element, is the opposite, $-\hat{r}$. Furthermore, the $\cos \theta_k$ term has replaced $\hat{n}_k \cdot \hat{s}_{\oplus}^i (= -\hat{n}_k \cdot \hat{r})$.

To obtain the derivative with respect to the satellite position, Equation (B.1) can first be written as

$$\vec{E} = A' B \sum_{k=1}^K A_k \cos \theta_k (t_1^k \hat{n}_k - t_2^k \hat{r}) \quad (\text{B.3})$$

The projected attenuated area of Equation (3.18) is now simply

$$A' = 2(1 - \cos \theta_{max}) \quad (\text{B.4})$$

and

$$B = -\frac{S_\odot}{c} \left(\frac{R}{R_\odot} \right)^2 \frac{1}{m} \left[\gamma_\oplus^a a_1 (\hat{r} \cdot \hat{R}_\odot) + \gamma_\oplus^e \frac{e_1}{4} \right] \quad (\text{B.5})$$

Neglecting the contributions made through the $\cos \theta_k$ terms, the derivative of Equation (B.3) with respect to the satellite position vector \vec{r} is

$$\begin{aligned} \frac{\partial \vec{E}}{\partial \vec{r}} &= B \sum_{k=1}^K A_k \cos \theta_k (t_1^k \hat{n}_k - t_2^k \hat{r}) \frac{\partial A'}{\partial \vec{r}} \\ &+ A' \sum_{k=1}^K A_k \cos \theta_k (t_1^k \hat{n}_k - t_2^k \hat{r}) \frac{\partial B}{\partial \vec{r}} + A' B \frac{\partial}{\partial \vec{r}} \left[\sum_{k=1}^K A_k \cos \theta_k (t_1^k \hat{n}_k - t_2^k \hat{r}) \right] \end{aligned} \quad (\text{B.6})$$

After substituting Equations (B.4) and (B.5), applying the definition of θ_{max} from Equation (3.19), computing the necessary partial derivatives, and collecting the resulting terms, Equation (B.6) becomes

$$\begin{aligned}
\frac{\partial \vec{E}}{\partial \vec{r}} = & \frac{2a_{\oplus}^2}{r^2 \sqrt{r^2 - a_{\oplus}^2}} \frac{S_{\odot}}{c} \left(\frac{R}{R_{\odot}} \right)^2 \frac{1}{m} \left[\gamma_{\oplus}^a a_1 (\hat{r} \cdot \hat{R}_{\odot}) + \gamma_{\oplus}^e \frac{e_1}{4} \right] \\
& \times \sum_{k=1}^K A_k \cos \theta_k (t_1^k \hat{n}_k - t_2^k \hat{r}) \hat{r}^T \\
& - 2(1 - \cos \theta_{\max}) \gamma_{\oplus}^a a_1 \frac{S_{\odot}}{c} \left(\frac{R}{R_{\odot}} \right)^2 \frac{1}{m} \\
& \times \sum_{k=1}^K A_k \cos \theta_k (t_1^k \hat{n}_k - t_2^k \hat{r}) \hat{R}_{\odot}^T \left(\frac{I - \hat{r} \hat{r}^T}{r} \right) \\
& + 2(1 - \cos \theta_{\max}) \frac{S_{\odot}}{c} \left(\frac{R}{R_{\odot}} \right)^2 \frac{1}{m} \left[\gamma_{\oplus}^a a_1 (\hat{r} \cdot \hat{R}_{\odot}) + \gamma_{\oplus}^e \frac{e_1}{4} \right] \\
& \times \sum_{k=1}^K A_k \cos \theta_k t_2^k \left(\frac{I - \hat{r} \hat{r}^T}{r} \right)
\end{aligned} \tag{B.7}$$

B.2 Macro-Model Surface Properties

The macro-model properties for each surface k consist of an area A_k , a diffuse reflectivity δ_k , and a specular reflectivity ρ_k . Since these parameters also appear in the MSODP Box-Wing Solar Radiation Pressure (BWSRP) subroutine, the partial derivatives of Equation (1.12) with respect to each include two separate contributions, which must be accumulated. Thus,

$$\begin{aligned}
\frac{\partial \vec{r}}{\partial A_k} &= \frac{\partial \vec{S}}{\partial A_k} + \frac{\partial \vec{E}}{\partial A_k} \\
\frac{\partial \vec{r}}{\partial \delta_k} &= \frac{\partial \vec{S}}{\partial \delta_k} + \frac{\partial \vec{E}}{\partial \delta_k} \\
\frac{\partial \vec{r}}{\partial \rho_k} &= \frac{\partial \vec{S}}{\partial \rho_k} + \frac{\partial \vec{E}}{\partial \rho_k}
\end{aligned} \tag{B.8}$$

Those from the solar radiation pressure perturbation \vec{S} are computed by the BWSRP subroutine, so only the Earth radiation pressure contributions are detailed here. The derivatives of the full BWERP model of Equation (3.26) with respect to each A_k are

$$\begin{aligned} \frac{\partial \vec{E}}{\partial A_k} = & -\frac{2(1 - \cos \theta_{max})}{N} \frac{S_{\odot}}{c} \left(\frac{R}{R_{\odot}} \right)^2 \frac{1}{m} \\ & \times \sum_{i=1}^N (\hat{n}_k \cdot \hat{s}_{\oplus}^i) \left[\gamma_{\oplus}^a a_i (\hat{n}_{\oplus}^i \cdot \hat{R}_{\odot}) + \gamma_{\oplus}^e \frac{e_i}{4} \right] (t_1^k \hat{n}_k + t_2^k \hat{s}_{\oplus}^i) \end{aligned} \quad (\text{B.9})$$

where t_1^k and t_2^k are defined by Equation (B.2). The derivatives with respect to each δ_k and ρ_k are

$$\begin{aligned} \frac{\partial \vec{E}}{\partial \delta_k} = & -\frac{4(1 - \cos \theta_{max})}{3N} \frac{S_{\odot}}{c} \left(\frac{R}{R_{\odot}} \right)^2 \frac{A_k}{m} \\ & \times \sum_{i=1}^N (\hat{n}_k \cdot \hat{s}_{\oplus}^i) \left[\gamma_{\oplus}^a a_i (\hat{n}_{\oplus}^i \cdot \hat{R}_{\odot}) + \gamma_{\oplus}^e \frac{e_i}{4} \right] \hat{n}_k \end{aligned} \quad (\text{B.10})$$

$$\begin{aligned} \frac{\partial \vec{E}}{\partial \rho_k} = & -\frac{2(1 - \cos \theta_{max})}{N} \frac{S_{\odot}}{c} \left(\frac{R}{R_{\odot}} \right)^2 \frac{A_k}{m} \\ & \times \sum_{i=1}^N (\hat{n}_k \cdot \hat{s}_{\oplus}^i) \left[\gamma_{\oplus}^a a_i (\hat{n}_{\oplus}^i \cdot \hat{R}_{\odot}) + \gamma_{\oplus}^e \frac{e_i}{4} \right] \left[2(\hat{n}_k \cdot \hat{s}_{\oplus}^i) \hat{n}_k - \hat{s}_{\oplus}^i \right] \end{aligned} \quad (\text{B.11})$$

B.3 Earth Radiation Scale Factors

The albedo scale factor γ_{\oplus}^a and the emissivity scale factor γ_{\oplus}^e appear only in the MSODP BWERP subroutine, so the partial derivatives of Equation (1.12) with respect to each are

$$\begin{aligned}\frac{\partial \ddot{\vec{r}}}{\partial \gamma_{\oplus}^a} &= \frac{\partial \vec{E}}{\gamma_{\oplus}^a} \\ \frac{\partial \ddot{\vec{r}}}{\partial \gamma_{\oplus}^e} &= \frac{\partial \vec{E}}{\gamma_{\oplus}^e}\end{aligned}\tag{B.12}$$

Taking derivatives of the full BWERP model of Equation (3.26) with respect to γ_{\oplus}^a and γ_{\oplus}^e :

$$\begin{aligned}\frac{\partial \vec{E}}{\partial \gamma_{\oplus}^a} &= -\frac{2(1 - \cos \theta_{max})}{N} \frac{S_{\odot}}{c} \left(\frac{R}{R_{\odot}} \right)^2 \frac{1}{m} a_i \\ &\times \sum_{i=1}^N \sum_{k=1}^K A_k (\hat{n}_k \cdot \hat{s}_{\oplus}^i) (\hat{n}_{\oplus}^i \cdot \hat{R}_{\odot}) (t_1^k \hat{n}_k + t_2^k \hat{s}_{\oplus}^i)\end{aligned}\tag{B.13}$$

$$\begin{aligned}\frac{\partial \vec{E}}{\partial \gamma_{\oplus}^e} &= -\frac{(1 - \cos \theta_{max})}{2N} \frac{S_{\odot}}{c} \left(\frac{R}{R_{\odot}} \right)^2 \frac{1}{m} \\ &\times \sum_{i=1}^N \sum_{k=1}^K A_k (\hat{n}_k \cdot \hat{s}_{\oplus}^i) e_i (t_1^k \hat{n}_k + t_2^k \hat{s}_{\oplus}^i)\end{aligned}\tag{B.14}$$

where t_1^k and t_2^k are defined by Equation (B.2).

B.4 Albedo Model Coefficients

The albedo model of Equation (2.36) relies on the coefficients a_0 , c_0 , c_1 , c_2 , and a_2 to determine the value a_i for each Earth area element. Since they are used only in computing the Earth radiation pressure perturbation, the partial derivatives of Equation (1.12) with respect to each become

$$\begin{aligned}
\frac{\partial \ddot{\vec{r}}}{\partial a_0} &= \frac{\partial \vec{E}}{\partial a_0} \\
\frac{\partial \ddot{\vec{r}}}{\partial c_0} &= \frac{\partial \vec{E}}{\partial c_0} \\
\frac{\partial \ddot{\vec{r}}}{\partial c_1} &= \frac{\partial \vec{E}}{\partial c_1} \\
\frac{\partial \ddot{\vec{r}}}{\partial c_2} &= \frac{\partial \vec{E}}{\partial c_2} \\
\frac{\partial \ddot{\vec{r}}}{\partial a_2} &= \frac{\partial \vec{E}}{\partial a_2}
\end{aligned} \tag{B.15}$$

Taking derivatives of the full BWERP model of Equation (3.26) with respect to each albedo-model coefficient:

$$\begin{aligned}
\frac{\partial \vec{E}}{\partial a_0} &= -\frac{2(1 - \cos \theta_{max})}{N} \frac{S_\odot}{c} \left(\frac{R}{R_\odot} \right)^2 \frac{\gamma_\oplus^a}{m} \\
&\times \sum_{i=1}^N \sum_{k=1}^K A_k (\hat{n}_k \cdot \hat{s}_\oplus^i) (\hat{n}_\oplus^i \cdot \hat{R}_\odot) (t_1^k \hat{n}_k + t_2^k \hat{s}_\oplus^i)
\end{aligned} \tag{B.16}$$

$$\begin{aligned}
\frac{\partial \vec{E}}{\partial c_0} &= -\frac{2(1 - \cos \theta_{max})}{N} \frac{S_\odot}{c} \left(\frac{R}{R_\odot} \right)^2 \frac{\gamma_\oplus^a}{m} \\
&\times \sum_{i=1}^N \sum_{k=1}^K A_k (\hat{n}_k \cdot \hat{s}_\oplus^i) (\hat{n}_\oplus^i \cdot \hat{R}_\odot) P_1(\sin \varphi_i) (t_1^k \hat{n}_k + t_2^k \hat{s}_\oplus^i)
\end{aligned} \tag{B.17}$$

$$\begin{aligned}
\frac{\partial \vec{E}}{\partial c_1} &= -\frac{2(1 - \cos \theta_{max})}{N} \frac{S_\odot}{c} \left(\frac{R}{R_\odot} \right)^2 \frac{\gamma_\oplus^a}{m} \cos \omega_\oplus (t - t_0) \\
&\times \sum_{i=1}^N \sum_{k=1}^K A_k (\hat{n}_k \cdot \hat{s}_\oplus^i) (\hat{n}_\oplus^i \cdot \hat{R}_\odot) P_1(\sin \varphi_i) (t_1^k \hat{n}_k + t_2^k \hat{s}_\oplus^i)
\end{aligned} \tag{B.18}$$

$$\begin{aligned} \frac{\partial \vec{E}}{\partial c_2} = & -\frac{2(1 - \cos \theta_{max})}{N} \frac{S_{\odot}}{c} \left(\frac{R}{R_{\odot}} \right)^2 \frac{\gamma_{\oplus}^a}{m} \sin \omega_{\oplus} (t - t_0) \\ & \times \sum_{i=1}^N \sum_{k=1}^K A_k (\hat{n}_k \cdot \hat{s}_{\oplus}^i) (\hat{n}_{\oplus}^i \cdot \hat{R}_{\odot}) P_1(\sin \varphi_i) (t_1^k \hat{n}_k + t_2^k \hat{s}_{\oplus}^i) \end{aligned} \quad (\text{B.19})$$

$$\begin{aligned} \frac{\partial \vec{E}}{\partial a_2} = & -\frac{2(1 - \cos \theta_{max})}{N} \frac{S_{\odot}}{c} \left(\frac{R}{R_{\odot}} \right)^2 \frac{\gamma_{\oplus}^a}{m} \\ & \times \sum_{i=1}^N \sum_{k=1}^K A_k (\hat{n}_k \cdot \hat{s}_{\oplus}^i) (\hat{n}_{\oplus}^i \cdot \hat{R}_{\odot}) P_2(\sin \varphi_i) (t_1^k \hat{n}_k + t_2^k \hat{s}_{\oplus}^i) \end{aligned} \quad (\text{B.20})$$

where t_1^k and t_2^k are defined by Equation (B.2).

B.5 Emissivity Model Coefficients

Similarly, the emissivity model of Equation (2.37) relies on the coefficients e_0 , k_0 , k_1 , k_2 , and e_2 to determine the value e_i for each Earth area element. They are also used only in computing the Earth radiation pressure perturbation, so the partial derivatives of Equation (1.12) with respect to each become

$$\begin{aligned} \frac{\partial \vec{r}}{\partial e_0} &= \frac{\partial \vec{E}}{\partial e_0} \\ \frac{\partial \vec{r}}{\partial k_0} &= \frac{\partial \vec{E}}{\partial k_0} \\ \frac{\partial \vec{r}}{\partial k_1} &= \frac{\partial \vec{E}}{\partial k_1} \\ \frac{\partial \vec{r}}{\partial k_2} &= \frac{\partial \vec{E}}{\partial k_2} \\ \frac{\partial \vec{r}}{\partial e_2} &= \frac{\partial \vec{E}}{\partial e_2} \end{aligned} \quad (\text{B.21})$$

Taking derivatives of the full BWERP model of Equation (3.26) with respect to each emissivity-model coefficient:

$$\begin{aligned} \frac{\partial \vec{E}}{\partial e_0} = & -\frac{(1 - \cos \theta_{max})}{2N} \frac{S_{\odot}}{c} \left(\frac{R}{R_{\odot}} \right)^2 \frac{\gamma_{\oplus}^e}{m} \\ & \times \sum_{i=1}^N \sum_{k=1}^K A_k (\hat{n}_k \cdot \hat{s}_{\oplus}^i) (t_1^k \hat{n}_k + t_2^k \hat{s}_{\oplus}^i) \end{aligned} \quad (\text{B.22})$$

$$\begin{aligned} \frac{\partial \vec{E}}{\partial k_0} = & -\frac{(1 - \cos \theta_{max})}{2N} \frac{S_{\odot}}{c} \left(\frac{R}{R_{\odot}} \right)^2 \frac{\gamma_{\oplus}^e}{m} \\ & \times \sum_{i=1}^N \sum_{k=1}^K A_k (\hat{n}_k \cdot \hat{s}_{\oplus}^i) P_1 (\sin \varphi_i) (t_1^k \hat{n}_k + t_2^k \hat{s}_{\oplus}^i) \end{aligned} \quad (\text{B.23})$$

$$\begin{aligned} \frac{\partial \vec{E}}{\partial k_1} = & -\frac{(1 - \cos \theta_{max})}{2N} \frac{S_{\odot}}{c} \left(\frac{R}{R_{\odot}} \right)^2 \frac{\gamma_{\oplus}^e}{m} \cos \omega_{\oplus} (t - t_0) \\ & \times \sum_{i=1}^N \sum_{k=1}^K A_k (\hat{n}_k \cdot \hat{s}_{\oplus}^i) P_1 (\sin \varphi_i) (t_1^k \hat{n}_k + t_2^k \hat{s}_{\oplus}^i) \end{aligned} \quad (\text{B.24})$$

$$\begin{aligned} \frac{\partial \vec{E}}{\partial k_2} = & -\frac{(1 - \cos \theta_{max})}{2N} \frac{S_{\odot}}{c} \left(\frac{R}{R_{\odot}} \right)^2 \frac{\gamma_{\oplus}^e}{m} \sin \omega_{\oplus} (t - t_0) \\ & \times \sum_{i=1}^N \sum_{k=1}^K A_k (\hat{n}_k \cdot \hat{s}_{\oplus}^i) P_1 (\sin \varphi_i) (t_1^k \hat{n}_k + t_2^k \hat{s}_{\oplus}^i) \end{aligned} \quad (\text{B.25})$$

$$\begin{aligned} \frac{\partial \vec{E}}{\partial e_2} = & -\frac{(1 - \cos \theta_{max})}{2N} \frac{S_{\odot}}{c} \left(\frac{R}{R_{\odot}} \right)^2 \frac{\gamma_{\oplus}^e}{m} \\ & \times \sum_{i=1}^N \sum_{k=1}^K A_k (\hat{n}_k \cdot \hat{s}_{\oplus}^i) P_2 (\sin \varphi_i) (t_1^k \hat{n}_k + t_2^k \hat{s}_{\oplus}^i) \end{aligned} \quad (\text{B.26})$$

where t_1^k and t_2^k are defined by Equation (B.2).

Appendix C:

MSODP Box-Wing Earth Radiation Pressure

Source Code

```

SUBROUTINE BWERP (ET, R, RDOT, R1, NOPART, ACC, &
    DADR, DADP)
!-----
!  MSODP1/BWERP(1.0)
!-----
!  PURPOSE:  TO COMPUTE THE ACCELERATION DUE TO EARTH
!            RADIATION PRESSURE USING BOX-WING MODEL
!-----
!  INPUT PARAMETERS:
!
!  ET      = DOUBLE PRECISION JULIAN DATE
!  R,RDOT  = SATELLITE POSITION AND VELOCITY IN J2000 SYSTEM
!  R1      = MAGNITUDE OF R
!  NOPART  = TRUE IF PARTIALS DESIRED, FALSE IF NOT
!  DADP    = ACCELERATION PARTIALS WRT COMMON DYN PARAMETERS
!-----
!  OUTPUT PARAMETERS:
!
!  ACC     = EARTH RADIATION PRESSURE ACCELERATIONS
!  DADP    = AUGMENTED PARTIALS WRT DYN PARAMETERS
!-----
!  INPUT COMMON PARAMETERS (MODULE NAME):
!
!  PLANPS(1:3,10) = EARTH-SUN POSITION VECTOR (M_PLANET)
!  PLANPS( 4,10)  = MAGNITUDE OF EARTH-SUN POSITION VECTOR
!  Z2NORM         = UNIT VECTORS NORMAL TO BOX-WING MODEL
!                  SURFACES (M_BWCONT)
!  RMASS          = SPACECRAFT MASS (M_SOLRAD)
!  NRING          = NUMBER OF RINGS TO BE USED IN ERP MODEL
!                  (M_ERADPR)
!  AEFF           = EFFECTIVE RADIUS OF EARTH (M_SOLRAD)
!  HG             = TRANSFORMATION MATRIX FROM J2000 TO
!                  BODY-FIXED (M_MATRIX)
!  NFACE          = NUMBER OF BOX-WING MODEL SURFACES
!                  (M_BWCONT)
!  BWAREA         = BOX-WING MODEL SURFACE AREAS (M_BWCONT)
!  BWSPEC         = BOX-WING MODEL SURFACE SPECULAR
!                  REFLECTIVITIES (M_BWCONT)

```

```

! BWDIFF      = BOX-WING MODEL SURFACE DIFFUSE
!              REFLECTIVITIES (M_BWCONT)
! NAEMAX      = MAXIMUM DEGREE, LEGENDRE POLYNOMIAL
!              (M_ALEMPR)
! AUS2        = 1 ASTRONOMICAL UNIT SQUARED, METERS^2
!              (M_EPHBLK)
! ISOLAX      = SOLAR PANEL AXIS ORIENTATION FLAG
!              (M_SAMAMT)
! SOLAX       = SOLAR PANEL AXIS ORIENTATION (M_PANEL)
! IRNFPIT     = RANDOM PITCH ANGLE ERROR FLAG (M_RNFPIT)
! PITERR      = PITCH ANGLE ERROR (M_ATTERR)
! TWOPI       = 2 * PI (M_CONVRT)
! IBWSTA      = BOX-WING SURFACE AREA ESTIMATION FLAG
!              (M_BWCONT)
! IBWA6       = AREA PARTIALS LOCATION IN DADP
!              (M_BWCONT)
! IBWSTD      = BOX-WING DIFFUSE REFLECTIVITY ESTIMATION
!              FLAG (M_BWCONT)
! IBWD6       = DIFFUSE REFLECTIVITY PARTIALS LOCATION
!              IN DADP (M_BWCONT)
! IBWSTS      = BOX-WING SPECULAR REFLECTIVITY
!              ESTIMATION FLAG (M_BWCONT)
! IBWS6       = SPECULAR REFLECTIVITY PARTIALS LOCATION
!              IN DADP (M_BWCONT)
! NUMALE      = NUMBER OF ESTIMATED ALBEDO AND
!              EMISSIVITY PARAMETERS (M_NUMALE)
! NUMAL       = NUMBER OF ESTIMATED ALBEDO PARAMETERS
!              (M_NUMAL)
! NUMEM       = NUMBER OF ESTIMATED EMISSIVITY
!              PARAMETERS (M_NUMEM)
! NSBASC      = NUMBER OF SUBARCS FOR ALBEDO SCALE
!              FACTORS (M_ERADPR)
! ALSCL       = SUBARC ALBEDO SCALE FACTORS (M_ERADPR)
! NSBESC      = NUMBER OF SUBARCS FOR EMISSIVITY SCALE
!              FACTORS (M_ERADPR)
! EMSCL       = SUBARC EMISSIVITY SCALE FACTORS
!              (M_ERADPR)
! TDAY        = INTEGRATION TIME, DAYS PAST ARC EPOCH
!              (M_TMJDNOW)
! -----
! COMPUTATIONAL VARIABLES:
!
! REFERENCE: P KNOCKE, EARTH RADIATION PRESSURE EFFECTS
! ON SATELLITES, PHD DISSERTATION, APPENDIX A, 1989
!
! RSUNU      = EARTH-SUN UNIT VECTOR
! RSATU      = EARTH-SATELLITE UNIT VECTOR
! UN         = UNIT VECTORS NORMAL TO BOX-WING MODEL SURFACES
! SOLAR      = SCALED ALBEDO CONSTANT (= ES/MC)

```



```

! EARTH      = SCALED EMISSIVITY CONSTANT (= MB/MC = ES/4MC)
! ALPHA      = HORIZON ANGLE CENTERED AT S/C CENTER-OF-MASS,
!             MEASURED FROM S/C NADIR TO RING BOUNDARY (ZETA)
! BETA       = CENTRAL ANGLE CENTERED AT EARTH CENTER-OF-MASS,
!             MEASURED FROM S/C NADIR TO RING BOUNDARY
! NS         = TOTAL NUMBER OF RING ELEMENTS
! BSTAR      = CENTRAL ANGLE IDENTIFYING RING CENTERS (BETA*)
! REU        = UNIT VECTOR FROM EARTH CENTER TO SEGMENT CENTER
! RSU        = UNIT VECTOR FROM SEGMENT CENTER TO SPACECRAFT
! WEIGHT     = RING SEGMENT PROJECTED ATTENUATED AREA (A')
! COS0       = SOLAR ZENITH ANGLE (= THETA-S)
! SLAT       = SEGMENT CENTER LATITUDE, FOR ALBEDO SUBROUTINE
! AL0,AL     = ALBEDO COEFFICIENTS OF CAP AND RING SEGMENTS
! EM0,EM     = CAP AND RING SEGMENT EMISSIVITY COEFFICIENTS
! CTHETA     = COSINE OF ANGLE BETWEEN SOURCE VECTOR AND
!             SEGMENT SURFACE NORMAL
! PLAREA     = PROJECTED AREA OF BOX-WING MODEL SURFACE
! ISBARCA    = CURRENT ALBEDO SCALE ARC NUMBER
! TARCA      = DAYS FROM START OF CURRENT ALB SCALE ARC
! KAPPA      = ALBEDO SCALE FACTOR FOR CURRENT ARC
! ISBARCE    = CURRENT EMISSIVITY SCALE ARC NUMBER
! TARCE      = DAYS FROM START OF CURRENT EMISS SCALE ARC
! KAPPE      = EMISSIVITY SCALE FACTOR FOR CURRENT ARC
! -----
! HISTORY:
!
! APR 2002  ORIGINALLY CODED BY C. WEBB
! -----
! MODULES
! -----
USE M_PAR_BW
USE M_ALEMPR
USE M_ATTERR
USE M_BWCONT
USE M_CONTRL
USE M_CONVRT
USE M_EPHBLK
USE M_ERADPR
USE M_MATRIX
USE M_NOWSAT
USE M_ORIENT
USE M_PANEL
USE M_PAREST
USE M_PLANET
USE M_RNFPIT
USE M_SAMAMT
USE M_SOLRAD
USE M_TMJDNOW
USE M_TMJDYW

```

```

!-----
  IMPLICIT NONE
!-----
!  DECLARE INPUT VARIABLES:

  DOUBLE PRECISION ET
  REAL, DIMENSION(3) :: R, RDOT, ACC
  REAL :: R1
  LOGICAL :: NOPART
  REAL, DIMENSION(3,3) :: DADR
  REAL, DIMENSION(3,1) :: DADP
!-----
!  DECLARE LOCAL VARIABLES:

  REAL, DIMENSION(3) :: RSUNU, RSATU, RSS, RSU
  REAL, DIMENSION(3) :: RE, REU, DUM
  REAL, DIMENSION(3) :: SUMA, US1, US2, UX, OP, DPC
  REAL, DIMENSION(7) :: BETA, BSTAR
  REAL, DIMENSION(3,3) :: RTN, DUM1, DUM2, DUM3, DUM4
  REAL, DIMENSION(3,3) :: DUM5, SCC, DADR_ERP
  REAL, DIMENSION(3,MAXFACE) :: UN
  REAL :: SOLAR, EARTH, ALPHA, COSINE, W0, GAMMA, WEIGHT
  REAL :: COS0, SLAT, ALFCTR, EMFCTR, FCTR, SUMB, PLAREA
  REAL :: TERM1, TERM2, DW, Q1, Q2, Q3, D, H, S, DELTH
  REAL :: CB, SB, CT, ST, CTMP, AL0, EM0, AL, EM, TEMP
  REAL :: TARCA, TARCE, KAPPA, KAPPE
  INTEGER :: NSEG, I, J, K, II, KK, IM6, ISBARCA, ISBARCE

  INTEGER, SAVE :: NR, NS, NUMAL, NUMEM
  REAL, SAVE :: APRES, EPRES
!-----
!  DECLARE PARAMETERS:
!
  REAL, PARAMETER :: HALFPI = 1.5707963267949E+0
  REAL, DIMENSION(3,3) :: XI = RESHAPE((/ 1., &
    (0., I=1,3), 1., (0., I=1,3), 1. /), (/3,3/))
!-----
!  COMPUTE CURRENT SUBARC ALBEDO SCALE FACTOR (KAPPA)

  IF (NSBASC(NOWSAT) > 1) THEN
    ISBARCA = INT(TDAY/ARCASC(NOWSAT)) + 1
    IF (ISBARCA < 1) ISBARCA = 1
    IF (ISBARCA > NSBASC(NOWSAT)) ISBARCA = NSBASC(NOWSAT)
    TARCA = TDAY - ARCASC(NOWSAT) * (ISBARCA-1)
  ELSE
    TARCA = TDAY
    ISBARCA = 1
  END IF
  KAPPA = ALSCL(ISBARCA,NOWSAT)

```

```

!-----
!  COMPUTE CURRENT SUBARC EMISSIVITY SCALE FACTOR (KAPPE)

  IF (NSBESC(NOWSAT) > 1) THEN
    ISBARCE = INT(TDAY/ARCESC(NOWSAT)) + 1
    IF (ISBARCE < 1) ISBARCE = 1
    IF (ISBARCE > NSBESC(NOWSAT)) ISBARCE = NSBESC(NOWSAT)
    TARCE = TDAY - ARCESC(NOWSAT) * (ISBARCE-1)
  ELSE
    TARCE = TDAY
    ISBARCE = 1
  END IF
  KAPPE = EMSCL(ISBARCE,NOWSAT)
!-----
!  NORMALIZE THE EARTH-SUN AND EARTH-SATELLITE VECTORS

  RSUNU(1:3) = PLANPS(1:3,10) / PLANPS(4,10)
  RSATU(1:3) = R(1:3) / R1
!-----
!  DETERMINE NORMAL VECTORS FOR ALL BOX-WING MODEL SURFACES
!  (SCCROT CALLS GLASNORM TO COMPUTE Z2NORM AT TMJD)

  CALL SCCROT(TMJDYAW, R, RDOT, NOWSAT, 0, SCC)
  DO I = 1, NFACE(NOWSAT)
    UN(1:3,I) = Z2NORM(NOWSAT,I,1:3)
  END DO
!-----
!  COMPUTE UNIT NORMAL TO SOLAR PANEL SURFACE IN SCC SYSTEM
!  NOTE THE IMPLICIT ASSUMPTION THAT THE +Y SOLAR ARRAY IS
!  SURFACE 7 (FRONT) AND SURFACE 8 (BACK), AND THAT THE -Y
!  SOLAR ARRAY IS SURFACE 9 (FRONT) AND SURFACE 10 (BACK)

  CALL M3331 (SCC, UN(1,7), US1)
  IF (IORIENT(NOWSAT) == 5) CALL M3331 (SCC, UN(1,9), US2)
  IF (ISOLAX(NOWSAT) > 0) THEN
    CALL CROSS (SOLAX(NOWSAT,1:3), US1, UX)
    CALL CROSS (UX, SOLAX(NOWSAT,1:3), US1)
    CALL NORM3 (US1, US1)
    IF (IORIENT(NOWSAT) == 5) THEN
      CALL CROSS (SOLAX(NOWSAT,1:3), US2, UX)
      CALL CROSS (UX, SOLAX(NOWSAT,1:3), US2)
      CALL NORM3 (US2, US2)
    ENDIF
  ENDIF
!-----
!  INCLUDE THE PITCH ANGLE ERROR (PITERR) IF REQUESTED

  IF (IRNFPIT(NOWSAT) > 0) THEN
    OP(1) = US1(1) * COS(PITERR) + US1(3) * SIN(PITERR)

```

```

      OP(2) = US1(2)
      OP(3) = -US1(1) * SIN(PITERR) + US1(3) * COS(PITERR)
      CALL VMOVE (OP, US1, 3)
      IF (IORIENT(NOWSAT) == 5) THEN
        OP(1) = US2(1) * COS(PITERR) + US2(3) * SIN(PITERR)
        OP(2) = US2(2)
        OP(3) = -US2(1) * SIN(PITERR) + US2(3) * COS(PITERR)
        CALL VMOVE (OP, US2, 3)
      ENDIF
    ENDIF
  !-----
  ! ROTATE UNIT NORMAL VECTOR BACK TO J2000 SYSTEM

  CALL M33T31 (SCC, US1, UN(1,7))
  UN(1:3,8) = -UN(1:3,7)
  IF (IORIENT(NOWSAT) == 5) THEN
    CALL M33T31 (SCC, US2, UN(1,9))
    UN(1:3,10) = -UN(1:3,9)
  ENDIF
!-----
! INITIALIZE ACCELERATIONS

  SUMA(1:3) = 0.0E+0
  ACC(1:3) = 0.0E+0
!-----
! ADJUST ALBEDO AND EMISSIVITY PRESSURES BASED ON EARTH
! DISTANCE FROM THE SUN

  SOLAR = -APRES/RMASS(NOWSAT)/PLANPS(4,10)/PLANPS(4,10)
  EARTH = -EPRES/RMASS(NOWSAT)/PLANPS(4,10)/PLANPS(4,10)
!-----
! CALCULATE LIMITS OF EARTH SURFACE VISIBLE FROM SATELLITE

  ALPHA = ASIN(AEFF/R1)
  BETA(NR) = HALFPI - ALPHA
  COSINE = COS(ALPHA)
  W0 = 2.0 * (1.0 - COSINE)
!-----
! DIVIDE VISIBLE SURFACE INTO CAP + RINGS, IF REQUESTED
!-----
  IF (NRING > 0) THEN

    !...CALCULATE LIMITS OF CENTRAL CAP

    COSINE = (COS(ALPHA) + NS - 1) / NS
    IF (ABS(COSINE) > 1.0E+0) COSINE = SIGN(1.0E+0, COSINE)
    ALPHA = ACOS(COSINE)
    GAMMA = ASIN(R1*SIN(ALPHA)/AEFF)
    BETA(1) = GAMMA - ALPHA

```

```

!...CALCULATE RING BOUNDARIES

IF (NRING > 1) THEN
  J = 1
  DO I = 2,NRING
    J = J + 6*(I-1)
    ALPHA = ACOS(J*COSINE - J + 1)
    GAMMA = ASIN(R1*SIN(ALPHA)/AEFF)
    BETA(I) = GAMMA - ALPHA
  END DO
END IF

!...CALCULATE RING CENTERS

DO I = 2,NR
  BSTAR(I) = (BETA(I) + BETA(I-1)) / 2.0
END DO

END IF
!-----
!  CALCULATE RADIATION PRESSURE DUE TO CENTRAL CAP
!-----

!...COMPUTE WEIGHT (PROJECTED ATTENUATED AREA)

WEIGHT = 2.0*(1.0 - COSINE)

!...COMPUTE COSINE OF SOLAR ZENITH ANGLE

COS0 = DOT_PRODUCT(RSATU(1:3),RSUNU(1:3))
IF (COS0 < 0.0E+0) COS0 = 0.0

!...COMPUTE ALBEDO AND EMISSIVITY

SLAT = DOT_PRODUCT(HG(3,1:3),RSATU(1:3))
CALL ALBEDO (ET, SLAT, AL0, EM0)

!...COMPUTE ALBEDO, EMISSIVITY AND TOTAL FACTORS

ALFCTR = KAPPA * SOLAR * COS0 * WEIGHT
EMFCTR = KAPPE * EARTH * WEIGHT
FCTR = AL0 * ALFCTR + EM0 * EMFCTR

!...INITIALIZE SUM TO BE USED FOR PARTIALS

SUMB = 0.0

```

```

!-----
!  SUM OVER ALL SURFACES IN BOX-WING MODEL

DO 40 I = 1, NFACE(NOWSAT)

    !...COMPUTE COSINE OF ANGLE BETWEEN SURFACE NORMAL AND
    !...SOURCE VECTOR (NOTE THAT -RSATU IS USED)

    CTHETA(NOWSAT,I) = DOT_PRODUCT(UN(1:3,I),-RSATU(1:3))
    IF (CTHETA(NOWSAT,I) .LE. 0.0) GO TO 40

    !...COMPUTE PROJECTED AREA AND REFLECTIVITY TERMS

    PLAREA = BWAREA(NOWSAT,I) * CTHETA(NOWSAT,I)
    TERM1 = 2.0*(BWDIFF(NOWSAT,I)/3.0 + &
        BWSPEC(NOWSAT,I)*CTHETA(NOWSAT,I))
    TERM2 = 1.0 - BWSPEC(NOWSAT,I)

    !...COMPUTE SUMS FOR USE IN ACCELERATIONS AND PARTIALS

    SUMA(1:3) = SUMA(1:3) + PLAREA * (TERM1*UN(1:3,I) - &
        TERM2*RSATU(1:3))
    SUMB = SUMB - PLAREA * TERM2

    !...COMPUTE REQUIRED ACCELERATION PARTIALS WRT SURFACE
    !...AREA, DIFFUSE AND SPECULAR REFLECTIVITIES.  NOTE
    !...THAT THEY ARE COMPUTED IN CONJUNCTION WITH THE SAME
    !...PARTIALS FROM THE BWSRP MODULE.

    IF (NOPART) GO TO 40

    !...SURFACE AREA

    IF (IBWSTA(NOWSAT,I) > 1) THEN
        IM6 = IBWA6(NOWSAT,I)
        DPC(1:3) = FCTR * CTHETA(NOWSAT,I) * &
            (TERM1*UN(1:3,I) - TERM2*RSATU(1:3))
        DADP(1:3,IM6) = DADP(1:3,IM6) + DPC(1:3)
    END IF

    !...DIFFUSE REFLECTIVITY

    IF (IBWSTD(NOWSAT,I) > 1) THEN
        IM6 = IBWD6(NOWSAT,I)
        DPC(1:3) = FCTR * PLAREA * (2.0/3.0) * UN(1:3,I)
        DADP(1:3,IM6) = DADP(1:3,IM6) + DPC(1:3)
    END IF

```

```

!...SPECULAR REFLECTIVITY

IF (IBWSTS(NOWSAT,I) > 1) THEN
  IM6 = IBWS6(NOWSAT,I)
  DPC(1:3) = FCTR * PLAREA * &
    (2.0*CTHETA(NOWSAT,I)*UN(1:3,I) + RSATU(1:3))
  DADP(1:3,IM6) = DADP(1:3,IM6) + DPC(1:3)
END IF

!  END OF SURFACE LOOP
!-----

40 CONTINUE

!...COMPUTE ACCELERATION DUE TO CENTRAL CAP

ACC(1:3) = FCTR * SUMA(1:3)

IF (NOPART) GO TO 60

!...COMPUTE REQUIRED PARTIALS WRT SATELLITE POSITION
!...(BASED ONLY ON CAP)

IF (COS0 == 0.0) AL0 = 0.0
DW = -2.0 * (AEFF/R1)**2 / SQRT(R1**2-AEFF**2)
Q1 = DW * (KAPPA * AL0 * SOLAR * COS0 + &
  KAPPE * EM0 * EARTH)
Q2 = W0 * KAPPA * AL0 * SOLAR
Q3 = W0 * (KAPPA * AL0 * SOLAR * COS0 + &
  KAPPE * EM0 * EARTH) * SUMB

DO I = 1,3
  DO J = 1,3
    DUM1(I,J) = SUMA(I) * RSATU(J)
    DUM2(I,J) = SUMA(I) * RSUNU(J)
    DUM3(I,J) = RSATU(I) * RSATU(J)
    DUM4(I,J) = (XI(I,J) - DUM3(I,J)) / R1
  END DO
END DO
CALL M3333(DUM2,DUM4,DUM5)

DADR_ERP(1:3,1:3) = Q1 * DUM1(1:3,1:3) + &
  Q2 * DUM5(1:3,1:3) + Q3 * DUM4(1:3,1:3)
DADR(1:3,1:3) = DADR(1:3,1:3) + DADR_ERP(1:3,1:3)

```

```

!...COMPUTE REQUIRED PARTIALS WRT ALBEDO AND EMISSIVITY
!...SCALE FACTORS

IF (IASCST(NOWSAT) > 0) THEN
  IM6 = IALBSCM6(NOWSAT) + IASCST(NOWSAT) * (ISBARCA-1)
  DADP(1:3,IM6) = AL0 * SOLAR * COS0 * WEIGHT * SUMA(1:3)
END IF

IF (IESCST(NOWSAT) > 0) THEN
  IM6 = IEMSCM6(NOWSAT) + IESCST(NOWSAT) * (ISBARCE-1)
  DADP(1:3,IM6) = EM0 * EARTH * WEIGHT * SUMA(1:3)
END IF

!...COMPUTE REQUIRED PARTIALS WRT ALBEDO AND EMISSIVITY
!...PARAMETERS

IF (NUMALE > 0) THEN
  KK = IALEM7(NOWSAT)
  IF (NUMAL > 0) THEN
    DO II = 1,NUMAL
      KK = KK + 1
      DADP(1:3,KK) = ALFCTR * SUMA(1:3) * DADALP(II)
    END DO
  END IF
  IF (NUMEM > 0) THEN
    DO II = 1,NUMEM
      KK = KK + 1
      DADP(1:3,KK) = EMFCTR * SUMA(1:3) * DEDEMP(II)
    END DO
  END IF
END IF

!-----
!  CALCULATE RADIATION PRESSURE FROM RINGS
!-----
60 IF (NRING > 0) THEN

  !...COMPUTE RTN TRANSFORMATION

  CALL RTNROT (R, RDOT, RTN)

!-----
!  SUM OVER RINGS

DO 140 I = 2, NR

  D = AEFF*SIN(BSTAR(I))
  H = AEFF*COS(BSTAR(I))
  S = 1.0/SQRT(AEFF**2 + R1**2 - 2.0*R1*H)

```



```

NSEG = 6*(I-1)
DELTH = TWOPI/NSEG
DUM(1) = H
CB      = COS(DELTH)
SB      = SIN(DELTH)
CT      = 1.0
ST      = 0.0

!-----
!  SUM OVER SEGMENTS IN RING

DO 140 J = 1,NSEG

    !...INITIALIZE ACCELERATION SUM

    SUMA(1:3) = 0.0

    !...COMPUTE J2000 EARTH-CENTERED VECTOR TO SEGMENT
    !...CENTER (RE)

    DUM(2) = D*CT
    DUM(3) = D*ST
    CTMP    = CT
    CT      = CT*CB - ST*SB
    ST      = ST*CB + CTMP*SB
    CALL M33T31 (RTN, DUM, RE)

    !...COMPUTE SEGMENT-TO-SPACECRAFT UNIT VECTOR (RSU)

    REU(1:3) = RE(1:3) / AEFF
    RSS(1:3) = R(1:3) - RE(1:3)
    RSU(1:3) = RSS(1:3) * S

    !...COMPUTE COSINE OF SOLAR ZENITH ANGLE FOR
    !...SEGMENT

    COSINE = DOT_PRODUCT(REU(1:3),RSUNU(1:3))
    IF (COSINE < 0.0E+0) COSINE = 0.0

    !...COMPUTE ALBEDO AND EMISSIVITY FOR SEGMENT

    SLAT = DOT_PRODUCT(HG(3,1:3),REU(1:3))
    CALL ALBEDO (ET, SLAT, AL, EM)

    !...COMPUTE ALBEDO, EMISSIVITY AND TOTAL FACTORS

    ALFCTR = KAPPA * SOLAR * COSINE * WEIGHT
    EMFCTR = KAPPE * EARTH * WEIGHT
    FCTR = AL * ALFCTR + EM * EMFCTR

```

```

!-----
!   SUM OVER ALL SURFACES IN BOX-WING MODEL

DO 130 K = 1, NFACE(NOWSAT)

    !...COMPUTE COSINE OF ANGLE BETWEEN SURFACE
    !...NORMAL AND SOURCE VECTOR (NOTE THAT -RSU IS
    !...USED)

    CTHETA(NOWSAT,K) = DOT_PRODUCT(UN(1:3,K), &
        -RSU(1:3))
    IF (CTHETA(NOWSAT,K) .LE. 0.0) GO TO 130

    !...COMPUTE PROJECTED AREA AND REFLECTIVITY TERMS

    PLAREA = BWAREA(NOWSAT,K)*CTHETA(NOWSAT,K)
    TERM1 = 2.0*(BWDIFF(NOWSAT,K)/3.0 &
        + BWSPEC(NOWSAT,K)*CTHETA(NOWSAT,K))
    TERM2 = 1.0 - BWSPEC(NOWSAT,K)

    !...COMPUTE SUM FOR ACCELERATIONS AND PARTIALS

    SUMA(1:3) = SUMA(1:3) + &
        PLAREA * (TERM1*UN(1:3,K) - TERM2*RSU(1:3))

    !...COMPUTE REQUIRED PARTIALS OF ACCELERATION WRT
    !...SURFACE AREA, DIFFUSE AND SPECULAR
    !...REFLECTIVITIES

    IF (NOPART) GO TO 130

    !...SURFACE AREA

    IF (IBWSTA(NOWSAT,K) > 1) THEN
        IM6 = IBWA6(NOWSAT,K)
        DPC(1:3) = FCTR * CTHETA(NOWSAT,K) * &
            (TERM1*UN(1:3,K) - TERM2*RSU(1:3))
        DADP(1:3,IM6) = DADP(1:3,IM6) + DPC(1:3)
    END IF

    !...DIFFUSE REFLECTIVITY

    IF (IBWSTD(NOWSAT,K) > 1) THEN
        IM6 = IBWD6(NOWSAT,K)
        DPC(1:3) = FCTR * PLAREA * (2.0/3.0) * &
            UN(1:3,K)
        DADP(1:3,IM6) = DADP(1:3,IM6) + DPC(1:3)
    END IF

```

```

      IF (IBWSTS(NOWSAT,K) > 1) THEN
        IM6 = IBWS6(NOWSAT,K)
        DPC(1:3) = FCTR * PLAREA * &
          (2.0*CTHETA(NOWSAT,K)*UN(1:3,K) + RSU(1:3))
        DADP(1:3,IM6) = DADP(1:3,IM6) + DPC(1:3)
      END IF

      !   END OF SURFACE LOOP
      !-----

130  CONTINUE

      !...COMPUTE AND ACCUMULATE ACCELERATIONS DUE TO
      !...SEGMENT

      ACC(1:3) = ACC(1:3) + FCTR * SUMA(1:3)

      !...COMPUTE AND ACCUMUALTE REQUIRED PARTIALS WRT
      !...ALBEDO AND EMISSIVITY SCALE FACTORS

      IF (IASCST(NOWSAT) > 0) THEN
        IM6 = IALBSCM6(NOWSAT) + IASCST(NOWSAT) * &
          (ISBARCA-1)
        DPC(1:3) = AL * SOLAR * COSINE * WEIGHT * &
          SUMA(1:3)
        DADP(1:3,IM6) = DADP(1:3,IM6) + DPC(1:3)
      END IF

      IF (IESCST(NOWSAT) > 0) THEN
        IM6 = IEMSCM6(NOWSAT) + IESCST(NOWSAT) * &
          (ISBARCE-1)
        DPC(1:3) = EM * EARTH * WEIGHT * SUMA(1:3)
        DADP(1:3,IM6) = DADP(1:3,IM6) + DPC(1:3)
      END IF

      !...COMPUTE AND ACCUMULATE REQUIRED PARTIALS WRT
      !...ALBEDO AND EMISSIVITY PARAMETERS

      IF (NUMALE > 0) THEN
        KK = IALEM7(NOWSAT)
        IF (NUMAL > 0) THEN
          DO II = 1,NUMAL
            KK = KK + 1
            DPC(1:3) = ALFCTR * SUMA(1:3) * DADALP(II)
            DADP(1:3,KK) = DADP(1:3,KK) + DPC(1:3)
          END DO
        END IF
      END IF

```

```

        IF (NUMEM > 0) THEN
            DO II = 1, NUMEM
                KK = KK + 1
                DPC(1:3) = EMFCTR * SUMA(1:3) * DEDEMP(II)
                DADP(1:3, KK) = DADP(1:3, KK) + DPC(1:3)
            END DO
        END IF
    END IF

    !   END OF SEGMENT LOOP
    !-----

    !   END OF RING LOOP
    !-----

140 CONTINUE

END IF

!-----
!   RETURN
!-----
    RETURN

!-----
!   ENTRY POINT TO INITIALIZE EARTH RADIATION PRESSURE MODEL
!-----
    ENTRY BWERP0

    IF (MODE == 1 .OR. MODE == 4) THEN
        NUMAL = NALEST + 2 * NPTALE
        NUMEM = NEMEST + 2 * NPTEME
    ELSE
        NALEST = 0
        NEMEST = 0
        NPTALE = 0
        NPTEME = 0
        NUMALE = 0
    END IF

    !...CALCULATE TOTAL NUMBER OF RING ELEMENTS

    NR = NRING + 1
    NS = 1
    DO I=1, NR
        NS = NS + 6*(I-1)
    END DO

```

```

!...INITIALIZE COEFFICIENTS FOR LEGENDRE POLYNOMIAL
!...RECURSION FORMULA

DO I = 3, NAEMAX
  TEMP = FLOAT(I-1)
  AN(I) = (2.0*TEMP - 1.0) / TEMP
  BN(I) = (TEMP - 1.0) / TEMP
END DO

!...SCALE SOLAR PRESSURE AT 1 AU

APRES = SPRES * AUS2

!...EMISSIVITY PARAMETERS WILL BE SCALED BY THE AVERAGE
!...IR FLUX OF THE EARTH (ASSUMING COMPLETE ABSORPTION
!...AND UNIFORM RERADIATION)

EPRES = SPRES * AUS2 / 4.0

!-----
  RETURN

!-----
END SUBROUTINE BWERP

```

Appendix D:

MSODP GLAS Solar Array Source Code

```

SUBROUTINE GLASSA(TMJD, X, V, SCC, ISAT, IFORCE, &
  ANGLE1, ANGLE2)
!-----
!  MSODP1/GLASSA(1.0)
!-----
!  PURPOSE: TO COMPUTE SOLAR ARRAY ORIENTATION ANGLES
!-----
!  INPUT PARAMETERS:
!
!    TMJD      MODIFIED JULIAN DATE
!    X         SATELLITE POSITION VECTOR, J2000 COORDINATES
!    V         SATELLITE VELOCITY VECTOR, J2000 COORDINATES
!    SCC       ROTATION MATRIX FROM J2000 TO SATELLITE
!              CENTERED COORDINATES
!    ISAT      SATELLITE SEQUENCE NUMBER
!    IFORCE    ALLOW UPDATE OF STOP ANGLE (= 0),
!              OTHERWISE AVOID (> 0)
!-----
!  OUTPUT PARAMETERS:
!
!    ANGLE1    +Y ARRAY ANGLE FROM BODY Z-AXIS,
!              POSITIVE TO +X AXIS (RAD)
!    ANGLE2    -Y ARRAY ANGLE FROM BODY Z-AXIS,
!              POSITIVE TO +X AXIS (RAD)
!-----
!  HISTORY:
!
!    OCT 2000  ORIGINALLY CODED BY H. RIM
!    APR 2002  SEPARATED FROM GLASATT BY S. YOON
!    APR 2002  ARTICULATION MODE FROM SOEFIL BY S. YOON
!    DEC 2002  ARTICULATION INHIBITION MODEL BY C. WEBB
!-----
!  MODULES
!-----

USE M_BTP, ONLY: BETAPRIME
USE M_CONVRT, ONLY: RAD, TWOPI, PI, DEG
USE M_GMVALU, ONLY: GM
USE M_MATRIX, ONLY: HG
USE M_ORIENT, ONLY: YAWLIM1, YAWLIM2
USE M_PERIOD, ONLY: PERIOD
USE M_PLANET, ONLY: PLANPS

```

```

      USE M_REFGEO, ONLY: BEA, GFLAT
      USE M_SOE
!-----
      IMPLICIT NONE
!-----
!  DECLARE INPUT AND OUTPUT VARIABLES

      INTEGER :: ISAT, IFORCE
      REAL :: TMJD, ANGLE1, ANGLE2
      REAL, DIMENSION(3) :: X, V
      REAL, DIMENSION(3,3) :: SCC
!-----
!  DECLARE LOCAL VARIABLES

      INTEGER :: ISOE, I, CUR_MODE, CUR_IDX
      REAL :: XLAT, DUM, RSUNX, RSUNZ
      REAL :: A, E, XINC, OM, CAP, XM, ARG, XMDOT
      REAL :: ARG_PASS, TPASS
      REAL, DIMENSION(3) :: XBF, RSOL, RSUN, RPASS
      REAL, DIMENSION(3) ONPASS, RSOL_PASS, RSUN_PASS
      REAL, DIMENSION(6) :: TEMP
      REAL, DIMENSION(3,3) :: SCC_PASS
      DOUBLE PRECISION :: TJD_PASS
!-----
!  SAVE VARIABLES (RETAINED BETWEEN SUBROUTINE CALLS)

      LOGICAL, SAVE :: FIRST = .TRUE.
      REAL, SAVE :: STOP_ANGLE
!-----
!  ASSIGN EARTH-SUN POSITION VECTOR TO LOCAL RSOL

      RSOL = PLANPS(1:3,10)
!-----
!  ROTATE SATELLITE POSITION TO EARTH BODY-FIXED FRAME
!  AND OBTAIN GEODETIC LATITUDE

      CALL M3331 (HG, X, XBF)
      CALL REFELL (XBF, BEA, GFLAT, .TRUE., XLAT, DUM, &
        DUM, DUM)
!-----
!  NOTE: IT IS ASSUMED THAT SCCROT IS CALLED BEFORE THE
!  CALL OF THIS SUBROUTINE AND THAT BETAPRIME HAS THE
!  CURRENT VALUE
!-----
!  IF REQUESTED, GET THE CURRENT SOLAR ARRAY MODE FROM
!  SEQUENCE OF EVENTS (SOE) FILE

```

```

IF (JSOEFIL(ISAT) > 0 .AND. JSOEFIL(ISAT) < 3) THEN

  ISOE = IND_SOE(ISAT)
  IF ((MODE_SA(ISOE,1,1) > TMJD) .OR. &
      (MODE_SA(ISOE,1,1) == 0.)) THEN
    PRINT *, ' ERR: SOLAR ARRAY ARTICULATION MODE &
              &IS NOT FOUND'
    PRINT *, '          AT ', TMJD, ' FOR SATID = ', ISAT
    CALL ABORT()
  END IF

  DO I = 1, IND_SA(ISOE)
    IF (MODE_SA(ISOE,I,1) == 0. .OR. &
        MODE_SA(ISOE,I,1) > TMJD) EXIT
    CUR_MODE = INT(MODE_SA(ISOE,I,2))
    CUR_IDX = I
  END DO

! -----
! OTHERWISE, DETERMINE THE CURRENT SOLAR ARRAY MODE
! USING THE BETA-PRIME ANGLE

ELSE

  IF (ABS(BETAPRIME(ISAT)*RAD) < YAWLIM2(ISAT)) THEN

    !...ARRAYS ARE NOT FIXED

    IF (ABS(XLAT*DEG) >= 60.0) THEN

      !...ARRAYS ARE INHIBITED

      CUR_MODE = 2
      IF (FIRST) THEN

        !...NO PRIOR STOP ANGLE AVAILABLE

        !...COMPUTE POLAR PASS START TIME (TPASS, MJD)

        TEMP(1:3) = X
        TEMP(4:6) = V
        CALL ORBELM (TEMP, GM, A, E, XINC, OM, CAP, &
                     XM, ARG)
        XMDOT = TWOPI * 86400.0 / PERIOD ! RAD/DAY
        IF (XLAT > 0.0) THEN

          !...NORTH POLAR PASS, ARGLAT = 60 DEG

          ARG_PASS = PI / 3.0

```



```

ELSE

    !...SOUTH POLAR PASS, ARGLAT = 240 DEG

    ARG_PASS = 4.0 * PI / 3.0

END IF
TPASS = TMJD + (ARG_PASS - ARG) / XMDOT

!...COMPUTE NORMALIZED POSITION VECTOR AT PASS
!...START (USE CURRENT XINC AND CAP)

RPASS(1) = COS(CAP) * COS(ARG_PASS) &
- SIN(CAP) * SIN(ARG_PASS) * COS(XINC)
RPASS(2) = SIN(CAP) * COS(ARG_PASS) &
+ COS(CAP) * SIN(ARG_PASS) * COS(XINC)
RPASS(3) = SIN(ARG_PASS) * SIN(XINC)

!...COMPUTE ORBIT NORMAL (USING CURRENT XINC
!...AND CAP)

ONPASS(1) = SIN(XINC) * SIN(CAP)
ONPASS(2) = -SIN(XINC) * COS(CAP)
ONPASS(3) = COS(XINC)

!...COMPUTE SCC MATRIX AT PASS START

SCC_PASS(1,:) = RPASS
IF (ABS(BETAPRIME(ISAT)*RAD) &
<= YAWLIM1(ISAT)) THEN

    IF (BETAPRIME(ISAT) <= 0.0) THEN
        SCC_PASS(2,:) = -ONPASS
    ELSE
        SCC_PASS(2,:) = ONPASS
    ENDIF
    CALL NORMALIZE(SCC_PASS(2,:))
    CALL CROSS(SCC_PASS(1,:), SCC_PASS(2,:), &
        SCC_PASS(3,:))
    CALL NORMALIZE(SCC_PASS(3,:))

ELSE

    IF (BETAPRIME(ISAT) <= 0.0) THEN
        SCC_PASS(3,:) = ONPASS
    ELSE
        SCC_PASS(3,:) = -ONPASS
    ENDIF

```

```

        CALL NORMALIZE(SCC_PASS(3,:))
        CALL CROSS(SCC_PASS(3,:), SCC_PASS(1,:), &
            SCC_PASS(2,:))
        CALL NORMALIZE(SCC_PASS(2,:))
    END IF

    !...COMPUTE SUN POSITION AT PASS START

    TJD_PASS = 2400000.5D+0 + DBLE(TPASS)
    CALL EPHEVL (TJD_PASS, .FALSE., 0)
    RSOL_PASS = PLANPS(1:3,10)

    !...COMPUTE SUN-POINTING ANGLE AT PASS START
    !...(STOP ANGLE, RADIANS)

    RPASS = A * RPASS
    RSUN_PASS = RSOL_PASS - RPASS
    CALL NORMALIZE(RSUN_PASS)
    CALL M3331(SCC_PASS, RSUN_PASS, RSUN_PASS)
    STOP_ANGLE = ATAN2(-RSUN_PASS(1), -RSUN_PASS(3))

    END IF

ELSE

    !...ARRAYS ARE ARTICULATING

    CUR_MODE = 0

    END IF

ELSE

    !...ARRAYS ARE FIXED

    CUR_MODE = 1

    END IF

END IF

!-----
! COMPUTE SOLAR ARRAY ANGLE BASED ON CURRENT MODE

IF (CUR_MODE == 0) THEN

    !...COMPUTE SATELLITE TO SUN VECTOR

    RSUN = RSOL - X
    CALL NORMALIZE(RSUN)

```

```

!...SUN VECTOR IN S/C BODY FRAME

CALL M3331(SCC, RSUN, RSUN)

! ROTATION ANGLE ABOUT Y-AXIS
! 0 DEG WHEN PANEL FACE IS TOWARD -Z-DIRECTION
! ROTATION IS POSITIVE SUCH THAT ANGULAR RATE
! VECTOR IS CONCORDANT WITH +Y

ANGLE1 = ATAN2(-RSUN(1), -RSUN(3))      ! RADIANS

!...UPDATE STOP ANGLE

IF (JSOEFIL(ISAT) == 0 .OR. JSOEFIL(ISAT) > 2) THEN

    ! FOR NOMINAL MODEL, UPDATE ONLY IF POLAR PASS
    ! IS DEFINITELY OVER (EQUATOR HAS BEEN CROSSED)

    IF ((XLAT > 0.0 .AND. V(3) > 0.0) .OR. &
        (XLAT < 0.0 .AND. V(3) < 0.0)) STOP_ANGLE = ANGLE1

ELSE

    ! ALWAYS UPDATE WHEN USING SOE FILE

    STOP_ANGLE = ANGLE1

END IF

ELSE IF (CUR_MODE == 1) THEN

    ANGLE1 = 0.0 ! RADIANS

ELSE

    ANGLE1 = STOP_ANGLE

END IF

ANGLE2 = ANGLE1
IF (FIRST) FIRST = .FALSE.

!-----
RETURN

!-----
END SUBROUTINE GLASSA

```

References

- Altamimi, Z., P. Sillard, and C. Boucher (2002), ITRF2000: A new release of the International Terrestrial Reference Frame for Earth science applications, *J. Geophys. Res.*, *107* (B10), 2214, doi: 10.1029/2001JB000561.
- American Society for Testing and Materials (2000), E-490-00a Standard solar constant and zero air mass solar spectral irradiance tables, American Society for Testing and Materials International, West Conshohocken, Pennsylvania.
- Anselmo, L., P. Farinella, A. Milani, and A. Nobili (1983), Effects of the Earth-reflected sunlight on the orbit of the LAGEOS satellite, *Astronomy and Astrophysics*, *117*, 3-8.
- Antreasian, P. (1992), Precision radiation force modeling for the TOPEX/Poseidon mission, Ph.D. dissertation, 223 pp., University of Colorado at Boulder, Boulder, Colorado.
- Arrhenius, S. (1900), Über die Ursache der Nordlichter, *Physikalische Zeitschrift*, *1* (6), 81-87.
- Bae, S., and B. Schutz (2002), Precision attitude determination (PAD), Version 2.2, Geoscience Laser Altimeter System (GLAS) algorithm theoretical basis document.
- Baker, R. (1966), Radiation on a satellite in the presence of partly diffuse and partly specular reflecting body, in *Trajectories of Artificial Celestial Bodies as Determined from Observations*, edited by J. Kovalevsky, pp. 85-150, Springer-Verlag, New York, New York.

- Bandeem, W., M. Halev, and I. Strange (1965), A radiation climatology in the visible and infrared from the TIROS meteorological satellites, *NASA Technical Note TN D-2534*, Goddard Space Flight Center, Greenbelt, Maryland.
- Bar-Sever, Y., and D. Kuang (2004), New empirically derived solar radiation pressure model for Global Positioning System satellites, *Interplanetary Network Progress Report 42-159*, Jet Propulsion Laboratory, Pasadena, California.
- Bartoli, A. (1876), *Sopra i Movimenti Prodotti dalla Luce e dal Calore e sopra il Radiometro di Crookes*, Le Monnier, Florence, Italy. Also: (1884): Il calorico raggiante e il secondo principio di termodinamica, *Il Nuovo Cimento*, 15, 193-202.
- Bell, M. and S. Green (1933), On radiometer action and the pressure of radiation, *Proceedings of the Physical Society*, 45 (2), 320-357.
- Bethe, H. (1939), Energy production in stars, *Phys. Rev.*, 55 (5), 434-456.
- Bettadpur, S., and R. Eanes (1994), Geographical representation of radial orbit perturbations due to ocean tides: implications for satellite altimetry, *J. Geophys. Res.*, 99 (C12), 24883-24894.
- Beutler, G., E. Brockmann, W. Gurtner, U. Hugentobler, L. Mervat, M. Rothacher, and A. Verdun (1994), Extended orbit modeling techniques at the CODE processing center of the international GPS service for geodynamics (IGS): theory and results, *Manuscripta Geodaetica*, 19, 367-386.
- Biermann, L. (1951), Kometenschweife und solare Korpuskularstrahlung, *Zeitschrift für Astrophysik*, 29, 274-286.

- Boltzmann, L. (1884a), Ueber eine von Hrn. Bartoli entdeckte Beziehung der Wärmestrahlung zum zweiten Hauptsatze, *Annalen der Physik und Chemie*, 22, 31-39.
- Boltzmann, L. (1884b), Ableitung des Stefan'schen Gesetzes, betreffend die Abhängigkeit der Wärmestrahlung von der Temperatur aus der electromagnetischen Lichttheorie, *Annalen der Physik und Chemie*, 22, 291-294.
- Boyle, P. (1977), Options: a Monte Carlo approach, *Journal of Financial Economics*, 4, 323-338.
- Brenner, A., et al. (2003), Derivation of range and range distributions from laser pulse waveform analysis for surface elevations, roughness, slope, and vegetation heights, Version 4.0, Geoscience Laser Altimeter System (GLAS) algorithm theoretical basis document.
- Byun, S. (1998), Satellite orbit determination using GPS carrier phase in pure kinematic mode, Ph.D. dissertation, 232 pp., University of Texas at Austin, Austin, Texas.
- Campbell, W., et al. (1979), Report of the Ice and Climate Experiment (ICEX) science and applications working group, Goddard Space Flight Center, Greenbelt, Maryland.
- Carazza, B. and H. Kragh (1989), Adolfo Bartoli and the problem of radiant heat, *Ann. Sci.*, 46, 183-194.
- Crookes, W. (1874), On attraction and repulsion resulting from radiation, *Phil. Trans. Roy. Soc.*, 164, 501-527.

- Danjon, A. (1954), Albedo, color, and polarization of the Earth, in *The Earth as a Planet*, edited by G. Kuiper, pp. 726-738, University of Chicago Press, Chicago, Illinois.
- Davis, G. (1996), GPS-based precision orbit determination for low altitude geodetic satellites, Ph.D. dissertation, 296 pp., University of Texas at Austin, Austin, Texas.
- de Pater, I., and J. Lissauer (2001), *Planetary Sciences*, 528 pp., Cambridge University Press, Cambridge, England.
- Debevec, D. (2002), ICESat mass properties — final report, revision E, *Systems Engineering Report 3257-MAS-007E*, Ball Aerospace & Technologies Corp., Commercial Space Operations, Boulder, Colorado, 4 Oct.
- Eddington, A. (1916), On the radiative equilibrium of the stars, *Monthly Notices of the Royal Astronomical Society*, 77, 16-35.
- Eddington, A. (1920), The internal constitution of stars, *Nature*, 106 (2653), 14-20.
- Eddington, A. (1924), On the relation between the masses and luminosities of the stars, *Monthly Notices of the Royal Astronomical Society*, 84, 308-332.
- Escobal, P. (1962), Orbital entrance and exit from the shadow of the Earth, *Amer. Rocket Soc. (ARS) J.*, 32, 1939-1941.
- Festou, M., H. Rickman, and R. West (1993), Comets: I. Concepts and observations, *Astronom. Astrophys. Rev.*, 4, 363-447.
- Feynman, R., R. Leighton, and M. Sands (1964), *The Feynman Lectures on Physics: Volume II*, p. 11, Addison-Wesley, London, England.

- Fliegel, H., W. Feess, W. Layton, and N. Rhodus (1985), The GPS radiation force model, in *Proceedings of the First International Symposium on Precise Positioning with the Global Positioning System*, pp. 113-119, National Geodetic Survey, NOAA, Rockville, Maryland.
- Fliegel, H., and T. Gallini (1989), Radiation pressure models for Block II GPS satellites, in *Proceedings of the Fifth International Geodetic Symposium on Satellite Positioning*, pp. 789-798, National Geodetic Survey, NOAA, Rockville, Maryland.
- Fliegel, H., T. Gallini, and E. Swift (1992), Global Positioning System radiation force model for geodetic applications, *J. Geophys. Res.*, *97* (B1), 559-568.
- Fröhlich, C., and J. Lean (1998), The Sun's total irradiance: cycles, trends and related climate change uncertainties since 1976, *Geophys. Res. Lett.*, *25* (23), 4377-4380.
- Galitzine, B. (1892), Ueber strahlende Energie, *Annalen der Physik*, *47*, 479-495. Also: translated (1893): On radiant energy, *Philosophical Magazine, Series 5*, *35* (213), 113-126.
- Garvin, J., J. Bufton, J. Blair, D. Harding, S. Luthcke, J. Frawley, and D. Rowlands (1998), Observations of the Earth's topography from the Shuttle Laser Altimeter (SLA): laser-pulse echo-recovery measurements of terrestrial surfaces, *Phys. Chem. Earth*, *23* (9-10), 1053-1068.
- Gebhart, B. (1957), Unified treatment for thermal radiation transfer processes — gray, diffuse radiators and absorbers, ASME Paper 57-A-34.
- Georgevic, R. (1971), Mathematical model of the solar radiation force and torques acting on the components of a spacecraft, *Technical Memorandum 33-494*, Jet Propulsion Laboratory, Pasadena, California.

- Georgevic, R. (1973), The solar radiation pressure on the Mariner 9 Mars orbiter, *Astronautica Acta*, 18 (2), 109-115.
- Georgevic, R. (1974), Mariner Venus/Mercury 1973 solar radiation force and torques, *Technical Memorandum 33-698*, Jet Propulsion Laboratory, Pasadena, California.
- Gibson, R. (1977), Creation of a “SHAPE” subroutine that accounts for both Earth and Moon shading, *GPS CELEST Change Request 10*, U.S. Naval Weapons Laboratory, Dahlgren, Virginia.
- GLAS Science Team (1997), Geoscience Laser Altimeter System (GLAS) science requirements, Version 2.01.
- Glassner, A. (1984), Space subdivision for fast ray tracing, *IEEE Computer Graphics and Applications*, 4 (10), 15-22.
- Granata, J. (2001), Personal communication.
- Graner, F., and J. Glazier (1992), Simulation of biological cell sorting using a two-dimensional extended Potts model, *Physical Review Letters*, 69 (13), 2013-2016.
- Haley, D. (1973), Solar radiation pressure calculations in the GEODYN program, *Planetary Sciences Department Report 008-73*, Goddard Space Flight Center, Greenbelt, Maryland.
- Hanson, R., and K. Haskell (1982), Algorithm 587: Two algorithms for the linearly constrained least squares problem, *ACM Transactions on Mathematical Software*, 8 (3), 323-333.

- Haskell, K., and R. Hanson (1981), An algorithm for linear least squares problems with equality and nonnegativity constraints, *Mathematical Programming*, 21, 98-118.
- Hellman, C. (1975), Kepler and comets, in *Four Hundred Years: Proceedings of Conferences Held in Honour of Johannes Kepler*, edited by A. Beer and P. Beer, pp. 789-796, Pergamon Press, New York.
- Herring, T., and K. Quinn (1999), Atmospheric delay correction to GLAS laser altimeter ranges, Version 1.0, Geoscience Laser Altimeter System (GLAS) algorithm theoretical basis document.
- Hertzsprung, E. (1905), Zur Strahlung der Sterne, *Zeitschrift für wissenschaftliche Photographie*, 3, 429-442.
- Hill, M., J. Marzouk, and J. Gill (2002), Personal communication.
- Hoffmann-Wellenhoff, B., H. Lichtenegger, and J. Collins (1997), *Global Positioning System: Theory and Practice*, 4th ed. (revised), 389 pp., Springer-Verlag/Wien, New York.
- Howell, J. (1982), *A Catalog of Radiation Configuration Factors*, 243 pp., McGraw-Hill, New York.
- Howell, J., and M. Perlmutter (1964), Monte Carlo solution of thermal transfer through radiant media between gray walls, *J. Heat Transfer*, 86 (1), 116-122.
- Iacometti, J. (2002), ICESat on-orbit center-of-gravity equations, *Systems Engineering Report 3257-MAS-013*, Ball Aerospace & Technologies Corp., Commercial Space Operations, Boulder, Colorado, 1 Oct.

- Khatib, A., and F. Sturms (1970), Umbra-penumbra shadow model for DPTRAJ, *Programming Request 392-36*, Jet Propulsion Laboratory, Pasadena, California, 24 June.
- Knocke, P. (1989), Earth radiation pressure effects on satellites, Ph.D. dissertation, 216 pp., University of Texas at Austin, Austin, Texas.
- Knocke, P., J. Ries, and B. Tapley (1988), Earth radiation pressure effects on satellites, Paper 88-4292-CP, AIAA/AAS Astrodynamics Specialists Conference, Minneapolis, Minnesota, 15-17 Aug.
- Kozai, Y. (1961), Effects of solar radiation pressure on the motion of an artificial satellite, *Smithsonian Astrophysical Observatory Special Report*, 56, 25-33.
- Krabill, W., R. Thomas, K. Jezek, K. Kuivinen, and S. Manizade (1995a), Greenland ice sheet thickness changes measured by laser altimetry, *Geophys. Res. Lett.*, 22 (17), 2341-2344.
- Krabill, W., R. Thomas, C. Martin, R. Swift, and E. Frederick (1995b), Accuracy of airborne laser altimetry over the Greenland ice sheet, *Int. J. Rem. Sens.*, 16 (7), 1211-1222.
- Kubitschek, D., and G. Born (1999), Radiation pressure forces, the anomalous acceleration, and center of mass motion for the TOPEX/Poseidon spacecraft, *Adv. Astronaut. Sci.*, 102, 667-683.
- Labs, D., and H. Neckel (1968), The radiation of the solar photosphere from 2000 Å to 100 μ , *Zeitschrift für Astrophysik*, 69, 1-73.
- Laboratory for Atmospheric and Space Physics (2003), ICESat mission operations center external interface control document, Revision B, Laboratory for Atmospheric and Space Physics, University of Colorado at Boulder, Boulder, Colorado.

- Lála, P., F. Barlier, and G. Oyharcabal (1978), Interpretation of the D5B satellite measurements and the new model of the Earth's albedo, *Bull. Astronom. Inst. Czech.*, 29 (4), 238-243.
- Lautman, D. (1977a), Perturbations of a close-earth satellite due to sunlight diffusely reflected from the Earth: I. Uniform albedo, *Celest. Mech.*, 15, 387-420.
- Lautman, D. (1977b), Perturbations of a close-earth satellite due to sunlight diffusely reflected from the Earth: II. Variable albedo, *Celest. Mech.*, 16, 3-25.
- Lawson, C., and R. Hanson (1974), *Solving Least Squares Problems*, 340 pp., Prentice-Hall, Englewood-Cliffs, New Jersey.
- Lebedev, P. (1901), Experimental examination of light pressure, *Annalen der Physik*, 6 (11), 433-458.
- Lemoine, F., D. Rowlands, N. Zelensky, S. Luthcke, C. Cox, and G. Marr (1999a), Precise orbit determination for the Geosat Follow-On spacecraft, NASA/CP-1999-209235, 1999 Flight Mechanics Symposium, NASA Goddard Spaceflight Center, Greenbelt, Maryland, 18-20 May.
- Lemoine, F., D. Rowlands, D. Smith, D. Chinn, D. Pavlis, S. Luthcke, G. Neumann, and M. Zuber (1999b), Orbit determination for Mars Global Surveyor during mapping, *Adv. Astronaut. Sci.*, 103, 435-452.
- Lochry, R. (1966), The perturbative effects of diffuse radiations from the Earth and the Moon on close satellites, Ph.D. dissertation, 177 pp., University of California Los Angeles, Los Angeles, California.
- Lundberg, J., M. Feulner, P. Abusali, and C. Ho (1991), Improving the numerical integration solution of satellite orbits in the presence of solar radiation

- pressure using modified back differences, *Adv. Astronaut. Sci.*, 75, 1227-1242.
- Luthcke, S., J. Marshall, S. Rowton, K. Rachlin, C. Cox, and R. Williamson (1997), Enhanced radiative force modeling of the Tracking and Data Relay Satellites, *J. Astronaut. Sci.*, 45 (3), 349-370.
- Luthcke, S., D. Rowlands, J. McCarthy, D. Pavlis, and E. Stoneking (2000), Spaceborne laser-altimeter-pointing bias calibration from range residual analysis, *J. Spacecraft and Rockets*, 37 (3), 374-384.
- Marshall, J., P. Antreasian, G. Rosborough, and B. Putney (1991), Modeling radiation forces acting on satellites for precision orbit determination, *Adv. Astronaut. Sci.*, 76, 73-96.
- Marshall, J., and S. Luthcke (1994a), Modeling radiation forces acting on TOPEX/Poseidon for precision orbit determination, *J. Spacecraft and Rockets*, 31 (1), 99-105.
- Marshall, J., and S. Luthcke (1994b), Radiative force model performance for TOPEX/Poseidon precision orbit determination, *J. Astronaut. Sci.*, 42 (2), 229-246.
- Martino, A. (2002), Personal communication.
- Maxwell, J. (1873), *A Treatise on Electricity and Magnetism*, Vol. II, p. 319, Clarendon Press, Oxford, England.
- McCarthy, D. (1996), International Earth Rotation Service (IERS) conventions, *IERS Technical Note 21*, U.S. Naval Observatory, Washington, D.C.

- McCarthy, J., and T. Martin (1977), A computer efficient model of Earth albedo satellite effects, *Planetary Sciences Department Report 012-77*, Goddard Space Flight Center, Greenbelt, Maryland.
- Metropolis, N., and S. Ulam (1949), The Monte Carlo method, *Journal of the American Statistical Association*, *44* (247), 335-341.
- Muhleman, D., R. Hudson, D. Holdridge, R. Carpenter, and K. Oslund (1960), Observed solar pressure perturbations for Echo I, *Science*, *132* (3438), 1487.
- Mullins, L. (1991), Calculating satellite umbra/penumbra entry and exit positions and times, *J. Astronaut. Sci.*, *39* (4), 411-422.
- Mulser, P. (1985), Radiation pressure on macroscopic bodies, *J. Opt. Soc. Amer. B*, *2* (11), 1814-1829.
- Musen, P., R. Bryant, and A. Bailie (1960), Perturbations in perigee height of Vanguard I, *Science*, *131* (3404), 935-936.
- National Research Council (1990), *Sea-Level Change*, 234 pp., National Academy Press, Washington, D.C.
- Naur, P. (1954), Two models for the interior of the Sun, *Astrophys. J.*, *119*, 365-370.
- Neta, B., and D. Vallado (1998), On satellite umbra/penumbra entry and exit positions, *J. Astronaut. Sci.*, *46* (1), 91-103.
- Newton, I. (1726), *The Principia: Mathematical Principles of Natural Philosophy*, 3rd ed., translated by I. Cohen and A. Whitman (1999), p. 924, University of California Press, Berkeley, California.

- Nichols, E. and G. Hull (1901), A preliminary communication on the pressure of heat and light radiation, *Physical Review (Series I)*, 13 (5), 307-320.
- O'Keefe, J., A. Eckels, and R. Squires (1959), The gravitational field of the Earth, *Astronom. J.*, 64 (7), 245-253.
- Panczak, T. (1989), A fast, linear time, Monte Carlo radiation interchange program utilizing adaptive spatially coherent subdivision, in *Proceedings of the Sixth International Conference on Numerical Methods in Thermal Problems*, pp. 702-712, Pineridge Press, Swansea, United Kingdom.
- Panczak, T., S. Rickman, L. Fried, and M. Welch (1991), Thermal synthesizer system: an integrated approach to spacecraft thermal analysis, Paper SAE-911582, 21st International Conference on Environmental Systems, Society of Automotive Engineers, San Francisco, California, 15-18 Jul.
- Parkinson, R., H. Jones, and I. Shapiro (1960), Effects of solar radiation pressure on Earth satellite orbits, *Science*, 131 (3404), 920-921.
- Planck, M. (1931), Maxwell's influence on theoretical physics in Germany, in *James Clerk Maxwell: A Commemorative Volume 1831-1931*, pp. 57-58, Cambridge University Press, Cambridge, England.
- Plummer, H. (1905), On the possible effects of radiation on the motion of comets, with special reference to Encke's comet, *Monthly Notices of the Royal Astronomical Society*, 65, 229-237.
- Plummer, H. (1906), On the effects of radiation on the motion of comets (second note), *Monthly Notices of the Royal Astronomical Society*, 67, 63-67.
- Poynting, J. (1904), Radiation in the solar system: its effect on temperature and its pressure on small bodies, *Phil. Trans. Roy. Soc. A*, 202, 525-552.

- Qiu, J., et al. (2003), Earthshine and the Earth's albedo: 1. Earthshine observations and measurements of the lunar phase function for accurate measurements of the Earth's Bond albedo, *J. Geophys. Res.*, *108* (D22), 4709, doi: 10.1029/2003JD003610.
- Raschke, E., T. Vonder Haar, M. Pasternak, and W. Bandeen (1973), The radiation balance of the Earth-atmosphere system from Nimbus 3 radiation measurements, *NASA Technical Note TN D-7249*, Goddard Space Flight Center, Greenbelt, Maryland.
- Reynolds, O. (1879), On certain dimensional properties of matter in the gaseous state, *Phil. Trans. Roy. Soc.*, *170*, 727-845.
- Ridley, J., and K. Partington (1988), A model of satellite radar altimeter return from ice sheets. *Int. J. Rem. Sens.*, *9* (4), 601-624.
- Ries, J. (1990), TOPEX precision orbit determination software intercomparison plan, Center for Space Research, University of Texas at Austin, Austin, Texas.
- Rim, H. (1992), TOPEX orbit determination using GPS tracking system, Ph.D. dissertation, 224 pp., University of Texas at Austin, Austin, Texas.
- Rim, H., G. Davis, and B. Schutz (1996), Dynamic orbit determination for the EOS laser altimeter satellite (EOS ALT/GLAS) using GPS measurements, *J. Astronaut. Sci.*, *44* (3), 409-424.
- Rim, H., C. Webb, and B. Schutz (1999), Analysis of GPS and satellite laser ranging (SLR) data for ICESat precision orbit determination, *Adv. Astronaut. Sci.*, *102*, 635-648.

- Rim, H., C. Webb, and B. Schutz (2000), Effect of GPS orbit errors on ICESat precision orbit determination, Paper AIAA-2000-4234, AIAA/AAS Astrodynamics Specialists Conference, Denver, Colorado, 14-17 Aug.
- Rim, H., and B. Schutz (2002), Precision orbit determination (POD), Version 2.2, Geoscience Laser Altimeter System (GLAS) algorithm theoretical basis document.
- Rim, H., C. Webb, S. Yoon, and B. Schutz (2007), Macro-model tuning experiment for ICESat precision orbit determination, Paper AAS-07-165, AAS/AIAA Space Flight Mechanics Meeting, Sedona, Arizona, 28 Jan–1 Feb.
- Robertson, H. (1937), Dynamical effects of radiation in the solar system, *Monthly Notices of the Royal Astronomical Society*, *97*, 423-438.
- Rubincam, D. (1982), On the secular decrease in the semimajor axis of LAGEOS's orbit, *Celest. Mech.*, *26*, 361-382.
- Rubincam, D., and N. Weiss (1986), Earth albedo and the orbit of LAGEOS, *Celest. Mech.*, *38*, 233-296.
- Rubincam, D. (1987), LAGEOS orbit decay due to infrared radiation from Earth, *J. Geophys. Res.*, *92* (B2), 1287-1294.
- Rubincam, D., P. Knocke, V. Taylor, and S. Blackwell (1987), Earth anisotropic reflection and the orbit of LAGEOS, *J. Geophys. Res.*, *92* (B11), 11662-11668.
- Rubincam, D. (1988), Yarkovsky thermal drag on LAGEOS, *J. Geophys. Res.*, *93* (B11), 13805-13810.

- Russell, H. (1910), Some hints on the order of stellar evolution, *Science*, 32 (833), 883-884.
- Sabra, A. (1967), *Theories of Light from Descartes to Newton*, 363 pp., Oldbourne Book Co., London, England.
- Salpeter, E. (1952), Nuclear reactions in the stars. I. Proton-proton chain, *Phys. Rev.*, 88 (3), 547-553.
- Schagrin, M. (1974), Early observations and calculations on light pressure, *Amer. J. Physics*, 42 (11), 927-940.
- Schuster, A. (1876), On the nature of the force producing the motion of a body exposed to the rays of heat and light, *Phil. Trans. Roy. Soc.*, 166, 715-724.
- Schutz, B. (1998), Spaceborne laser altimetry: 2001 and beyond, in *Book of Extended Abstracts, Wegener-98*, edited by H. Plag, Norwegian Mapping Authority, Honefoss, Norway.
- Schutz, B. (2002), Laser footprint location (geolocation) and surface profiles, Version 3.0, Geoscience Laser Altimeter System (GLAS) algorithm theoretical basis document.
- Schutz, B., M. Lisano, G. Davis, M. Watkins, and G. Powell (1994), Precision orbit determination for the EOS laser altimeter satellite (EOS ALT/GLAS), *Adv. Astronaut. Sci.*, 87, 497-506.
- Schwarzschild, K. (1901), Der Druck des Lichts auf kleine Kugeln und die Arrhenius'sche Theorie der Cometenschweife, *Sitzungsberichte der mathematisch-physikalischen Classe der k.b. Akademie der Wissenschaften zu München*, 31, 293-338.

- Sehna, L. (1966a), The perturbations of the orbital elements caused by the pressure of the radiation reflected from the Earth, in *Trajectories of Artificial Celestial Bodies as Determined from Observations*, edited by J. Kovalevsky, pp. 80-84, Springer-Verlag, New York, New York.
- Sehna, L. (1966b), The influence of the re-radiation of the Earth on the motion of the artificial satellites, in *The Theory of Orbits in the Solar System and in Stellar Systems*, edited by G. Kontopoulos, pp. 345-354, Academic Press, London, England.
- Sehna, L. (1979), The Earth albedo model in spherical harmonics, *Bull. Astronom. Inst. Czech.*, 30 (4), 199-204.
- Sehna, L. (1981), Effects of the terrestrial infrared radiation pressure on the motion of an artificial satellite, *Celest. Mech.*, 25, 169-179.
- Shapiro, I. (1963), The prediction of satellite orbits, in *Dynamics of Satellites*, edited by M. Roy, pp. 257-312, Springer-Verlag, Berlin, Germany.
- Shapiro, I., and H. Jones (1960), Perturbations of the orbit of the Echo balloon, *Science*, 132 (3438), 1484-1486.
- Shu, F. (1982), *The Physical Universe: An Introduction to Astronomy*, 584 pp., University Science Books, Mill Valley, California.
- Siegel, R. and J. Howell (2002), *Thermal Radiation Heat Transfer*, 868 pp., Taylor and Francis, New York, New York.
- Silverman, E. (1995), Space environmental effects on spacecraft: LEO materials selection guide, *NASA Contractor Report 4661*, Langley Research Center, Hampton, Virginia.

- Smith, D. (1970), Earth-reflected radiation pressure, in *Dynamics of Satellites*, edited by B. Morando, Springer-Verlag, New York, New York.
- Smith, D., and P. Dunn (1980), Long term evolution of the LAGEOS orbit, *Geophys. Res. Lett.*, *7*, 437-440.
- Springer, T., G. Beutler, and M. Rothacher (1998), A new solar radiation pressure model for the GPS satellites, IGS 1998 Analysis Center Workshop, ESOC, Darmstadt, Germany, 9-11 Feb.
- Stephens, G., G. Campbell, and T. Vonder Haar (1981), Earth radiation budgets, *J. Geophys. Res.*, *86* (C10), 9739-9760.
- Sun, X. and J. Marzouk (2003), Personal communication.
- Tapley, B. (1973), Statistical orbit determination, in *Recent Advances in Dynamical Astronomy*, edited by B. Tapley and V. Szebehely, pp. 396-425, Reidel, Dordrecht, Netherlands.
- Tapley, B., et al. (1994), Precision orbit determination for TOPEX/Poseidon, *J. Geophys. Res.*, *99* (C12), 24383-24404.
- Tapley, B., S. Bettadpur, M. Watkins, and C. Reigber (2004a), The Gravity Recovery and Climate Experiment: mission overview and early results, *Geophys. Res. Lett.*, *31* (5), L09607, doi: 10.1029/2004GL019920.
- Tapley, B., B. Schutz, and G. Born (2004b), *Statistical Orbit Determination*, 547 pp., Elsevier Academic Press, Boston, Massachusetts.
- Tapley, B., J. Ries, S. Bettadpur, D. Chambers, M. Cheng, F. Condi, B. Gunter, Z. Kang, P. Nagel, R. Pastor, et al. (2005), GGM02 — An improved Earth gravity field model from GRACE, *J. Geodesy*, *79*, 467-478, doi: 10.1007/s00190-005-0480-z.

- Wahr, J., D. Wingham, and C. Bentley (2000), A method of combining ICESat and GRACE satellite data to constrain Antarctic mass balance, *J. Geophys. Res.*, *105* (B7), 16279-16294.
- Warrick, R., C. LeProvost, M. Meier, J. Oerlemans, and P. Woodworth (1996), Changes in sea level, in *Climate Change 1995: The Science of Climate Change*, edited by J. Houghton et al., pp. 361-405, Cambridge University Press, Cambridge, England.
- Webb, C. (2002), The ICRF-to-ITRF transformation: a comparison of fundamental Earth orientation models found in MSODP and CALC, *Technical Report CSR-02-01*, Center for Space Research, University of Texas at Austin, Austin, Texas.
- Webb, C., H. Rim, and B. Schutz (2001), Radiation force modeling for ICESat precision orbit determination, *Adv. Astronaut. Sci.*, *109*, 501-518.
- Whitted, T. (1980), An improved illumination model for shaded display, *Communications of the Association for Computing Machinery (ACM)*, *23* (6), 343-349.
- Willson, R. (1978), Accurate solar ‘constant’ determinations by cavity pyrhelimeters, *J. Geophys. Res.*, *83* (C8), 4003-4007.
- Willson, R., and H. Hudson (1991), The Sun’s luminosity over a complete solar cycle, *Nature*, *351*, 42-44.
- Willson, R., and A. Mordvinov (2003), Secular total solar irradiance trend during solar cycles 21-23, *Geophys. Res. Lett.*, *30* (5), 1199, doi: 10.1029/2002GL016038.

- Woodburn, J. (2001), Mitigation of the effects of eclipse boundary crossings on the numerical integration of orbit trajectories using an Encke type correction algorithm, *Adv. Astronaut. Sci.*, 108, 1679-1690.
- Worrall, J. (1982), The pressure of light: the strange case of the vacillating ‘crucial experiment’, *Stud. Hist. Phil. Sci.*, 13 (2), 133-171.
- Wu, S., T. Yunck, and C. Thornton (1987), Reduced-dynamic technique for precise orbit determination of low Earth satellites, *Adv. Astronaut. Sci.*, 65, 101-113.
- Wyatt, S. (1963), The effect of terrestrial radiation pressure on satellite orbits, in *Dynamics of Satellites*, edited by M. Roy, pp. 180-196, Springer-Verlag, Berlin, Germany.
- Yi, D., J. Minster, and C. Bentley (1999), Ocean tidal loading corrections, Version 1.0, Geoscience Laser Altimeter System (GLAS) algorithm theoretical basis document.
- Zwally, H. (1975), General discussion: the state of the art – and where do we go from here? *J. Glaciology*, 15 (73), 444.
- Zwally, H., and A. Brenner (2001), Ice sheet dynamics and mass balance, in *Satellite Altimetry and Earth Sciences: A Handbook of Techniques and Applications*, edited by L. Fu and A. Cazenave, pp. 351-369, Academic Press, San Diego, California.
- Zwally, H., et al. (2002), ICESat’s laser measurements of polar ice, atmosphere, ocean, and land, *J. Geodynamics*, 34, 405-445.

Vita

Charles Edward Webb was born at George Air Force Base, in Victorville, California, on May 3, 1968, to Paul Carr and Verna Mae (Schouten) Webb. After graduating in 1986, as valedictorian of Judson High School, in Converse, Texas, he enrolled as a freshman at Cornell University, in Ithaca, New York. During his junior and senior years, he worked as a systems engineer in the Space Station program office at GE Astro Space, in Valley Forge, Pennsylvania. He graduated Tau Beta Pi in 1990, receiving the Bachelor of Science degree in mechanical and aerospace engineering. Soon thereafter, he joined the GE Edison Engineering Program, moving to the Astro Space facility in Princeton, New Jersey. While there, he held positions in mechanical systems, propulsion systems design, and mission design and analysis. He earned the Master of Science in Engineering degree, in systems engineering, from the University of Pennsylvania, in 1994. He continued to serve as a Senior Engineer in mission design and analysis until 1995, when he entered the Graduate School of the University of Texas at Austin, under the guidance of Professor Bob E. Schutz.

Permanent address: 10307 Morado Cove #203, Austin, Texas 78759-6622.

This dissertation was typed by the author.